

DISS. ETH NO. 29973

***CHEMICAL AND CLIMATIC IMPACTS OF SOLID PARTICLES FOR  
STRATOSPHERIC SOLAR CLIMATE INTERVENTION***

A thesis submitted to attain the degree of

DOCTOR OF SCIENCES

(Dr. sc. ETH Zurich)

presented by

*SANDRO VATTIONI*

*MSc ETH in Atmospheric and Climate Science*

born on 21.12.1991

accepted on the recommendation of  
Prof. Dr. Thomas Peter, examiner  
Dr. Gabriel Chiodo, co-examiner  
Prof. Dr. Heini Wernli, co-examiner  
Prof. Dr. James Haywood, co-examiner

2024



*“It’s not a matter of predicting the future, but of being prepared for it.”*

— Pericles, 490-429 BC

*“The greatest threat to our planet is the belief that someone else will save it.”*

— Robert Swan, \*1959





# Table of contents

<b>Abstract</b>	<b>ix</b>
<b>Zusammenfassung</b>	<b>xi</b>
<b>1 Introduction</b>	<b>1</b>
1.1 Ethics and governance of SAI . . . . .	2
1.2 State of research . . . . .	4
1.3 Motivation . . . . .	6
1.4 Research questions . . . . .	7
1.5 Thesis outline . . . . .	7
<b>2 Importance of microphysical settings for climate forcing by stratospheric SO<sub>2</sub> injections as modelled by SOCOL-AERv2</b>	<b>9</b>
2.1 Introduction . . . . .	11
2.2 Model description and experimental setup . . . . .	13
2.2.1 SOCOL-AERv2 . . . . .	13
2.2.2 SOCOLv4 . . . . .	14
2.2.3 Experimental setup . . . . .	15
2.3 Results . . . . .	17
2.3.1 Influence of microphysical settings on aerosol size distribution . . .	17
2.3.2 Influence of microphysical settings on global means of particle size, aerosol burden and radiative forcing . . . . .	21
2.3.3 Influence of settings on meridional distributions of aerosol burden, radiative forcing, and ozone . . . . .	22
2.3.4 Influence of settings on SAD and stratospheric temperature . . . .	23
2.3.5 Influence of settings on modeling the eruption of Mt. Pinatubo . .	25
2.4 Comparison with other work and conclusions . . . . .	26
Appendix 2: Supplementary information . . . . .	30
A: Summary of sulfur burdens and fluxes . . . . .	30
B: Importance of proper treatment of gasphase H <sub>2</sub> SO <sub>4</sub> concentrations . . .	32
C: Influence of settings on aerosol surface area density . . . . .	33
D: Influence of settings on atmospheric temperature profile . . . . .	36
<b>3 A fully coupled solid particle microphysics scheme for stratospheric aerosol injections within the aerosol-chemistry-climate-model SOCOL-AERv2</b>	<b>39</b>
3.1 Introduction . . . . .	41
3.2 Model description . . . . .	44
3.2.1 SOCOL-AERv2 . . . . .	44
3.2.2 The interactive solid particle microphysics module . . . . .	45
3.2.3 Alumina particles . . . . .	50
3.2.4 Calcite particles . . . . .	53
3.3 Experimental setup . . . . .	55
3.4 Results . . . . .	56

TABLE OF CONTENTS

---

3.4.1	Radiative forcing efficiency . . . . .	57
3.4.2	Coagulation . . . . .	57
3.4.3	The Stratospheric Sulfur Cycle under conditions of SAI of alumina particles . . . . .	59
3.4.4	Contact angle sensitivity analysis . . . . .	62
3.4.5	The Stratospheric sulfur cycle under conditions of SAI of calcite particles . . . . .	63
3.4.6	Solid particle number concentrations and surface area densities . . .	63
3.4.7	Ozone response to calcite and alumina particle injection . . . . .	64
3.5	Conclusions . . . . .	67
Appendix 3: Supplementary Information . . . . .		70
A: Discrete Element Model simulations . . . . .		70
B: Sedimentation velocities in SOCOL-AERv2 . . . . .		73
C: Optical Properties used in SOCOL-AERv2 . . . . .		74
D: Stratospheric aerosol size distributions . . . . .		77
E: The stratospheric sulphur cycle under different alumina injection rates .		78
F: The stratospheric sulphur cycle under different calcite injection rates . .		80
G: Number concentrations and surface area densities for calcite particles .		81
<b>4</b>	<b>Chemical impact of stratospheric alumina particle injection for solar radiation modification and related uncertainties</b>	<b>83</b>
4.1	Introduction . . . . .	84
4.1.1	Aging and non-aging solid particles . . . . .	84
4.1.2	Experimental data on heterogeneous chemistry on alumina particles	85
4.1.3	Previous modeling studies on SAI of alumina particles . . . . .	86
4.2	Methods . . . . .	88
4.2.1	Reactive uptake on alumina surfaces . . . . .	88
4.2.2	Aerosol-Chemistry-Climate Model description . . . . .	90
4.2.3	Modeling scenarios . . . . .	91
4.3	Results . . . . .	91
4.4	Summary and conclusions . . . . .	93
Appendix 4: Supplementary information . . . . .		95
A: The different parameterizations assumed in this study . . . . .		95
B: Details and caveats of the Molina et al. 1997 measurements . . . . .		96
C: Weisenstein et al. (2015) modeling details . . . . .		98
D: Contact angle measurements of sulfuric acid on alumina particles . . . . .		99
E: Experimental evidence for chemically aging and non-aging materials . .		101
F: Langmuir-Hinshelwood kinetics of ClONO <sub>2</sub> + HCl on an HNO <sub>3</sub> -dosed surface . . . . .		102
G: Sensitivity to injected particle size and surface area availability . . . . .		108
H: Composition changes . . . . .		110
I: Sensitivity to injection altitude and to other heterogeneous reactions on solid particles . . . . .		114
<b>5</b>	<b>X-ray photoelectron spectroscopy and elastic recoil detection analysis to quantify uptake of HCl and HNO<sub>3</sub> on calcite surfaces</b>	<b>117</b>
5.1	Introduction . . . . .	119
5.1.1	Factors influencing uptake coefficient measurements . . . . .	120

TABLE OF CONTENTS

---

5.1.2	The importance of "long-term" depth-resolving experiments under stratospheric conditions . . . . .	122
5.2	Methods . . . . .	123
5.2.1	Ambient Pressure X-ray Photoelectron Spectroscopy (AP-XPS) . . . . .	124
5.2.2	Heavy Ion Elastic Recoil Detection Analysis (HI-ERDA) . . . . .	128
5.3	Results . . . . .	131
5.3.1	AP-XPS results . . . . .	131
5.3.2	HI-ERDA results . . . . .	137
5.4	Discussion . . . . .	141
5.4.1	Uptake coefficients representative for calcite particles throughout their stratospheric residence time . . . . .	142
5.4.2	Estimate of gas phase HNO <sub>3</sub> depletion through uptake by calcite particles . . . . .	143
5.5	Conclusions and outlook . . . . .	144
Appendix 5: Supplementary information . . . . .		146
A:	Uptake of HCl and HNO <sub>3</sub> on calcite . . . . .	146
B:	Proposed Mechanisms . . . . .	159
C:	AP-XPS experimental setup . . . . .	163
D:	Attenuation Model . . . . .	164
E:	HI-ERDA experimental setup . . . . .	165
F:	ERDA experimental setup . . . . .	165
<b>6</b>	<b>Concluding Perspectives</b> . . . . .	<b>167</b>
6.1	Introduction . . . . .	168
6.2	The interactive solid particle microphysics scheme in SOCOL-AERv2 . . . . .	169
6.3	Experimental setup . . . . .	170
6.4	Different perspectives on RF efficiency . . . . .	171
6.5	Stratospheric chemistry . . . . .	174
6.6	Stratospheric warming and dynamical response . . . . .	177
6.7	Ecological impacts . . . . .	180
6.8	Conclusion and Discussion . . . . .	182
Appendix 4: Supplementary information . . . . .		185
A:	Absolute global mean quantities . . . . .	185
B:	Zonal mean particle number densities . . . . .	187
C:	Global mean quantities normalised per injection rate and per resulting stratospheric aerosol burden . . . . .	188
D:	Zonal mean SAD . . . . .	189
E:	Zonal mean dynamical impacts for 2020 and 2090 conditions . . . . .	191
<b>7</b>	<b>Outlook</b> . . . . .	<b>195</b>
7.1	Aerosol Microphysics, Optics and Radiation Model Intercomparison Project (AMOR-MIP) . . . . .	196
7.1.1	Anticipated outcomes . . . . .	198
7.2	Stratospheric Aerosol Injection across Scales (SAIaS): From near-field agglomerates and size distributions to global and regional impacts . . . . .	198
7.2.1	Objectives and Research Questions . . . . .	198
7.2.2	Proposed work in SAIaS . . . . .	199
7.2.3	Relevance and impact of SAIaS . . . . .	201

TABLE OF CONTENTS

---

<b>Addenda</b>	<b>203</b>
Bibliography . . . . .	204
Thanks and acknowledgements . . . . .	229
CV . . . . .	233

# Abstract

The increasingly dismal prospects for climate change mitigation are driving research on stratospheric aerosol injection (SAI), i.e., the injection of aerosols or their precursors into the stratosphere with the aim of increasing the Earth's albedo to cool the global climate. SAI aims to quickly mitigate some of the adverse effects of climate change at low cost. The idea arose mainly from observations of the cooling effect of explosive volcanic eruptions, which explains why research on SAI has so far focused on the emission of  $\text{SO}_2$ , the main precursor of volcanic sulfuric acid aerosols in the stratosphere. However, SAI by means of sulfuric acid aerosols could lead to a number of negative side effects such as impacts on the ozone layer and stratospheric heating, and sizable effects on the large scale atmospheric circulation.

A recent model intercomparison of chemistry-climate models with interactive stratospheric  $\text{H}_2\text{SO}_4/\text{H}_2\text{O}$  aerosol has revealed large uncertainties in how the microphysical aerosol processes are implemented. In particular, it was shown that compared to short-duration volcanic  $\text{SO}_2$  emission, the continuous  $\text{SO}_2$  injections in climate intervention scenarios can pose a greater challenge to the numerical implementation of microphysical processes such as nucleation, condensation, and coagulation. This thesis shows how simply changing the timesteps and the sequencing of microphysical processes in the sectional aerosol-chemistry-climate model SOCOL-AERv2 can result in globally averaged radiative forcing ranging from -2.3 to -5.3 W/m<sup>2</sup> when 25 Mt/yr  $\text{SO}_2$  is injected. This is mostly a result of a too long microphysical timestep in combination with the strong non-linearity of aerosol nucleation to  $\text{H}_2\text{SO}_4$  supersaturation. Taken together these results underscore how structural aspects of model representation of aerosol microphysical processes become important under conditions of elevated stratospheric sulfur in determining atmospheric chemistry and climate impacts.

Recent studies also suggest that the injection of solid particles such as calcite or alumina particles could lead to more effective cooling per aerosol burden compared to SAI via sulfuric acid aerosols. At the same time, solid particles could reduce some of the negative side effects such as ozone depletion or stratospheric heating due to their better optical, chemical and microphysical properties. However, this thesis shows that some of these studies relied on highly simplified aerosol model approaches or nonphysical assumptions on heterogeneous chemistry. Through experimental laboratory work and climate modeling, this thesis presents a holistic assessment of SAI using calcite and alumina particles and their uncertainties compared to SAI using sulfuric acid aerosols .

Calcite particles have been proposed as potential injection candidates for SAI since they can react with acidic gases in the stratosphere (i.e., HCl,  $\text{HNO}_3$  and  $\text{H}_2\text{SO}_4$ ). Removal of HCl can lead to faster healing of the ozone layer. Conversely, strong removal of  $\text{HNO}_3$  could also result in enhanced ozone depletion due to decreased deactivation of chlorine. This work used in situ X-ray photoelectron spectroscopy (XPS) and elastic recoil detection analysis (ERDA) to measure the uptake of  $\text{HNO}_3$  and HCl on calcite under near-stratospheric conditions, and determined their penetration into deeper layers below the surface and the subsequent chemical transformation of calcite into calcium chlorides and nitrates. Uptake coefficients ranging from  $\gamma_{\text{HNO}_3} = 10^{-5}$  to  $10^{-4}$  were measured for  $\text{HNO}_3$  with XPS and ranging from  $\gamma_{\text{HNO}_3, \text{HCl}} = 10^{-6}$  to  $10^{-5}$  for both  $\text{HNO}_3$  and HCl measured with ERDA. Putting these results into context of SAI, the uptake of HCl and  $\text{HNO}_3$

decreases with stratospheric exposure time due to the formation of product layers at the surface and subsequent limitation of the uptake by slow ion diffusion. The measurements indicate that exposure of these particles to typically 5 ppb  $\text{HNO}_3$  and 1 ppb  $\text{HCl}$  over stratospheric residence times of about 1 year leads to mean uptake coefficients  $< 10^{-4}$ , which represents a strong constraint to the uptake. Owing to the limited gas uptakes, the effects of calcite SAI on ozone may be much smaller than previously thought.

To investigate this in more detail, this work has developed an interactive microphysical scheme for solid particles and integrated it into the aerosol-chemistry climate-model SOCOL-AERv2 and the Earth System Model SOCOLv4. These models make it possible to investigate the risks and benefits of SAI of solid particles. The solid particles considered in these models are fully interactive with the stratospheric sulfur cycle via the models' microphysical scheme. The models allow for uptake of sulfuric acid at the particle surface via coagulation with sulfuric acid aerosols and condensation of  $\text{H}_2\text{SO}_{4(g)}$  on the particle surfaces, as well as the formation of solid particle agglomerates via coagulation of solid particles. Furthermore, the solid particles are subject to advection, sedimentation and interactive wet and dry deposition in the troposphere. Most importantly, the models represent the interaction of the solid particles with the radiative transfer code of the model. Finally, they include the heterogeneous chemistry on the particle surface. The modular design of the models allows switching on and off the coupling of individual processes, which enables them to investigate the sensitivity and importance of the different processes relevant for the assessment of risks and benefits of SAI by means of solid particles.

Using these models, we show that SAI with alumina and calcite particles achieves a larger effective radiative forcing (RF) compared to sulfuric acid aerosols only if the same aerosol burden is maintained, but not when referring to the same unit of injected mass. Reduced warming of the tropical lower stratosphere remains a major advantage of SAI of alumina and calcite particles over  $\text{SO}_2$  injections, as well as reduced ozone depletion and reduced diffuse radiation. However, the effects on stratospheric composition are highly uncertain, as they largely depend on the assumptions made regarding the heterogeneous chemistry on the solid particles.

The extremely limited availability of experimental studies on heterogeneous chemistry on alumina under the influence of stratospheric concentrations of  $\text{HCl}$ ,  $\text{HNO}_3$ ,  $\text{H}_2\text{SO}_4$ , and  $\text{H}_2\text{O}$  leads to large uncertainties in the impact of alumina injection on stratospheric ozone. In order to quantify these uncertainties, we integrated the currently available knowledge about the most important heterogeneous reaction  $\text{ClONO}_2 + \text{HCl} \xrightarrow{\text{surf}} \text{Cl}_2 + \text{HNO}_3$  into SOCOL-AERv2. The uncertainty in the resulting heterogeneous reaction rate is more than two orders of magnitude depending on the partitioning of  $\text{HCl}$ ,  $\text{H}_2\text{SO}_4$  and  $\text{HNO}_3$  on the alumina surface. This could lead to global ozone column depletion ranging between almost negligible and up to 9%, which would be more than twice as much as the ozone loss caused by chlorofluorocarbons in the late 1990s.

Given the current level of scientific understanding, sulfur-based SAI appears to have smaller uncertainties than solid particles, and could therefore be considered potentially safer. Conversely, SAI using solid particles has more potential for reduced side effects but also greater uncertainties. To constrain this structural uncertainty in models, both dedicated laboratory experiments as well as small scale field experiments will be required.

# Zusammenfassung

Die sich zunehmend verschlechternden Aussichten für die Eindämmung des Klimawandels treiben die Forschung zu künstlicher stratosphärischer Aerosolinjektion (SAI) voran. Die Injektion von Aerosolen oder deren Vorläufersubstanzen in die Stratosphäre hat zum Ziel, die Albedo der Erde zu erhöhen, um das globale Klima abzukühlen. SAI zielt darauf ab, einige der negativen Auswirkungen des Klimawandels schnell und kostengünstig abzuschwächen. Die Idee entstand hauptsächlich aus Beobachtungen der kühlenden Wirkung explosiver Vulkanausbrüche, was erklärt, warum sich die SAI-Forschung bisher auf die Injektion von  $\text{SO}_2$ , der wichtigsten Vorläufersubstanz von vulkanischen Schwefelsäureaerosole in der Stratosphäre, konzentriert hat. SAI durch Schwefelsäureaerosole könnte jedoch eine Reihe negativer Nebeneffekte haben, wie z.B. Auswirkungen auf die Ozonschicht und die Erwärmung der Stratosphäre sowie erhebliche Auswirkungen auf die globale atmosphärische Zirkulation.

Ein kürzlich durchgeführter Modellvergleich zwischen verschiedenen Klimamodellen mit interaktiven stratosphärischen  $\text{H}_2\text{SO}_4/\text{H}_2\text{O}$ -Aerosolen hat grosse Unsicherheiten in der Implementierung der mikrophysikalischen Aerosolprozesse aufgezeigt. Insbesondere hat sich gezeigt, dass im Vergleich zu kurzzeitigen vulkanischen  $\text{SO}_2$ -Injektion kontinuierliche  $\text{SO}_2$ -Injektionen in Klimainterventionsszenarien eine grössere Herausforderung für die numerische Implementierung mikrophysikalischer Prozesse wie Nukleation, Kondensation und Koagulation darstellen können. In dieser Arbeit wird gezeigt, wie eine einfache Modifikation der Zeitschritte und der Abfolge der mikrophysikalischen Prozesse im sektionalen Aerosol-Chemie-Klimamodell SOCOL-AERv2 zu Unterschieden im resultierenden global gemittelten Strahlungsantrieb von  $-2.3$  bis  $-5.3$   $\text{W}/\text{m}^2$  führen kann, wenn 25 Mt pro Jahr  $\text{SO}_2$  injiziert werden. Dies ist hauptsächlich das Ergebnis eines zu langen mikrophysikalischen Zeitschrittes in Kombination mit der starken Nichtlinearität der Aerosolkeimbildung in Abhängigkeit von der  $\text{H}_2\text{SO}_4$  Übersättigung. Zusammengenommen unterstreichen diese Ergebnisse die Bedeutung struktureller Aspekte bei der Modellierung mikrophysikalischer Aerosolprozesse unter Bedingungen von erhöhter stratosphärischer Schwefelkonzentrationen für die Bestimmung der Auswirkungen auf das Klima und die stratosphärische Zusammensetzung von Klimaintervention via  $\text{SO}_2$ -Injektion.

Neuere Studien deuten auch darauf hin, dass die Injektion von Feststoffpartikeln wie Kalzit- oder Aluminiumoxidpartikeln im Vergleich zu SAI via Schwefelsäureaerosolen zu einer effektiveren Kühlung pro Aerosolladung führen könnte. Gleichzeitig könnten Feststoffpartikel aufgrund ihrer besseren optischen, chemischen und mikrophysikalischen Eigenschaften einige der negativen Nebeneffekte wie den Ozonabbau oder die Erwärmung der Stratosphäre reduzieren. Die vorliegende Arbeit zeigt jedoch, dass einige dieser Studien auf stark vereinfachten Aerosolmodellansätzen oder unphysikalischen Annahmen zur heterogenen Chemie beruhen. Durch experimentelle Laborarbeit und Klimamodellierung wird in dieser Arbeit eine ganzheitliche Bewertung der SAI unter Verwendung von Kalzit- und Aluminiumoxidpartikeln und ihrer Unsicherheiten im Vergleich zur SAI unter Verwendung von Schwefelsäureaerosolen vorgenommen.

Kalzitpartikel wurden als potentielle Injektionskandidaten für SAI vorgeschlagen, da sie mit sauren Gasen in der Stratosphäre reagieren können. Die Aufnahme von HCl auf Kalzitpartikeln zu einer schnelleren Erholung der Ozonschicht führen. Umgekehrt kann eine starke Aufnahme von  $\text{HNO}_3$  auch zu einem verstärkten Ozonabbau führen, da die

Deaktivierung von Chlor verringert wird. In dieser Arbeit wurde die Aufnahme von  $\text{HNO}_3$  und  $\text{HCl}$  auf Kalzit unter stratosphärischen Bedingungen mit Hilfe von In-situ-XPS und ERDA gemessen und ihr Eindringen in tiefere Schichten unter der Oberfläche sowie die anschliessende chemische Umwandlung von Kalzit in Kalziumchlorid und -nitrat bestimmt. Mit XPS wurden Absorptionskoeffizienten von  $\gamma_{\text{HNO}_3} = 10^{-5}$  bis  $10^{-4}$  für  $\text{HNO}_3$  und mit ERDA von  $\gamma_{\text{HNO}_3, \text{HCl}} = 10^{-6}$  bis  $10^{-5}$  für  $\text{HNO}_3$  und  $\text{HCl}$  gemessen. Wenn man diese Ergebnisse in den Kontext von SAI stellt, nimmt die Aufnahme von  $\text{HCl}$  und  $\text{HNO}_3$  mit der Expositionszeit in der Stratosphäre ab, was auf die Bildung von Produktschichten an der Oberfläche und die anschliessende Begrenzung der Absorption durch langsame Ionendiffusion zurückzuführen ist. Die Messungen zeigen, dass die Exposition dieser Partikel mit typischerweise 5 ppb  $\text{HNO}_3$  und 1 ppb  $\text{HCl}$  über stratosphärische Verweilzeiten der Partikel von etwa 1 Jahr zu mittleren Absorptionskoeffizienten  $< 10^{-4}$  führt, was eine starke Begrenzung der Aufnahme darstellt. Aufgrund der begrenzten Gasaufnahme könnte die Wirkung von SAI von Kalzitpartikeln auf Ozon wesentlich geringer sein als bisher angenommen.

Um dies genauer zu untersuchen, wurde in dieser Arbeit ein interaktives mikrophysikalisches Schema für Feststoffpartikel entwickelt und in das Aerosol-Chemie-Klimamodell SOCOL-AERv2 und das Erdsystemmodell SOCOLv4 integriert. Diese Modelle ermöglichen es, das Potential und die Risiken der SAI von Feststoffpartikeln zu untersuchen. Die in diesen Modellen berücksichtigten Feststoffpartikel sind über das mikrophysikalische Modul der Modelle vollständig mit dem stratosphärischen Schwefelkreislauf verbunden. Die Modelle berücksichtigen die Aufnahme von Schwefelsäure an den Partikeloberflächen durch Koagulation mit Schwefelsäureaerosolen und Kondensation von  $\text{H}_2\text{SO}_{4(g)}$  auf der Partikeloberflächen. Darüber hinaus unterliegen die Feststoffpartikel der Advektion, der Sedimentation und der interaktiven Deposition. Am wichtigsten ist, dass die Modelle die Wechselwirkung der Feststoffpartikel mit dem Strahlungstransportcode des Modells abbilden. Schliesslich berücksichtigen die Modelle auch die heterogene Chemie auf der Partikeloberfläche. Der modulare Aufbau der Modelle erlaubt es, die Kopplung einzelner Prozesse an- und abzuschalten und so die Empfindlichkeit und Bedeutung der verschiedenen Prozesse zu untersuchen, die für die Abschätzung von Risiken und Nutzen von SAI mit Feststoffpartikeln relevant sind.

Mit diesen Modellen zeigen wir, dass SAI mit Aluminiumoxid- und Kalzitpartikeln im Vergleich zu Schwefelsäureaerosolen nur dann einen grösseren effektiven Strahlungsantrieb erzielt, wenn die gleiche Aerosolbeladung beibehalten wird, nicht aber, wenn auf die gleiche Einheit der eingebrachten Masse Bezug genommen wird. Die geringere Erwärmung der unteren tropischen Stratosphäre bleibt ein wesentlicher Vorteil der SAI von Aluminiumoxid- und Kalzitpartikeln gegenüber der  $\text{SO}_2$ -Injektion, ebenso wie der geringere Ozonabbau und die geringere diffuse Strahlung. Die Auswirkungen auf die Zusammensetzung der Stratosphäre sind jedoch sehr unsicher, da sie weitgehend von Annahmen über die heterogene Chemie auf den Feststoffpartikel abhängen.

Die äusserst begrenzte Verfügbarkeit experimenteller Studien zur heterogenen Chemie von Aluminiumoxid unter dem Einfluss stratosphärischer Konzentrationen von  $\text{HCl}$ ,  $\text{HNO}_3$ ,  $\text{H}_2\text{SO}_4$  und  $\text{H}_2\text{O}$  führt zu grossen Unsicherheiten hinsichtlich der Auswirkungen der Aluminiumoxid-Injektion auf das stratosphärische Ozon. Um diese Unsicherheiten zu quantifizieren, haben wir das derzeit verfügbare Wissen über die wichtigste heterogene Reaktion  $\text{ClONO}_2 + \text{HCl} \xrightarrow{\text{surf}} \text{Cl}_2 + \text{HNO}_3$  in SOCOL-AERv2 integriert. Die Unsicherheit der resultierenden heterogenen Reaktionsrate beträgt mehr als zwei Grössenordnungen, abhängig von der Verteilung von  $\text{HCl}$ ,  $\text{H}_2\text{SO}_4$  und  $\text{HNO}_3$  auf der Aluminiumoxidoberfläche.



Dies könnte zu einem weltweiten Abbau der Ozonsäule führen, der zwischen fast vernachlässigbar und bis zu 9% liegen könnte, was mehr als doppelt so viel wäre wie der Ozonverlust durch Fluorchlorkohlenwasserstoffe Ende der 1990er Jahre.

In Anbetracht des derzeitigen wissenschaftlichen Erkenntnisstandes scheint SAI via Schwefelinjektion mit geringeren Unsicherheiten behaftet zu sein als SAI von festen Partikeln und könnte daher als potenziell sicherer angesehen werden. Umgekehrt hat die SAI mit festen Partikeln ein grösseres Potenzial für geringere Nebenwirkungen, aber auch grössere Unsicherheiten. Um diese strukturellen Unsicherheiten in Modellen einzugrenzen, sind sowohl Laborexperimente als auch Feldversuche in kleinem Massstab erforderlich.



# Chapter 1

## Introduction

Since preindustrial times the atmospheric greenhouse gas (GHG) concentrations have risen to levels never experienced by humankind. As stated by the Intergovernmental Panel on Climate Change (IPCC, 2023): "Human activities, principally through emissions of greenhouse gases, have unequivocally caused global warming, with global surface temperature reaching 1.1°C above 1850-1900 in 2011-2020". Immediate global action would be necessary to curb GHG emissions and thereby to reduce dangerous impacts on the environment and society. Even if society achieved elimination of emissions today, global warming and its impacts would linger for centuries if carbon dioxide removal techniques turn out to not gain sufficient efficacy or to be unaffordable for large-scale application.

These dismal prospects have motivated researchers to reconsider the ideas of Budyko (1974), who proposed to inject sulphuric acid aerosols or its precursors into the stratosphere with the aim of increasing Earth's albedo and cooling the planet. For many years this was looked at as an unsubstantiated supposition and became tabooed until Crutzen (2006) suggested — driven by despair over the lack of progress in political climate protection — that sulfur-based "stratospheric aerosol injection" (SAI) should be scientifically explored as a potential climate change mitigation tool. Studies confirmed that compared to other actions against global warming, SAI could create an immediate global cooling effect and deployment would not be expensive (Robock et al., 2009). Crutzen left no doubt that this would not be a desirable development and that reducing GHG emissions are the only real solution, yet his proposal received countless negative or rejecting responses as to its imponderable political, social and ethical concerns, as climate effects of SAI might not be equally distributed globally (Szerszynski et al., 2013). Research on the scientific aspects of SAI highlighted risks entailed (Robock, 2000), e.g. that SAI is not directly comparable with volcanic eruptions but requires much higher sustained input rates, resulting in different aerosol size distributions (Heckendorn et al., 2009; Vattioni et al., 2019; Weisenstein et al., 2022), and that SAI introduces several environmental risks such as stratospheric ozone depletion (Tilmes et al., 2008) or changes in the hydrological cycle (Niemeier et al., 2013). These impacts are subject to large model uncertainties and depend on the SAI scenario applied. Finally, lacking intergovernmental collaboration (e.g. Tollefson, 2019) leads to legal loopholes, potentially enabling single, powerful nations to unilaterally start SAI (Rabitz, 2016).

What remains is the potential that SAI might serve as temporary supplement to other measures against climate change such as GHG mitigation and adaptation, until we have reached net zero GHG emissions and until society finds solutions how to remove long-lived GHGs from the atmosphere (MacMartin et al., 2014; Keith and MacMartin, 2015, see Figure 1.1). Some experts therefore argue that SAI may be needed until appropriate technologies are scaled up to decarbonise the global economy and remove greenhouse gases from the air. Others argue that the necessary technologies have long been available and that SAI would only delay their implementation (Tsipiras and Grant, 2022; Biermann et al., 2022). However, proposals for SAI suggest that SAI could keep global warming below 1.5°C (MacMartin et al., 2018), which is the target set by the Paris Agreement

(UNFCCC; The Paris Agreement, <https://unfccc.int/documents/184656>, last access: 10 December, 2023). This motivates new research on the risks and benefits of SAI.

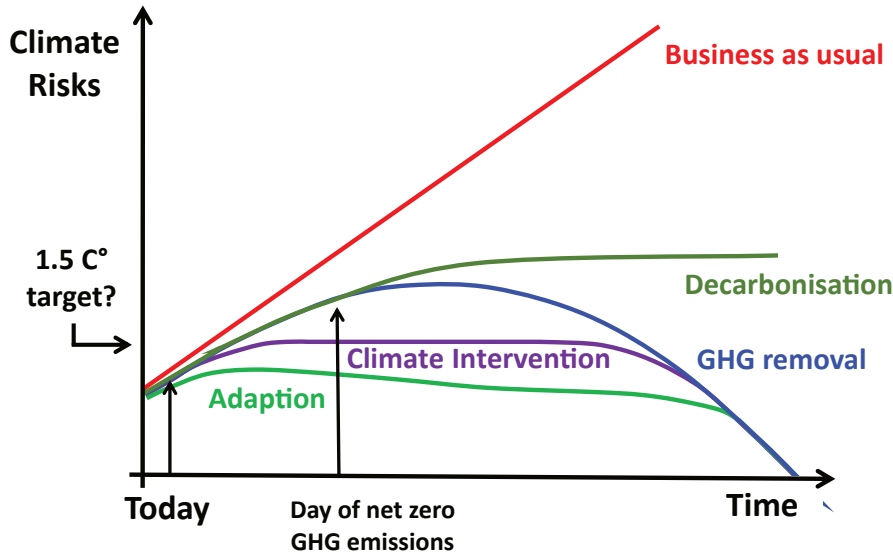


Figure 1.1: Schematic illustration adapted from (MacMartin et al., 2018) showing a potential scenario for stratospheric solar climate intervention to keep globally averaged warming below  $1.5^{\circ}\text{C}$ . To stop global warming and to mitigate associated climate risks decarbonization of the global economy is required to arrive at net zero GHG emissions. This might only be possible with negative injections such as GHG removal techniques (IPCC, 2023). Climate risks could still rise due to positive climate feedbacks after net zero GHG are reached. Scenarios presented in (MacMartin et al., 2018) would temporally reduce climate risks resulting from overshooting the  $1.5^{\circ}\text{C}$  global warming target until net zero GHG emissions are reached and GHG removal techniques are scaled up.

Detailed assessments of risks and benefits need to be conducted, before the feasibility of certain SAI techniques can be assessed. The National Research Council in the US (NRC, 2015), the British Royal Society (Shepherd, 2009), the European EuTRACE initiative (Schäfer et al., 2015) and the US National Academies of Sciences, Engineering, and Medicine (Field et al., 2021) presented assessments of the risks and benefits of SAI in detailed reports and recommend conducting research on SAI, with the aim of gaining further understanding of the climate system, and its human dimensions. However, an international UN-based report was missing until the assessment of SAI was included first in the "Scientific Assessment of Ozone Depletion" (WMO, 2022) and subsequently for the first time in the latest assessment report of the Intergovernmental Panel on Climate Change (IPCC, 2023).

## 1.1 Ethics and governance of SAI

There is growing evidence that the  $1.5^{\circ}\text{C}$ -goal may not be achievable by cutting GHG emissions alone, given that without other measures full decarbonization would be needed before 2050. This is not reflected in current policy plans based on submitted "Intended Nationally Determined Contributions", which would result in a global mean warming between  $2.6^{\circ}\text{C}$  and  $3.1^{\circ}\text{C}$  by the end of the century according to Rogelj et al. (2016).

Therefore, an open societal conversation addressing also the emerging topic of climate engineering is required (Honegger et al., 2017). Apart from the scientific and technical challenges facing SAI, international political collaboration and governance of SAI are needed to prevent misuse (Pasztor, 2017). This has motivated Switzerland to submitting a draft of a resolution to the United Nations National Assembly together with nine other countries (Tollefson, 2019) in which they asked for the production of a new report about guidance on possible future governance options and analysis of the implications of climate intervention in addition to the scientific assessment by IPCC (2023). Unfortunately, the draft was rejected due to strong refusal from the USA, Saudi Arabia and Brazil (Goering, 2019; Chemnick, 2019).

However, it has been shown that research on SAI is mainly conducted and funded by rich, developed countries and private institutions in the Global North, which are the countries having contributed the most to climate change, while the developing countries and least developed countries, who are most vulnerable to impacts from climate change do not have the resources to conduct research on SAI themselves (Winickoff et al., 2015; Rahman et al., 2018). This is why the "DEveloping country Governance REsearch and Evaluation for SRM" (DEGREES, <https://www.degrees.ngo/>) initiative was launched in 2010 aiming for informed and confident representation from developing countries in SAI research, outreach and community building. This is the basis for creating governance frameworks, which account for global and inter-generational climate justice, while it does not yet address the lack of enforceable political control of Global South countries in global politics (Stephens and Surprise, 2020).

Due to the rapidly growing number of publications in the field and the coverage of the topic in international assessments, combined with the controversial nature of the topic, SAI is receiving increasing attention. This has led to a polarisation of the scientific community on whether or not SAI should be assessed as part of potential climate change mitigation strategies. On the one hand, there is a growing number of scientists across the globe calling for an "International Non-Use Agreement on Solar Geoengineering" (<https://www.solargeoeng.org/>, Biermann et al., 2022), which calls for a ban of national research funding, outdoor experiments, patents and deployment of SAI as well as support from international institutions. The main argument of this call is that SAI is only a technical fix and symptom treatment of climate change, but not a real solution (i.e., not removing GHGs from the air). However, Figure 1.1 provides a potential scenario in which SAI could be part of a strategy to mitigate some climate risks. The call raises some important aspects and concerns about the risks and ethical aspects of SAI including global equality and missing involvement of the Global South. On the other hand, in response to the above call, another open letter calls for "balanced research and assessment of solar radiation modification" (<https://www.call-for-balance.com/about>, Wieners et al., 2023). This letter clearly states that limiting greenhouse gas concentrations is the only solution to climate change. However, it also states that SAI could reduce some climate impacts, but that not enough is known yet to judge its merits. Therefore, balanced deliberation and transparent, interdisciplinary research on SAI must begin now, along with comprehensive impact assessments, because the basis for deliberation and governance is research and assessment.

It is important to note that the work presented here does not suggest actual deployment of SAI, but only explores potential environmental risks and benefits. Any proposals for deployment would not be ethical at this stage, given the lack of governance and knowledge of intended and unintended environmental impacts (Preston, 2020). Rather, the aim

of this thesis is to assess the environmental and climatic risks faced by SAI in comparison with the impacts of anthropogenic climate change.

## 1.2 State of research

It was found that SAI via gaseous SO<sub>2</sub> injection has several limitations, including (1) unfavourable size distributions due to continuous nucleation and condensation processes (Heckendorn et al., 2009; Niemeier et al., 2011; English et al., 2011; Vattioni et al., 2019); (2) stratospheric ozone depletion due to increased heterogeneous reactions and longer lifetime of greenhouse gases (Pitari et al., 2014; Tilmes et al., 2018; Vioni et al., 2017; Tilmes et al., 2022); (3) Disturbances in the hydrological cycle (Bala et al., 2008; Niemeier et al., 2013; Tilmes et al., 2013; Kleidon et al., 2015); (4) Impacts on upper tropospheric ice clouds (Kuebbeler et al., 2012; Vioni et al., 2018); (5) stratospheric heating (Heckendorn et al., 2009; Ferraro et al., 2011), which modifies the Brewer-Dobson circulation, increases stratospheric humidity (Ferraro et al., 2015; Simpson et al., 2019) and alters surface climate such as the North Atlantic Oscillation and the Quasi Biennial Oscillation (Jones et al., 2022); and (6) enhanced diffuse light at the Earth's surface with implications for ecosystems (Kravitz et al., 2012b).

Limitation (1) is due to the continuous flow of freshly nucleated particles, which leads to increased coagulation and shifts the size distribution towards larger particles over time. This leads to an increase in the sedimentation rate of the aerosols, reducing their stratospheric residence time, its efficiency in backscattering solar radiation, and thus its cooling potential (Heckendorn et al., 2009; Vattioni et al., 2019; Weisenstein et al., 2022). Therefore, it is essential to obtain an optimal aerosol size distribution to achieve the most efficient backscattering of solar radiation per injected aerosol mass, while minimising the SAD available for heterogeneous chemistry. This limitation has been addressed by directly injecting sulphuric acid droplets with a tailored size distribution into the stratosphere (e.g., in the lower accumulation mode, AM, between 0.1  $\mu\text{m}$  and 0.3  $\mu\text{m}$ ) or by adjusting the dilution and injection rates of gaseous H<sub>2</sub>SO<sub>4</sub> injection plumes to achieve the desired aerosol size distributions after plume dilution with background air (Pierce et al., 2010; Benduhn et al., 2016; Vattioni et al., 2019). However, feasibility of AM–H<sub>2</sub>SO<sub>4</sub> production within a injection plume or direct injection is subject to large uncertainty and is also subject to limitations (2) to (6), which depend on the microphysical, chemical and optical properties of the aerosols. Recent studies have shown that some of these limitations could be reduced by injecting outside the tropical pipe, as this region is particularly sensitive to stratospheric disturbances (Kravitz et al., 2019; Vioni et al., 2021), but adverse side effects remain.

It has been recently suggested that injection of solid particles, such as calcite (CaCO<sub>3</sub>), alumina (Al<sub>2</sub>O<sub>3</sub>), diamond (C), silicon carbide (SiC) or zirconium dioxide (ZrO<sub>2</sub>) might overcome several of these limitations, while simultaneously increasing the cooling potential per resulting aerosol burden (Weisenstein et al., 2015; Dykema et al., 2016; Keith et al., 2016). However, contrary to sulfuric acid aerosols, the solid particle types proposed for SAI do not occur naturally in the stratosphere. The only solids occurring in the stratosphere to date are meteoritic dust particles (Biermann et al., 1996), metal particles resulting from satellite re-entries (Maloney et al.), black carbon (BC) emitted from aircraft, aerosols from large wild fires (Solomon et al., 2023) as well as some other nanoparticles such as nano-plastics (Revell et al., 2021), which get transported to the

stratosphere via cross tropopause transport. However, their burdens are too small to be of significance for the Earth's radiative balance. Other naturally occurring solids are polar stratospheric clouds (PSC, i.e., nitric acid trihydrate and ice PSC), which are relatively well studied (WMO, 2022), but have significantly different surface properties, which are not applicable to the solid particles proposed for SAI. Therefore, relatively little is known about their microphysical interactions and chemical ageing processes, which could alter their scattering properties, their stratospheric residence time as well as heterogeneous chemistry hosted on the particles. This makes it very difficult to model the impacts of solid particle injections on stratospheric chemistry and climate (Visioni et al., 2023).

Nevertheless, there have been several studies which investigated scenarios of SAI of solid particles. The conceptual studies on calcite particles (Fujii, 2011) as well as on  $\text{TiO}_2$ ,  $\text{Al}_2\text{O}_3$ , diamond (C),  $\text{Al}_2\text{O}_3$ ,  $\text{ZrO}_2$ , NaCl SiC and  $\text{CaCO}_3$  particles (Pope et al., 2012) showed that these particles have larger refractive indexes compared to sulfuric acid aerosols, which would reduce the stratospheric aerosol mass required for a given radiative forcing. The latter study highlighted the large refractive index of  $\text{TiO}_2$ . Ferraro et al. (2011) was the first study which used a radiative transfer code to quantify stratospheric heating rates resulting from SAI of  $\text{CaCO}_3$ ,  $\text{TiO}_2$  and black carbon (BC) particles. In other follow-up studies, the dynamical feedbacks of SAI by  $\text{TiO}_2$  and BC on the global circulation (Ferraro et al., 2015; Jones et al., 2016) as well as the impact on stratospheric ozone from BC (Kravitz et al., 2012b) were investigated with global climate models and chemistry climate models, respectively, but without interactively simulating microphysics. In summary, the conclusion from these studies on SAI by BC and  $\text{TiO}_2$  is that these materials are not suitable as injection species for SAI since both,  $\text{TiO}_2$  and BC have strong UV-VIS absorption, which results in significant stratospheric heating. However, while injection of BC would result in substantial ozone depletion, experimental studies on heterogeneous chemistry on  $\text{TiO}_2$  surfaces indicated reduced impacts on modelled stratospheric ozone (Tang et al., 2014, 2016; Moon et al., 2018) compared to sulfuric acid aerosols, providing additional motivation for exploration of other species.

At the same time, Dykema et al. (2016) performed detailed radiative transfer calculations of various solid particles and concluded that solid particles such as calcite, diamond, alumina and silicon carbide scatter solar radiation with better mass efficiency and less stratospheric heating compared to sulfuric acid aerosols. Weisenstein et al. (2015) was the first study who used a 2D chemistry transport model with interactive solid particle microphysics as well as microphysical interactions of solid particles with condensed and gaseous sulfuric acid to assess impacts from heterogeneous chemistry on alumina particle surfaces. The resulting zonal mean number concentrations were then fed into a radiative transfer code (RTC) offline to simulate the resulting radiative forcing. Limitations of this study are stemming from a simplified representation of heterogeneous chemistry on alumina particles (Vattioni et al., 2023a) as well as from the 2-D approach which causes significant simplifications in atmospheric dynamics and transport of the injected particles. Keith et al. (2016) used the same model to propose substantial stratospheric ozone increase through removal of HCl from the stratosphere via uptake on calcite particle surfaces and subsequent sedimentation. Later, Cziczo et al. (2019) pointed to the over simplified assessment used in Keith et al. (2016), which applied simplified heterogeneous chemistry such as neglecting the formation of hydrates at the particle surface and a potential sealing effect (Dai et al., 2020) due to the formation of reaction products at the surface. However, most importantly, this latter study showed that especially  $\text{CaCO}_3$  and  $\text{Ca}(\text{NO}_3)_2$  as well as their hydrates are good ice condensation nucleation materials, which could result in a

33% reduction of the radiative forcing compared to Keith et al. (2016) due to increased cirrus cloud coverage. Furthermore, also the interactions of aerosols with polar stratospheric clouds could create a feedback on polar ozone concentrations, which has not been investigated so far (Cziczo et al., 2019). Despite the large uncertainties on the stratospheric ozone response IPCC (2023) concludes that: "Injection of non-sulphate aerosols is likely to result in less stratospheric heating and ozone loss" (AR6, WG1, Chapter 4, Page 629).

### 1.3 Motivation

This motivates further research on the risks and benefits of solid particles. The over simplified modelling frameworks used in previous studies (Weisenstein et al., 2015; Keith et al., 2016; Dai et al., 2020) as well as the poorly constrained heterogeneous chemistry on calcite particle (Cziczo et al., 2019) motivates a new assessment of potential risks and benefits of SAI of solid particles, which will be done via a combination of modelling and experimental work. For the modelling part we will use the aerosol-chemistry climate model SOCOL-AERv2 (Feinberg et al., 2019). The interactive coupling of aerosol microphysics with heterogeneous chemistry and radiation make the SOCOL models (Feinberg et al., 2019; Sukhodolov et al., 2021) a powerful tool to explore feedbacks between microphysics, stratospheric chemistry, and radiation as well as tropospheric and stratospheric climate. The SOCOL model family has been successfully used to reproduce the global sulfur cycle under volcanically active (e.g., Mt. Pinatubo 1991) and quiescent conditions (e.g., Sheng et al., 2015; Sukhodolov et al., 2018; Feinberg et al., 2019; Brodowsky et al., 2021; Quaglia et al., 2023; Brodowsky et al., 2023) as well as to evaluate impacts of sulfur-based SAI scenarios (Heckendorn et al., 2009; Vattioni et al., 2019; Weisenstein et al., 2022), which makes them the tools of choice to evaluate SAI of solid particles.

The experimental work will mainly focus on calcite particles. Dai et al. (2020) has highlighted the importance of potential passivisation effects with increasing exposure time of HCl and HNO<sub>3</sub> uptake at the surface. Therefore, experimental methods are required that probe the very outer-most surface and also allow monitoring the slow diffusional exchange processes on larger depth scales for calcite surfaces. Ambient Pressure X-ray Photoelectron Spectroscopy (AP-XPS Orlando et al., 2016) and Heavy Ion Elastic Recoil Detection Analysis (HI-ERDA Döbeli et al., 2005) are perfectly suited to robustly provide the required chemical and physical information (see Figure 4.1 for details). While AP-XPS allows us to analyse the chemical composition of the upper 2-3 nm near-surface bulk in-situ at stratospheric temperature, relative humidity and relevant trace gas concentrations, HI-ERDA is an ion beam detection method which allows us to analyse the depth-resolved elemental composition of the upper few 100 nm of a sample offline after longer time periods of up to months to assess long term solid diffusion of ions into particles. Combining these techniques will allow us to observe diffusive processes within the sample to subsequently quantify time dependent uptake coefficients of HCl and HNO<sub>3</sub>. The measured uptake coefficients will then be used in SOCOL-AERv2 to quantify impacts on global stratospheric ozone.

In this thesis, the focus is on calcite and alumina particles since these are the only potential solid particle types for which some information on heterogeneous chemistry is available. For alumina there have been investigations on the impact of alumina-containing solid-fuel space rocket exhaust on stratospheric ozone and radiative forcing. These studies used flow-tube experiments (Molina et al., 1997), 2D-chemistry transport modelling



(Jackman et al., 1998; Danilin et al., 2001) as well as conceptual methods (Ross and Sheaffer, 2014). For calcite particles the study by Keith et al. (2016) has propelled some experimental work on the measurement of uptake coefficients of HCl and HNO<sub>3</sub> on calcite particles which will be extended by measurements in this thesis (Dai et al., 2020; Huynh and McNeill, 2020, 2021).

## 1.4 Research questions

This thesis aims at providing a holistic assessment of SAI by alumina and calcite particles based on current scientific evidence, which will be extended by novel experimental and modelling work. The goal is to assess impacts of solid particles on the Earth’s radiative balance, stratospheric warming and stratospheric composition, in particular stratospheric ozone.

This was done by (1) performing laboratory studies to test chemical properties of calcite particles at stratospheric conditions in respect to temperature, trace gas concentrations and relative humidity using HI-ERDA and AP-XPS and by (2) extending the sectional aerosol-chemistry climate model SOCOL-AERv2 (Feinberg et al., 2019) by an interactive solid-particle microphysics module, to explore the chemical, radiative and climatic effects of these particles. The interdisciplinary approach of combining experimental and modelling work fosters the understanding and identification of process uncertainties to make suggestions for further research needs.

This thesis aims to be the first quantitative assessment of impacts of SAI of solid particles within a coupled Earth System Model incorporating a interactive solid particle microphysics scheme. The goal is to provide improved, more objective scientific basis for the assessment of the risks and benefits of SAI approaches by solid particles in comparison to SO<sub>2</sub> injection. Furthermore, the first chapter of the thesis highlights the importance of the microphysical timestep lengths under conditions of SAI via SO<sub>2</sub> injections, which is an issue that was discovered during the implementation of solid particle microphysics module into SOCOL-AERv2.

Therefore this project aims to answer the following research questions (RQs):

- **RQ 1.0:** What role do microphysical processes play in climate intervention strategies that use sulphate, calcite or alumina particles, and what uncertainties are associated with them?
- **RQ 2.0:** How can we better constrain the microphysical, chemical and radiative processes of alumina and calcite particles and improve their representation in aerosol chemistry climate models for the simulation of climate impact scenarios?
- **RQ 3.0:** Compared to sulfur-based stratospheric aerosol injection, what effects do alumina or calcite aerosols have on the ozone layer, on Earth’s radiative balance including diffuse radiation, and on the atmospheric circulation?

## 1.5 Thesis outline

Chapter 2 will address RQ1, which highlights model uncertainties resulting from the representation of sulphuric acid aerosol microphysics in SOCOL-AERv2 under SAI conditions (RQ 1). This is a paper resulting from the discovery of some inaccuracies in the

aerosol microphysics module during the implementation of the solid particle microphysics in SOCOL-AERv2. This chapter serves as a good start to get familiar with the the aerosol microphysics module of SOCOL-AERv2. Chapter 3 then describes the solid particle microphysics module which was implemented in SOCOL-AERv2. It also discusses the main uncertainties for the modelling of solid particles in aerosol chemistry climate models (RQ 1 and 2). Chapter 4 provides a parameterisation for extrapolation of experimental data to stratospheric conditions in terms of partial pressures of reactants, and highlights the significant associated uncertainties in quantifying impacts on stratospheric ozone (RQ 2). Chapter 5 presents experimentally measured uptake coefficients of HCl and HNO<sub>3</sub> on calcite surfaces measured under stratospheric conditions with respect to temperature, relative humidity and trace gas concentrations using AP-XPS and ERDA. Also it provides suggestions and conclusions for modelling the heterogeneous chemistry of SAI of calcite particles in aerosol chemistry climate models (RQ 2). The final chapter "Concluding perspectives" provides a summary of the findings of this thesis and puts the results into perspective by addressing RQ 3.

## Chapter 2

# Importance of microphysical settings for climate forcing by stratospheric SO<sub>2</sub> injections as modelled by SOCOL-AERv2

### Abstract

Climate intervention as a sustained deliberate source of SO<sub>2</sub> into the stratosphere has been proposed as an option for climate intervention. Global interactive aerosol-chemistry-climate models are often used to investigate the potential cooling efficiencies and associated side effects of hypothesised climate intervention scenarios. A recent model inter-comparison study for composition-climate models with interactive stratospheric aerosol suggests that the modelled climate response to a particular assumed injection strategy, depends on the type of aerosol microphysical scheme used (e.g., modal or sectional representation), alongside also host model resolution and transport. Compared to short-duration volcanic SO<sub>2</sub> emission, the continuous SO<sub>2</sub> injections in climate intervention scenarios may pose a greater challenge to the numerical implementation of microphysical processes such as nucleation, condensation, and coagulation. This study explores how changing the timesteps and sequencing of microphysical processes in the sectional aerosol-chemistry-climate model SOCOL-AERv2 (40 mass bins) affect model predicted climate and ozone layer impacts considering climate intervention by SO<sub>2</sub> injections of 5 and 25 Tg(S) yr<sup>-1</sup> at 20 km altitude between 30°S and 30°N. The model experiments consider year 2040 boundary conditions for ozone depleting substances and green house gases. We focus on the length of the microphysical timestep and the call sequence of nucleation and condensation, the two competing sink processes for gaseous H<sub>2</sub>SO<sub>4</sub>. Under stratospheric background conditions, we find no effect of the microphysical setup on the simulated aerosol properties. However, at the high sulfur loadings reached in the scenarios injecting 25 Mt/yr of sulfur with a default microphysical timestep of 6 min, changing the call sequence from the default "condensation first" to "nucleation first" leads to a massive increase in the number densities of particles in the nucleation mode ( $R < 0.01 \mu\text{m}$ ) and a small decrease in coarse mode particles ( $R > 1 \mu\text{m}$ ). As expected, the influence of the call sequence becomes negligible when the microphysical timestep is reduced to a few seconds, with the model solutions converging to a size distribution with a pronounced nucleation mode. While the main features and spatial patterns of climate forcing by SO<sub>2</sub> injections are not strongly affected by the microphysical configuration, the absolute numbers vary considerably. For the extreme injection with 25 Tg(S) yr<sup>-1</sup>, the simulated net global radiative forcing ranges from  $-2.3 \text{ W m}^{-2}$  to  $-5.3 \text{ W m}^{-2}$ , depending on the microphysical configuration. "Nucleation first" shifts the size distribution towards radii better suited for solar scattering ( $0.3 \mu\text{m} < R < 0.4 \mu\text{m}$ ), enhancing the intervention efficiency. The size-distribution shift however generates more ultra-fine aerosol particles, increasing the surface area density, resulting in 10 DU less ozone (about 3% of total column) in the northern midlatitudes and 20 DU less ozone (6%) over the polar caps, compared to the "condensation first" approach. Our results suggest that a reasonably short microphysical

time step of 2 minutes or less must be applied to accurately capture the magnitude of the H<sub>2</sub>SO<sub>2</sub> supersaturation resulting from SO<sub>2</sub> injection scenarios or volcanic eruptions. Taken together these results underscore how structural aspects of model representation of aerosol microphysical processes become important under conditions of elevated stratospheric sulfur in determining atmospheric chemistry and climate impacts.

### **This chapter was published as a research paper:**

**Vattioni, S.**, Stenke, A., Luo, B., Chiodo, G., Sukhodolov, T., Wunderlin, E., and Peter, T.: Importance of microphysical settings for climate forcing by stratospheric SO<sub>2</sub> injections as modeled by SOCOL-AERv2, **Geoscientific Model Development**, 17, 4181–4197, <https://doi.org/10.5194/gmd-17-4181-2024>, 2024.

## 2.1 Introduction

The idea of increasing the Earth’s albedo by injecting sulfur containing gases into the stratosphere to reduce some of the adverse effects of greenhouse-gas (GHG) induced global warming dates back to the 1970s (Budyko, 1974), and was 30 years later further elaborated by Crutzen (2006). The arguments presented by Crutzen called for active scientific research of the kind of activity, which became known under the somewhat misleading term ”geoengineering”. We term this here ”climate intervention”, following the recommendation of the NRC (2015). Crutzen’s idea is based on the fact that sulfur containing gases, such as SO<sub>2</sub>, H<sub>2</sub>S or OCS, injected into the lower stratosphere will form aqueous sulfuric acid aerosol particles via a chain of chemical and microphysical processes (Thomason and Peter, 2006; Kremser et al., 2016). The resulting binary H<sub>2</sub>SO<sub>4</sub>-H<sub>2</sub>O solution droplets scatter solar radiation back to space, causing a cooling at the Earth’s surface. At the same time, however, they heat the stratosphere due to absorption of upwelling long-wave radiation. Moreover, sulfate aerosols play an important role in stratospheric ozone chemistry by providing surfaces for heterogeneous reactions (Solomon, 1999). While the infrared absorptivity is determined to good approximation by the total aerosol volume, the efficiency of scattering solar radiation depends strongly on the detailed aerosol size distribution: Many small particles are more efficient than a few large particles, but they also provide a larger surface area density (SAD) accelerating heterogeneous chemistry (Heckendorn et al., 2009).

In the stratosphere, the total aerosol number density and size distribution are governed by the microphysical processes of nucleation, coagulation, condensation, evaporation, and gravitational settling (Kremser et al., 2016, and references therein). The formation of new sulfate aerosol particles occurs via binary homogeneous nucleation of H<sub>2</sub>SO<sub>4</sub> and H<sub>2</sub>O molecules, or, via heterogeneous nucleation in the presence of appropriate condensation nuclei like meteoritic dust or ions, which requires lower saturation ratios than homogeneous nucleation. The freshly formed particles can grow further through coagulation as well as condensation of H<sub>2</sub>SO<sub>4</sub> (together with H<sub>2</sub>O). As stratospheric temperatures increase with altitude, the sulfate aerosol particles eventually evaporate above 32 to 35 km, releasing H<sub>2</sub>SO<sub>4</sub> back to the gas phase.

The effectiveness of climate intervention by SO<sub>2</sub> emission has been intensively investigated by using models of different complexity and assuming different injection scenarios (e.g., Heckendorn et al., 2009; Pierce et al., 2010; Niemeier et al., 2011; English et al., 2011; Niemeier and Timmreck, 2015; Tilmes et al., 2018; Vattioni et al., 2019; Weisenstein et al., 2022; Laakso et al., 2022; Tilmes et al., 2022). Such modelling studies have advanced our understanding of stratospheric aerosols, but they also highlighted uncertainties regarding the transport, chemistry, and microphysics of the aerosol size distribution. In a recent study, Weisenstein et al. (2022) presented a model intercomparison exploring the impacts of stratospheric injections of SO<sub>2</sub> gas as well as accumulation-mode sulfuric acid aerosol (AM-H<sub>2</sub>SO<sub>4</sub>) on atmospheric chemistry and climate. Three general circulation models (GCMs) with interactive aerosol microphysics conducted strictly coordinated model experiments within the framework of the Geoengineering Model Intercomparison Project (GeoMIP, Kravitz et al., 2011), namely the Community Earth System Model (CESM2) with the Whole Atmosphere Community Climate Model (WACCM) atmospheric configuration (Danabasoglu et al., 2020), the middle atmosphere version of ECHAM5 with the HAM microphysical module (MA-ECHAM5-HAM; Stier et al., 2005), and the Solar Climate Ozone Links model with AER microphysics (Feinberg et al., 2019, SOCOL-AERv2;).

The model experiments included injections of 5 and 25 Tg(S) yr<sup>-1</sup> in form of SO<sub>2</sub> gas or AM-H<sub>2</sub>SO<sub>4</sub>, emitted either as two point injections at 30° N and 30° S or as regional injection between 30° N and 30° S. Two of the participating models, CESM2 and MA-ECHAM5-HAM, assume the aerosol size distribution can be described by superimposed lognormal size distributions (modal scheme), while SOCOL-AERv2 uses a size-resolving (sectional) scheme.

The analysis of the simulated particle size distributions for the SO<sub>2</sub> injection scenarios revealed substantial differences between each pair of the three models. CESM2 generates new particles and adds them directly to the Aitken mode ( $R \gtrsim 10$  nm), so that there are no nm-sized particles. In contrast, SOCOL-AERv2 treats these tiny particles down to 0.4 nm. Compared to MA-EACHM-HAM, SOCOL shows substantially fewer nucleation mode particles, suggesting different roles of nucleation and condensation in both models: the microphysical scheme in SOCOL-AERv2 appears to prefer condensational growth of existing particles by uptake of H<sub>2</sub>SO<sub>4</sub> over the formation of new particles, while the opposite seems to be the case for MA-ECHAM5-HAM. The description of the results of the microphysical processes by means of lognormal functions in modal models, such as CESM2 and MA-ECHAM5-HAM, further complicates the interpretation.

Nucleation and condensation are competing sink processes for gas-phase H<sub>2</sub>SO<sub>4</sub>, which occur simultaneously in the atmosphere, but typically with different speeds. The characteristic time scale  $\tau$  for removal of H<sub>2</sub>SO<sub>4</sub> molecules by condensation is given by the following equation:

$$\tau_{\text{cond}} = \frac{4}{Av}, \quad (2.1)$$

with  $A$  being the aerosol surface area density and  $v$  the mean thermal velocity of H<sub>2</sub>SO<sub>4</sub> molecules. For background conditions with typical SAD values of 5 to 10  $\mu\text{m}^2 \text{cm}^{-3}$  in nucleation regions, the equilibrium time scale for condensation is around 0.5–1 h. This value decreases inversely with increasing SAD. Under volcanic or climate intervention conditions with SAD  $\sim 80 \mu\text{m}^2 \text{cm}^{-3}$ , typical for the 25 Tg(S) yr<sup>-1</sup> injection scenario, the equilibrium time scale is less than 5 minutes. As the nucleation rate strongly depends on the gas-phase H<sub>2</sub>SO<sub>4</sub> supersaturation, the model timestep used for condensation and nucleation must be significantly smaller than the time required to approach gas-phase equilibrium in order to avoid one process erroneously dominating the gas-to-particle transfer of H<sub>2</sub>SO<sub>4</sub>. Furthermore, coagulation is also affected by the competition between nucleation and condensation, as it is most efficient at (initially) high number densities and between particles of different size. Small particles move fast, but have only small cross-sections for collision, while large particles exhibit slower Brownian motion, but provide good collision targets for smaller particles (Seinfeld and Pandis, 1997). The correct numerical representation of these simultaneously occurring processes is challenging, especially under sulfur-rich conditions, when characteristic time scales become extremely short. This motivated us to critically question the microphysical scheme of the sectional SOCOL-AERv2 model and to systematically test the impact of the call sequence of the subroutines for condensation and nucleation, as well as the microphysical timestep on the simulated aerosol properties and the modeled climate response to stratospheric SO<sub>2</sub> injection.

The paper is organised as follows: Section 2.2 presents a brief description of the SOCOL-AERv2 model and details of the experimental setup. Section 2.3 discusses the impact of the microphysical settings on the aerosol size distribution under stratospheric background conditions as well as under stratospheric injections of SO<sub>2</sub> gas (2.3.1), on the global mean particle size, aerosol burden and radiative forcing (2.3.2), and on the

meridional distributions of aerosol burden, radiative forcing, and ozone (2.3.3) resulting from the SO<sub>2</sub> injections. The influence of the microphysical settings on profiles of various quantities is briefly mentioned (2.3.4) and detailed in the Appendix. To evaluate the changes in SOCOL aerosol microphysics against observations we also tested different settings for the 1991 eruption of Mt. Pinatubo (2.3.5). Section 2.4 includes a summary and discussion.

## 2.2 Model description and experimental setup

### 2.2.1 SOCOL-AERv2

A first version of the aerosol-chemistry-climate model SOCOL-AER had been introduced by Sheng et al. (2015), who integrated the size-resolving (sectional) sulfate aerosol module AER (Weisenstein et al., 1997) into the three dimensional grid of the chemistry-climate model (CCM) SOCOLv3 (Stenke et al., 2013), which consists of the middle atmosphere version of the spectral general circulation model MA-ECHAM5 (Roeckner et al., 2003, 2006) and the chemistry-transport model MEZON (Rozanov et al., 1999; Egorova et al., 2003). Since then, the model’s tropospheric and stratospheric sulfur cycle have undergone several improvements, resulting in the publication of SOCOL-AERv2 (Feinberg et al., 2019).

SOCOL-AERv2 resolves the sulfate aerosol particles in 40 mass bins, ranging from 0.39 nm to 3.2 μm in radius. Since the mass bins refer to dry aerosol radius, they can also be interpreted as aerosol H<sub>2</sub>SO<sub>4</sub> mass bins, ranging from about 2.8 molecules to  $1.6 \times 10^{12}$  molecules of H<sub>2</sub>SO<sub>4</sub> per aerosol particle. Neighboring mass bins differ by molecule number doubling.

Detailed descriptions of the original AER microphysics and their adaptations for the coupled model are provided in Weisenstein et al. (1997, 2007) and Sheng et al. (2015), respectively. Aerosol composition, i.e. the sulfuric acid weight percent in the particles, is calculated as function of ambient temperature and H<sub>2</sub>O partial pressure using the parameterization of Tabazadeh et al. (1997), which is also used for the calculation of the wet aerosol radius of each mass bin. For the formation of new particles by binary homogeneous nucleation the scheme of Vehkamäki et al. (2002) is used. The scheme calculates the nucleation rate as well as the radius and composition of new particles, meaning that the nucleated mass is added to a single mass bin. The particles can grow through H<sub>2</sub>SO<sub>4</sub> condensation and shrink through evaporation, both processes depending on the equilibrium concentration of H<sub>2</sub>SO<sub>4</sub> above the particle surface (Ayers et al., 1980; Kulmala and Laaksonen, 1990). Condensational growth leads to an increase of mass in the aerosol phase and a shift of particles to larger mass bins, while evaporation does the opposite. Changes in the net number density occur only upon evaporation from the smallest mass bin or condensational growth of the largest mass bin. Finally, coagulation reduces number densities and shifts aerosol mass to larger bins. Coagulation is solved by a semi-implicit method (Jacobson and Seinfeld, 2004), whereas at most 90% of the available mass in one mass bin is allowed to be lost by coagulation within one microphysical time step. Otherwise, the coagulation timestep is reduced. The coagulation kernel, which defines the collision probability of two particles, depends on the particle radius and the diffusion coefficient (Fuchs, 1964). Finally, sedimentation, which affects the vertical distribution of aerosol particles and reduces their residence time in the stratosphere, is parameterised following the numerical scheme of Walcek (2000). The gravitational settling velocities of

aerosol particles are calculated following Kasten (1968).

The CCM SOCOLv3 and the aerosol module AER are interactively coupled via the chemistry and radiation routines. Sulfur chemical reactions (Sheng et al., 2015, see Table 1) are fully integrated into the model’s chemical solver, which is based on the implicit iterative Newton-Raphson scheme (Stott and Harwood, 1993). In addition to gas-phase chemistry, the model includes aqueous-phase oxidation of S(IV) to S(VI) by ozone (O<sub>3</sub>) and hydrogen peroxide (H<sub>2</sub>O<sub>2</sub>) in cloud water (Jacob, 1986). The modeled sulfate aerosol is fed directly into the heterogeneous chemistry and radiation schemes. The aerosol radiative properties (extinction coefficients, single scattering albedos, and asymmetry factors as functions of wavelength) required to drive the model dynamics are calculated online from the aerosol size distribution using Mie theory with a temperature- and humidity-dependent look-up table, which accounts for the aerosol H<sub>2</sub>O<sub>2</sub> weight percent.

The model uses operator splitting. The dynamics module is called every 15 min, whereas the chemistry, aerosol microphysics, and radiation schemes are called every 2 h. For the microphysical processes, especially for nucleation with its highly nonlinear dependence on gaseous H<sub>2</sub>SO<sub>4</sub> concentration, sub-timesteps are used within the 2-h chemistry loop, to avoid that the process called first mistakenly dominates the H<sub>2</sub>SO<sub>4</sub>-to-particle exchange rate. The default procedure is to use  $N_{\text{micro}} = 20$  sub-loops within the chemical timestep, which results in a microphysical timestep of 6 minutes ( $2 \text{ h}/N_{\text{micro}} = 2 \text{ h}/20 = 6 \text{ min}$ ). The parameter  $N_{\text{micro}}$  can be easily adjusted between runs. By default, the call sequence for the microphysical processes is condensation first, followed by nucleation (see "CN" sequence in Fig. 2.1), and finally coagulation. At each chemical timestep, the model first calculates the new H<sub>2</sub>SO<sub>4</sub> gas-phase concentration resulting from chemical production and transport. In the microphysical loop, the H<sub>2</sub>SO<sub>4</sub> concentration is then consecutively updated by condensation and nucleation. As we will see later, it is also important to distribute the gaseous H<sub>2</sub>SO<sub>4</sub> molecules produced during the 2-h chemical timestep homogeneously over the  $N_{\text{micro}}$  sub-timesteps (see  $\Delta \text{H}_2\text{SO}_4$  in Fig. 2.1), rather than passing them as a total amount at the beginning of the microphysical loop. Otherwise, under conditions of SO<sub>2</sub> injections the 2-hourly call frequency of the chemistry scheme would lead to initially unrealistically high H<sub>2</sub>SO<sub>4</sub> supersaturations in the microphysical loop, which then causes artefacts in the aerosol microphysics. The aerosol composition as well as the coagulation kernel are calculated only once every 2 h and are kept constant for the microphysical calculations. Finally, sedimentation is calculated after the microphysical sub-loop, again once every 2 h. To test the implications of the aerosol microphysics on the simulated aerosol size distribution under various stratospheric sulfur loadings, we performed several sensitivity simulations, for which we changed the call sequence for condensation and nucleation or increased the number of microphysical sub-timesteps  $N_{\text{micro}} > 20$ .

### 2.2.2 SOCOLv4

Additionally, we performed simulations with the fully coupled Earth System Model (ESM) SOCOLv4 (Sukhodolov et al., 2021), which is a further development of SOCOL-AERv2. SOCOLv4, incorporates the same aerosol module, AER, as SOCOL-AERv2 (Sect. 2.2.1). The major differences between the model versions is that SOCOLv4 is based on the MPI-ESM1.2 (Mauritsen et al., 2019), which incorporates the fully coupled interactive ocean module MPIOM (Jungclaus et al., 2013). SOCOLv4 has a finer atmospheric horizontal and vertical resolution with T63 truncation (1.9° x 1.9°) and 47 vertical pressure lev-



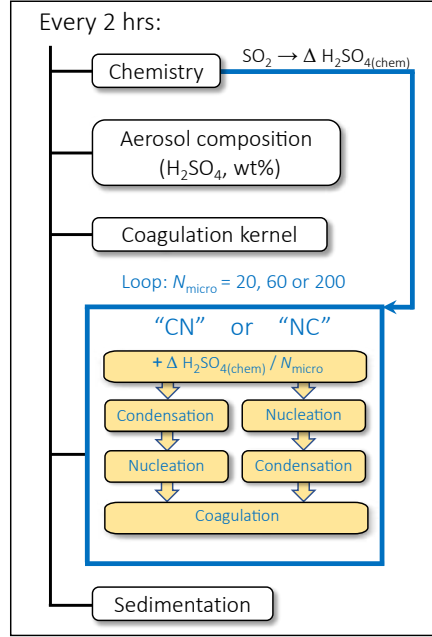


Figure 2.1: Schematic representation of the call sequence for the microphysical processes in SOCOL-AERv2. The scheme shows the setup with the microphysical sub-loop with  $N_{\text{micro}} = 20$  steps by default, or an increased number of steps (60, 80, or 200) in the test runs. By default, the condensation routine is called first and nucleation second (“CN”), which was reversed (“NC”) for the tests. Furthermore, the amount of  $\text{H}_2\text{SO}_2$  gas molecules produced by the chemistry scheme is uniformly distributed over the  $N_{\text{micro}}$  time steps, instead of providing the total amount at the first microphysical time step, as done in the original set-up.

els also reaching up to 0.01 hPa. Compared to SOCOL-AERv2 the default dynamical timestep was halved to 7.5 min, while the default chemical and microphysical time steps are the same as for SOCOL-AERv2 (2h and 6 min, respectively). The interactive ocean as well as the finer spatial resolution make SOCOLv4 computationally much more expensive than SOCOL-AERv2. Therefore, we performed most sensitivity simulations with SOCOL-AERv2 using fixed sea surface temperatures (SST) and sea ice coverage (SIC, see Section 2.2.3), while SOCOLv4 was primarily used to look at the impact on surface temperature anomalies.

### 2.2.3 Experimental setup

For the present study, we employed SOCOL-AERv2 with a resolution of 39 hybrid sigma-pressure levels in the vertical and a horizontal truncation of T42 ( $\sim 2.8^\circ \times 2.8^\circ$  in latitude and longitude). The simulations for this study include a reference scenario for stratospheric background conditions as well as two perturbation scenarios including stratospheric sulfur injections. The boundary conditions are identical to the GeoMIP test-bed experiment “accumH2SO4” (Details of the experiment protocol: <http://climate.envsci.rutgers.edu/geomip/testbed.html> with GHGs and ozone-depleting substances taken from the projections for 2040 from the SSP5-8.5 scenario (see also Weisenstein et al. (2022)). SST and SIC are prescribed using an average of the years 1988–2007 of the CMIP5 PCMDI-AMIP-1.1.0 SST/Sea Ice dataset (Taylor et al., 2000).

As SOCOL-AERv2 with 39 vertical levels does not generate a quasi-biennial oscillation (QBO) internally, the simulated wind in the equatorial stratosphere is nudged towards observed wind profiles (Stenke et al., 2013). We ran 20 model years for each scenario. The first 5 years are considered as spin-up period (sufficient for the present application), and we use the subsequent 15 years for our analysis.

Consistent with Weisenstein et al. (2022), the intervention scenarios examined here apply gaseous SO<sub>2</sub> injections of 5 and 25 Tg(S) yr<sup>-1</sup> emitted uniformly in a 2 km thick layer centred around 20 km altitude in the region between 30° S and 30° N over all longitudes. These so-called "regional injections" are complemented by an example of a "point injection" performed with SOCOLv4 (see Section 2.2.2) injecting 5 Tg(S) yr<sup>-1</sup> of SO<sub>2</sub> at the same vertical extent but constrained to a region from 10°N to 10°S at the equator only emitting at the 0° meridian. These point emission scenarios followed the G4 GeoMIP scenario (Kravitz et al., 2011) with transient SSP5-8.5 boundary conditions and allow us to explore the sensitivity of surface temperature to the call sequence in a fully coupled ESM.

To determine the effects of the setup of the microphysical scheme (see Fig. 2.1) on the computed size distribution and aerosol burden, we performed several model simulations for background conditions as well as conditions of climate intervention. The different simulations vary by reversing the call sequence of the condensation and nucleation routines, or by increasing the number of microphysical timesteps  $N_{\text{micro}}$ . The model simulations are summarized in Table 2.1. The experiment BG\_CN\_20 represents the default setup of the microphysical scheme in SOCOL-AERv2 and is used as the reference simulation.

In the absence of observational data of the stratospheric aerosol layer under climate intervention conditions, we also tested the effect of different microphysical settings in the modeling of the 1991 Mt. Pinatubo eruption, following the experimental setup of the Interactive Stratospheric Aerosol Model Intercomparison Project (ISA-MIP, Quaglia et al., 2023).

Table 2.1: Overview of model simulations performed with SOCOL-AERv2 (except for S5p, which was performed with SOCOLv4). Simulation names refer to the following naming convention: "SO<sub>2</sub> emission scenario"\_"Call sequence"\_"N<sub>micro</sub>". BG: background; S5: 5 Tg(S) yr<sup>-1</sup>, regional emission; S5p: 5 Tg(S) yr<sup>-1</sup>, point emission simulated with SOCOLv4; S25: 25 Tg(S) yr<sup>-1</sup>, regional emission; PIN: Pinatubo eruption ("shallow injection" scenario of ISA-MIP (Timmreck et al., 2018)); CN: condensation first; NC: nucleation first; N<sub>micro</sub>: number of microphysical timesteps.

Simulation name	SO <sub>2</sub> emission scenario	Microphysical call sequence	Microphysical timesteps
BG_CN_20	background	Cond-Nuc	20
BG_NC_20		Nuc-Cond	20
S5_CN_20	5 Tg(S) yr <sup>-1</sup> (regional)	Cond-Nuc	20
S5_CN_200		Cond-Nuc	200
S5_NC_20		Nuc-Cond	20
S5_NC_200		Nuc-Cond	200
S5p_CN_20	5 Tg(S) yr <sup>-1</sup> (point)	Cond-Nuc	20
S5p_NC_20		Nuc-Cond	20
S25_CN_20	25 Tg(S) yr <sup>-1</sup> (regional)	Cond-Nuc	20
S25_CN_200		Cond-Nuc	200
S25_NC_20		Nuc-Cond	20
S25_NC_60		Nuc-Cond	60
S25_NC_200		Nuc-Cond	200
PIN_CN_20	Pinatubo 5 Tg(S) (single event, point)	Cond-Nuc	20
PIN_NC_20		Nuc-Cond	20
PIN_NC_200		Nuc-Cond	200

## 2.3 Results

In this section, we first analyze how the microphysical settings in SOCOL-AERv2 affect the calculated aerosol size distributions under stratospheric background conditions and under scenarios with SO<sub>2</sub> injection. Next, we examine how the changes in size distributions affect global aerosol properties, such as aerosol loading and net radiative forcing. Finally, we show that microphysical settings directly affect stratospheric chemistry and thus the ozone layer via aerosol surface area density under conditions with climate intervention.

### 2.3.1 Influence of microphysical settings on aerosol size distribution

The upper row of panels in Fig. 2.2 shows particle size distributions at 55 hPa in the low latitudes (30°S-30°N) for unperturbed conditions and for conditions with climate intervention. As obvious from panel (a), changing the call sequence of the nucleation and condensation subroutines does not influence the simulated aerosol size distribution under background conditions. Since maximum nucleation rates occur about 2-3 km below the tropical tropopause (Thomason and Peter, 2006), we also examined the size distributions at 115 hPa (not shown), and again find that the call sequence has no impact on the model

results. This indicates that the default microphysical timestep of 6 min is sufficiently shorter than the characteristic times of nucleation and condensation under background conditions, so that none of the two processes inappropriately dominates the H<sub>2</sub>SO<sub>4</sub>-to-particle conversion.

In contrast to background conditions, the SO<sub>2</sub> injections scenarios are highly sensitive to the microphysical settings. Initially, we kept the microphysical timestep constant ( $N_{\text{micro}} = 20$ ), but reversed the call sequence from the default "condensation first" (CN) to "nucleation first" (NC). This modification leads to a massive increase of nucleation mode particles ( $R < 0.01 \mu\text{m}$ ) (Fig. 2.2c, e, yellow and blue dotted lines).

To highlight differences in the coarse mode ( $R > 1 \mu\text{m}$ ), we calculated the fifth moment of the corresponding size distributions (lower row in Fig. 2.2). This provides an estimate of the downward mass flux due to aerosol sedimentation, which is determined by the product of particle volume (proportional to the third moment) and sedimentation speed (roughly proportional to the second moment). Swapping from CN to NC leads to a significant decrease of coarse mode particles (by one order of magnitude) for the S25 scenario (inset in Fig. 2.2f).

These significant differences in the size distributions demonstrate the dominating role of the first-called process as H<sub>2</sub>SO<sub>4</sub> sink, either condensation or nucleation, indicating that the default timestep ( $2 \text{ h}/N_{\text{micro}} = 2 \text{ h}/20 = 6 \text{ min}$ ) is too long to properly handle elevated stratospheric sulfur loadings. Therefore, we increased the number of microphysical substeps until the resulting particle size distributions of the CN and NC simulations converge. For a sufficiently short microphysical timestep (0.6 min with  $N_{\text{micro}} = 200$ ), the simulations develop a pronounced peak of nucleation mode particles (Fig. 2.2c, e, orange and blue solid lines) similar to the CN<sub>20</sub> simulations, but with somewhat lower particle number densities.

As expected, the computational costs of the model increase with a shorter microphysical timestep. Increasing the number of microphysical substeps from 20 to 200 almost doubles the required wall-clock time per model year from 4.6 h to 9 h, using parallel computing on 64 CPUs. To assess possibilities to reduce the computational costs, we tested the efficiency of  $N_{\text{micro}} = 60$  (and 80, not shown).

The red lines in Fig. 2.2e,f show the results for S25\_NC\_60, demonstrating excellent agreement with  $N_{\text{micro}} = 200$ , which gives us confidence in the accuracy of the model solution. Furthermore, the computational demand increased only moderately by about 33% (60 min) per model year (relative to  $N_{\text{micro}} = 20$ ). In conclusion, in SOCOL-AERv2 nucleation first with  $N_{\text{micro}} = 60$  provides a very good description of climate intervention scenarios, even when the loading is extremely high.

We also explored the effects of the distribution of gaseous H<sub>2</sub>SO<sub>4</sub> molecules produced during the 2-hourly call of the chemistry routine, either homogeneously across the  $N_{\text{micro}}$  sub-timesteps or as a total amount at the beginning of the microphysical loop. As Figure 2.6 in Appendix 2B shows, proper partitioning of the H<sub>2</sub>SO<sub>4</sub> molecules among the  $N_{\text{micro}}$  sub-timesteps is critical to avoid an excessive formation of nucleation mode particles due to artificially high H<sub>2</sub>SO<sub>4</sub> supersaturations at the beginning of the microphysical substepping. More details can be found in the Appendix (see Section 2.4).

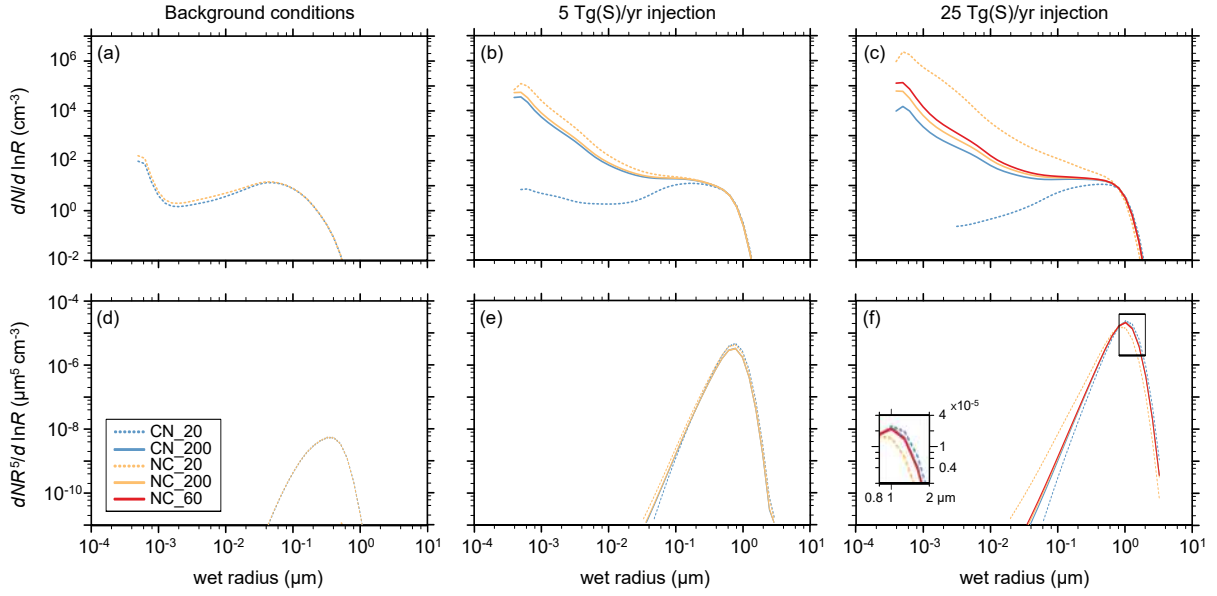


Figure 2.2: Upper row: Size distributions ( $dN/d \ln R$ , particles  $\text{cm}^{-3}$ ) averaged between 30° S and 30° N at 55 hPa for the model simulations with (a) stratospheric background conditions, (c) regional SO<sub>2</sub> injections of 5 Tg(S) yr<sup>-1</sup>, and (e) 25 Tg(S) yr<sup>-1</sup>. Lower row: The fifth moment ( $dNR^5/d \ln R$ ,  $\mu\text{m}^5 \text{cm}^{-3}$ ) of the aerosol size distributions as an estimate for aerosol sedimentation mass flux (particle volume ( $\propto R^3$ ) times sedimentation velocity ( $\propto R^2$ )). Blue lines: simulations with condensation first; orange and red lines: nucleation first. Dashed lines:  $N_{\text{micro}} = 20$  microphysical timesteps; solid orange and blue lines:  $N_{\text{micro}} = 200$ ; solid red lines in (e) and (f):  $N_{\text{micro}} = 60$ . Insert in (f) highlights the differences for coarse particles.

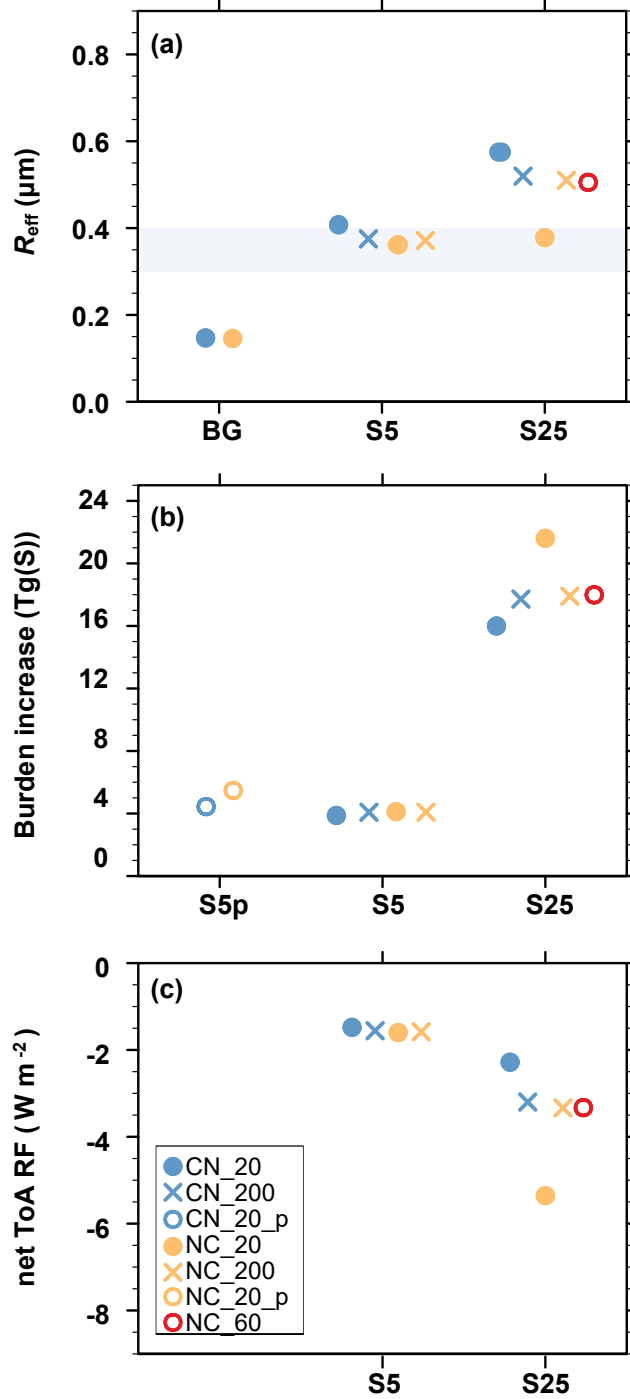


Figure 2.3: Effect of microphysical settings on the global averages of various calculated aerosol and radiative quantities. **(a)** Global mean effective radius ( $\mu\text{m}$ ) at 55 hPa. **(b)** Global mean sulfuric acid aerosol burden increase (Tg(S)). **(c)** Global mean change in net top-of-atmosphere (shortwave + longwave) radiative forcing ( $\text{Wm}^{-2}$ ). Injection scenarios are: BG = background conditions (no injection); S5 = 5 Tg(S)  $\text{yr}^{-1}$  regional SO<sub>2</sub> injection; S5p = 5 Tg(S)  $\text{yr}^{-1}$  point SO<sub>2</sub> injection; and S25 = 25 Tg(S)  $\text{yr}^{-1}$  regional SO<sub>2</sub> injection. Blue symbols: condensation first. Orange and red symbols: nucleation first. Open or filled circles:  $N_{\text{micro}} = 20$  (or 60). Crosses:  $N_{\text{micro}} = 200$ . Light blue shading in **(a)**: optimal effective radii for scattering of solar radiation from Dykema et al. (2016) and Figure 4 in Weisenstein et al. (2022).

### 2.3.2 Influence of microphysical settings on global means of particle size, aerosol burden and radiative forcing

The large differences in the simulated size distribution have wide implications for other key metrics of stratospheric aerosols, namely the average size of the aerosol particles, burden and radiative forcing: these are collectively shown in Fig. 2.3 in the three sets of experiments. Figure 2.3a shows the globally averaged effective radius ( $R_{\text{eff}}$ ) at 55 hPa. For background conditions both microphysical settings, CN and NC, result in an average  $R_{\text{eff}}$  of 0.15  $\mu\text{m}$ . For the SO<sub>2</sub> injections scenarios, most of the additional sulfur condenses onto existing particles or is consumed in nucleation of new particles, which coagulate preferentially onto the larger background particles. This increases the simulated  $R_{\text{eff}}$  compared to the background case, moving towards and into the range of optimal effective radius for scattering of solar radiation between 0.3 and 0.4  $\mu\text{m}$  (Weisenstein et al., 2022, see their Fig. 4). The standard microphysical setup (CN,  $N_{\text{micro}} = 20$ , solid blue circles) result in the largest simulated  $R_{\text{eff}}$ , as condensation partly suppresses the subsequent formation of smaller particles via nucleation. Conversely, nucleation first with long microphysical timesteps (NC,  $N_{\text{micro}} = 20$ , solid orange circles) exaggerates the formation of small particles, resulting in an underestimation of  $R_{\text{eff}}$ . Given a sufficiently short timestep ( $N_{\text{micro}} = 200$ ), CN and NC converge to  $R_{\text{eff}}$  of 0.38  $\mu\text{m}$  for the S5 scenario, and 0.48  $\mu\text{m}$  for the S25 scenario (blue and orange crosses). Compared to the modal models MA-ECHAM5-HAM and CESM2, the sectional SOCOL-AER in general produces smaller  $R_{\text{eff}}$  for the regional injections. Hence, improving the SOCOL-AER aerosol microphysics by swapping the sequence to nucleation first and increasing  $N_{\text{micro}}$  leads to a slight reduction in the spread in  $R_{\text{eff}}$  among these models.

Figure 2.3b shows the impact of microphysical settings on the total (troposphere and stratosphere) aerosol burden increase in the intervention scenarios compared to background conditions. For background conditions, CN and NC with  $N_{\text{micro}} = 20$  show an almost identical aerosol burden (see also Table 2.2 in Appendix 2A). For the SO<sub>2</sub> injection scenarios, the original setup CN<sub>20</sub> reveals the smallest aerosol burden. The largest aerosol burden is simulated by the simulation with NC<sub>20</sub> setting, since this setup shifts the size distribution towards small particles, which have a longer stratospheric residence time. For the S5 scenario the dependence on call sequence is small, but for S25 the simulated aerosol burdens differ by more than 30% (Table 2.2). Despite this large spread in the simulated burden increase, SOCOL-AERv2 still falls between the CESM2 and the MA-ECHAM5-HAM models, which showed for most of the simulated injection scenarios the largest and smallest burden increase, respectively (Weisenstein et al., 2022, their Fig. 1).

Figure 2.3c displays globally averaged changes in the net top-of-atmosphere short- and longwave radiative forcing (RF) due to SO<sub>2</sub> injections. Since SOCOL-AERv2 uses prescribed SST and SIC, the climate intervention runs remain in non-equilibrium and the perturbation in radiative fluxes at TOA directly quantify the Effective RF (Forster et al., 2016). All S5 simulations show a rather consistent RF change of around -1.5 W m<sup>-2</sup>. For the S25 simulations, however, we find a large spread in RF, ranging from -2.3 W m<sup>-2</sup> for the original microphysical setup (CN<sub>20</sub>) to -5.4 W m<sup>-2</sup> for the simulation with reversed call sequence (NC<sub>20</sub>). As already mentioned in Weisenstein et al. (2022), the differences in RF between the various SOCOL-AERv2 simulations, but also between different models, are mainly related to the respective burden increases (Fig. 2.3b). The simulations with the largest burden increase also show the smallest  $R_{\text{eff}}$ , which efficiently scatters the incoming

solar radiation and enhances the negative RF.

As discussed in previous studies (Heckendorn et al., 2009; Kleinschmitt et al., 2018), the efficacy of the SO<sub>2</sub> injection, i.e. the RF per Tg of sulfur injected annually, decreases with increasing injection rate, since the aerosol particles grow larger, which increases sedimentation and decreases scattering efficiency. However, the model intercomparison by Weisenstein et al. (2022) revealed that not only the radiative efficacy itself, but also its decrease with increasing injection rates is strongly model dependent. For SOCOL in Fig. 2.3c, the radiative efficacy of the various S5 simulations ranges moderately between -0.28 and -0.34 W m<sup>-2</sup> (Tg(S) yr<sup>-1</sup>)<sup>-1</sup>. For the S25 simulations, the simulations with strongest and weakest efficacy differ by more than a factor of 2. The applied microphysical improvements lead to a significantly stronger radiative efficacy (-0.09 W m<sup>-2</sup> (Tg(S) yr<sup>-1</sup>)<sup>-1</sup> for S25\_NC\_60) compared to the default setup (-0.13 W m<sup>-2</sup> (Tg(S) yr<sup>-1</sup>)<sup>-1</sup> for S25\_CN\_20).

As SOCOL-AERv2 does not include an interactive ocean model, but prescribed SSTs, it is unfeasible to test the impact of the call sequence on surface temperature anomalies. To overcome this limitation, we performed the G4 GeoMIP scenario with the NC setup (S5p\_NC\_20) using the ESM SOCOLv4, a coupled model which shares the same exact aerosol module as SOCOL-AERv2 (see methods). In this model, we use point injections, in keeping with the G4 protocol (see Section 2.2.3). The simulation shows an increase of 25% in stratospheric aerosol burden compared to the conventional S5p\_CN\_20 scenario (see Fig. 2.3b, left). The corresponding global averaged surface cooling is 0.65 K and 1.02 K for S5p\_CN\_20 and S5p\_NC\_20, respectively, which is an increase of 57%, whereas no significant differences in global stratospheric aerosol burden and RF were found among regional S5 scenarios performed with SOCOL-AERv2 (see Fig. 2.3b, middle). This underlines the sensitivity of our results to the chosen injection scenario (point vs. regional) as well as to the model resolution (Section 2.2.2). Both the model resolution and the injection scenario can lead to locally very different H<sub>2</sub>SO<sub>4</sub> supersaturation.

### 2.3.3 Influence of settings on meridional distributions of aerosol burden, radiative forcing, and ozone

Figure 2.4a,b show the influence of microphysical settings on the modeled latitudinal variation of the sulfate aerosol column burden (stratosphere plus troposphere) for the climate intervention scenarios simulated with SOCOL-AERv2 (S5 and S25). In contrast, background simulations (not shown) have almost no dependence on the call sequence (see Table 2.2 in Appendix 2A). The SO<sub>2</sub> injection scenarios show similar latitudinal patterns, with aerosol column burdens peaking over the inner tropics, confined by the tropical leaky pipe. After overcoming the subtropical jet, the burden again maximizes around 45° N/S in the stratospheric surf zone, whereas the polar regions are isolated by the polar jets. As discussed before (Fig. 2.3b), the original setting CN\_20 results in the smallest aerosol burden, whereas NC\_20 with "nucleation first" shifts the size distribution towards smaller particles with less gravitational settling (see also Table 2.2).

The latitudinal variations of the radiative forcing (RF) in Fig. 2.4c,d show the mirror image of the burden in Fig. 2.4a,b, with reduced irradiance at high aerosol loading, and illustrate the direct radiative effects of the aerosol. However, in contrast to the smooth distributions of aerosol loading, RF exhibits a much higher degree of small fluctuations due to tropospheric cloud variability. The latitudinal variations in RF are very similar for all S5 simulations and the S25 simulations also show a consistent geographic pattern.



The negative RF covers more than 80% of the globe, with the exception of the polar caps where absorption of outwelling infrared radiation by the aerosol predominates and the RF becomes positive. The differences between the individual simulations become largest in the tropics, reflecting the sensitivity of the aerosol loading to the microphysical setup.

Figure 2.4e,f shows the impact of the simulated SO<sub>2</sub> injections on zonally averaged total column ozone as difference to the reference simulation BG\_CN\_20. As already discussed by Weisenstein et al. (2022), the SO<sub>2</sub> injections lead to a massive reduction of the ozone column. This is caused by accelerated ClO<sub>x</sub>-induced and HO<sub>x</sub>-induced ozone destruction cycles, which in turn are due to heterogeneous N<sub>2</sub>O<sub>5</sub> hydrolysis on the aerosol particles (leaving less NO<sub>2</sub> required for ClO<sub>x</sub> and HO<sub>x</sub> deactivation). The N<sub>2</sub>O<sub>5</sub> hydrolysis rate is proportional to the SAD (see next Section and Figs. 2.7 and 2.8 in Appendix 2C). Both injection scenarios, S5 and S25, show similar patterns with the most pronounced changes in mid- to high latitudes. In the polar regions, the ozone loss is mainly caused by enhanced heterogeneous ClONO<sub>2</sub> activation on the additional aerosol SAD. Furthermore, in agreement with the CESM2 model, SOCOL-AER simulates a decrease of the ozone column in the tropics, where the accelerated Brewer-Dobson circulation leaves less time for ozone formation by molecular oxygen photolysis. In the tropics, the presented microphysical modifications do not show any significant impact on the simulated ozone decrease (Figure 2.4e and f), despite clear differences in the simulated SAD for the same sulfur injection (Figs. 2.7 and 2.8). This result indicates that above a certain threshold a further SAD increase does not affect the NO<sub>x</sub> cycle and its coupling to the ClO<sub>x</sub> and HO<sub>x</sub> cycles anymore. The fact that the S25 simulations result in a more pronounced total column ozone change than the S5 simulations is related to a more pronounced strengthening of the Brewer-Dobson circulation, which reduces the time for chemical ozone formation, and the increased stratospheric H<sub>2</sub>O entry, which enhances ozone loss by the HO<sub>x</sub> cycle (Tilmes et al., 2018).

In mid-to high latitudes both injection scenarios, S5 and S25, reveal substantial differences in the total ozone loss simulated, depending on the microphysical settings used in the simulations. For the S5 simulations (Fig. 2.4e), the total ozone losses over Antarctica range between 24 and 30 DU. For the Northern Hemisphere, the spread in simulated polar ozone losses is with 6 to 24 DU even larger. For the S25 simulations (Fig. 2.4e and f), the simulated polar ozone loss range between 60 and 80 DU over the Southern Hemisphere, and between 35 and 60 DU over the Northern Hemisphere. It should be noted that the microphysical setup with the smallest ozone change in one hemisphere, does not necessarily also show the smallest ozone change on the other hemisphere, which might be related to the dynamical variability.

It should be emphasized that the discussed changes in total column ozone caused by stratospheric SO<sub>2</sub> injections refer to stratospheric concentrations of ozone depleting substances and GHGs projected for the year 2040. With further decreasing stratospheric chlorine loadings in the future, the impact of the enhanced aerosol SAD under SO<sub>2</sub> injections on total column ozone might change as the coupling between the ClO<sub>x</sub> and NO<sub>x</sub> cycle becomes less important.

### 2.3.4 Influence of settings on SAD and stratospheric temperature

Climate intervention by stratospheric SO<sub>2</sub> emission yields an increase in aerosol surface area density (SAD), which enables heterogeneous chemical reactions such as N<sub>2</sub>O<sub>5</sub> hy-

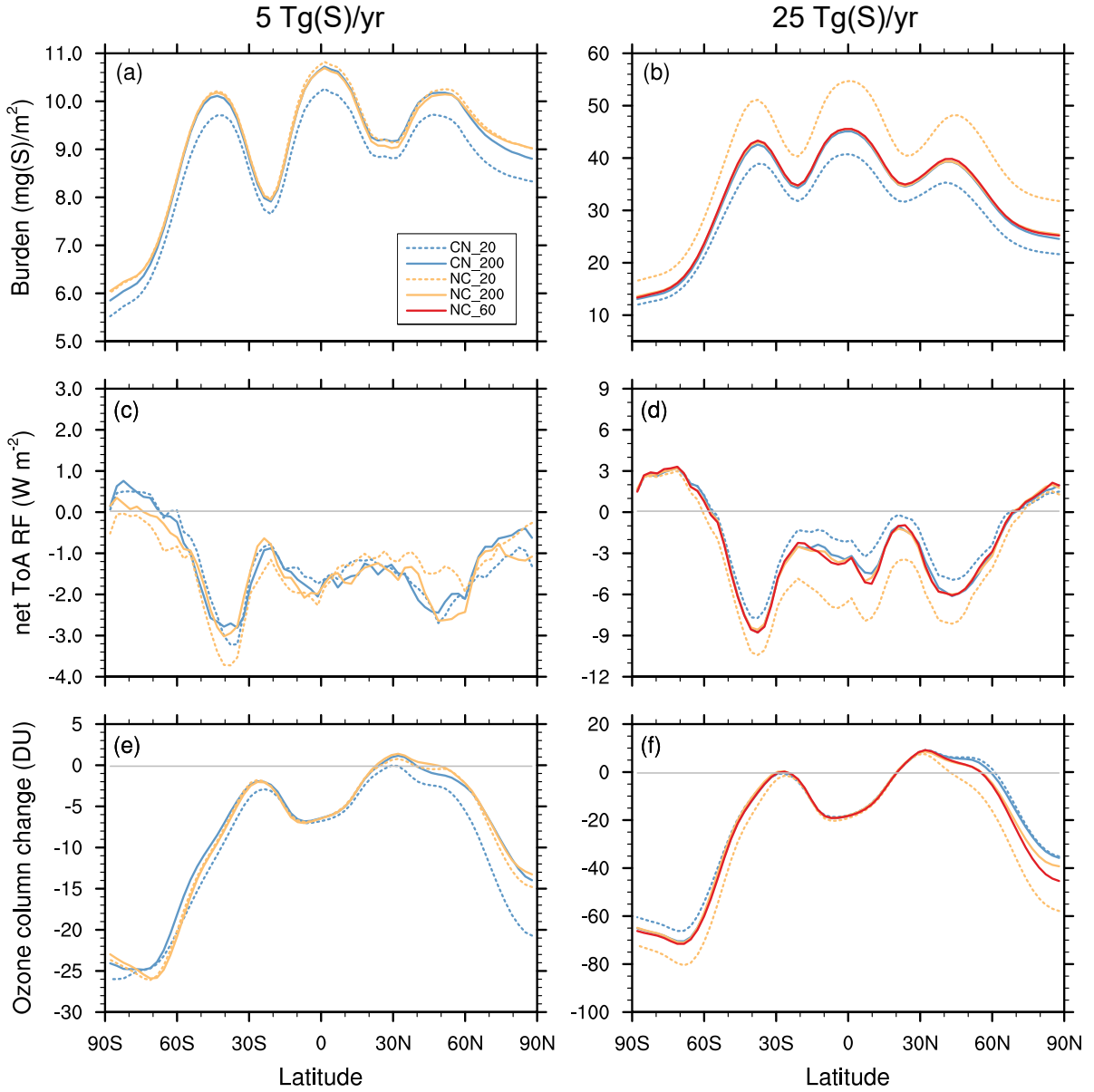


Figure 2.4: Effect of microphysical settings on the zonal averages of various calculated aerosol, radiative and chemical quantities. Left column: regional SO<sub>2</sub> injections of 5 Tg(S) yr<sup>-1</sup>. Right column: regional SO<sub>2</sub> injections of 25 Tg(S) yr<sup>-1</sup>. **(a,b)** Sulfuric acid aerosol burden per square meter (mg(S) m<sup>-2</sup>). **(c,d)** Zonal mean net top-of-atmosphere (shortwave + longwave) radiative forcing (Wm<sup>-2</sup>). **(e,f)** Change in zonal average column ozone (Dobson units). Blue lines: simulations with condensation first; orange and red lines: nucleation first. Dashed lines:  $N_{\text{micro}} = 20$  microphysical timesteps; solid orange and blue lines:  $N_{\text{micro}} = 200$ ; solid red lines:  $N_{\text{micro}} = 60$ . All panels use the simulation BG\_CN\_20 as reference.

drolysis, but which is also an approximate measure of the extinction and, hence, the backscatter of shortwave radiation. Moreover, the aqueous H<sub>2</sub>SO<sub>4</sub> aerosol absorbs outwelling longwave radiation and some incoming solar radiation, which increases the air temperature, with repercussions for stratospheric dynamics.

Both quantities, SAD and temperature, are also affected by the microphysical settings CN versus NC and  $N_{\text{micro}}$ . In brief, the NC setting with  $N_{\text{micro}} = 200$  yields higher SAD than CN with  $N_{\text{micro}} = 20$ , roughly by 20%. This is due to the smaller particles with higher SAD and larger burden (see Figs. 2.7 and 2.8 in the Appendix 2C). The larger burden, in turn, leads to more longwave radiative heating, which increases stratospheric temperatures. This is a marginal effect in the S5 scenario, but corresponds to about 1 K higher temperatures under S25 conditions (see Figure 2.9 in Appendix 2D). A strongly temperature dependent reaction such as  $\text{O}_3 + \text{O} \rightarrow 2 \text{O}_2$  changes by about 4% for  $\Delta T = 1$  K, so that the impact of microphysical settings on ozone via SAD-changes is by far more important than the impact via  $T$ -changes. Also differences from dynamical feedbacks between the different settings are likely small since the absolute temperature increase from the S25 scenarios is up to 15 K and thus much larger.

### 2.3.5 Influence of settings on modeling the eruption of Mt. Pinatubo

So far, our study has highlighted the impacts of the microphysical settings for continuous injections in climate intervention scenarios. Here, we expand this analysis, by evaluating the effects under conditions of volcanic eruptions on the 1991 eruption of Mt. Pinatubo by using the PIN\_CN\_20, PIN\_NC\_20 and the PIN\_NC\_200 settings (Table 2.1). We compared the evolution of the computed global stratospheric aerosol burden with SAGE and HIRS satellite data and the evolution of the computed mean effective particle radius with balloon measurements over Laramie (Wyoming, see Figure 2.5). Details on the observational data sets and their uncertainties as well as model and inter-model uncertainties can be found in Sukhodolov et al. (2018) and Quaglia et al. (2023). All model settings show a very similar peak in the stratospheric aerosol burden, but distinctly different declines during the years 1992/93. "Nucleation first" shifts the size distribution towards smaller particles, which have a longer stratospheric residence time. The slower decline is in better agreement with observations, although it should be mentioned that the agreement with observations strongly depends on the assumed SO<sub>2</sub> emissions profile (Quaglia et al., 2023). Regarding the mean  $R_{\text{eff}}$ , PIN\_NC\_20 simulates smaller values than PIN\_CN\_20 for the first couple of months after the eruption and higher values later on, as PIN\_CN\_20 returns faster towards background conditions due to faster sedimentation of larger particles. Overall, the microphysical modifications do not overly influence the discrepancy between modeled and observed  $R_{\text{eff}}$  (Fig. 2.5b).

However, other than under climate intervention conditions the evolution of the aerosol burden and  $R_{\text{eff}}$  in the PIN\_NC\_200 scenario are much closer to PIN\_CN\_20 than to PIN\_NC\_20. The volcanic eruption is a point event in time and space, whereas the climate intervention scenarios have continuous emissions across all longitude and 30°N and 30°S in latitude, which establish a steady-state situation. This leads to H<sub>2</sub>SO<sub>4</sub> production rates, which locally are about  $10^4 - 10^5$  times larger in the Mt. Pinatubo case compared to S5 and S25. Since nucleation is exponentially dependent on the H<sub>2</sub>SO<sub>4</sub> supersaturation this leads to erroneously large nucleation rates in the PIN\_NC\_20 scenario. Coagulation is not efficient enough to remove the large amount of nucleation mode particles in that

scenario. When increasing  $N_{\text{micro}}$  to 200 (PIN\_NC\_200) the burden and the  $R_{\text{eff}}$  of the plume evolve following the PIN\_CN\_20 scenario since local supersaturation are smaller now and coagulation can keep up with efficiently removing the nucleation mode particles.

Therefore, for volcanic eruptions, where  $\text{H}_2\text{SO}_4$  supersaturations are locally much larger compared to climate engineering scenarios, the correct solution is much closer to CN\_20, since otherwise nucleation would erroneously dominate over condensation. This is a good example of how the very different distributions of  $\text{H}_2\text{SO}_4$  supersaturation in space and time when simulating volcanic eruptions and climate intervention scenarios lead to different challenges within aerosol microphysics schemes (Heckendorn et al., 2009; Vattioni et al., 2019).

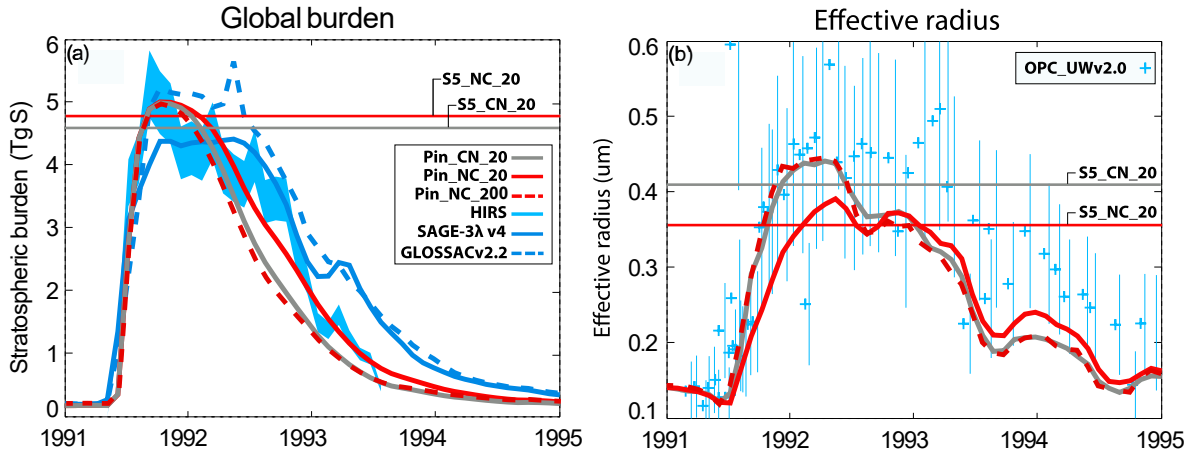


Figure 2.5: (a) Evolution of the simulated global stratospheric aerosol burden (Tg(S)) for PIN\_CN\_20 and PIN\_NC\_20 compared with HIRS- and SAGE-II-derived data (SAGE-3,4 $\lambda$  and GLOSSACv2.2, Arfeuille et al., 2013; Thomason et al., 2018; Kovilakam et al., 2020). HIRS-derived total (troposphere and stratosphere) aerosol sulfur burden assumes 75% sulfuric acid by weight (Baran and Foot, 1994). Light blue shaded area: uncertainties of HIRS. (b) Effective particle radius ( $\mu\text{m}$ ) averaged over the altitude range from 14 to 30 km compared to in-situ measurements taken at Laramie, Wyoming (OPC UWv2.0, Deshler et al., 2019). Thin blue whiskers reflect the measurement uncertainty (adapted from Quaglia et al., 2023). For comparison the steady-state values for S5\_CN\_20 and S5\_NC\_20 from this work are shown as thin horizontal red and gray lines in both panels.

## 2.4 Comparison with other work and conclusions

In this study, we have shown the importance of properly setting the length of the microphysical timestep and the call sequence of nucleation and condensation for modeling the global stratospheric sulfuric acid aerosol under conditions of  $\text{SO}_2$  injections for climate engineering. In the aerosol-chemistry-climate model SOCOL-AERv2, the evolution of the  $\text{H}_2\text{SO}_4$  concentration in the gas-phase is determined by sequential operator splitting using a sub-stepping approach for aerosol microphysics with a default timestep of 6 min, i.e. the  $\text{H}_2\text{SO}_4$  gas-phase concentration is consecutively updated by  $\text{H}_2\text{SO}_4$  production from chemistry, condensation and nucleation. We found the following:

- Under stratospheric background conditions, the call sequence does not affect the

model results, indicating that the default number of microphysical sub-timesteps is sufficient to prevent the first called process from spuriously dominating the size distribution.

- Under elevated H<sub>2</sub>SO<sub>4</sub> supersaturations in the stratosphere the characteristic times for nucleation and condensation may become shorter than the default microphysical timestep. In such cases, the competition between the two H<sub>2</sub>SO<sub>4</sub> sinks affects the simulated aerosol size distribution and the microphysical time step must be reduced.
- The default setting "condensation first" can massively underestimate the fraction of nucleation mode particles, whereas "nucleation first" tends to underestimate the number of coarse mode particles. Tests of numerical convergence with very short timesteps indicate that "nucleation first" yields smaller numerical errors for regional SO<sub>2</sub> injections, whereas condensation first yields smaller numerical errors for the simulation of volcanic eruptions with locally and temporally extremely high H<sub>2</sub>SO<sub>4</sub> supersaturations.
- Despite significant shifts in simulated aerosol size distributions, the main response patterns of atmospheric chemistry and climate to stratospheric SO<sub>2</sub> injections as simulated with SOCOL-AERv2 are robust to microphysical time integration adjustments, but the strength of the response can differ substantially in the case of high injection rates (such as 25 Tg(S) yr<sup>-1</sup>) or point injections (such as 5 Tg(S) yr<sup>-1</sup> point injections, S5p), which both lead to large H<sub>2</sub>SO<sub>4</sub> supersaturations.
- The radiative forcing found for the 25 Tg(S) yr<sup>-1</sup> injection scenario varies by more than a factor of 2 between the different microphysical settings. Nevertheless, this model-internal uncertainty in SOCOL-AERv2 is still smaller than the scatter between the three GCMs with interactive aerosol microphysics – CESM2-WACCM6, MA-ECHAM5-HAM, and SOCOL-AERv2 – compared by Weisenstein et al. (2022) in strictly coordinated climate intervention modeling.

The first part of our conclusions confirms the study by Wan et al. (2013), who investigated different time integration methods to solve the H<sub>2</sub>SO<sub>4</sub> continuity equation using two versions of the ECHAM-HAM model: HAM1 with an Euler forward scheme with sequential operator splitting similar to SOCOL-AERv2, but without microphysical substeps; HAM2 with a two-step time integration scheme implemented by Kokkola et al. (2009). They identified sequential operator splitting with too long timesteps as major source of numerical error in HAM1, and proposed simultaneous processing of condensation and nucleation to better represent the competition between both processes. The microphysical sub-stepping technique as applied in SOCOL-AERv2 improves the results of the operator splitting approach, but requires a sufficiently large number of substeps. Instead of using a fixed number of substeps, a dynamical timestep adjustment could be beneficial, but we have not tested this here.

The importance of aerosol microphysics and the competition between nucleation and condensation on the simulated aerosol size distribution and the radiative efficiency of stratospheric sulfur injections was also shown by Laakso et al. (2022), who investigated different injection strategies using the ECHAM-HAMMOZ model with two different aerosol schemes, the sectional SALSA scheme as well as the modal M7 scheme. SALSA describes the aerosol size distribution in 10 mass bins, while M7 uses 7 lognormal modes. The authors found that nucleation of new particles dominates over condensational particle

growth in the sectional SALSA scheme, while the opposite is the case in the modal M7 module. In addition, the use of lognormal modes results in a minimum in the particle size distribution in the optimal size range for solar scattering and restricts the growth of particles in accumulation mode, tending to underestimate gravitational settling. These differences resulted in smaller particles in SALSA and, therefore, a higher radiative forcing. For an injection scenario of 20 Tg(S) yr<sup>-1</sup>, SALSA revealed a global net ToA radiative forcing of around -8 W m<sup>-2</sup>, M7 resulted in -3 W m<sup>-2</sup>. This spread is even larger than what we found for the S25 simulations S25\_CN\_20 and S25\_NC\_20. Laakso et al. (2022) further investigated the impact of the competition between nucleation and condensation by performing simulations with the nucleation being switched off in both aerosol modules by emitting 25% of the sulfur directly as 3 nm particles. The results of these sensitivity studies indicate that the different treatment of nucleation and condensation explains the differences in radiative forcing between SALSA and M7 only partly: The difference in radiative forcing was weakened from -5 W m<sup>-2</sup> to about -3 W m<sup>-2</sup>.

Apart from time integration or representation of the aerosol size distribution, numerical parameterizations of individual processes are another source of uncertainty. The binary-homogeneous nucleation scheme by Vehkamäki et al. (2002), for example, is widely used in models, including SOCOL-AERv2 or the above mentioned aerosol schemes SALSA and M7. The latter two include an extension of the scheme for high sulfate concentrations implemented by Kokkola et al. (2009), using the collision rate as maximum possible nucleation rate. In a very recent study, Yu et al. (2023) evaluated simulated nucleation rates in the lowermost stratosphere by CLOUD laboratory measurements under stratospheric temperatures. They found that the Vehkamäki scheme overestimates observed nucleation rates by 3 to 4 orders of magnitude. As the particle size distribution is not only determined by nucleation, but also by particle growth through condensation and coagulation, Yu et al. (2023) compared the simulated size distributions to in-situ measurements of the particle number densities down to a diameter of 3 nm obtained during the NASA Atmospheric Tomography Mission (ATom) between 2016 and 2018. In the size range between 3 to 10 nm, the number densities simulated with the GEOS-Chem model using the Vehkamäki et al. scheme were 1-2 orders of magnitude higher than observed. The same holds true for SOCOL-AERv2: under background conditions in the southern hemisphere lowermost stratosphere (70 ° S, 12 km altitude), modeled number densities for particles smaller than 10 nm in diameter range between 10<sup>3</sup> and 10<sup>4</sup> cm<sup>-3</sup>, while the ATom observations indicate values between slightly below 10<sup>1</sup> to 10<sup>2</sup> cm<sup>-3</sup>. Using the kinetic scheme for ion-mediated and binary homogeneous nucleation (Yu et al., 2020) calculated nucleation rates, but also the size distributions simulated by GEOS-Chem were closer to ATom. Furthermore, the results by Yu et al. (2023) suggest that under low stratospheric background H<sub>2</sub>SO<sub>4</sub> concentrations nucleation on ions, which is usually not represented in global models, dominates over binary homogeneous H<sub>2</sub>SO<sub>4</sub>-H<sub>2</sub>O nucleation. However, the importance of binary homogeneous nucleation is expected to increase under high H<sub>2</sub>SO<sub>4</sub> concentrations. Unfortunately, CLOUD measurements of nucleation rates refer to stratospheric background conditions only and do not cover strongly elevated H<sub>2</sub>SO<sub>4</sub> concentrations under SO<sub>2</sub> injection scenarios or after volcanic eruptions, but based on the findings of Yu et al. (2023) it may be that all models using the Vehkamäki scheme overestimate the role of nucleation. This might explain the low bias in the simulated mean effective radius compared to in-situ measurements following the eruption of Mt. Pinatubo. Furthermore, this might have substantial repercussions on the simulated aerosol size distribution, aerosol burdens and radiative forcing under climate intervention conditions,

most likely resulting in a decreased efficiency of SO<sub>2</sub> injections.

This work adds to a series of recent publications that highlight the crucial role of aerosol microphysics for simulated aerosol properties and modeled estimates of climate intervention effects on atmospheric chemistry and climate. Our results clearly demonstrate that there is considerable uncertainty when numerical schemes like the aerosol microphysics in SOCOL-AERv2 are applied under unprecedented conditions, such as climate intervention with continuously large SO<sub>2</sub> emissions, even if these models have been thoroughly evaluated and are well capable of reproducing observations under background or moderately perturbed conditions like volcanic eruptions. It should be emphasized that our conclusions are mainly based on simulations of regional SO<sub>2</sub> injections, which are supported by point injection scenarios and simulations of the 1991 Mt. Pinatubo eruption. As the nucleation rate strongly depends on the gas-phase H<sub>2</sub>SO<sub>4</sub> concentration, ambient temperatures and relative humidities, the optimal number of microphysical (sub-)timesteps will depend on the assumed SO<sub>2</sub> injection rates, but also on the injection scenario and region. Point injections of SO<sub>2</sub>, for example result in very high, but locally confined H<sub>2</sub>SO<sub>4</sub> supersaturations, potentially making the results more sensitive to the details of the microphysical approach. The intention of this paper is to raise awareness within the (aerosol) modelling community for potential numerical problems within conventional aerosol microphysics modules when applying them to unprecedented extreme conditions such as high H<sub>2</sub>SO<sub>4</sub> supersaturations from SO<sub>2</sub> injection for climate intervention.

While this study focused on the importance of a proper temporal resolution of aerosol microphysics, it did not address effects of spatial resolution. Properly resolving the various temporal and spatial scales, ranging from nanometers and seconds for microphysical processes to kilometers and decades for global climate, remains a significant challenge for aerosol-chemistry-climate models (Vattioni et al., 2019; Weisenstein et al., 2022). Continuous model development, such as embedded SO<sub>2</sub> emission plume modelling (Sun et al., 2022), is indispensable to close the spatial and temporal gap between aircraft emission plumes and large-scale model grids, and to effectively reduce existing model uncertainties with respect to the effectiveness of climate intervention by stratospheric sulfur injections. Furthermore, additional laboratory or small-scale field studies of aerosol formation, growth and dispersion under various stratospheric conditions could also be beneficial to evaluate and improve existing numerical models.

## Data Availability

The original SOCOL-AERv2 code is available at <https://doi.org/10.5281/zenodo.5733121> (Brodowsky et al., 2018). The simulation data using that model code, which does not account for the interpolation of H<sub>2</sub>SO<sub>4</sub> production within the microphysical sub-loop are available at <https://doi.org/10.3929/ethz-b-000610854> (Stenke et al., 2023). The modified source code of SOCOL-AERv2 handling the microphysical sub-loop by taking into account the interpolation of H<sub>2</sub>SO<sub>4</sub> production within the microphysical sub-loop can be found here: (<https://doi.org/10.3929/ethz-b-000610854>) and the data from these simulations are available at <http://hdl.handle.net/20.500.11850/622193> (Vattioni et al., 2023b).

## Author Contributions

SV proposed the study and implemented the modifications to the microphysical scheme. SV and AS performed the climate intervention simulations with SOCOL-AERv2 and analysed the model results. EW performed and analyzed the simulations with SOCOLv4. TS conducted and analyzed the Pinatubo simulations. Significant scientific guidance on the overall project was provided by TP and BL. AS drafted a first version of the manuscript. All co-authors contributed to the discussion and the text.

## Acknowledgements

Our special thanks go to Debra Weisenstein for discussions about the original AER code. We also thank Ilaria Quaglia for providing the processed OPC data. Support for Gabriel Chiodo and Andrea Stenke was provided by the Swiss Science Foundation within the Ambizione grant no. PZ00P2\_180043. Support for Sandro Vattioni was provided by the ETH Research grant no. ETH-1719-2 as well as by the Harvard Geoengineering Research Program. Timofei Sukhodolov acknowledges the support from the Swiss National Science Foundation (grant no. 200020-182239) and the Karbacher Fonds, Graubünden, Switzerland.

## Appendix 2: Supplementary information

### A: Summary of sulfur burdens and fluxes

Table 2.2 summarizes numerical results of sulfur burdens and fluxes for most of the simulations performed in this study. Simulations names are the same as in Table 1. In addition, the index "\_no\_interp." refers to the old representation of passing the H<sub>2</sub>SO<sub>4</sub> produced from the gas-phase chemistry routine to the microphysics module in one go, rather than splitting it properly among the  $N_{\text{micro}}$  substeps.



Table 2.2: Global total and stratospheric aerosol burden (Gg(S)), as well as stratospheric sulfur fluxes between condensed and gas phase due to nucleation, condensation and evaporation (Gg(S) yr<sup>-1</sup>). The net cross-tropopause flux of sulfate aerosol (Gg(S) yr<sup>-1</sup>) is calculated by balancing the stratospheric sulfur fluxes between condensed and gas phase, assuming the stratospheric aerosol burden to be in equilibrium.

Simulation name	Total burden	Stratospheric burden	Nucleation	Condensation	Evaporation	Net cross-tropopause
BG_CN_20_no_interp.	708.8	167.7	29.9	82.7	5.9	106.7
BG_CN_20	704.4	164.6	1.4	113.1	5.3	109.2
BG_NC_20_no_interp.	709.1	165.7	32.0	80.9	4.9	108.0
BG_NC_20	705.4	166.1	9.6	109.0	5.8	112.8
S5_CN_20	4582.0	3710.9	1.8	5076.3	4.6	5073.5
S5_CN_200	4787.3	3916.4	78.2	5005.8	5.5	5078.5
S5_NC_20	4825.2	3954.7	532.4	4549.1	5.9	5075.6
S5_NC_200	4788.0	3924.2	113.9	4967.8	5.6	5076.1
S25_CN_20	16699.6	14663.5	1.9	25050.1	4.1	25047.9
S25_CN_200_no_interp.	18687.9	16667.5	9138.8	15572.3	4.6	24706.5
S25_CN_200	18423.3	16396.8	102.1	24951.5	4.2	25049.4
S25_NC_20	22309.2	20296.3	11345.9	14152.5	447.2	25051.2
S25_NC_200_no_interp.	18865.9	16840.9	21090.5	3623.2	7.2	24706.5
S25_NC_200	18610.1	16587.2	331.7	24725.6	4.0	25053.3
S25_NC_60	18694.9	16677.8	1086.9	23965.0	4.1	25047.8
BG_CN_20 (SOCOLv4)	432	150	10	110	10	110
S5p_CN_20 (SOCOLv4)	4875	4240	10	4960	20	4970
S5p_NC_20 (SOCOLv4)	5907	5290	4290	840	180	4950

## B: Importance of proper treatment of gasphase H<sub>2</sub>SO<sub>4</sub> concentrations

In previous versions of SOCOL-AER the total amount of H<sub>2</sub>SO<sub>4</sub> molecules produced by the chemistry scheme, which is called every two hours, was directly passed to the microphysical loop. The gaseous H<sub>2</sub>SO<sub>4</sub> concentration was then consecutively updated by condensation and nucleation. This approach leads to an artificial spike in H<sub>2</sub>SO<sub>4</sub> concentrations and supersaturations each time at the beginning of the microphysical calculation, which then gradually decreased over the microphysical loop. In reality, however, chemical H<sub>2</sub>SO<sub>4</sub> production as well as nucleation and condensation occur continuously, resulting in a smoother evolution of atmospheric H<sub>2</sub>SO<sub>4</sub> supersaturations. Therefore, it is important to distribute the chemical H<sub>2</sub>SO<sub>4</sub> production uniformly among the  $N_{\text{micro}}$  substeps, in particular under high sulfur conditions. This is done by updating the gasphase H<sub>2</sub>SO<sub>4</sub> concentration by the term  $\Delta \text{H}_2\text{SO}_4 / N_{\text{micro}}$  after each microphysical substep, with  $\Delta \text{H}_2\text{SO}_4 = \text{H}_2\text{SO}_{4\text{afterchemistry}} - \text{H}_2\text{SO}_{4\text{beforechemistry}}$  being the total amount of chemically produced H<sub>2</sub>SO<sub>4</sub> molecules produced in one chemical timestep (Figure 2.1). This avoids erroneously large H<sub>2</sub>SO<sub>4</sub> concentrations at the beginning of the microphysical loop.

Figure 2.6 compares the resulting size distributions for the model versions with and without (`_no_interp.`) interpolation of the chemical H<sub>2</sub>SO<sub>4</sub> production with  $N_{\text{micro}} = 200$ . In the `_no_interp.` case, the gas-phase H<sub>2</sub>SO<sub>4</sub> reaches its equilibrium vapor pressure through nucleation and condensation within the first few iterations of  $N_{\text{micro}}$ . During the remaining iterations of  $N_{\text{micro}}$  coagulation is the only process influencing the size distribution. This results in a peak in the nucleation mode around 3 nm and in higher number concentrations below 0.3 μm compared with S25\_NC\_200. The new setup which accounts for the interpolation of H<sub>2</sub>SO<sub>4</sub> production within the microphysical sub-loop, however, results in more reasonable nucleation and condensation rates in which the nucleation mass flux is only 1-4 % of the condensation mass flux (see Table 2.2). The new treatment of the gas-phase H<sub>2</sub>SO<sub>4</sub> is especially important when dealing with high H<sub>2</sub>SO<sub>4</sub> supersaturations, but has no significant effect under background conditions (see BG simulations in Table 2.2). All the data presented in this paper account for the interpolation of H<sub>2</sub>SO<sub>4</sub> production within the microphysical sub-loop.

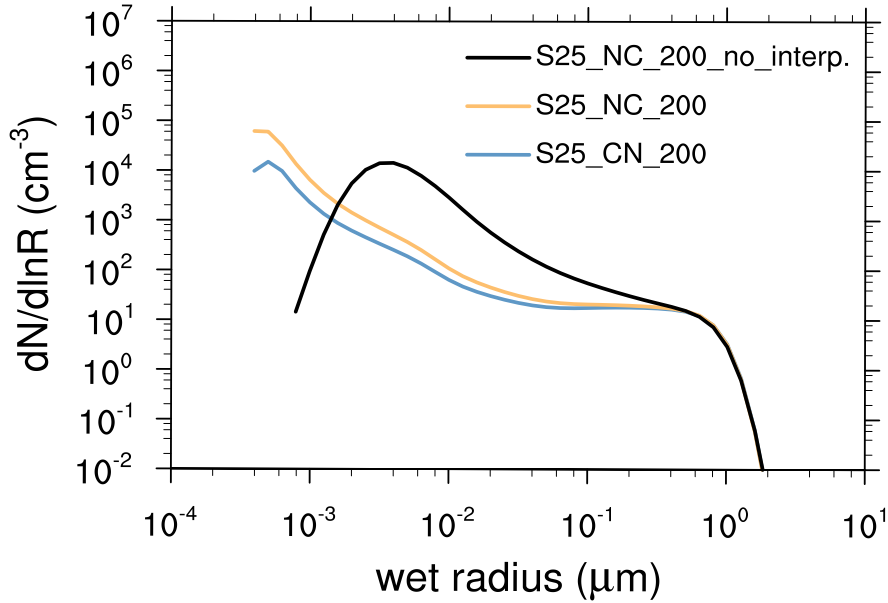


Figure 2.6: Size distributions ( $dN/d\ln R$ , particles  $\text{cm}^{-3}$ ) averaged between  $30^\circ$  S and  $30^\circ$  N at 55 hPa for the model simulations with regional SO<sub>2</sub> injections of 25 Tg(S)  $\text{yr}^{-1}$ . While the blue and orange curves show the convergence of the size distribution when interpolating the H<sub>2</sub>SO<sub>4</sub> molecules produced during the 2h-chemical timestep equally over  $N_{\text{micro}}$ , the black curve shows the resulting size distribution when passing the produced H<sub>2</sub>SO<sub>4</sub> molecules to the microphysical sub-loop in one go.

## C: Influence of settings on aerosol surface area density

Climate intervention by stratospheric SO<sub>2</sub> emission yields an increase in aerosol burden and, thus, to a larger surface area density (SAD) available for heterogeneous chemistry. The SAD does not only depend on the total burden, but also on the detailed size distribution, as smaller particles have a greater surface area per unit mass.

Figures 2.7 and 2.8 show the zonal mean surface area density (SAD) of sulfate aerosol for January and July. The injection of SO<sub>2</sub> leads to a massive increase in SAD throughout the whole lower stratosphere, with the highest SAD occurring in the polar lowermost stratosphere, particularly during winter, and in the tropical lower stratosphere, i.e. the injection region. Figure 2.7 reveals substantial differences between the two S5 simulations, with S5\_NC\_200 showing about 20% higher SAD values, which can be explained by a 5% increase in the stratospheric aerosol burden (Table 2.2), combined with a shift in the size distribution towards smaller particles (Figure 2.2).

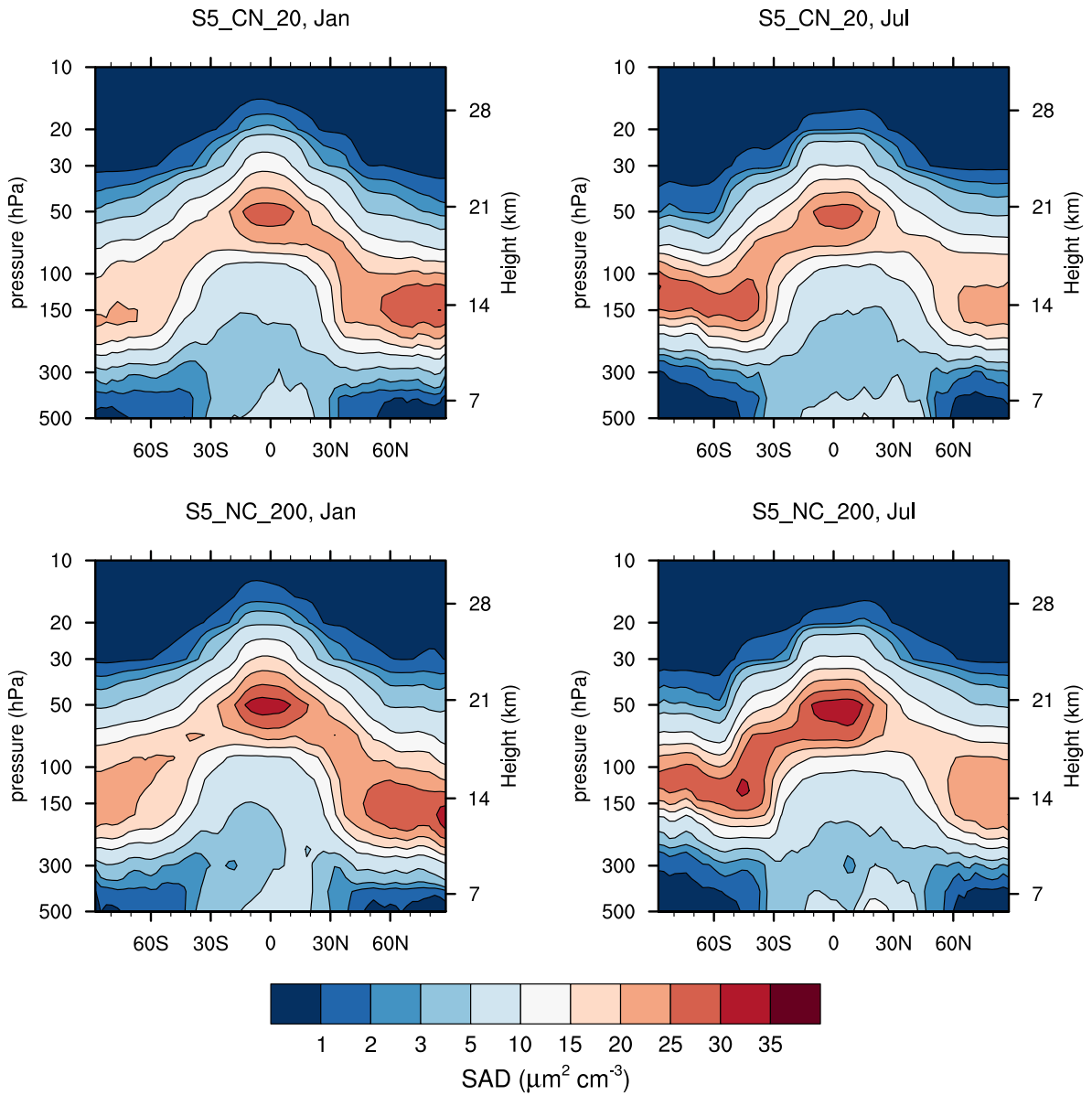


Figure 2.7: Zonal mean surface area density ( $\mu\text{m}^2 \text{cm}^{-3}$ ) for January (left) and July (right) for the model simulations with  $5 \text{ Tg(S) yr}^{-1}$ . Top: S5\_CN\_20, i.e. the original setting in SOCOL-AER biased towards condensation. Bottom: the unbiased S5\_NC\_200 setting.

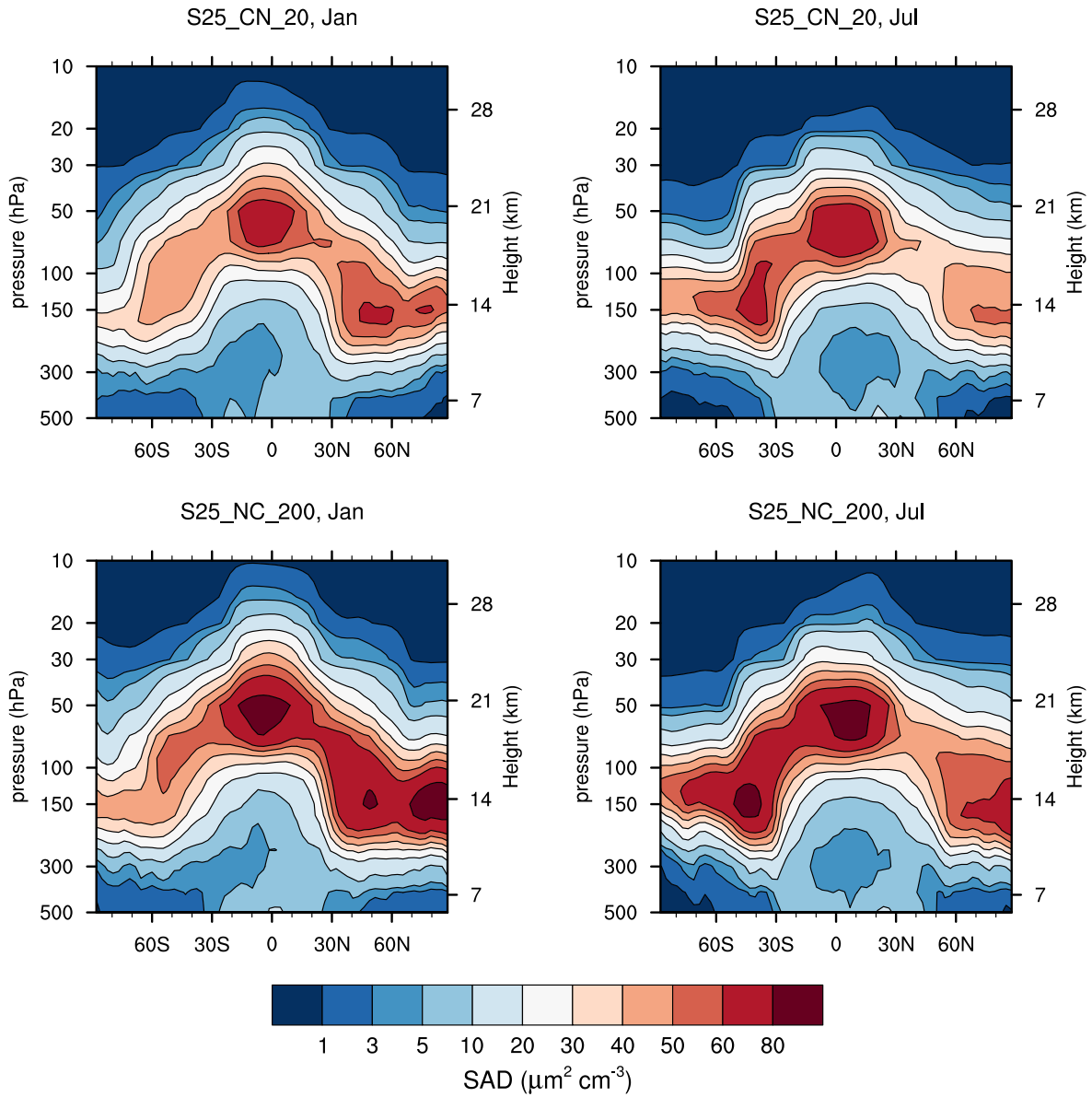


Figure 2.8: Same as Fig. 2.7, but for 25 Tg(S) yr<sup>-1</sup>.

## D: Influence of settings on atmospheric temperature profile

Figure 2.9 presents changes in the tropical temperature profile for the two SO<sub>2</sub> injection scenarios. The simulations show a heating of the lower stratosphere caused by the absorption of longwave radiation by the aqueous sulfuric acid aerosol, and a cooling above the aerosol layer due to reduced IR heating from below. For the S5 simulations, the maximum temperature change ranges between 4.5 and 5 K. For the S25 simulations, the warming of the lower stratosphere is much more pronounced and peaks around 15 K. For a given mass loading, the longwave absorption by sulfate aerosol does not strongly depend on the particle sizes (Lacis, 2015), so that the differences between the simulations mostly reflect differences in aerosol mass loading and its vertical distribution. The difference between the simulations increases at higher levels, reflecting the enhanced upward transport of aerosol particles for simulations with many small, and thus lighter, particles. However, the range spanned by different microphysical settings is not sufficient to explain the inter-model spread presented in Weisenstein et al. (2022, their Fig. 10): While the modeled temperature increase in MA-ECHAM5-HAM was only around 2 K for 5Mt/yr injection with an aerosol burden increase smaller by about 30% compared to SOCOL-AER, CESM2 showed a similar warming as SOCOL-AER, despite simulating a 50% higher aerosol burden increase.

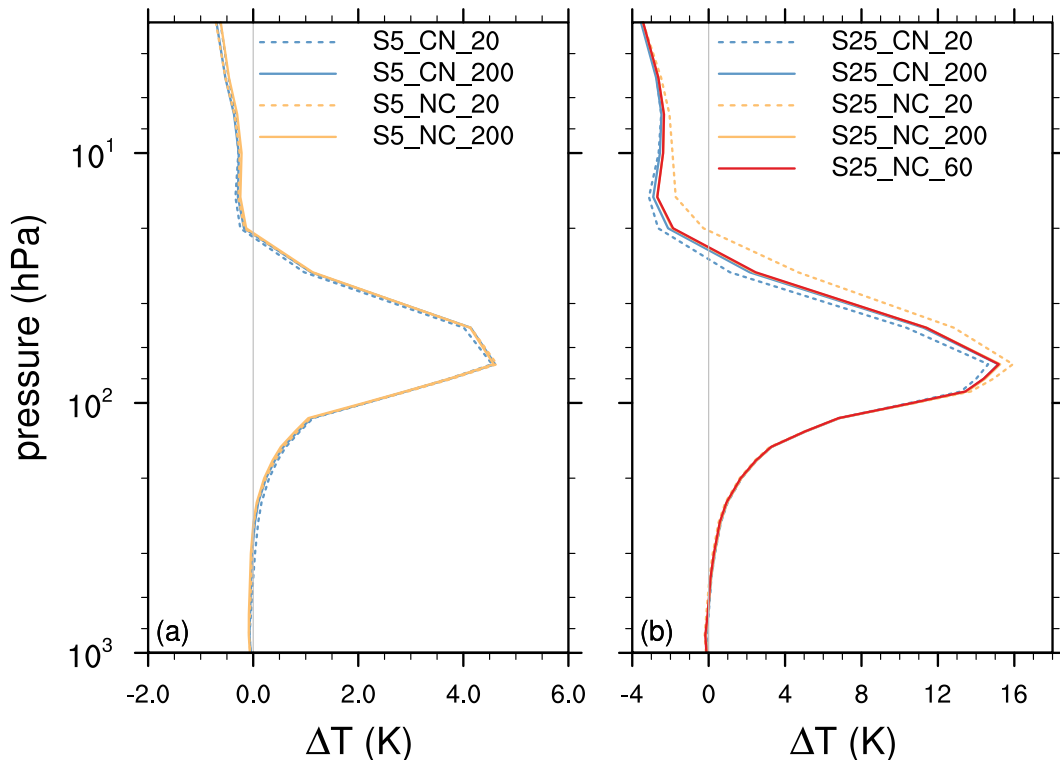


Figure 2.9: Change in atmospheric temperature (K) averaged between 30° S and 30° N due to SO<sub>2</sub> gas injections of (a) 5 Tg(S) yr<sup>-1</sup>, and (b) 25 Tg(S) yr<sup>-1</sup>. The simulation BG\_CN\_20 is used as reference.

As discussed in Weisenstein et al. (2022), the stratospheric warming could lead to a

strengthening of the Brewer–Dobson circulation, which in turn might enhance the transport of H<sub>2</sub>O into the stratosphere. The actual amount of H<sub>2</sub>O entering the stratosphere, however, is largely controlled by the temperature at the tropical cold point tropopause ( $\sim 90$  hPa). As Fig. 2.9 does not indicate any significant differences in the simulated temperature changes at the cold point tropopause, we do not expect an influence of the settings on the modeled changes in stratospheric H<sub>2</sub>O concentrations.





## Chapter 3

# A fully coupled solid particle microphysics scheme for stratospheric aerosol injections within the aerosol-chemistry-climate-model SOCOL-AERv2

### Abstract

Recent studies have suggested that injection of solid particles such as alumina and calcite particles for stratospheric aerosol injection (SAI) instead of sulfur-based injections could reduce some of the adverse side effects of SAI such as ozone depletion and stratospheric heating. However, the heterogeneous chemistry and microphysical interactions of solid particles with sulfuric acid are subject to large uncertainties due to lack of experimental data and observations under stratospheric conditions, which allows only for simplified assumptions in modelling studies. Here, we present a version of the global aerosol-chemistry-climate model SOCOL-AERv2 and the Earth System Model (ESM) SOCOLv4 which incorporate a solid particle microphysics scheme for assessment of SAI of solid particles. Microphysical interactions of the solid particle with the stratospheric sulfur cycle were interactively coupled to the heterogeneous chemistry scheme and the radiative transfer code (RTC) for the first time within an ESM. Therefore, the model allows simulation of heterogeneous chemistry at the particle surface as well as feedbacks between microphysics, chemistry, radiation and climate. We show that sulfur based SAI results in a doubling of the stratospheric aerosol burden compared to the same injection rate of calcite and alumina particles with radius of 240 nm, mainly due to the smaller density and the smaller average particle size of sulfuric acid aerosols and thus, slower sedimentation. Therefore, SAI using solid particles only leads to more effective radiative forcing per resulting aerosol burden compared to sulfur-based SAI, not per injected mass. The stratospheric sulfur cycle would be significantly perturbed, with a reduction in stratospheric sulfuric acid burden by 53%, when injecting 5 Mt/yr of alumina or calcite particles of 240 nm radius. We show that alumina particles will acquire a sulfuric acid coating equivalent of about 10 nm thickness, if the sulfuric acid is equally distributed over the whole available particle surface area in the lower stratosphere. However due to a steep contact angle of sulfuric acid on alumina particles the sulfuric acid coating would likely not cover the entire alumina surface, which results in available surface for heterogeneous reactions other than the ones on sulfuric acid. When applying uptake coefficients of 1.0,  $10^{-5}$  and  $10^{-4}$  for  $\text{H}_2\text{SO}_4$ ,  $\text{HCl}$  and  $\text{HNO}_3$ , respectively, the same scenario with injections of calcite particles results in 94% of the particle mass remaining in the form of  $\text{CaCO}_3$ . This likely maintains the optical properties of the calcite particles, but could significantly alter heterogeneous chemistry occurring on the particle surface. However, due to the very limited amount of experimental data on heterogeneous chemistry and solid particle microphysics under stratospheric conditions the modelled ozone and radiative forcing responses are subject to substantial uncertainty, which could only be addressed with extensive, co-

ordinated, experimental research efforts. To reduce this uncertainty we suggest research on 1) the solid particle microphysics in the injection plume and degree of agglomeration of solid particles on the sub-ESM grid scale, 2) the scattering properties of the resulting agglomerates 3) heterogeneous chemistry on the particle surface and 4) aerosol-cloud interactions. The model presented in this work offers a useful tool for sensitivity studies and impact analysis of new experimental results on points 1) to 3) for SAI of solid particles.

## **This chapter was published as a research paper:**

**Vattioni, S.**, Weber, R., Feinberg, A., Stenke, A., Dykema, J. A., Luo, B., Kelesidis, G. A., Bruun, C. A., Sukhodolov, T., Keutsch, F. N., Peter, T., and Chiodo, G.: A fully coupled solid particle microphysics scheme for stratospheric aerosol injections within the aerosol-chemistry-climate-model SOCOL-AERv2, **EGUsphere, Geoscientific Model Development, GMD** [preprint], <https://doi.org/10.5194/egusphere-2024-444>, 2024.

## 3.1 Introduction

Even if greenhouse gas (GHG) emissions stopped today, high GHG concentrations and their effects would persist for centuries, if GHG removal techniques can not be scaled up fast enough (IPCC, 2023). Stratospheric aerosol injection (SAI) has the potential to rapidly mitigate some of the adverse impacts of climate warming by increasing the Earth’s albedo. SAI would be feasible at low cost (Smith, 2020, i.e., about \$ 18 billion per year), but it also entails considerable risks such as adverse environmental side effects and challenges such as governance of ethical considerations on global and inter-generational equity and the power of decision (e.g. Robock, 2008; Burns, 2011). For these reasons, the US National Academy of Sciences and others have proposed research, which explores the risks and benefits of SAI (e.g., Shepherd, 2012; Schäfer et al., 2015; NRC, 2015; Field et al., 2021).

The idea of SAI evolved from the temporary cooling effect of sulfuric acid aerosols formed after stratospheric SO<sub>2</sub> injections of large explosive volcanic eruptions and was first proposed by Budyko (1974). In addition, solid particles as alternative materials were explored in conceptual studies and reports on various climate engineering techniques (e.g. Keith and Dowlatabadi, 1992; Teller et al., 1996; Keith, 2000). However, research on SAI was initially a taboo among researchers since it does not present an actual solution to climate change, but instead at best a treatment of some of its symptoms (MacMartin et al., 2014; Keith and MacMartin, 2015). The need for research on SAI only became more to the forefront with the growing appearance of impacts of climate change and after the proposal to investigate the risks, benefits and the feasibility of SAI by Crutzen (2006). Potential scenarios for SAI involve reducing the current rate of climate change or in what is referred to as an "overshoot scenario", where SAI would aim at keeping global temperature increase below 1.5 K, the target set by the Paris agreement in 2015, until global net zero GHG emissions are achieved, and until solutions are found on how to remove GHG from the air efficiently (MacMartin et al., 2014; Keith and MacMartin, 2015; MacMartin et al., 2022).

To date, research on SAI has mainly focused on injection of sulfuric acid aerosol precursor species such as SO<sub>2</sub>. This has a number of reasons: Due to the natural occurrence of sulfuric acid aerosols in the atmosphere, the stratospheric sulfur cycle is relatively well known and interactively simulated in many chemistry climate models (e.g. Thomason and Peter, 2006; Deshler, 2008; Feinberg et al., 2019; Brodowsky et al., 2023), which makes it easier for modellers to investigate sulfur-based SAI scenarios. Furthermore, heterogeneous chemistry and optical properties of sulfuric acid aerosols in the stratosphere are also relatively well known from experimental studies (e.g., Burkholder et al., 2020; Ammann et al., 2013). In addition, observations after large explosive volcanic eruptions such as the Mt. Pinatubo eruption 1991 (e.g., Arfeuille et al., 2013; Thomason et al., 2018; Baran and Foot, 1994; Kovilakam et al., 2020) allow for model evaluation of the chemical and radiative impacts of large stratospheric sulfur emissions (e.g., Deshler et al., 2019; Quaglia et al., 2023).

However, SAI via SO<sub>2</sub> injections also are subject to several limitations making sulfuric acid aerosols less attractive for a potential use in SAI. These limitations include (1) aerosol size distributions that are inefficient for backscattering solar radiation with either too many large or too many small particles (Vattioni et al., 2019), (2) ozone depletion due to chlorine activation on aerosols (Tilmes et al., 2008; Weisenstein et al., 2022), (3) stratospheric warming resulting in changes of the large-scale atmospheric circulation

(Aquila et al., 2014; Tilmes et al., 2017; Visioni et al., 2021; Jones et al., 2022) as well as (4) substantial inter-model uncertainties on resulting stratospheric aerosol burden and radiative effects (Weisenstein et al., 2022).

Recent studies have shown that injection of solid particles could overcome several of these limitations (e.g., Pope et al., 2012; Weisenstein et al., 2015; Keith et al., 2016; Dykema et al., 2016). Many solid particle candidates such as alumina ( $\text{Al}_2\text{O}_3$ ), calcite ( $\text{CaCO}_3$ ) or diamond particles have larger backscatter efficiencies per stratospheric burden compared to sulfuric acid aerosols (Dykema et al., 2016). Furthermore, the absorption efficiency of radiation per resulting aerosol burden is significantly smaller for many solid materials compared to sulfuric acid aerosols, resulting in reduced stratospheric warming. Other studies showed that the injection of alumina or calcite particles would result in less ozone depletion (Weisenstein et al., 2015; Dai et al., 2020) or even in ozone increase in the case of calcite particles (Keith et al., 2016).

However, contrary to sulfuric acid aerosols, the solid particle types proposed for SAI do not occur naturally in the stratosphere. Therefore, relatively little is known about their microphysical interactions and chemical ageing processes, which could alter their scattering properties, their stratospheric residence time as well as heterogeneous chemistry hosted on the particles. This makes it very difficult to have confidence in the modeled impacts of solid particle injections on stratospheric chemistry and climate.

There have been investigations on the impact of alumina-containing solid-fuel space rocket exhaust on stratospheric ozone and radiative forcing. These studies used flow-tube experiments (Molina et al., 1997), 2D-chemistry transport modelling (Jackman et al., 1998; Danilin et al., 2001) as well as conceptual methods (Ross and Sheaffer, 2014). However, the rocket exhaust investigated in these studies also contains other species such as water, HCl and black carbon, which makes attribution of the alumina particles effects on ozone alteration and radiative forcing difficult (Vattioni et al., 2023a). Therefore, microphysical interactions of solid particles with background aerosols, as well as their impact on stratospheric chemistry and radiative forcing, remain subject to large uncertainties.

Nevertheless, there have been several studies that investigated SAI scenarios using solid particles. Fujii (2011) and Pope et al. (2012) were among the first conceptual studies which pointed at potential benefits, such as better scattering properties, from SAI of various solid materials in their studies. At the same time Ferraro et al. (2011) and Ferraro et al. (2015) used an RTC and a general circulation model, respectively, to quantify stratospheric heating resulting from some materials as well as the dynamical stratospheric feedbacks, while prescribing the stratospheric solid particle number densities. Later, Jones et al. (2016) was the first study that compared tropospheric climate impacts from SAI of sulfuric acid aerosols with injections of  $\text{TiO}_2$  and BC using a global circulation model with an interactive ocean module, while simulating injection and transport of solid particles with prescribed size distributions. However, none of these studies accounted for heterogeneous chemistry on particle surfaces nor for microphysical processes. Impacts on stratospheric ozone from SAI of solid particles were first assessed by Kravitz et al. (2012b) who investigated SAI with BC aerosols using a chemistry climate model. In summary, the conclusion from these first studies which mainly investigated SAI of BC and  $\text{TiO}_2$  particles is that these materials are not suitable as injection species for SAI since both,  $\text{TiO}_2$  and BC have strong UV-VIS absorption, which results in significant stratospheric heating. However, while injection of BC would result in substantial ozone depletion, experimental studies on heterogeneous chemistry on  $\text{TiO}_2$  surfaces indicated reduced impacts on model stratospheric ozone (Tang et al., 2014, 2016; Moon et al., 2018) compared to sulfuric acid

aerosols, providing additional motivation for exploration of other species.

At the same time, Dykema et al. (2016) performed detailed radiative transfer calculations of various solid particles, including feedbacks from stratospheric water vapor and concluded that solid particles such as calcite, diamond, alumina and SiC scatter solar radiation with better mass efficiency and less stratospheric heating compared to sulfuric acid aerosols. Weisenstein et al. (2015) was the first study to use a 2D chemistry transport model with interactive solid particle microphysics as well as microphysical interactions of solid particles with condensed and gaseous sulfuric acid to assess impacts from heterogeneous chemistry on alumina particle surfaces. The resulting zonal mean number concentrations were then fed into a RTC offline to simulate the resulting radiative forcing. Limitations of this study stem from a simplified representation of heterogeneous chemistry on alumina particles (Vattioni et al., 2023a) as well as from the 2-D approach which causes significant simplifications in atmospheric dynamics and transport of the injected particles. Keith et al. (2016) used the same model to propose substantial stratospheric ozone increase through removal of HCl from the stratosphere via uptake on calcite particle surfaces and subsequent sedimentation. Later, Cziczo et al. (2019) pointed to the over simplified assessment used in the latter study, which applied over simplified heterogeneous chemistry such as neglecting the formation of hydrates as well as a potential sealing effect due to the formation of reaction products at the surface. However, most importantly, this latter study showed that especially  $\text{CaCO}_3$  and  $\text{Ca}(\text{NO}_3)_2$  as well as their hydrates are good ice nucleation materials, which could result in a 33% reduction of the radiative forcing compared to Keith et al. (2016) due to increased cirrus cloud coverage. Furthermore, the interactions of aerosols with polar stratospheric clouds could create a feedback on polar ozone concentrations, which has not been investigated so far (Cziczo et al., 2019).

Therefore, to assess the real risks and benefits of SAI of solid particles compared to the more conventionally researched sulfur based approach, it is important to interactively couple 1) microphysical processes such as agglomeration and sedimentation of solid particles and their microphysical interaction with condensed and gaseous sulfuric acid with 2) heterogeneous chemistry on the particle surface and the subsequent impacts on stratospheric ozone and with 3) aerosol cloud interactions, as well as with 4) the resulting dynamical feedbacks from changes in ozone, stratospheric warming and cooling of tropospheric climate interactively in one model. Simulating all these effects in a self-consistent way is crucial, because (1) strong agglomeration can significantly decrease the backscatter efficiency or increase the sedimentation speed compared to a compact monomer, while (2) can lead to significant ozone alteration depending on the material and (3) can result in a positive or negative feedback on radiative forcing through cirrus cloud alteration (e.g., Cziczo et al., 2019). The combination of these processes ultimately determines the large-scale circulation response and surface climate response to SAI with alternate materials.

This study presents a microphysics module for solid particles within the aerosol-chemistry-climate model SOCOL-AERv2, which represents injected solid particles interactively coupled to advection and sedimentation as well as to the model's radiative transfer and heterogeneous chemistry modules (see Figure 3.1). Additionally, the module calculates microphysical interactions between solid particles and background sulfuric acid in gaseous and condensed form online. This allows us to account for feedbacks between different processes, which enables to comprehensively assess the risks and benefits of SAI of solid particles. However, it has to be kept in mind that direct aerosol-cloud interactions are not considered in this model, which could alter the resulting radiative forcing through cirrus cloud feedbacks (e.g., Cziczo et al., 2019). In this study, we focus on the injection

of alumina and calcite particles since these are some of the few potential particle types for which some heterogeneous reaction rates have previously been measured (Molina et al., 1997; Huynh and McNeill, 2020; Dai et al., 2020; Huynh and McNeill, 2021).

## 3.2 Model description

The interactive coupling of aerosol microphysics with heterogeneous chemistry and radiation makes the SOCOL models (Feinberg et al., 2019; Sukhodolov et al., 2021) suitable to explore feedbacks between microphysics, stratospheric chemistry, radiation as well as tropospheric and stratospheric climate. The SOCOL model family has been successfully used to reproduce the global sulfur cycle under volcanically active (e.g., Mt. Pinatubo 1991) and quiescent conditions (e.g., Sheng et al., 2015; Sukhodolov et al., 2018; Feinberg et al., 2019; Brodowsky et al., 2021; Quaglia et al., 2023; Brodowsky et al., 2023) as well as to evaluate impacts of sulfur-based SAI scenarios (Heckendorn et al., 2009; Vattioni et al., 2019; Weisenstein et al., 2022), which makes them the tools of choice to evaluate SAI of solid particles.

### 3.2.1 SOCOL-AERv2

SOCOL-AERv2 is based on the chemistry climate model SOCOLv3 (Stenke et al., 2013) which consists of the middle atmosphere version of the spectral general circulation model ECHAM5 (Roeckner et al., 2003, 2006) and the chemistry transport model MEZON (Rozanov et al., 1999; Egorova et al., 2003). MEZON treats 59 gaseous species of the nitrogen, oxygen, carbon, chlorine, bromine and sulfur families, which are subject to ECHAM5.4 advection. The chemical solver of MEZON is based on the implicit iterative Newton-Raphson scheme (Ozolin, 1992; Stott and Harwood, 1993) and accounts for 16 heterogeneous, 58 photolysis and 160 gas-phase reactions, which represent the most relevant aspects of stratospheric chemistry. The sectional (size resolved) aerosol-microphysics module of the chemistry transport model 2D-AER (Weisenstein et al., 1997, 2007) was then interactively integrated into the three dimensional grid of SOCOLv3 resulting in the first version of SOCOL-AERv2 (Sheng et al., 2015, i.e., SOCOL-AERv1), which was later further updated by Feinberg et al. (2019, i.e., SOCOL-AERv2). SOCOL-AERv2 tracks sulfuric acid aerosols within 40 dry aerosol mass bins ranging from 2.8 molecules to  $1.6 \times 10^{12}$  molecules corresponding to dry radii from 0.39 nm to  $0.32 \mu\text{m}$  (assuming a density of  $1.8 \text{ g/cm}^3$ ) with the number of molecules doubling for subsequent bins. The wet aerosol properties are then calculated in every SOCOL grid box taking into account the  $\text{H}_2\text{SO}_4$  weight percent as a function of relative humidity and temperature (Tabazadeh et al., 1997). AER calculates microphysical processes such as sulfuric acid aerosol formation from gaseous  $\text{H}_2\text{SO}_4$  via nucleation (Vehkamäki et al., 2002) and condensation as well as their evaporation (Ayers et al., 1980; Kulmala and Laaksonen, 1990). Coagulation of sulfuric acid aerosols is calculated using the semi-implicit method of Jacobson and Seinfeld (2004) while the coagulation kernel is calculated using the empirical formula of Fuchs (1964). Finally, sedimentation is treated based on Kasten (1968) adopting the numerical scheme of Walcek (2000) and aerosols are removed from the model via interactive calculation of wet and dry deposition (Tost et al., 2006, 2007; Kerkweg et al., 2006, 2009; Revell et al., 2018). While in the troposphere prescribed aerosol quantities are used and aerosol-cloud interactions are not accounted for, in the stratosphere the aerosol number densities, the wet aerosol volume, the surface area density (SAD) as well as the

H<sub>2</sub>SO<sub>4</sub> weight percent of the aerosols resulting from AER are subsequently passed on to the heterogeneous chemistry scheme and to the RTC of SOCOL-AER, which makes the stratospheric aerosol module fully interactive.

The LW scheme of the RTC of ECHAM5.4 is based on the Rapid Radiative Transfer Model (RRTM Mlawer et al., 1997) using the correlated k-method with a resolution of 16 bands in the spectral range from 10 cm<sup>-1</sup> to 3000 cm<sup>-1</sup>. The shortwave (SW) code is based on Fouquart and Bonnel (1980) and has a spectral resolution of 6 bands ranging from 185 nm to 4 μm. While the short wave code accounts for scattering and absorption of radiation on aerosols the RRTM accounts for absorption and emission of radiation. Tabulated values of absorption and scattering efficiencies as well as asymmetry factors are used together with the model’s aerosol number densities to calculate the scattering and absorption coefficients of the aerosol size distribution, which are then fed into the RTC of SOCOL-AERv2. The tabulated absorption and scattering efficiencies were calculated as a function of aerosol size, H<sub>2</sub>SO<sub>4</sub> weight percent and spectral resolution based on Mie theory with refractive indexes from Yue et al. (1994) and Biermann et al. (1996).

The version of SOCOL-AERv2 used for this study has a vertical resolution of 39 sigma-pressure levels reaching up to 0.01 hPa (about 80 km altitude) and T42 horizontal resolution (2.8° × 2.8°). The dynamical time step is 15 minutes, while chemistry is calculated every 2 hours. The aerosol microphysics (nucleation, condensation and coagulation) is calculated with operator splitting by applying a loop of 20 iterations within the chemistry call every 2 hours, making the microphysical time step 6 minutes. However, Vattioni et al. (2023b) have shown that for enhanced H<sub>2</sub>SO<sub>4</sub> supersaturations a microphysical timestep of 6 minutes is not short enough. Therefore, we applied a microphysical timestep of 2 minutes (60 subloops within the chemistry routine) for all SO<sub>2</sub> emission scenarios. Other processes relevant for aerosols such as wet and dry deposition and sedimentation as well as calculations of aerosol quantities relevant for radiative transfer and heterogeneous chemistry such as SAD, pH and number densities are calculated and updated every 2 hours.

The same solid particle microphysics module was also incorporated in the fully coupled ESM SOCOLv4 (Sukhodolov et al., 2021) a further development of SOCOL-AERv2 which is based on the CMIP6 version of MPI-ESM (Mauritsen et al., 2019). While SOCOL-AERv2 and SOCOLv4 share the chemistry and aerosol microphysics scheme, SOCOLv4 is based on ECHAM6 (Stevens et al., 2013), which incorporates an interactive ocean module (Jungclaus et al., 2013). Furthermore, it provides a finer resolution of the short-wave spectrum as well as a higher spatial resolution and a smaller dynamical timestep, which makes it computationally much more expensive. This paper is based on SOCOL-AERv2, which uses prescribed sea surface temperatures and sea ice concentrations to study the effective radiative forcing as well as microphysics and impacts on heterogeneous chemistry, while SOCOLv4 will be used in the near future for studies on tropospheric climate impacts of solid particle injections.

### 3.2.2 The interactive solid particle microphysics module

For the representation of the solid particles we use a similar sectional approach as for the sulfuric acid aerosols. Particles are injected as monomers, which can grow to larger order agglomerates via coagulation (see subsections on "Coagulation"). The injected monomer radius can be determined in the model and varies between 80 nm and 320 nm in this study to investigate trade offs between agglomeration, sedimentation speed and

backscatter efficiency of different injected monomer radii. To keep track of the monomers and their agglomerates the solid particles are represented by different mass bins ( $i=1-10$ ), with mass doubling between subsequent bins (i.e., 1-, 2-, 4-, 8-, 16-, 32-, 64-, 128-, 256- and 512-mers). Since coagulation is much more efficient for smaller particles we only used all 10 solid particle mass bins (up to 512-mer) for injections of particles with small monomer radii, while for radii larger than 200 nm 5 mass bins (up to 16-mers) are sufficient due to only little agglomeration. The solid particles are fully interactive with the stratospheric sulfur cycle including sulfuric acid aerosols (see subsections on "Coagulation and Condensation"). We also accounted for heterogeneous chemistry taking place on solid particle surfaces (see subsections "Heterogeneous Chemistry") as well as for scattering and absorption of radiation (see subsection "Radiation"), which makes this the first fully coupled aerosol chemistry climate model to simulate SAI of solid particles except for aerosol cloud interactions. The various processes, which are accounted for in the model are depicted in Figure 3.1 and described in detail in the following subsections.

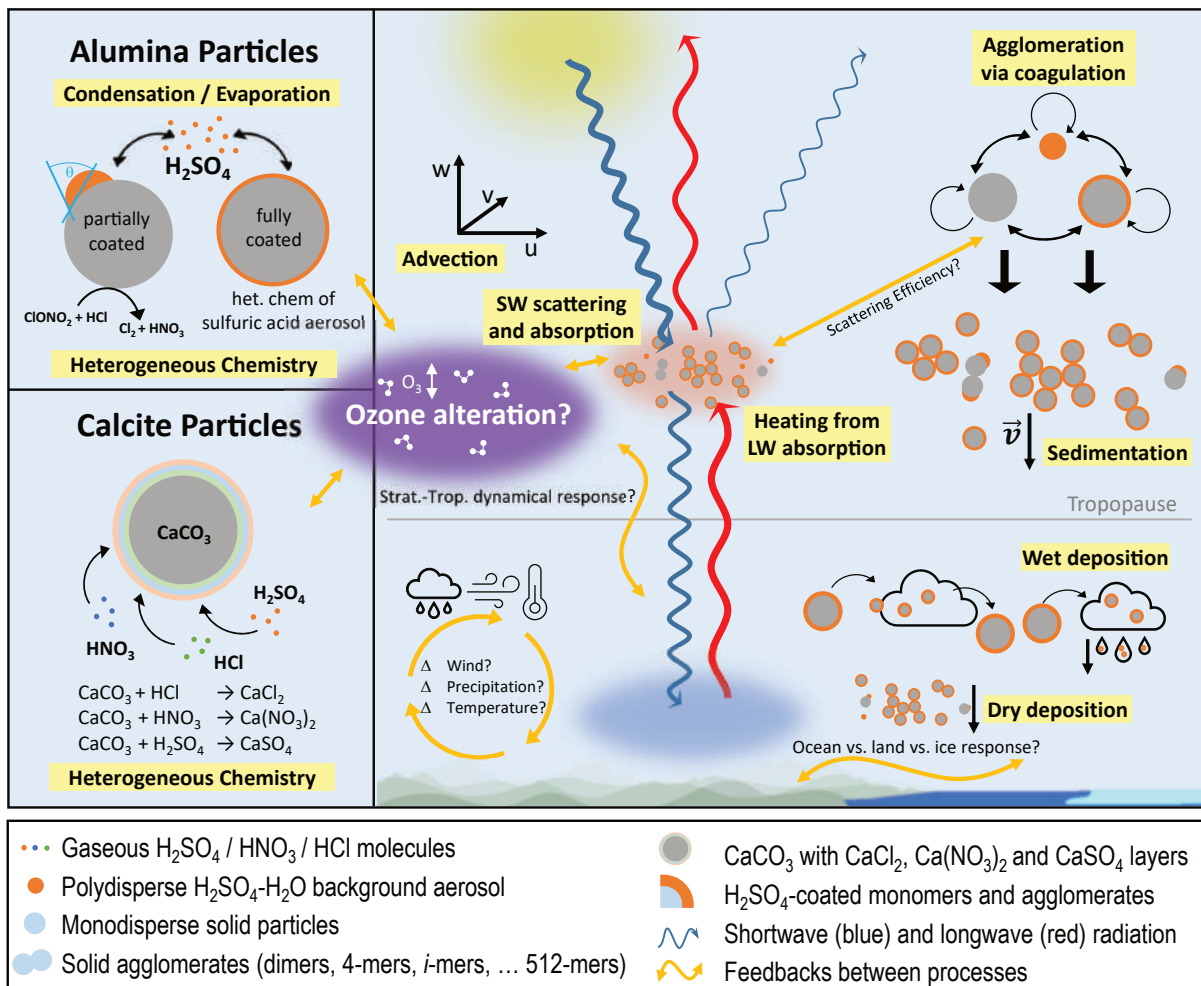


Figure 3.1: Schematic illustration of the different processes (yellow boxes) represented in the solid particle microphysics model incorporated in SOCOL-AERv2 and SOCOLv4. The right side of the figure depicts processes relevant for solid particles in general and the left side depicts specific processes relevant to alumina (upper part) and calcite (lower part) particles. Orange arrows represent most important feedbacks between processes considered in the model.



### 3.2.2.1 Mobility radius

To represent processes such as sedimentation and coagulation of agglomerates the mobility radius of the agglomerates ( $r_{m,i}$ ) is required (Spyrogianni et al., 2018). The mobility radius of alumina ( $\rho = 3.98 \text{ g/cm}^3$ ) and calcite ( $\rho = 2.71 \text{ g/cm}^3$ ) agglomerates with primary particle radii of 5 nm, 80 nm, and 215 nm for alumina particles as well 5 nm, 80 nm, and 275 nm for calcite particles were determined by using a discrete element model (DEM) of particle motion and coagulation (Kelesidis and Kholghy, 2021). The model simulates the coagulation dynamics of nanoparticles and has been validated with experimental data from black carbon (Kelesidis et al., 2017a,b), zirconia (Eirini Goudeli and Pratsinis, 2016) and silica (Kelesidis and Goudeli, 2021) nanoparticles. Furthermore, it was recently interfaced with the discrete dipole approximation (Kelesidis and Pratsinis, 2019; Kelesidis et al., 2020, 2023) and global climate models (Kelesidis et al., 2022) to accurately estimate the direct radiative forcing from black carbon agglomerates. In brief, 1000 monodisperse alumina or calcite particles with initial number concentration of  $10^7 - 10^{14} \text{ cm}^{-3}$  and radii of 5, 80 as well as 215 or 275 nm are randomly distributed in a cubic simulation box at constant pressure and temperature of 50 hPa and 240 K, respectively. Then, the particle motion and coagulation are derived using an event driven method (Goudeli et al., 2015). That way, the evolution of the total number concentration (Section S1, Fig. S1) and size distribution (Fig. S2) can be derived accounting for the realistic agglomerate structure. Furthermore, the agglomerate  $r_{m,i}$  can be obtained from its projected area,  $A_{\text{proj},i}$  (Rogak et al., 1993):

$$r_{m,i} = \sqrt{\frac{A_{\text{proj},i}}{\pi}}. \quad (3.1)$$

No significant differences in the resulting average mobility radius of the agglomerates could be observed resulting from the modelled range of initial concentrations (see Figure 3.2, S1 and S2). The mobility radii of other particle sizes (i.e., 160 nm, 240 nm, and 320 nm, see Section 3.3) can be linearly extrapolated from the radii resulting for 80 nm, 215 nm, and 275 nm particles. Further details on the DEM simulations can be found in Appendix 3A (Figures 3.12 and 3.13). The representation of the particles with the mobility radius is an improvement compared to previous studies (e.g. Weisenstein et al., 2015, who used the radius of gyration assuming the same fractal dimensions of 1.6 or 2.6 for all agglomerates, see Figure 3.14 in Appendix 3A), especially for representation of sedimentation and thus, the resulting stratospheric aerosol burden. It should be noted that the agglomerate fractal dimension evolves during coagulation and attains its asymptotic value of 1.6-1.8 when agglomerates containing at least 15 monomers are formed (Goudeli et al., 2015). Thus, assuming constant fractal dimensions can result in an overestimation of the agglomerate number density and mobility radius (see Figure 3.14 in Appendix 3A Kelesidis and Kholghy, 2021).

However, these DEM simulations also showed that it could be challenging to reduce initial particle concentrations in an aircraft wake to levels that are small enough to avoid rapid agglomeration in an aircraft wake (see 3.13). Most simulations showed agglomerates size distributions peaking at agglomerates between  $10^1$  and  $10^3$  primary particles per agglomerate after only two hours, which would reduce scattering efficiencies as well as increase sedimentation speeds of the solid particles. However, these simulations neglected the effect of dilution, which could reduce number concentrations and thus, coagulation. Nevertheless, the neglected injection plume processes at the sub ESM grid scale remain one of the major limitations of most global models including the one used in this study.

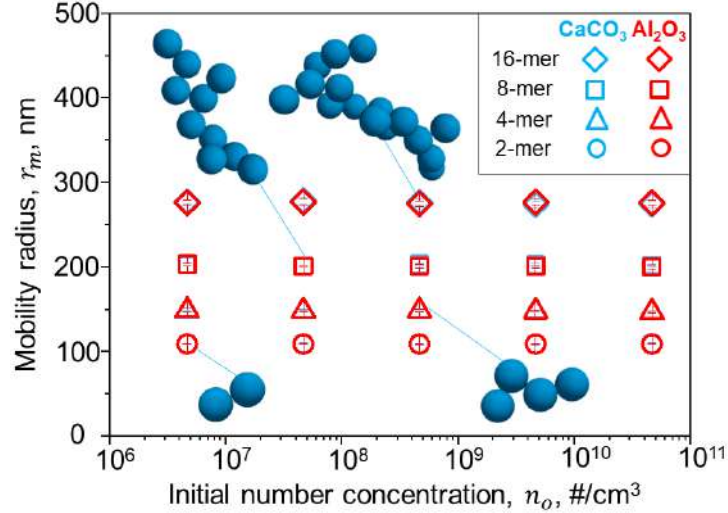


Figure 3.2: The averaged mobility radius of different agglomerates for calcite (blue) and alumina (red) particles with primary particle radius of 80 nm as a function of initial concentrations modelled by a DEM. The averaged shape of agglomerates resulting from initial concentrations of  $2 \times 10^{12} \text{ cm}^{-3}$  is illustrated in dark blue.

### 3.2.2.2 Sedimentation

The solid particles were integrated into the same sedimentation scheme as applied for sulfuric acid aerosols in SOCOL-AERv2, which is based on Kasten (1968) and Walcek (2000). Following Spyrogianni et al. (2018) we used the mobility radius for calculation of the terminal velocity. The terminal velocity of a falling particle in a fluid can be described with Stokes law, when the Reynolds number is significantly smaller than 1 (Seinfeld and Pandis, 1997). This applies to falling sub-micron particles in the atmosphere. Assuming buoyancy is negligible, the terminal velocity is reached when the drag force ( $F_D$ , equation 3.3) and the gravitation force ( $F_G$ , equation 3.2) of a falling particle are in equilibrium (i.e.,  $F_G = F_D$ ).

$$F_D = \frac{6 \pi \eta_{air} r_{m,i}}{C(r_{m,i})} v_{t,i} \quad (3.2)$$

$$F_G = m_i g = \rho_p \frac{4}{3} r_0^3 g \quad (3.3)$$

In equation 3.3 and 3.2  $m_i$  is the particle mass of mass bin  $i$ ,  $g$  the gravitational constant,  $\eta_{air}$  the viscosity of air,  $\rho_p$  the density of the particle,  $r_{m,i}$  the mobility radius of the particle,  $C(r_i)$  the Cunningham correction of the particles in mass bin  $i$ , and  $r_0$  the monomer radius. Solving for  $v_{t,i}$  gives equation 3.4 which is used to calculate the sedimentation speed of the solid particles in the aerosol sedimentation scheme of SOCOL-AERv2 Feinberg et al. (2019):

$$v_{t,i} = \frac{m_i g C(r_{m,i})}{6 \pi \eta_{air} r_{m,i}} \quad (3.4)$$

The resulting sedimentation speeds of solid particles and their agglomerates calculated in SOCOL-AERv2 are shown in Figure 3.15 in Appendix 3B.

### 3.2.2.3 Wet and dry deposition

Solid particles are removed from the atmosphere via the same interactive wet and dry deposition schemes as used for sulfuric acid aerosols in SOCOL-AERv2, which were im-

plemented and tested in Feinberg et al. (2019, see Section 3.2.1). Uptake of solid particles in cloud and rain droplets is calculated based on a mobility radius-dependent calculation of nucleation and impaction scavenging. Solid particle mass released to the atmosphere after cloud evaporation is added back to the largest available solid particle mass bin. Dry deposition velocities are calculated following the resistance approach by Wesely (1989) using the mobility radius (see Section 3.2.2.1) and the corresponding densities of the solid particles.

### 3.2.2.4 Radiation

To make the solid particles interact with the RTC code, SOCOL-AERv2 requires a lookup table with the absorption and scattering efficiencies ( $Q_{\text{abs}}$  and  $Q_{\text{sca}}$ ) normalized to the geometric cross-section obtained from their volume equivalent radii ( $r_{\text{ve},i}$ ) as well as the asymmetry factor ( $g_{\text{asy}}$ ) for all mass bins,  $i$ . The volume equivalent radius is given by

$$r_{\text{ve},i} = \sqrt[3]{i \frac{4}{3} \pi r_0^3}, \quad (3.5)$$

where  $r_0$  is the primary particle radius (i.e., monomer radius). While  $Q_{\text{abs}}$ ,  $Q_{\text{sca}}$  and  $g_{\text{asy}}$  are required for all spectral SW bands, the LW bands only require the look up table for  $Q_{\text{abs}}$ , since the RRTM (Mlawer et al., 1997) incorporated in SOCOL-AERv2 does not account for scattering in the LW spectral bands.

For the monomers these optical properties are calculated from Mie theory utilizing the solution of (Bohren and Huffman, 2008) for calcite and alumina particles, implemented with an open source MATLAB code (Mätzler, 2002). For the aggregates the code developed by Rannou et al. (1999) was applied, which is a semi-empirical fit to a mean-field theory solution of the Maxwell equations for interaction of fractal agglomerates with electromagnetic waves. Both of these codes provide the full scattering phase function, although it is not utilized by SOCOL-AER's RTC. The required inputs for the monomer code are complex refractive index as a function of wavelength and monomer size, which were taken from Tropf and Thomas (1997) for alumina and from Ghosh (1999) and Long et al. (1993) for calcite. This is also consistent with (Dykema et al., 2016). For the aggregates, the number of monomers comprising the aggregate and the fractal dimension are also required as an input. Within each SW radiative transfer model band the optical scattering and absorption are weighted by the incident top-of-the-atmosphere (TOA) solar spectrum and averaged, whereas in the LW bands scattering is neglected and absorption is given as a simple average over each spectral band. The resulting  $Q_{\text{abs}}$  for all spectral bands as well as  $Q_{\text{sca}}$  and  $g_{\text{asy}}$  for the SW bands, which were subsequently used into SOCOL-AERv2 are shown in Figure 3.16 and Figure 3.17 in Appendix 3C.

In SOCOL-AERv2 the scattering and absorption cross sections ( $\sigma_{\text{sca},i}$  and  $\sigma_{\text{abs},i}$ ) of a particle in mass bin  $i$  is given by:

$$\sigma_i = \pi r_{\text{ve},i}^2 Q_i \quad (3.6)$$

The scattering and absorption coefficients,  $\epsilon_{\text{sca},i}$  and  $\epsilon_{\text{abs},i}$  of each mass bin are then calculated via equation 3.7 by multiplying the cross sections of each mass bin with the number densities ( $N_i$ ) of each mass bin. Summing up over all mass bins yields the total scattering and absorption coefficient ( $\epsilon_{\text{sca}}$  and  $\epsilon_{\text{abs}}$ ) for each spectral SW band:

$$\epsilon = \sum_{i=1}^{10} \epsilon_i = \sum_{i=1}^{10} N_i \sigma_i \quad (3.7)$$

The extinction coefficient ( $\epsilon_{\text{ext}}$ ) as well as the single scattering albedo ( $\omega_{\text{ssa}}$ ) are given by

$$\epsilon_{\text{ext}} = \epsilon_{\text{sca}} + \epsilon_{\text{abs}} \quad (3.8)$$

$$\omega_{\text{ssa}} = \frac{\epsilon_{\text{sca}}}{\epsilon_{\text{ext}}} \quad (3.9)$$

Additionally, the bulk asymmetry factor ( $g_{\text{asy}}$ ) for the solid aerosol size distribution is calculated by the sum of each mass bin's asymmetry factor ( $g_{\text{asy},i}$ ) weighted by the corresponding scattering coefficient:

$$g_{\text{asy}} = \frac{1}{\epsilon_{\text{sca}}} \sum_{i=1}^{10} g_{\text{asy},i} \epsilon_{\text{sca},i} \quad (3.10)$$

Parameters derived from equations 3.7 to 3.10 are then fed to the RTC of SOCOL-AERv2, where the absorption and the scattering due to solid particles is calculated for each spectral band.

For simplicity, the optical properties of the monomers comprising all particles were calculated assuming pure, unaged spheres for interactions of the particles with radiation, although the model would allow applying optical properties as a function of particle aging if data were available. We used the semi-empirical code of Rannou et al. (1999) to look at the change of the optical properties of alumina particles with radius of 240 nm when assuming a 10 nm thick spherical sulfuric acid coating (a valid assumption, see Section 3.4.3), but found only very little changes in scattering and absorption properties (not shown). However, for this calculation an effective medium approximation (i.e., using a volume-weighted function of the refractive indices of the constituent materials Lesins et al., 2002) was applied to provide an effective refractive index for the alumina-sulfuric acid core-shell. This was necessary because the Rannou et al. (1999) code can only handle homogeneous spherical constituent monomers. Since composition changes of the particles resulting from the simulations in this study are only small (see Section 3.4) with only little impact on optical properties, we only accounted for the optical properties of bare calcite and alumina particles. Changes in optical properties as a result of composition changes of the solid particles through aging processes such as uptake of  $\text{HNO}_3$  on calcite particles resulting in  $\text{Ca}(\text{NO}_3)_2$  (see Section 3.2.4) or as a result of sulfuric acid uptake at the alumina particle surface (see Section 3.2.3) were not accounted for.

### 3.2.3 Alumina particles

Alumina particles are represented with two sets of prognostic variables representing two times the 10 mass bins for solid particle monomers and agglomerates. One set of mass bins represents particles partially coated by sulfuric acid, while the other set represents particles fully coated by sulfuric acid. Particles are emitted as spherical monomers with density  $\rho=3.98 \text{ g/cm}^3$  and a molar weight of 101.1 g/mol into the partially coated alumina monomer mass bin. They can acquire a sulfuric acid coating via condensation of  $\text{H}_2\text{SO}_{4(g)}$  or via coagulation with sulfuric acid aerosols. When the coating mass per primary particle reaches a certain threshold (see Section 3.2.3.3, "Contact angle") they are moved to the fully coated mass bins.

#### 3.2.3.1 Coagulation of alumina particles

The coagulation dynamics of solid particles and their interaction with sulfuric acid aerosols were integrated in the same semi-implicit coagulation schemes for sulfuric acid aerosols

presented in Sheng et al. (2015) and Feinberg et al. (2019, see subsection "SOCOL-AERv2"). Coagulation of solid particles and sulfuric acid aerosols are represented following the description in Weisenstein et al. (2015, see their Appendix A), with the only difference that here we do not account for pure solid particles and coated solid particles, but for partially coated and fully coated particles (see Figure 3.1, alumina particles). We account for self coagulation of sulfuric acid aerosols, partially coated solid particles and fully coated sulfuric acid particles as well as coagulation between these three categories. This results in a total of 2 sets of 10 solid particle mass bins for partially coated and fully coated particles as well as one additional prognostic variable for each solid particle mass bin to keep track of the sulfuric acid coating, which results in a total amount of  $4 \times 10$  additional prognostics variables for solid particle representation.

As already stated in Weisenstein et al. (2015) applying a mass doubling between subsequent bins leads to an artificial broadening of the particle size distribution since coagulation would often result in agglomerates of sizes, which fall in between two mass bins. In these cases the resulting mass is split up between neighboring mass bins by applying a statistical weighting Weisenstein et al. (see 2015, Appendix A). The errors resulting from this discrete aerosol mass binning could lead to a broadening of the size distribution during the coagulation process, which could result in somewhat overestimated sedimentation of solid particles (Weisenstein et al., 2015). The resulting error depends on the coarseness of the bin spacing (Weisenstein et al., 1997, 2007), which is a mass doubling in this case. The mass doubling between subsequent mass bins applied in this model is a good compromise between accuracy of representation and usage of computational resources, since computational resources increase with every additional prognostic variable.

The coagulation kernel was calculated using the mobility radius for solid particle agglomerates (see previous section "Mobility radius") and the spherical radius for liquid sulfuric acid aerosols for every possible combination of collisions i.e., self coagulation between aerosol mass bins of every category (40 liquid sulfuric acid mass bins, 10 partially coated and 10 fully coated solid particle mass bins) as well as coagulation between all mass bins of every aerosol particle category. The calculation of the coagulation kernel followed the same methodology as for sulfuric acid aerosols in SOCOL-AERv2 (see Section 3.2.1) and was implemented following (Weisenstein et al., 2015, Appendix A). The representation applied only accounts for Brownian coagulation and neglects gravitational, convective and Van der Waals corrections, which results in slight underestimation of coagulation efficiencies.

### 3.2.3.2 Condensation and evaporation of $\text{H}_2\text{SO}_4$

Condensation of  $\text{H}_2\text{SO}_4$  on alumina particles and evaporation of  $\text{H}_2\text{SO}_4$  from alumina particles was treated the same way as described in Weisenstein et al. (2015, Appendix A) following the methodology described in Jacobson and Seinfeld (2004). However, contrary to Weisenstein et al. (2015) we accounted for condensation of  $\text{H}_2\text{SO}_4$  not only on fully coated, but also on partially coated solid particles. The  $\text{H}_2\text{SO}_4$  condensation rates on solid particles are calculated as a function of the SAD of a solid particle, their number density, the molecular diffusion coefficient of  $\text{H}_2\text{SO}_4$ , the difference between the  $\text{H}_2\text{SO}_4$  partial pressure and the  $\text{H}_2\text{SO}_4$  equilibrium vapour pressure as well as the primary particle radius of every agglomerate to account for the Kelvin effect. Evaporation of  $\text{H}_2\text{SO}_4$  is represented with the same scheme as for coagulation and occurs when the partial pressure of  $\text{H}_2\text{SO}_4$  is smaller than the equilibrium vapour pressure of  $\text{H}_2\text{SO}_4$ , which mainly occurs above 35 km altitude.

### 3.2.3.3 Contact angle of $\text{H}_2\text{SO}_{4(\text{aq})}$ on solid particles

For partially coated alumina particles sulfuric acid coating is represented by accounting for the contact angle ( $\theta$ ) of  $\text{H}_2\text{SO}_4\text{-H}_2\text{O}$  on alumina particles to differentiate between surface area covered by sulfuric acid and uncovered  $\text{Al}_2\text{O}_3$  surface area. Figure 3.3 a) shows the basic geometry of a partial sphere from which equations were derived to calculate the share of the two types of surface area (Polyanin and Manzhurov, 2006). The volume of liquid sulfuric acid per monomer ( $V_{\text{liq}}$ ) as well as the contact angle ( $\theta$ ) is known and  $\beta$  can then be determined by inserting 3.12-3.16 into 3.11 (see Figure 2c). In 3.11  $V_{\text{p}}$  and  $V_{\text{l}}$  are the volumes of the partial spheres of the solid particle and the liquid sulfuric acid respectively (see Figure 3.3a), while  $h$  is referring to the height of the missing part of the sphere,  $r$  to the radius of the partial spheres and  $c$  to the base radius of the partial spheres (see Figure 3.3a) of liquid sulfuric acid (l) and the solid particle (p, see Figure 3.3c).

$$V_{\text{liq}} = V_{\text{l}} - V_{\text{p}} = \frac{\pi}{6} h_{\text{l}} (3c^2 + h_{\text{l}}^2) - \frac{\pi}{6} h_{\text{p}} (3c^2 + h_{\text{p}}^2) \quad (3.11)$$

$$h_{\text{l}} = r_{\text{l}} - r_{\text{l}} (\cos(\theta + \beta)) \quad (3.12)$$

$$h_{\text{p}} = r_{\text{p}} - r_{\text{p}} (\cos(\beta)) \quad (3.13)$$

$$c = r_{\text{p}} \sin(\beta) \quad (3.14)$$

$$c = r_{\text{l}} \sin(\theta + \beta) \quad (3.15)$$

$$r_{\text{l}} = \frac{\sin(\beta) r_{\text{p}}}{\sin(\theta + \beta)} \quad (3.16)$$

The solid particle surface area and the sulfuric acid surface area per solid particle monomer can then be calculated with 3.17 and 3.18.

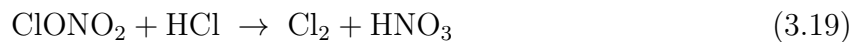
$$S_{\text{liq}} = \pi (c^2 + h_{\text{l}}^2) \quad (3.17)$$

$$S_{\text{solid}} = 4 \pi r_{\text{p}}^2 - \pi (c^2 + h_{\text{p}}^2) \quad (3.18)$$

The liquid sulfuric acid volume of each mass bin is assumed to be equally distributed over all primary particles within one agglomerate assuming that every primary particle hosts the same amount of sulfuric acid. The whole alumina and sulfuric acid coating mass is transferred to the fully coated mass bins as soon as  $\beta$  is larger than  $90^\circ$ , an arbitrarily but realistic criteria for immersion (see Figure 3.3b). The fully coated mass bins assume the alumina particles to be equally spherical and fully covered by sulfuric acid (see Figure 3.1, "Alumina particles").

### 3.2.3.4 Heterogeneous chemistry on alumina particles

The sulfuric acid SAD resulting from the partially coated alumina particles as well as the one from fully coated alumina particles is added to the total available sulfuric acid aerosol SAD and the same heterogeneous chemistry is assumed to take place on this surface area as for sulfuric acid aerosols (Sheng et al., 2015). On alumina SAD of partially coated alumina particles, we accounted for reactions 3.19 to 3.21:



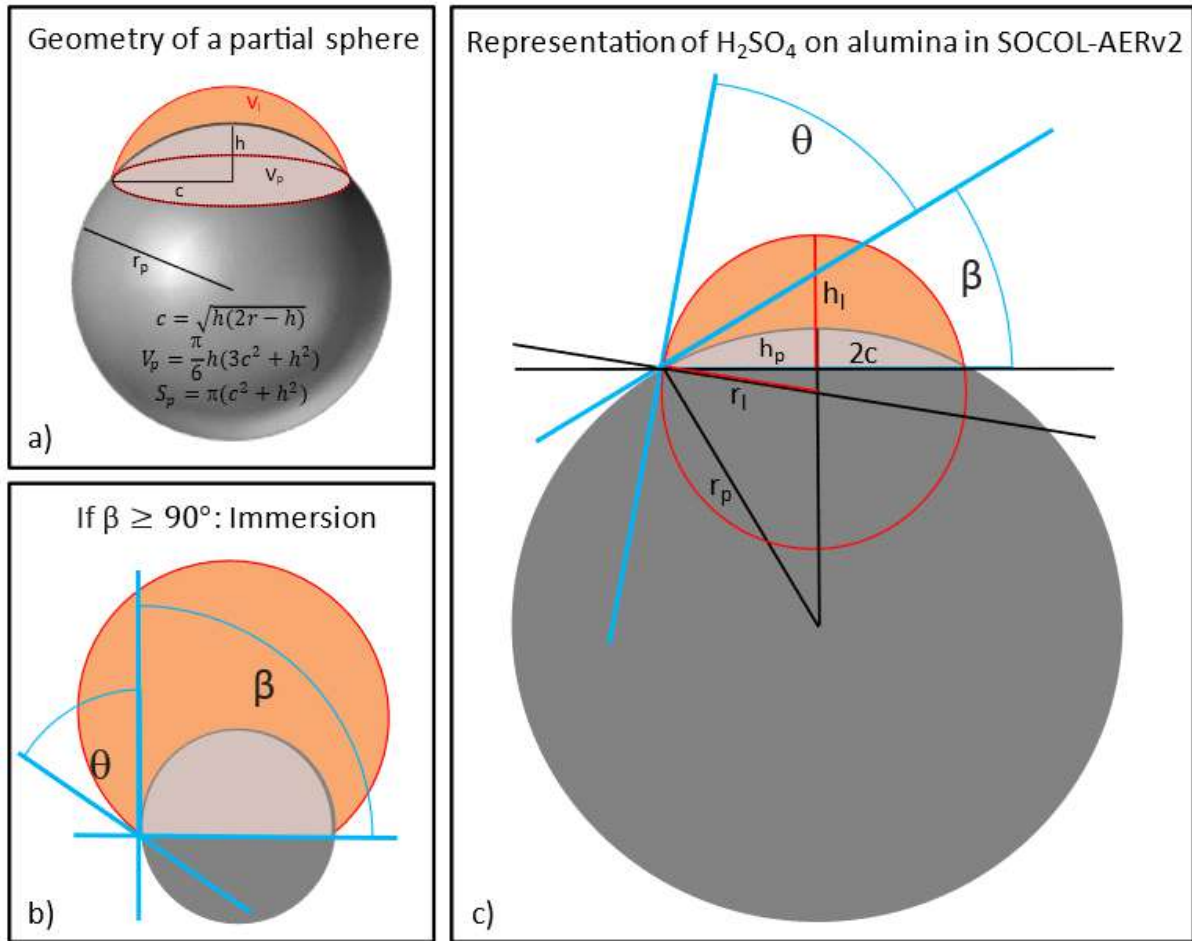


Figure 3.3: Schematic illustration of the representation of the contact angle of  $\text{H}_2\text{SO}_4$  (depicted in orange) on alumina particles (depicted in grey). Panel a) depicts the general geometry of a partial sphere with basic equations. The criteria for immersion is illustrated in panel b). An additional molecule of  $\text{H}_2\text{SO}_4$  acquired on this particle will lead to transfer of the particle mass to the fully coated mass bins. Panel c) illustrates the quantities used for the equations used in the main text to determine the angle  $\beta$  (see 3.11-3.16), which is then used to determine the sulfuric acid SAD and the alumina SAD (see 3.17 and 3.18).

Though Molina et al. (1997) measured uptake coefficients for reaction 3.19, their data are not representative for low stratospheric HCl partial pressures. To extrapolate the experimental data of Molina et al. (1997) to typical stratospheric values, we applied a Langmuir-Hinshelwood representation of adsorption and reaction as detailed in Vattioni et al. (2023a). For this study we used the scenario “dissociative  $\gamma$ ,  $\alpha=0.1$ ” to calculate the uptake coefficient of  $\text{ClONO}_2$  on alumina particles for R1. Due to the lack of experimental data on other heterogeneous reactions we only accounted for reaction 3.20 and 3.21 by assuming the same reaction rates as on sulfuric acid aerosols, which is an upper limit estimate (Vattioni et al., 2023a).

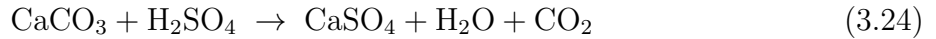
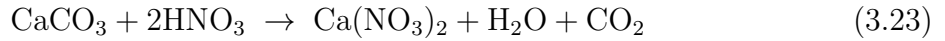
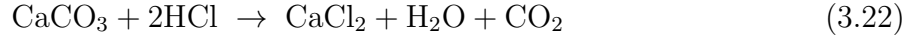
### 3.2.4 Calcite particles

In contrast to alumina, calcite is alkaline and thus reactive towards the acids in the stratosphere. Therefore, calcite particle can change their composition by forming salts at

the surface (Keith et al., 2016; Cziczo et al., 2019; Huynh and McNeill, 2020; Dai et al., 2020; Huynh and McNeill, 2021). This requires a different treatment than for alumina particles, which do not undergo compositional changes, but only acquire a sulfuric acid coating at the surface.

### 3.2.4.1 Heterogeneous chemistry on calcite particles

For calcite particles the following heterogeneous reactions upon uptake of HCl, HNO<sub>3</sub> and H<sub>2</sub>SO<sub>4</sub> are considered (3.19-3.21):



To keep track of the reaction products (Ca(NO<sub>3</sub>)<sub>2</sub>, CaCl<sub>2</sub> and CaSO<sub>4</sub>) additional prognostic variables for all three products were implemented for every calcite mass bin, resulting in a total of 40 prognostic variables (4 species times 10 mass bins). The total number of molecules per particle is always the same, but depending on the uptake of acids they are either in the form of CaCO<sub>3</sub>, Ca(NO<sub>3</sub>)<sub>2</sub>, CaCl<sub>2</sub> and CaSO<sub>4</sub>. This changes the density of the particles (i.e.,  $\rho_{\text{CaCO}_3}=2.71 \text{ g/cm}^3$ ,  $\rho_{\text{CaSO}_4}=2.32 \text{ g/cm}^3$ ,  $\rho_{\text{Ca}(\text{NO}_3)_2}=2.50 \text{ g/cm}^3$ ,  $\rho_{\text{CaCl}_2}=2.15 \text{ g/cm}^3$ ) and therefore also their radius, which is accounted for in the model. As stated by Cziczo et al. (2019) this is a simplification since in reality the reaction products would form hydrates, which are less dense than their anhydrous forms, and likely also mixed salts.

Reactions 3.22-3.24 are treated as first order reactions resulting in the following mass balance for calcite and the reaction products:

$$\frac{d[\text{CaCO}_3]}{dt} = -0.5[\text{HCl}]k_{\text{HCl}+\text{CaCO}_3} - [\text{H}_2\text{SO}_4]k_{\text{H}_2\text{SO}_4+\text{CaCO}_3} - 0.5[\text{HNO}_3]k_{\text{HNO}_3+\text{CaCO}_3} \quad (3.25)$$

$$\frac{d[\text{CaCl}_2]}{dt} = 0.5[\text{HCl}]k_{\text{HCl}+\text{CaCO}_3} \quad (3.26)$$

$$\frac{d[\text{Ca}(\text{NO}_3)_2]}{dt} = 0.5[\text{HNO}_3]k_{\text{HNO}_3+\text{CaCO}_3} \quad (3.27)$$

$$\frac{d[\text{CaSO}_4]}{dt} = [\text{H}_2\text{SO}_4]k_{\text{H}_2\text{SO}_4+\text{CaCO}_3} \quad (3.28)$$

Values in brackets are the molecule number densities of the different species. The resulting CO<sub>2</sub> and H<sub>2</sub>O from reactions 3.22 to 3.24 is not further tracked since resulting quantities are very small compared to background concentrations of these species. For the calculation of heterogeneous chemistry CaCO<sub>3</sub> molecules of all bins are summed up, but the resulting products are redistributed to the different size bins depending on the share of available SAD from each mass bin. The SAD is always assumed to be pure CaCO<sub>3</sub>, which means that all reaction sites are always available for reaction. Therefore, no passivation occurs, but instead a constant uptake coefficient ( $\gamma$ ) is applied to calculate the reaction rate ( $k$ ) for reaction 3.22 to 3.24 following equation 3.29, where  $\bar{v}$  is the thermal velocity of the molecule colliding with the surface (i.e., HCl, HNO<sub>3</sub> or H<sub>2</sub>SO<sub>4</sub> in this case):

$$k = \frac{\gamma \bar{v} \text{SAD}}{4} \quad (3.29)$$



The passivation effect of the surface must be accounted for via the uptake coefficient  $\gamma$ , which should be representative for the whole stratospheric lifetime of the calcite particles (about 1 year) and not only for the generally much larger initial reactive uptake on pure calcite particles such as measured in Huynh and McNeill (2020, 2021). However, neglecting the surface passivation effect over time is again a simplification, since in reality the surface would most likely undergo passivation through the uptake of reaction products. The reaction products would also form hydrates which might host other heterogeneous reactions (Cziczo et al., 2019). However, the setup presented here allows for sensitivity analysis of different processes such as varying the uptake coefficients and analyzing the total uptake of HCl, HNO<sub>3</sub> and H<sub>2</sub>SO<sub>4</sub>.

In this study we applied uptake coefficients of  $10^{-4}$  and  $10^{-5}$  for the uptake of HNO<sub>3</sub> (3.23) and HCl (3.22), respectively, following Dai et al. (2020), and an uptake coefficient of 1.0 for H<sub>2</sub>SO<sub>4</sub> (3.24), assuming that every collision of a H<sub>2</sub>SO<sub>4</sub> molecule with a calcite particle results in immediate uptake and reaction to CaSO<sub>4</sub>. Other heterogeneous chemistry on calcite particles is neglected.

### 3.2.4.2 Coagulation of calcite particles

Coagulation of calcite particles is calculated by the same schemes as for alumina particles. However, instead of tracking the sulfuric acid coating, the CaCO<sub>3</sub>, Ca(NO<sub>3</sub>)<sub>2</sub>, CaCl<sub>2</sub> and CaSO<sub>4</sub> mass per bin is tracked. Additionally, coagulation of calcite particles with sulfuric acid aerosols is assumed to result in instantaneous and irreversible formation of CaSO<sub>4</sub> (same as reaction 3.24).

## 3.3 Experimental setup

Each injection scenario (see Table 3.1) emitted continuously between 30°S and 30°N at all longitudes at 54 hPa ( $\sim$ 20 km altitude). The baseline scenarios injected alumina and calcite particles at particle radii of 240 nm at a rate of 5 Mt/yr. Additionally, we performed sensitivity analyses with respect to the injected particle radius, the injection rate, as well as the sulfuric acid contact angle on alumina particles (see Table 1 for details). For comparison with sulfur-based SAI, different scenarios with injections of gaseous SO<sub>2</sub> as well as accumulation-mode aerosol of condensed H<sub>2</sub>SO<sub>4</sub>, assuming a log-normal distribution with a mean radius of 0.95  $\mu$ m and a  $\sigma$  of 1.5, were also simulated (see Vattioni et al., 2019; Weisenstein et al., 2022, see Table 1 for details). The latter scenario assumes that an optimised aerosol size distribution with a mean radius of 0.095  $\mu$ m can be produced by injecting gaseous H<sub>2</sub>SO<sub>4</sub> into an aircraft plume Pierce et al. (2010); Benduhn et al. (2016); Vattioni et al. (2019); Weisenstein et al. (2022). The resulting aerosol size distribution could result in larger RF, while simultaneously reducing some side effects such as ozone depletion compared to SO<sub>2</sub> injections. However, the underlying assumptions are subject to large uncertainty (Vattioni et al., 2019).

All simulations are time-slices spanning 20 years with all boundary conditions set to the year 2020. For sea surface temperatures (SST) and sea ice concentrations (SIC), a climatological 10-year (2010-2019) average seasonal cycle from the Hadley dataset was used (Kennedy et al., 2019), while GHG and ODS concentrations were taken from SSP5-8.5 (O'Neill et al., 2015) and WMO (2018), respectively. The first 5 years of each simulation served as spin-up to equilibrate stratospheric aerosol burdens. Hence, all SOCOL-AERv2

data shown in this study are 15-year averages. The boundary conditions follow the GeomIP test-bed experiment "accumH2SO4"<sup>1</sup> except for injecting the absolute mass of each species and not the equivalent sulfur mass as well as for the boundary conditions following the year 2020 instead of 2040 (see also Weisenstein et al., 2022).

Table 3.1: Overview of the simulations performed in this study. Columns show the emitted species, the injection rate, the injected primary particle radius as well as the contact angle where applicable. Injections were emitted continuously between 30°N and 30°S at 20 km altitude. The baseline configurations are marked in bold.

Emitted Species	Injection Rate (Mt yr <sup>-1</sup> )	Injected Primary Particle Radius	Contact Angle
Alumina	1, <b>5</b> , 10 and 25	<b>240 nm</b>	15°, <b>30°</b> , 45°, 60°, fully covered
Alumina	<b>5</b>	80 nm, 160 nm, <b>240 nm</b> , 320 nm	<b>30°</b>
Calcite	1, <b>5</b> , 10 and 25	<b>240 nm</b>	n/a
Calcite	<b>5</b>	80 nm, 160 nm, <b>240 nm</b> , 320 nm	n/a
SO <sub>2</sub>	1, <b>5</b> , 10 and 25	n/a	n/a
AM-H <sub>2</sub> SO <sub>4</sub>	1, <b>5</b> , 10 and 25	r=0.95 μm, σ=1.5	n/a

### 3.4 Results

The stratospheric sulfur cycle is usually represented with sulfur equivalent burden (i.e., GgS), fluxes and injection rates (i.e., GgS/yr) in both, SAI and non-SAI studies (e.g. Feinberg et al., 2019; Weisenstein et al., 2022; Brodowsky et al., 2023). This allows easy comparison of burden and fluxes of different sulfur species. However, when comparing SAI scenarios with injection rates and burden from gaseous (e.g., SO<sub>2</sub>), liquid (e.g., H<sub>2</sub>SO<sub>4</sub>) and solid (e.g., CaCO<sub>3</sub> and Al<sub>2</sub>O<sub>3</sub>) species to each other it is important to compare the absolute burden and injection rates to allow for direct comparison (see Figure 3.4). Thus, compared to the sulfur equivalent burden the resulting H<sub>2</sub>SO<sub>4</sub>-H<sub>2</sub>O burden is larger by a factor of about 3 when accounting for H<sub>2</sub>SO<sub>4</sub> plus another 40-50% when accounting for the water content. Therefore, the resulting sulfuric acid aerosol burden reported in Figure 3.4a are much larger compared to previous studies (e.g., Weisenstein et al., 2015), which compared the solid particle burden and injection rates to sulfur equivalent quantities without accounting for H<sub>2</sub>O. The comparison shown in Figure 3.4a shows that, for a given injection rate, the resulting sulfuric acid burden is about a factor of ~2 larger compared to the burden resulting from calcite and alumina particle injections. This is mainly due to the larger densities (i.e., 1.69 g/cm<sup>3</sup> for 70 wt% H<sub>2</sub>SO<sub>4</sub>, 2.71 g/cm<sup>3</sup> for CaCO<sub>3</sub> and 3.95 g/cm<sup>3</sup> for Al<sub>2</sub>O<sub>3</sub>) as well as the larger particle radius for the solids, which makes them sediment much faster.

<sup>1</sup>Details of the experiment protocol: <http://climate.envsci.rutgers.edu/geomip/testbed.html>

The resulting globally averaged alumina particle burdens for an injection of 5 Mt/yr of 80 nm, 160 nm, 240 nm and 320 nm particles are 5.6 Mt, 4.7 Mt, 3.8 Mt and 3.0 Mt, respectively, and therefore about one third smaller compared to the ones found in Weisenstein et al. (2015). This is likely not a result of differences in sedimentation speeds between the models since our modelled sedimentation velocities are slightly smaller compared to the ones shown in (Weisenstein et al., 2015, see Figure 3.15) despite applying different representations of the agglomerate particle radius (see Section 3.2.2.1). However, compared to the original 2D-AER code used in Weisenstein et al. (2015) SOCOL-AERv2 has undergone several updates (e.g., Sheng et al., 2015; Feinberg et al., 2019; Vattioni et al., 2023b), most notably the replacement of the simple updraft sedimentation scheme by the numerical scheme of Walcek (2000) to reduce numerical diffusion, interactive wet and dry deposition schemes and updates to the coagulation kernel. The difference in burden might also be affected by the three dimensional representation of dynamics and transport in our model compared to the 2D-zonal mean representation in 2D-AER. The large number of differences between the two models make it difficult to identify which specific processes are responsible for the difference in the results.

### 3.4.1 Radiative forcing efficiency

For the same injection rates we find that AM-H<sub>2</sub>SO<sub>4</sub> injections result in the largest net all sky ToA RF, slightly larger than CaCO<sub>3</sub> injections of 240 nm radius. Injecting SO<sub>2</sub> results in similar net ToA all sky RF as for AM-H<sub>2</sub>SO<sub>4</sub> for injection rates of 10 Mt/yr and smaller. At very large injection rates of 25 Mt/yr, a non-linearity in the RF efficiency of SO<sub>2</sub> injections becomes apparent; SO<sub>2</sub> injections result in smallest net ToA all sky RF values compared to injections of the other species investigated in this study. This is mainly due to the unfavourable aerosol size distribution resulting from the large continuous condensation fluxes at large SO<sub>2</sub> injection rates, which shifts the aerosol size distribution towards larger particles, which settle faster (Heckendorn et al., 2009; Vattioni et al., 2019; Weisenstein et al., 2022). The injection of Al<sub>2</sub>O<sub>3</sub> particles of 240 nm radius results in about 25% less net ToA all sky RF compared to injections of AM-H<sub>2</sub>SO<sub>4</sub> and CaCO<sub>3</sub> particles with radii of 240 nm across all the investigated injection rates. However, both the injection of Al<sub>2</sub>O<sub>3</sub> and CaCO<sub>3</sub> particles result in larger RF per unit of stratospheric aerosol burden compared with the sulfur based injection scenarios. Despite the larger aerosol burden in our model, the resulting net top of the atmosphere (ToA) all sky radiative forcing (RF) shown in Figure 3.4b is in agreement with the net clear sky RF values found in Weisenstein et al. (2015). However, the largest net all sky ToA RF is achieved with SAI of 160 nm particles, which is in contrast with Weisenstein et al. (2015) for alumina particles, where the largest RF was obtained for the slightly larger particles (240 nm).

### 3.4.2 Coagulation

Both the resulting stratospheric burden as well as the RF scale almost linearly with increasing injection rate for solid particles (see Figure 3.4). This linearity is mainly due to the relatively small agglomeration found for the injected 240 nm particles even at large injection rates (see Figure 3.5). This is likely different for injection of smaller particles (e.g., r=80 nm) at larger injection rates or for more confined injection scenarios. The fraction of monomers for injections of 5 Mt/yr of 80 nm, 160 nm, 240 nm and 320 nm

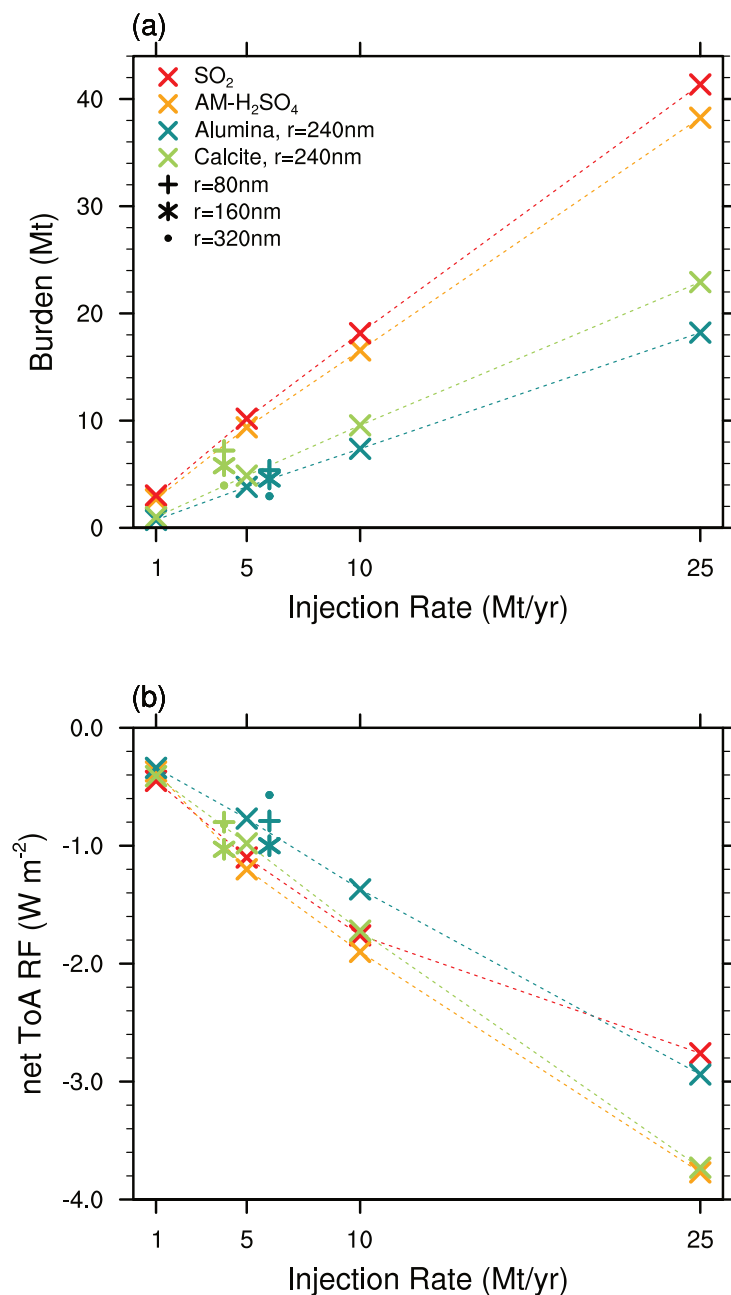


Figure 3.4: Resulting stratospheric aerosol burden (a) and total net all sky ToA RF (b) as a function of injection rate. Shown are absolute injection rates (i.e. Mt H<sub>2</sub>SO<sub>4</sub>/yr and SO<sub>2</sub>/yr and not Mt S/yr) and absolute burdens (i.e., the wet sulfuric acid burden in Mt H<sub>2</sub>SO<sub>4</sub>-H<sub>2</sub>O and not Mt S).

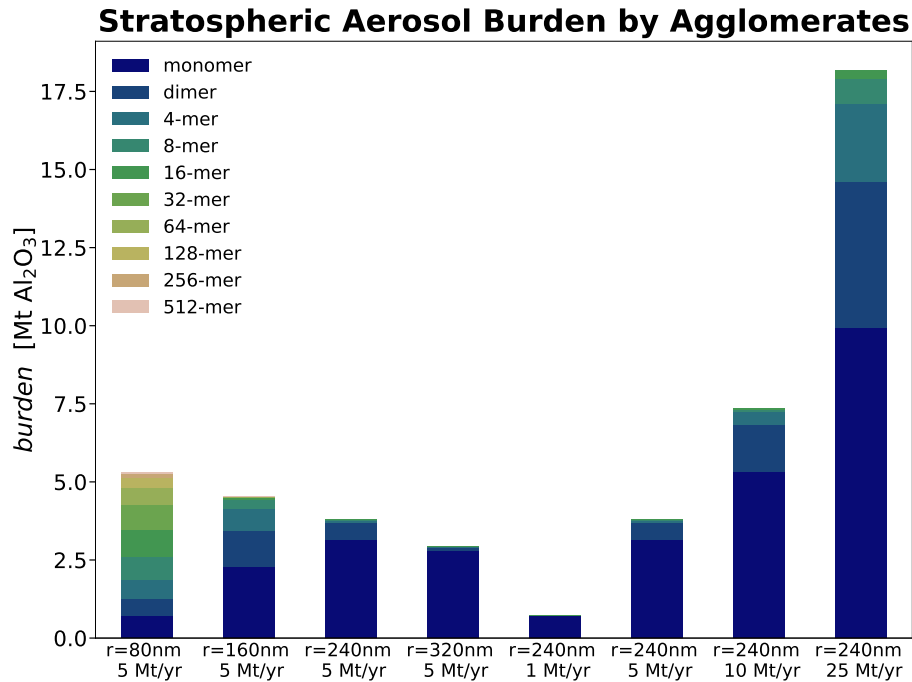


Figure 3.5: The resulting globally averaged stratospheric aerosol burden resolved for the contribution of the individual mass bins resulting from 5 Mt/yr injection of 80 nm, 160 nm 240 nm and 320 nm particles as well as 1 Mt/yr, 5 Mt/yr, 10 Mt/yr and 25 Mt/yr injection of 240 nm particles.

particles amounts to 13%, 48%, 82% and 92%, respectively, which is slightly more than what was found in Weisenstein et al. (2015). The more efficient formation of agglomerates in Weisenstein et al. (2015) could be due to the different representation of the radius of the agglomerates (see Section 3.2.2.1) or updates in the coagulation scheme (see subsection "Coagulation"). In our model, the only injection resulting in significant agglomeration is that of 80 nm particles, where most of the particle mass is in the form of 16-mers (i.e., mass bin 5, see Figure 3.5). However, these results are subject to large uncertainties due to neglecting sub-ESM grid scale injection plume processes in our model (Blackstock et al., 2009). In the injection plume (e.g. of an aircraft) the particle concentrations would be significantly higher, which could result in effective agglomeration, whereas we only assume injections equally distributed to the grid of our climate model (i.e., about 325 km x 325 km x 1.5 km in SOCOL-AERv2 at the equator at 50 hPa).

### 3.4.3 The Stratospheric Sulfur Cycle under conditions of SAI of alumina particles

Previous studies showed that injection of solid particles will likely result in uptake of sulfuric acid at the particle surface via coagulation with sulfuric acid aerosols and via condensation of gaseous sulfuric acid Weisenstein et al. (2015); Keith et al. (2016). These processes are also represented in the model presented here (see Figure 3.6). On the one hand, injecting 5 Mt per year of alumina particles will deplete the global stratospheric background sulfuric acid layer mass by 86%, 69%, 54% and 45% for injection of 80 nm, 160 nm, 240 nm and 320 nm particles, respectively (see Figure 3.6). The depletion of the background sulfuric acid aerosols can also be seen in decreased number concentrations in

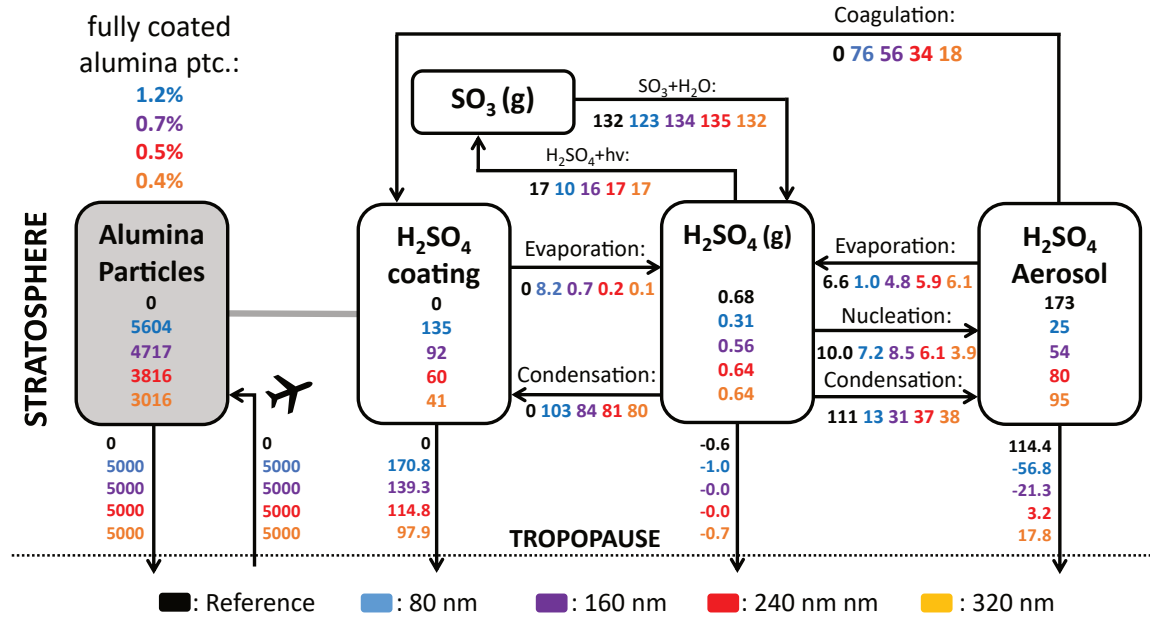


Figure 3.6: The stratospheric sulfur cycle under conditions of SAI of 5 Mt/yr alumina particles with radii of 80 nm (blue), 160 nm (violet), 240 nm (red) and 230 nm (orange). All sulfur species are shown in Gg Sulfur for burden (boxes) and Gg Sulfur per year for net fluxes (arrows). The alumina burden (gray box) is given as Gg Al<sub>2</sub>O<sub>3</sub> and Gg Al<sub>2</sub>O<sub>3</sub> per year. Cross tropopause fluxes are calculated by balancing the mass balance of the individual species.

the sulfuric acid size distributions (see Figure 3.15 in Appendix 3D). On the other hand, the mass of sulfuric acid coating on alumina particles reaches values of 78%, 53%, 35% and 24% of the unperturbed global stratospheric sulfuric acid aerosol burden, respectively. Therefore, the sum of the globally averaged stratospheric coating and sulfuric acid aerosol mass are smaller than the unperturbed stratospheric sulfuric acid aerosol burden, which is due to the faster removal via sedimentation of condensed sulfuric acid mass on heavier solid particles compared to sulfuric acid aerosols. Injection of 80 nm particles results in the largest coating mass of sulfuric acid; this is mainly due to the larger coagulation efficiency with sulfuric acid aerosols of small particles, as well as due to the larger surface area availability for condensation. The bigger fraction of sulfuric acid coating is acquired via direct condensation of H<sub>2</sub>SO<sub>4(g)</sub> in all scenarios. However, the share of acquisition via coagulation increases with decreasing alumina particle size from 18% for 320 nm particle injection to 42% for 80 nm particle injection. The same tendencies in the response of the stratospheric sulfur cycle to alumina injection can be observed when increasing the injection rate from 1 Mt/yr to 25 Mt/yr (see Appendix 3E, Figure 3.19).

When distributing the sulfuric acid coating (i.e., the total condensed H<sub>2</sub>SO<sub>4</sub>-H<sub>2</sub>O mass on the alumina particles) equally on the alumina particles the corresponding coating thickness would reach values of maximal 6-10 nm, 4-8 nm, 7-14 nm and 8-16 nm for injections of 5 Mt/yr of 80 nm, 160 nm, 240 nm and 320 nm particles in the lower stratosphere (see Figure 3.9). Similar coating thicknesses can be found for different injection rates of particles with radius of 240 nm (see Figure 3.20 in Appendix 3E).

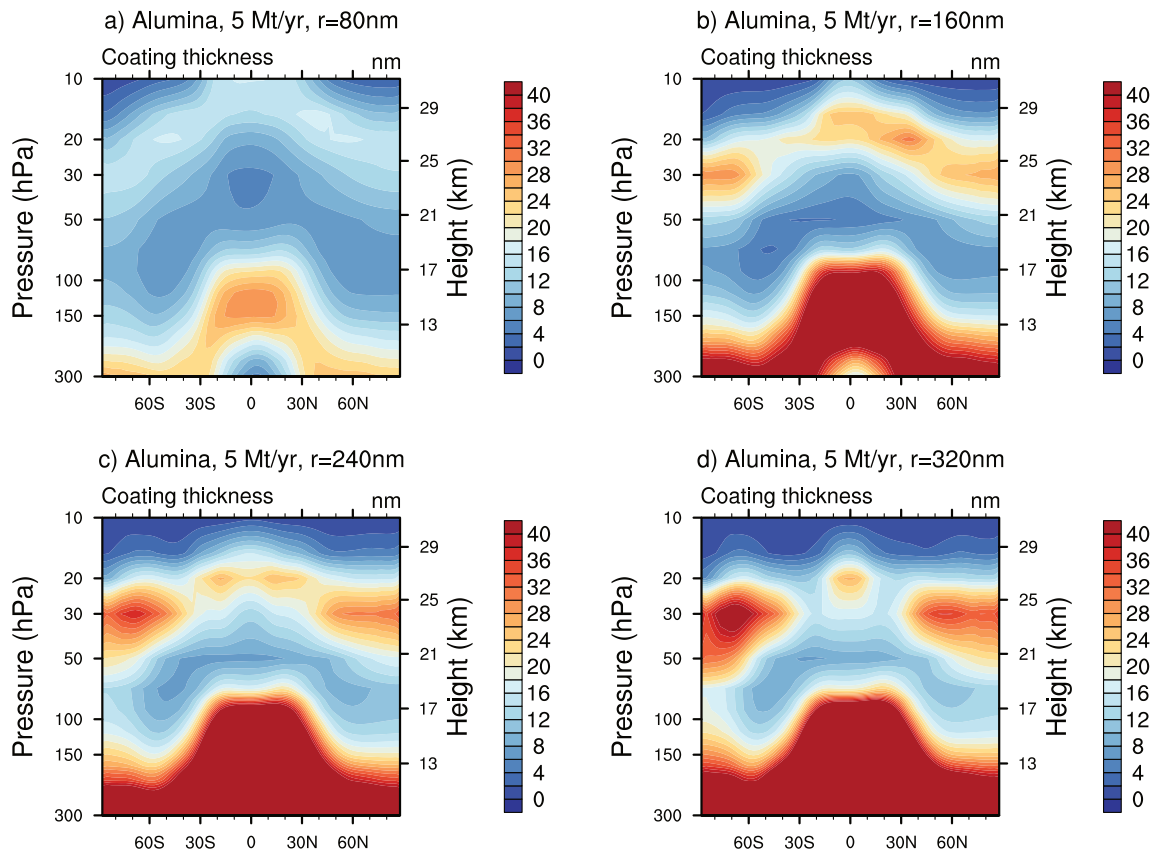


Figure 3.7: The resulting coating thickness when injecting 5Mt/yr of alumina particles with radii of 80 nm (a), 160 nm (b), 240 nm (c) and 320 nm (d). The values listed above correspond to the average coating thickness of the mass bin with the largest coating thickness, which is at the same time also the mass bin with the largest share of alumina burden (i.e., bin 5 for 80 nm particle injection and bin 1 for the others). Other mass bins have smaller coating thicknesses.

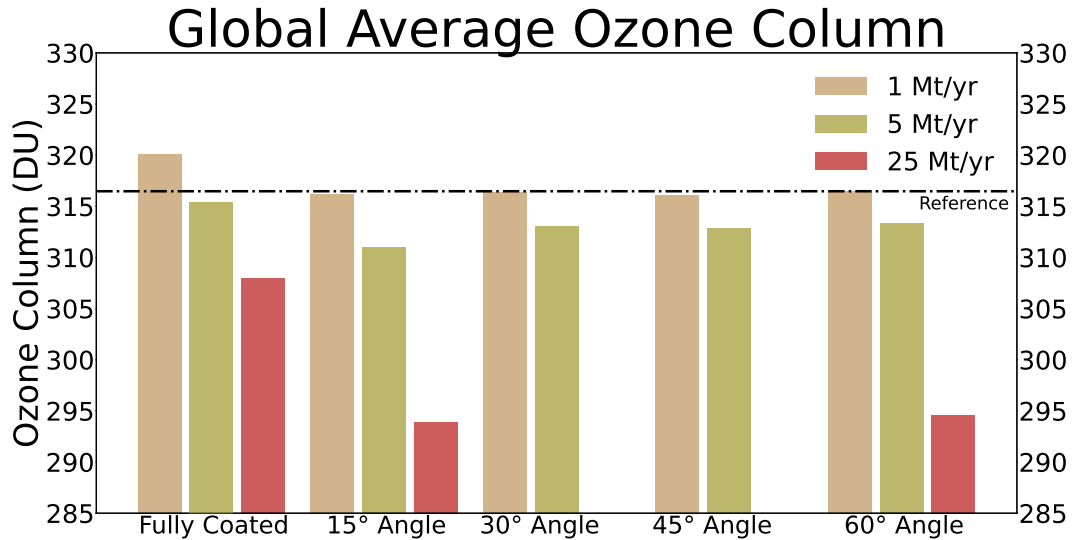


Figure 3.8: The resulting globally averaged total ozone column from 1 Mt/yr, 5 Mt/yr, 10 Mt/yr and 25 Mt/yr alumina injections when applying a  $\text{H}_2\text{SO}_4$ – $\text{H}_2\text{O}$  contact angle of  $15^\circ$ ,  $30^\circ$ ,  $45^\circ$  and  $60^\circ$  as well as when assuming the alumina particles to be fully covered by sulfuric acid.

### 3.4.4 Contact angle sensitivity analysis

The coating on alumina particles shown in Figure 3.7 is only representative if the sulfuric acid coating is distributed uniformly on the alumina particle surface, which is likely not true for the real system. In Vattioni et al. (2023a) we have performed contact angle measurements of  $\text{H}_2\text{SO}_4$  at different weight percentages and we found a contact angle of about  $31^\circ \pm 7^\circ$  at 70 wt%  $\text{H}_2\text{SO}_4$ . This measurement is subject to large uncertainty, since the contact angle is dependent on factors such as the relative humidity and the temperature during the measurement as well as the surface characteristics (polished vs. unpolished, cleaned vs. uncleaned). However, the results show that  $\text{H}_2\text{SO}_4$  is likely contracting on alumina surfaces, which would leave parts of the alumina surface uncovered from  $\text{H}_2\text{SO}_4$ – $\text{H}_2\text{O}$ . This is why the sulfuric acid coating on alumina particles is represented by accounting for the contact angle in our model (see Section 3.2.3.3). We have performed sensitivity simulations on the stratospheric ozone response from applying contact angles ranging from  $15^\circ$  to  $60^\circ$  as well as assuming the alumina particles to be fully coated by sulfuric acid (see Figure 3.8).

This sensitivity analysis shows that particles assumed to be fully covered with sulfuric acid lead to smallest impacts on stratospheric ozone. This is mostly due to the relatively small resulting SAD of alumina particles when injecting 5 Mt/yr particles with 240 nm radius (Fig. 3.10e). Depletion of background sulfuric acid aerosol SAD, which consist mostly of much smaller particles (size distribution peaking at  $r=80$  nm, see Figure 3.18 in the Appendix 3D) is compensated by the additional alumina SAD covered by sulfuric acid. In the case of 1 Mt/yr injections, this reduces the overall sulfuric acid SAD and thus even results in an ozone increase. However, as discussed previously complete coverage of alumina particle by sulfuric acid is unlikely. Therefore, contact angles between  $15^\circ$  and  $60^\circ$  lead to higher ozone depletion, mainly due to the availability of uncoated alumina surface and the resulting chlorine activation (see Subsection "Heterogeneous chemistry on alumina particles"). However, there are no significant differences between different



contact (Fig. 3.8) angles since for all case at least 50% of the alumina surface will remain uncovered by sulfuric acid and the sulfuric acid coating SAD does not significantly change when represented with contact angles of 15° and 60°. Therefore, we use the measured contact angle of 30° for the representation of the sulfuric acid coating on alumina particles. This is a valid assumption given the only small coating thickness.

### 3.4.5 The Stratospheric sulfur cycle under conditions of SAI of calcite particles

For the injection of calcite particles, the depletion of the background sulfuric acid aerosol layer as well as condensation and coagulation fluxes on calcite particles are very similar compared to the injection of alumina particles (Fig. 3.9). The only difference compared to alumina particles is that sulfuric acid on calcite particles is immediately assumed to undergo irreversible reaction with  $\text{CaCO}_3$  to form  $\text{CaSO}_4$ . The resulting globally averaged  $\text{CaSO}_4$  burden varies between 90 Gg and 296 Gg for 80 nm and 320 nm particles, respectively. This corresponds to only 4.1 % and 2.3% of the entire stratospheric calcite burden, respectively. The uptake of the acids is mainly dependent on the available SAD (see Appendix 3G, Figure 3.22). The uptake of HCl on calcite with a uptake coefficient of  $10^{-5}$  results in  $\text{CaCl}_2$  burdens of 2 Gg and 24 Gg for 320 nm and 80 nm particle injections respectively, which is 0.05% and 0.3% of the resulting total globally averaged stratospheric calcite burden. The biggest fraction other than  $\text{CaCO}_3$  makes calcium nitrate, which results from uptake of  $\text{HNO}_3$  at an uptake coefficient of  $10^{-4}$ .  $\text{Ca}(\text{NO}_3)_2$  burdens are between 65 Gg and 456 Gg for 80 nm and 320 nm particle injection, respectively, accounting for 1.6% and 6.3% of the resulting total globally averaged stratospheric calcite burden, respectively. Therefore, between 89% and 96% of the calcite burden will remain unchanged in the form of  $\text{CaCO}_3$  during the entire stratospheric residence time for injection of 80 nm particles and 320 nm particles, respectively. Thus, the scattering and absorption properties of the calcite particles are unlikely to change significantly due to ageing processes. However, the ageing has significant consequences for heterogeneous chemistry on the particle surfaces, since these salts might host different heterogeneous reactions at different reaction rates. The sensitivity analysis to detailed heterogeneous chemistry of calcite particles using this model will be topic of another publication.

### 3.4.6 Solid particle number concentrations and surface area densities

The resulting solid particle number concentrations reach values of up to 7 particles per  $\text{cm}^3$  in the lower stratosphere when injecting 5 Mt/yr of alumina particles with radius 240 nm (Fig. 3.10b). For 25 Mt/yr of 240 nm particles or 5 Mt/yr of particles with 80 nm radius, these number concentrations reach values of up to 30 and 80 particles per  $\text{cm}^3$ , respectively (see Figure 3.10a and c; see Figure 3.22 in Appendix 3G for corresponding resulting number densities from calcite injections). This is a substantial perturbation to the otherwise relatively clean air in the lower stratosphere and the upper troposphere. These particles will likely influence cirrus and polar stratospheric cloud abundances (e.g., Cziczo et al., 2019), an effect not accounted for by our model. However, we account for heterogeneous chemistry on alumina and calcite surfaces (see Subsection "Heterogeneous Chemistry"). The total sulfuric acid SAD (i.e., sum of sulfuric acid coating and sulfuric acid aerosols) for injection rates of 5 Mt/yr and 25 Mt/yr alumina particles with 240 nm

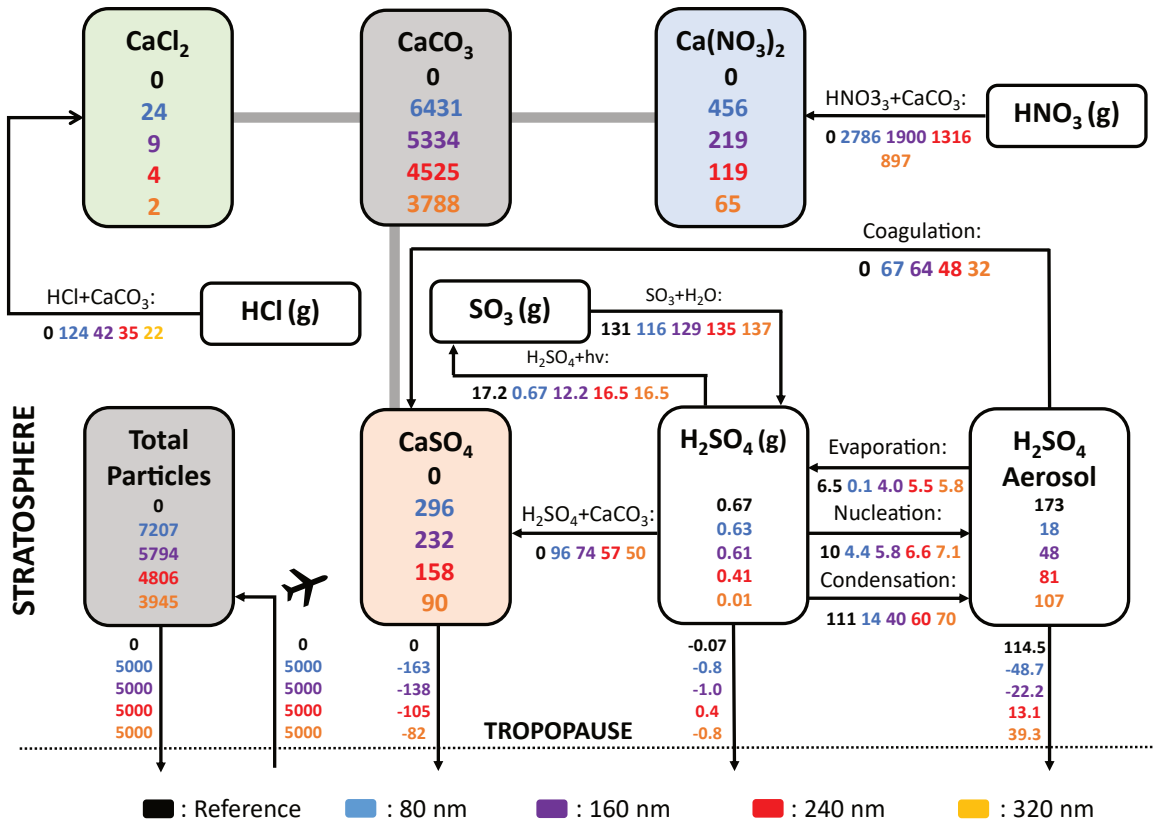


Figure 3.9: The stratospheric sulfur cycle under conditions of SAI of 5 Mt/yr calcite particles with radii of 80 nm (blue), 160 nm (violet), 240 nm (red) and 320 nm (orange). All sulfur species (except CaSO<sub>4</sub>) are shown in Gg Sulfur for burden (boxes) and Gg Sulfur per year for net fluxes (arrows). The solid species (colored boxes) are given in Gg of the corresponding material. The HNO<sub>3</sub> and HCl flux to Ca(NO<sub>3</sub>)<sub>2</sub> and CaCl<sub>2</sub> are given in Gg HNO<sub>3</sub> per year and Gg HCl per year. Cross tropopause fluxes are calculated by balancing the mass balance of the individual species. See Appendix 3F, Figure 3.21 for the response of the stratospheric sulphur cycle to different injection rates of calcite particles.

radius is not significantly different from the SAD of the reference simulation (see Figure 3.10h, 3.10i and also Section 3.4.4). This is mostly due to the small angle  $\beta$  for a constant contact angle ( $\theta$ ) when the amount of sulfuric acid volume is small compared to the solid particle volume (i.e., for large alumina burden and large primary particle radius, see Figure 3.3). When emitting 5 Mt/yr of 80 nm particles,  $\beta$  gets much larger and so does also the sulfuric acid surface area per particle (see Figure 3.10g). The alumina particle number density and SAD increase linearly with injection rate when keeping the radius constant. For the same injection rate, the number density is inversely proportional to the radius with a cubic power law, while the SAD increases linearly with decreasing particle radius, as observed in Figure 3.10a-f).

### 3.4.7 Ozone response to calcite and alumina particle injection

The resulting SAD presented in the previous section (see Figure 3.10) results in depletion of the total ozone column (TOC), which mainly correlates with the available alumina

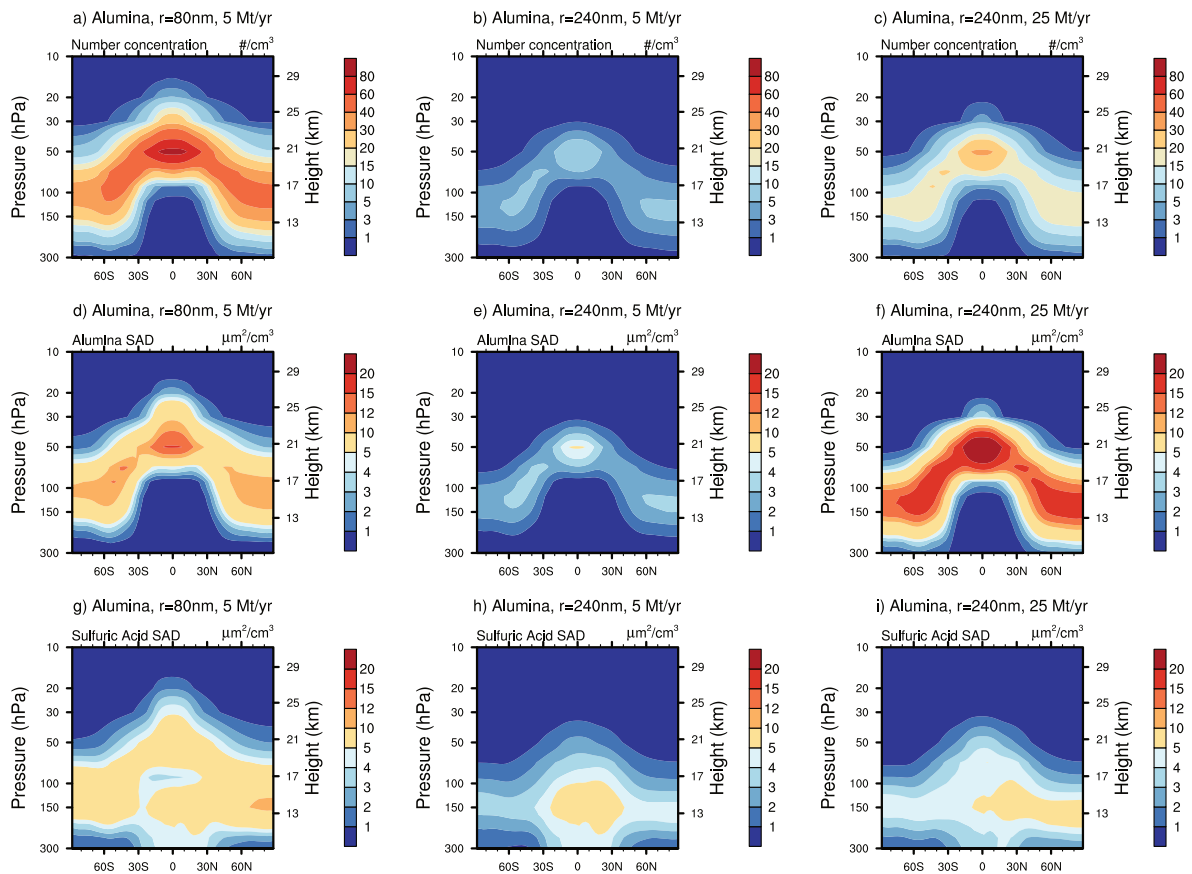


Figure 3.10: The resulting zonal mean number densities (a-c), alumina SAD (d-f) and total sulfuric acid SAD (sum of sulfuric acid aerosols SAD and SAD from sulfuric acid coating on alumina particles, g-i) from injection of 5 Mt/yr of particles with 80 nm (a,d,f), 5 Mt/yr of particles with 240 nm particles (b,e,h) and 25 Mt/yr of particles with 240 nm radius (c,f,i). The same Figure for calcite particles is shown in the Appendix G, Figure 3.22.

SAD (see Figure 3.11). Injection of 5 Mt/yr of 80 nm particles and 25 Mt/yr of 240 nm particles both result in TOC depletion of more than 4% in the tropics and up to 16% and 12% in the polar regions, respectively. Our baseline scenario, which injected 5Mt/yr of alumina particles with radius of 240 nm only resulted in TOC depletion of less than 2% across all latitudes. Only the injection of 5 Mt/yr of alumina particles of 320 and 240 nm results in a smaller TOC depletion than the sulfur-based scenarios. For 80 and 160 nm alumina particles the TOC depletion is enhanced (Fig. 3.11a). When injecting 25 Mt/yr of alumina particles with radius 240 nm the ozone depletion is 50% larger compared to the injection of SO<sub>2</sub> (see Figure 3.11). However, these results are subject to large uncertainty (see Vattioni et al., 2023a) due to the lack of experimental data on heterogeneous chemistry on alumina particles.

All calcite injection scenarios result in an increase of TOC in the polar regions of up to about 6%, but almost no change at midlatitudes. This is mostly due to the removal of HCl from the stratosphere on calcite particles in agreement with the findings of Dai et al. (2020). However, the uptake of HCl, HNO<sub>3</sub> and H<sub>2</sub>SO<sub>4</sub> (Reactions 3.22-3.24) is the only heterogeneous chemistry process considered on calcite particles, which is a simplification. The resulting products will likely form hydrates (Cziczo et al., 2019), which may host other heterogeneous reactions such as 3.19-3.21; our study only considers them on alumina particles. However, there is no experimental data on such reactions available for calcite surfaces, which makes the modelled response of the stratospheric ozone layer to calcite particle injections highly uncertain.

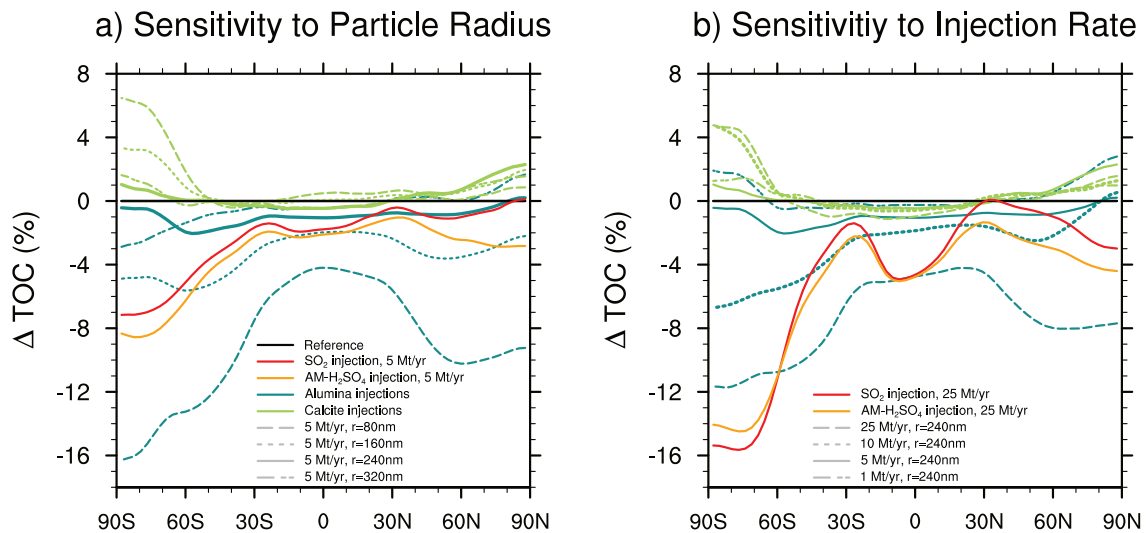


Figure 3.11: The simulated zonal mean total ozone column anomaly resulting from (a) injecting 5 Mt/yr of alumina and calcite particles with radii of 80 nm, 160 nm, 240 nm and 320 nm as well as 5 Mt/yr injections of SO<sub>2</sub> and AM-H<sub>2</sub>SO<sub>4</sub> and (b) from injecting 1 Mt/yr, 5 Mt/yr, 10 Mt/yr and 25 Mt/yr calcite and alumina particles at radius of 240 nm as well as 25 Mt/yr SO<sub>2</sub> and AM-H<sub>2</sub>SO<sub>4</sub> injections.

## 3.5 Conclusions

This study presents the first aerosol-chemistry climate-model incorporating an interactive solid particle microphysics scheme to investigate the risks and benefits of SAI of solid particles. The solid particles considered in this study are fully interactive with the stratospheric sulfur cycle. The model also allows for uptake of sulfuric acid at the particle surface via coagulation with sulfuric acid aerosols and condensation of  $\text{H}_2\text{SO}_{4(g)}$  on the particle surfaces, as well as for the formation of agglomerates via coagulation of solid particles. The solid particles are subject to advection, sedimentation and interactive wet and dry deposition in the troposphere. Furthermore, the model allows for representation of heterogeneous chemistry on the particle surface, and in particular, for the representation of the radiative effects of the particles, even after their microphysical interactions. The modular design of the model allows switching on and off the coupling of individual processes, which makes it perfectly suited to investigate sensitivity and importance of the different processes relevant for the assessment of the risks and benefits of SAI of solid particles.

While this model was primarily developed for the evaluation of potential SAI scenarios of calcite and alumina injections, the model could also easily be adapted for representation of any other potential particle type or even for other applications. This could for example be the re-evaluation of radiative and chemical impacts of alumina particles emitted to the atmosphere from solid fuel space shuttle rocket launches, which will likely increase significantly in the future (Jackman et al., 1998; Danilin et al., 2001; Ross and Sheaffer, 2014), the evaluation of the growing impacts of microplastic nanoparticles transported in the atmosphere (Revell et al., 2021), analysis of wildfire impacts on stratospheric ozone (Solomon et al., 2023), and analysis of the role of meteoritic dust in the upper atmosphere (Biermann et al., 1996).

By using the model documented here, we show that the injection of solid particles likely results in significantly smaller stratospheric aerosol burdens compared to the same injection rate of  $\text{SO}_2$  and  $\text{AM-H}_2\text{SO}_4$ , even when injecting small particles with radius of 80 nm. This is mainly due to the larger average particle radius and the larger density of solid particles compared to sulfuric acid aerosols. Therefore, the corresponding net all sky ToA RF is largest for sulfur based injection scenarios when injecting the same amount of material per year (see Figure 3.4). Thus, alumina and calcite particles injected at a radius of 240 nm are only more effective in backscattering solar radiation per resulting aerosol burden, but not per injection rate of material.

Furthermore, we show that injection of solid particles to the stratosphere would deplete the stratospheric background sulfuric acid aerosol layer by more than 50% when injecting 5 Mt/yr of particles at 240 nm radius or smaller. Alumina particles would acquire a sulfuric acid coating through condensation of gaseous sulfuric acid on the particle surface and through coagulation of sulfuric acid aerosols with solid particles. The acquired sulfuric acid coating would have the equivalent thickness of about 10 nm if equally distributed over the resulting alumina SAD when injecting particles at 5 Mt/yr with radii of 240 nm. The resulting coating thickness would be smaller when increasing the injection rate due to a larger alumina SAD to sulfuric acid ratio. However, a sulfuric acid coating distributed homogeneously over the alumina particles is unlikely due to a rather steep contact angle of about  $30^\circ$  of sulfuric acid on alumina surfaces (Vattioni et al., 2023a). Thus, it is likely that also some alumina surface would be available for heterogeneous chemistry.

Therefore, the response on TOC from alumina particle injections is largely dependent

on the resulting SAD, which is a function of the alumina injection rate and the injected particle size. While for small injection rates a large fraction of the alumina particles would be covered by sulfuric acid, for large injection rates this fraction decreases significantly when assuming injection of alumina particles with radii of 240 nm. We assumed a realistic parameterisation from (Vattioni et al., 2023a, dissociative, HCl only with  $\alpha_{\text{ClONO}_2}=0.1$ ) for the heterogeneous reaction of  $\text{ClONO}_2$  with HCl (reaction 3.19) on alumina SAD and the same heterogeneous chemistry on sulfuric acid coating as on sulfuric acid aerosols to quantify the expected TOC alteration from alumina particle injections. Compared to the same injection rate of sulfuric acid aerosols the resulting response of the zonal mean TOC from injection of alumina particles is only smaller for small injection rates or large injected particle radii (see Figure 3.11).

For the injection of calcite particles we find similar perturbations to the stratospheric sulfur cycle as for alumina particles. However, the sulfuric acid taken up on calcite particles would react to  $\text{CaSO}_4$ . Assuming uptake coefficients of  $10^{-4}$  for  $\text{HNO}_3$  and  $10^{-5}$  for HCl following Dai et al. (2020), 92% of average solid particle burden would remain in the form of  $\text{CaCO}_3$  at injection rates of 5 Mt/yr  $\text{CaCO}_3$ . This would likely not change the scattering properties of calcite particles, but could significantly alter heterogeneous chemistry hosted on the particle surface. Accounting for the uptake of HCl,  $\text{HNO}_3$  and  $\text{H}_2\text{SO}_4$  alone is not expected to alter stratospheric ozone significantly.

The two biggest limitations of the model which result in major uncertainty of the presented results are the 1) missing interactions of the solid particles with clouds, such as polar stratospheric clouds and cirrus clouds as well as 2) the missing sub-grid scale microphysical injection plume-scale processes. Solid particles could serve as ice condensation nuclei for cirrus clouds in the upper troposphere after re-entry to the troposphere via sedimentation. Altering the cirrus cloud thickness could result in a strong positive (cirrus cloud thickening) or a negative (cirrus cloud thinning) feedback on climate (Cziczo et al., 2019). Furthermore, the effect of solid particles on polar stratospheric clouds is unclear, but theoretically, the solid particles could also serve as cloud condensation nuclei for PSCs. It is only speculation whether this would result in overall less, but larger, or more, but smaller, PSCs. The latter case could for example result in less denitrification over the winter poles, which would result in less ozone depletion. This increases uncertainty of impacts on stratospheric ozone even more.

The second major limitation concerns the dispersion methods within the stratosphere (see also Blackstock et al., 2009). In contrast to a gas like  $\text{SO}_2$ , solid particles cannot be easily released to the stratosphere. They would require a carrier gas or a carrier liquid which could add further perturbation to stratospheric composition. Furthermore, the DEM modelling presented in this study (see Section S1 in the SI) shows that it could be challenging to release solid particles to the stratosphere without immediate agglomeration. However, processes such as wind speed, turbulence, dilution and Van der Waals forces affect coagulation efficiencies. On the one hand, this could result in rapid formation of big agglomerates, which significantly reduce the stratospheric residence time as well as the backscattering efficiencies of the particles. On the other hand, particles could spend more time as monomers if collision speeds in the turbulent plume overcome the large Van der Waals forces of small particles. This limitation poses major uncertainty to the results presented here and they can only be addressed via injection plume modelling at the sub-grid scale or small scale field experiments such as proposed in Dykema et al. (2014).

With this study, we have shown that our model can be a useful tool to explore risks and benefits of SAI of solid particles. However, the results are still uncertain due to a number

of limitations, such as lack of experimental data needed to refine the parameterizations of microphysical processes and heterogeneous chemistry. Given this model uncertainty, it is presently unclear whether SAI of alumina and calcite particles would result in smaller or larger adverse side effects compared to sulfur-based SAI. This is in contrast to (Arias et al., 2021, IPCC, AR6, WG1, Chapter 4, Page 629 ) which states: "Injection of non-sulphate aerosols is likely to result in less stratospheric heating and ozone loss", but more in alignment with what was stated on SAI of solid particles in the latest ozone assessment report (WMO, 2022), which highlights uncertainties.

## Data Availability

The model code of SOCOL-AERv2 incorporating the presented solid particle microphysics scheme is available in Vattioni (2023b) and the simulation data presented in this study is available in Vattioni (2024a).

## Author contributions

SV wrote the paper draft, created most of the figures, developed the model, tested the model and did the data analysis. RW performed some of the simulations, provided support with data analysis and created some of the figures. AF and AS contributed to model development as well as debugging and sanity checking of the model code. JAD performed the Mie-calculations to get the optical properties for alumina and calcite particles and their agglomerates. BL helped with the implementation of microphysics such as the contact angle on solid particles as well as implementation of optical properties. GAK and CAB run the DEM to determine the mobility radius of alumina and calcite particles and all authors contributed to the discussion of the results.

## Acknowledgements

We especially thank Debra Weisenstein for discussions about her original solid particle AER code as well as David Keith for valuable discussion of our results. We also thank Claudia Marcolli for bringing up the idea of representing the sulfuric acid coating on alumina particles by accounting for the contact angle. Support for Gabriel Chiodo and Andrea Stenke was provided by the Swiss Science Foundation within the Ambizione grant no. PZ00P2\_180043. Support for Sandro Vattioni was provided by the ETH Research grant no. ETH-1719-2 as well as by the Harvard Geoengineering Research Program. JD was also supported by the Harvard Solar Geoengineering Research Program. Timofei Sukhodolov acknowledges the support from the Swiss National Science Foundation (grant no. 200020-182239) and the Karbacher Fonds, Graubünden, Switzerland. GAK and CAB acknowledge the support from the Particle Technology Laboratory, ETH Zurich and, in part, the Swiss National Science Foundation (grant no. 200020\_182668, 250320\_163243 and 206021\_170729).

## Appendix 3: Supplementary information

### A: Discrete Element Model simulations

We have performed DEM simulations to quantify the resulting mobility radius of the agglomerates represented in the solid particle microphysics scheme. The model (Kelesidis and Kholghy, 2021) was run under a initial concentrations spanning 5 to 6 orders of magnitude with primary particle radius of 5 nm, 80 nm and 215 nm for alumina particles and 5 nm, 80 nm and 275 nm for calcite particles (see Figure 3.12). We assumed that a global injection rate of 5 Mt/yr could be achieved with 200 airplane flights per day, each with a flight distance of 1000 km in the stratosphere and by assuming each airplane injecting a total of 69 t of particles from two injectors of which both have a square area of 1 m<sup>2</sup>. This would result in an initial concentration of about  $2 \times 10^{13}$  particles per cm<sup>3</sup> when injecting 5 nm particles,  $4 \times 10^{12}$  particles per cm<sup>3</sup> when injecting particles at a primary radius of 80 nm and about  $1 \times 10^8$  particles per cm<sup>3</sup> when injecting particles at a radius of 240 nm. Figure 3.12 shows the resulting number concentration as a function of time, while the DEM did not account for dilution of the air parcel with time, which would additionally reduce the resulting number density with time significantly. Since the simulations run for a fixed amount of computational time, the simulations with lower initial concentrations and larger primary radius and thus less coagulation resulted in simulation of a longer time period. The resulting size distribution at the end of each simulation is shown in Figure 3.13. Most initial concentrations for alumina particles of radius 215 nm and calcite particles of radius 275 nm result in size distributions peaking at agglomerates of  $10^1$  to  $10^3$  monomers per agglomerate, which would result in significantly decreased back scatter efficiencies and increased sedimentation rates for injection of alumina particles with radius of 215 nm and calcite particles with radius of 275 nm particles. At this injection radii, only the lowest initial concentration of  $10^5$  particles per cm<sup>3</sup> would result in 20% of the alumina particles and about 50% of the calcite particles remaining as monomers. This initial concentration is 3 orders of magnitudes less than the initial assumption derived from injection of 200 airplane flights per day stated above. It is still an open question whether taking into account dilution of air would reduce the formation of larger agglomerates for 80 nm particle injection and 215 nm or 275 nm particle injection to a level, which does not result in agglomerates with significantly reduced back scatter efficiency or significantly increased sedimentation speeds.

Figure 3.14 shows the mobility radius of the agglomerates resulting from the DEM simulations. The resulting radii are slightly larger compared to the coated alumina particles assuming a fractal dimension of 2.6 in (Weisenstein et al., 2015, see their equation 1) and significantly smaller compared to their pure alumina radii with fractal dimension of 1.6.



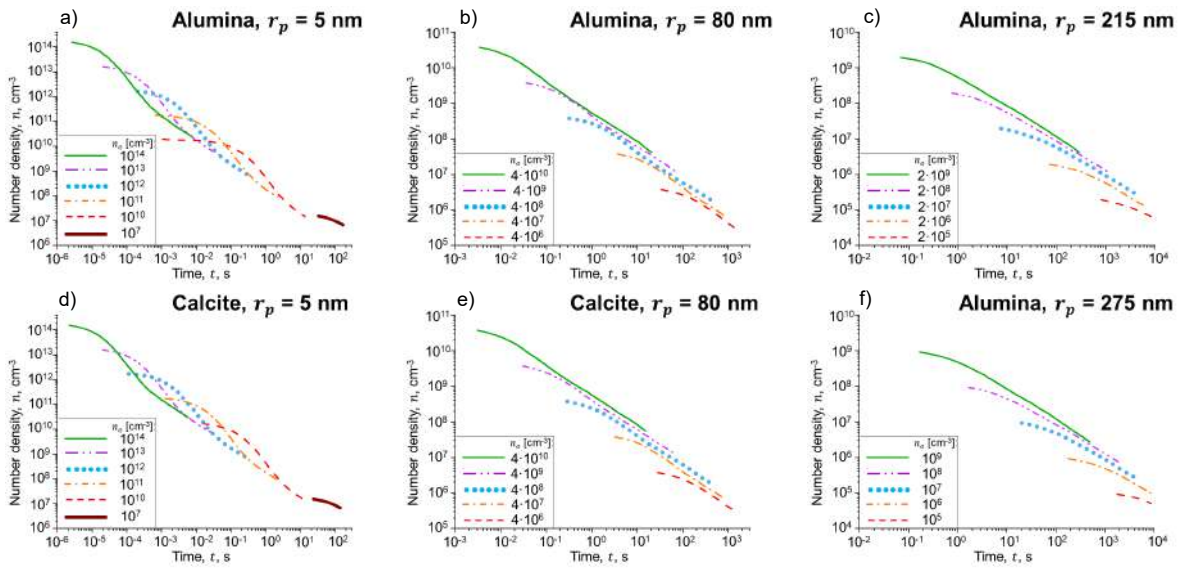


Figure 3.12: The evolution of the total particle number density as a function of time assuming different initial number concentrations of particles with radii of 5 nm (a and d), 80 nm (b and e) as well as 215 nm (for alumina, c) and 275 nm (for calcite, f) simulated with a DEM (Kelesidis et al., 2021).

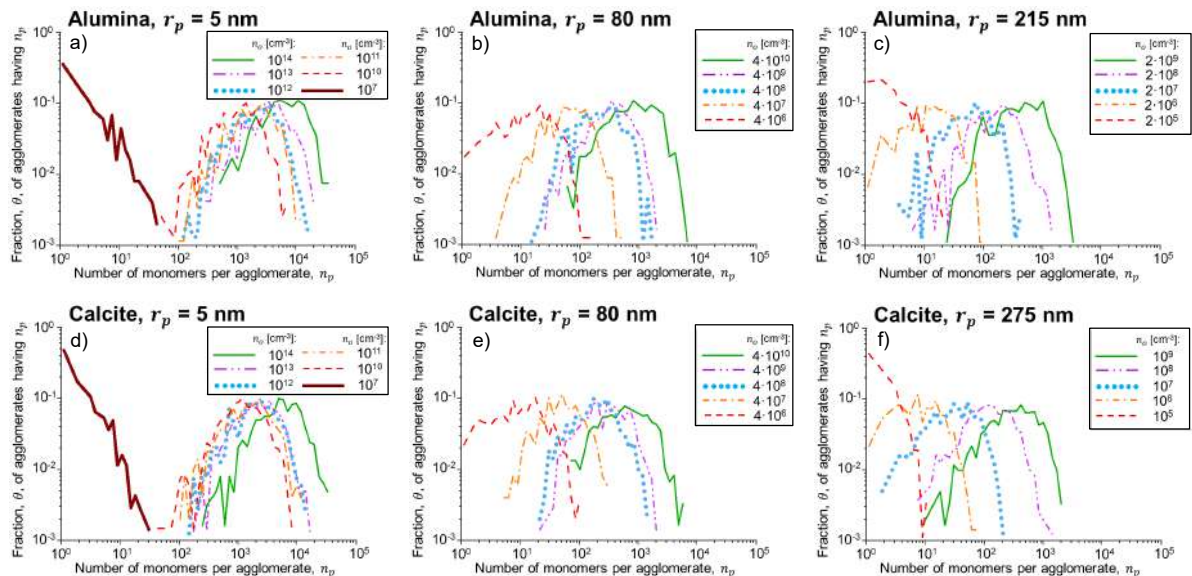


Figure 3.13: The resulting size distribution at the end of the simulations resulting from coagulation with different initial concentrations of particles with radii of 5 nm (a and d), 80 nm (b and e) as well as 215 nm (for alumina, c) and 275 nm (for calcite, f) simulated with a DEM (Kelesidis et al., 2021). Depicted size distribution are the one resulting at the end of the simulations shown in Figure 3.12. The model does not account for dilution, which would reduce the number densities with time.

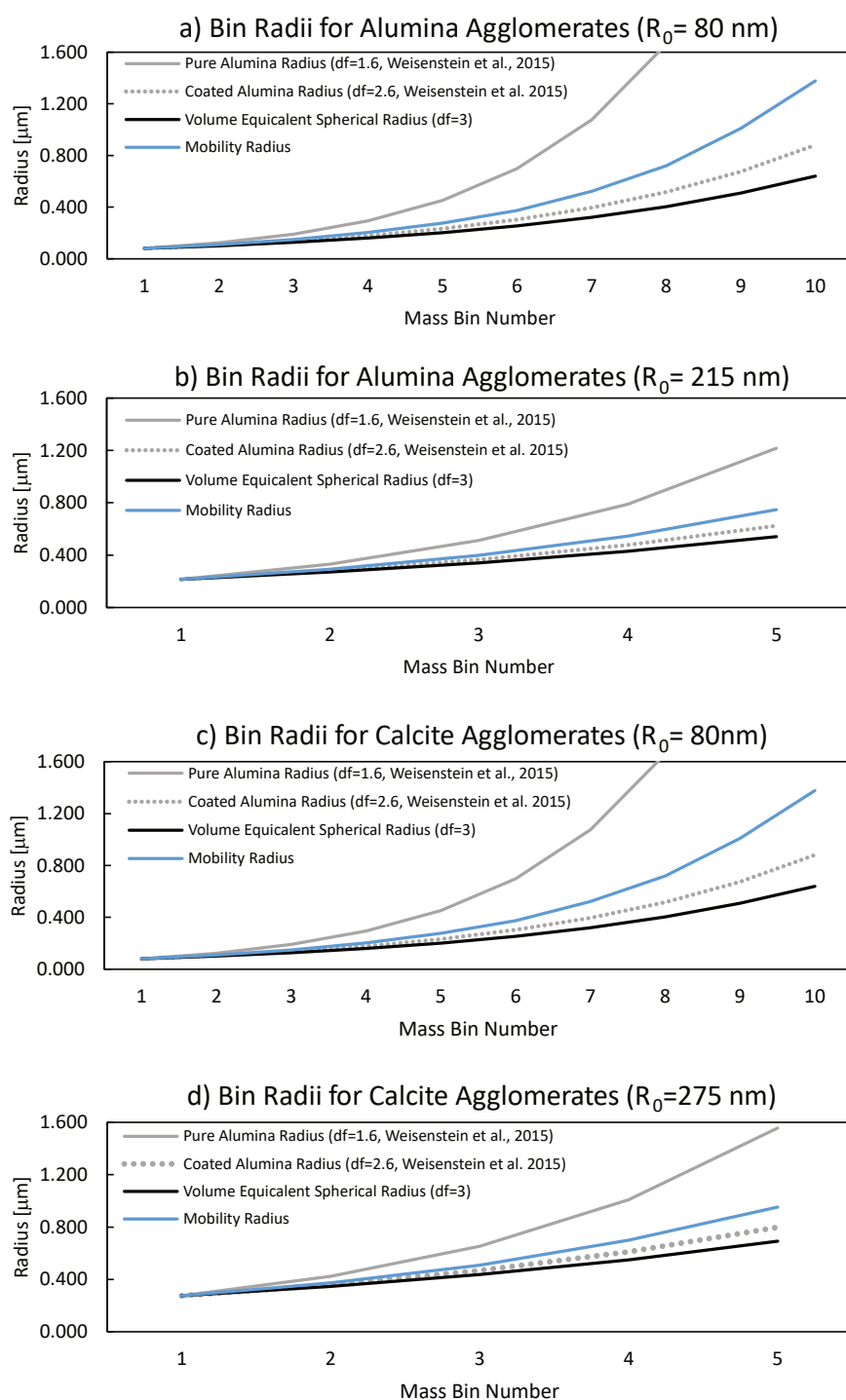


Figure 3.14: Different radii for the agglomerates of primary particle radius of 80 nm (a) and 215 nm (b) for alumina particles as well as of 80 nm (c) and 275 nm (d) for calcite particles. Shown are calculated agglomerate radii applied in (Weisenstein et al., 2015, see their equation 1) with fractal dimensions of 1.6 for their bare alumina particles (gray solid line) and 2.6 for their coated alumina particles (grey stippled line), the resulting mobility radii from the DEM simulations (blue), which are used in this study, as well as the volume equivalent radii (black) for reference.

## B: Sedimentation velocities in SOCOL-AERv2

The resulting calculated aerosol sedimentation velocities in SOCOL-AERv2 are slightly smaller than in Weisenstein et al. (2015), but compare generally well within the stratosphere (see Figure 3.15), while some deviations occur in the troposphere which might be due the three dimensional resolution of the dynamics in SOCOL-AERv2 compared to 2D-AER.

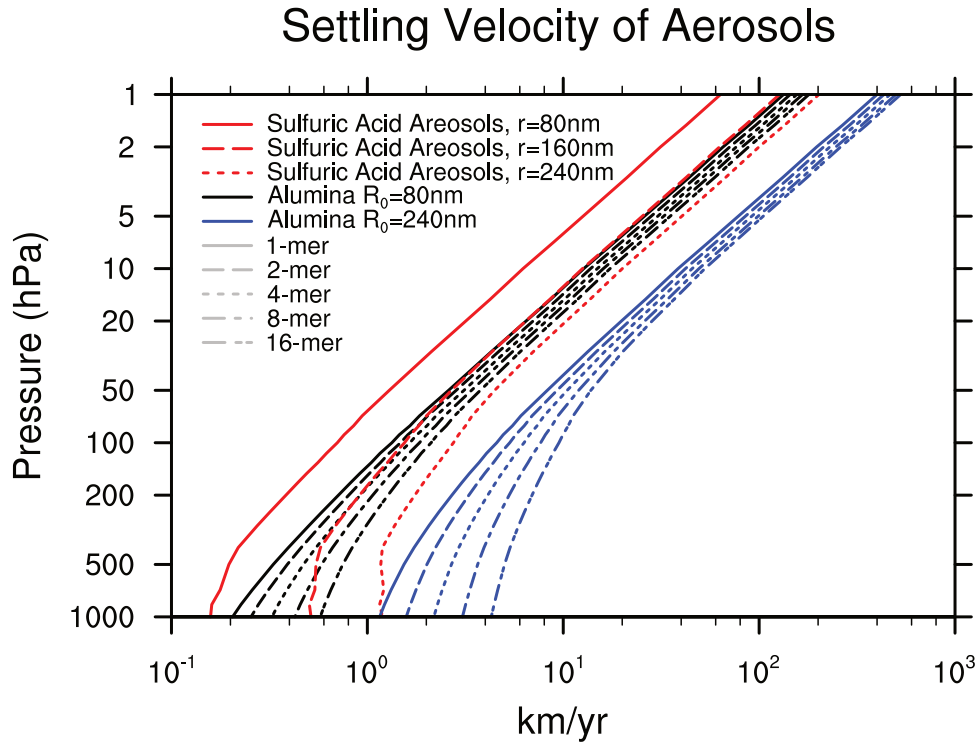


Figure 3.15: The sedimentation velocities calculated by SOCOL-AERv2 with equation 3.4 in the main text zonally averaged between  $15^\circ\text{N}$  and  $15^\circ\text{S}$  over 15 years.

## C: Optical Properties used in SOCOL-AERv2

Figure 3.16 shows the absorption cross sections ( $\sigma_{\text{abs}}$ ) for all spectral bands as well as the scattering cross section ( $\sigma_{\text{sca}}$ ) and the asymmetry factors ( $g_{\text{asy}}$ ) for the shortwave (SW) bands of SOCOL-AERv2 for alumina and calcite particles as well as for 70 wt%  $\text{H}_2\text{SO}_4$  aerosols of monomer radii of 80 nm, 160 nm, 240 nm and 320 nm. To get the absorption and scattering cross sections, the scattering and absorption efficiencies ( $Q_{\text{abs}}$  and  $Q_{\text{sca}}$ ), which were derived from Mie theorie (Mätzler, 2002; Rannou et al., 1999), were multiplied with  $r_{\text{ve},i}^2$  (see Section "Radiation" in the main text). Calcite particles show a relatively large absorption in the visible and UV wavelengths, whereas sulfuric acid and alumina particles only absorb little SW radiation (Figure 3.16a). In the longwave (LW) bands, sulfuric acid is showing the largest absorption except for the bands  $700\text{-}800\text{ cm}^{-1}$  and  $1390\text{-}1480\text{ cm}^{-1}$  where alumina and calcite particles absorb more LW radiation, respectively compared to sulfuric acid aerosols. While the absorption peak for alumina is at the edge of the  $\text{CO}_2$  absorption band ( $\sim 7\text{ }\mu\text{m}$ ) close to the atmospheric window of outgoing LW radiation, the peak for the calcite particles is in the tail of the outgoing LW radiation spectra within the water absorption band where outgoing LW radiation is absorbed anyway ( $\sim 13.3\text{ }\mu\text{m}$ ). Therefore, SAI of alumina particles is likely resulting in more stratospheric warming compared to calcite particles. Figure 3.17 shows the optical properties derived with the semi-empirical code from Rannou et al. (1999) fed into SOCOL-AERv2 for agglomerates. The absorption cross sections in Figure 3.16 and 3.17 are largest for 80 nm particles and monomers, respectively. However, this is only valid on a per particle basis. Normalized per mass the particles would all show similar absorption coefficients since absorption is proportional to mass. The scattering cross section (Figure 3.16d) is largest for 320 nm particles and lowest for 80 nm particles. However, 320 nm particles also result in smallest stratospheric aerosol burden since they sediment faster. The asymmetry factor (Figure 3.16b) is also generally largest for 320 nm particles and sulfuric acid aerosols in the visible band between 440 nm and 690 nm and lowest for alumina particles. A large asymmetry factor stands for a large forward scattering fraction. The larger the agglomerate the larger the scattering cross section and the larger the asymmetry factor, which results in more forward scattering.

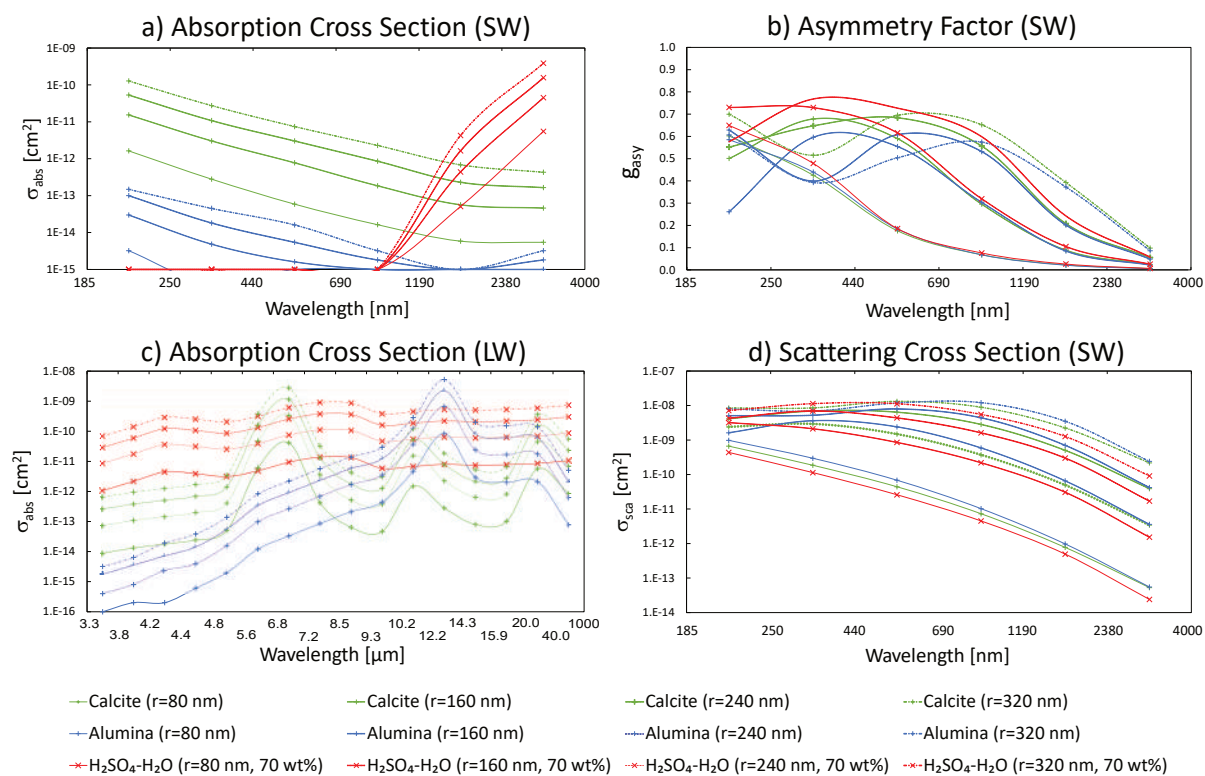


Figure 3.16: Shown are the absorption cross section for the SW bands (a), the asymmetry factor for the SW bands (b), the absorption cross section of the LW bands (c) as well as the scattering cross section for the SW bands (d) for alumina and calcite monomers with primary radius of 80 nm, 160 nm, 240 nm and 320 nm. The optical properties were derived with the code of Mätzler (2002). As a reference, the optical properties for sulfuric acid aerosols used in SOCOL-AERv2, which are based on Yue et al. (1994) and Biermann et al. (1996) are also shown for aerosols with 70 wt% sulfuric acid.

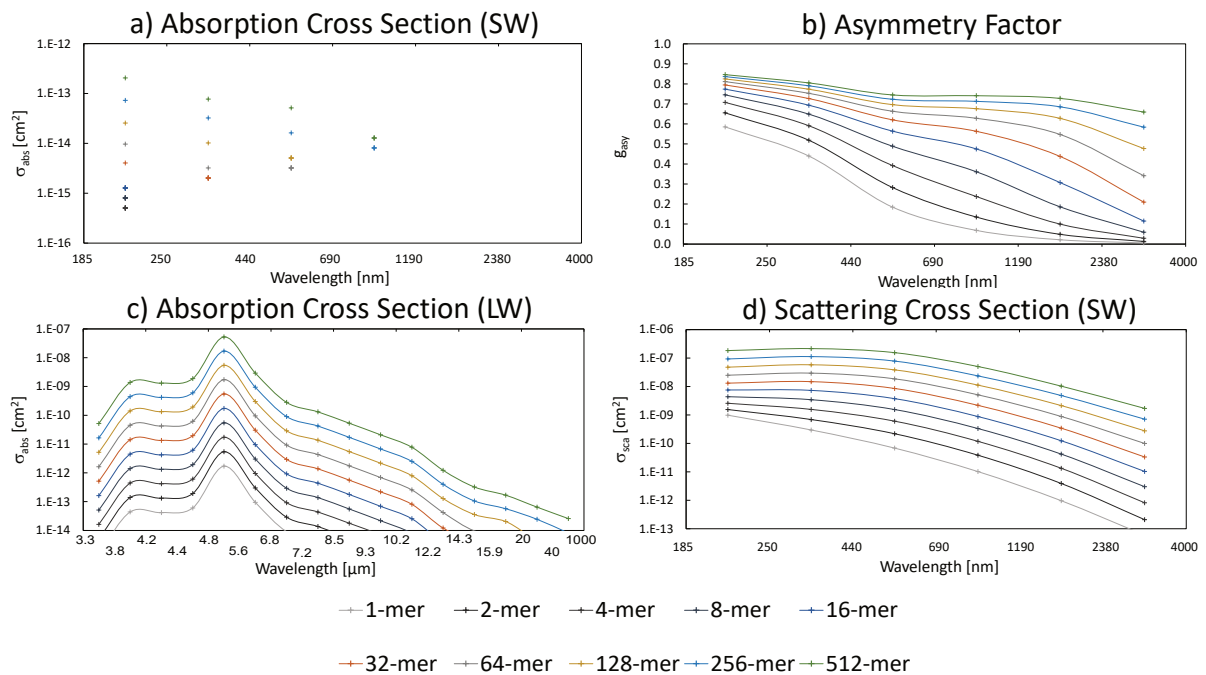


Figure 3.17: Shown are the optical properties of alumina particles with 80 nm primary radius as well as of the corresponding agglomerates up to 512-mers implemented in SOCOL-AERv2. Optical properties for agglomerates were derived using the semi-empirical code of Rannou et al. (1999). Shown are the absorption cross section for the SW bands (a), the asymmetry factor for the SW bands (b), the absorption cross section of the LW bands (c) as well as the scattering cross section for the SW bands (d).

## D: Stratospheric aerosol size distributions

The stratospheric aerosol size distribution for the injection scenarios of 5 Mt/yr calcite particles ( $r=240$  nm), alumina particles ( $r=240$  nm),  $\text{SO}_2$ , and  $\text{AM-H}_2\text{SO}_4$  ( $r=0.95$   $\mu\text{m}$  and  $\sigma=1.5$ ). The size distributions clearly indicate a decrease in sulfuric acid particle concentrations in the solid particle injection scenarios. The calcite particles result in slightly larger agglomeration due to larger stratospheric aerosol burden and a smaller density which makes coagulation more efficient compared to alumina particle emission. It can also be seen that the sulfuric acid aerosol size distributions resulting from  $\text{AM-H}_2\text{SO}_4$  result in larger number concentrations between  $0.1$   $\mu\text{m}$  and  $0.2$   $\mu\text{m}$  radius, which explains the larger net TOA radiative forcing despite the slightly lower stratospheric aerosol burden (see Figure 4 in the main text).

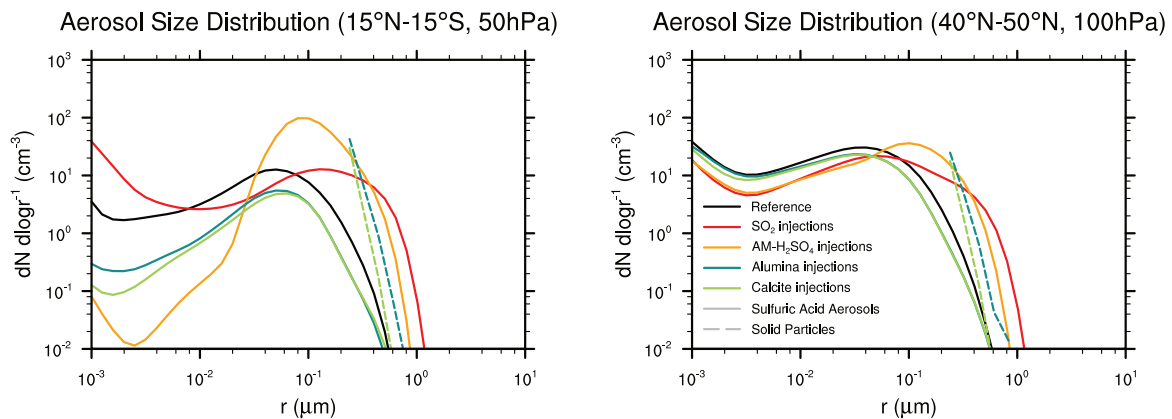


Figure 3.18: The resulting aerosol size distribution averaged between  $15^\circ\text{N}$  and  $15^\circ\text{S}$  at 50 hPa altitude (a) and between  $40^\circ\text{N}$  and  $50^\circ\text{N}$  at 100 hPa altitude (b). Solid lines show the sulfuric acid aerosol size distribution and dashed lines the solid particle size distributions for the 5 Mt/yr injection scenarios as well as the reference simulation (black).

### E: The stratospheric sulphur cycle under different alumina injection rates

Figure 3.19 shows the stratospheric sulfur cycle response to injection of alumina particles with radii of 240 nm at different injection rates. The response of the stratospheric sulfur cycle is proportional to the available solid particle surface area density (SAD), which increases for larger injection rates. Therefore the response of the stratospheric sulfur cycle when increasing the injection rate while keeping the alumina particle radius constant is the same as when decreasing the particle radius at constant injection rate (see Figure 6 in the main text). Figure 3.20 shows the corresponding sulfuric acid coating thickness if the sulfuric acid was distributed equally on the alumina particles. If the aerosol burden is very small (i.e., 1 Mt/yr in Figure 3.20a) the coating thickness could be up to 44 nm in the lower stratosphere, whereas the thickness would only be 2-4 nm for injection of 25 Mt/yr of alumina particles with radii of 240 nm.

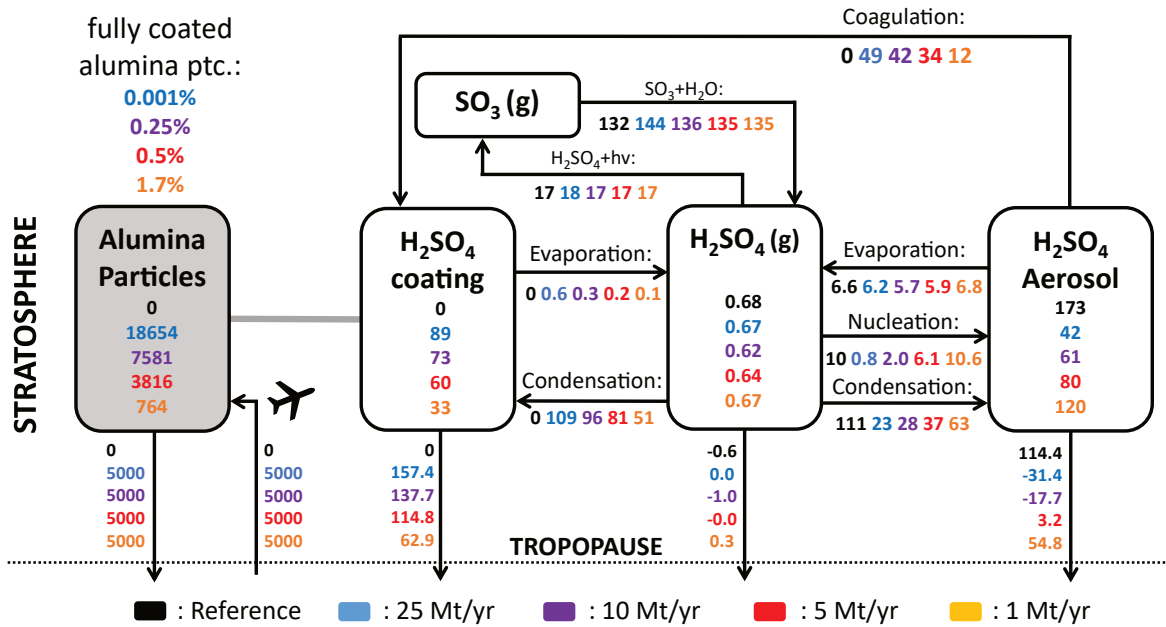


Figure 3.19: The stratospheric sulfur cycle under conditions of SAI with particles at radii of 240 nm and injection rates of 25 Mt/yr (blue), 10 Mt/yr (violet), 5 Mt/yr (red) and 1 Mt/yr (orange). All sulfur species are shown in Gg Sulfur for burden (boxes) and Gg Sulfur per year for net fluxes (arrows). The alumina burden (gray box) is given as Gg  $\text{Al}_2\text{O}_3$  and Gg  $\text{Al}_2\text{O}_3$  per year. Net cross tropopause fluxes are calculated by balancing the stratospheric mass fluxes of the individual species.



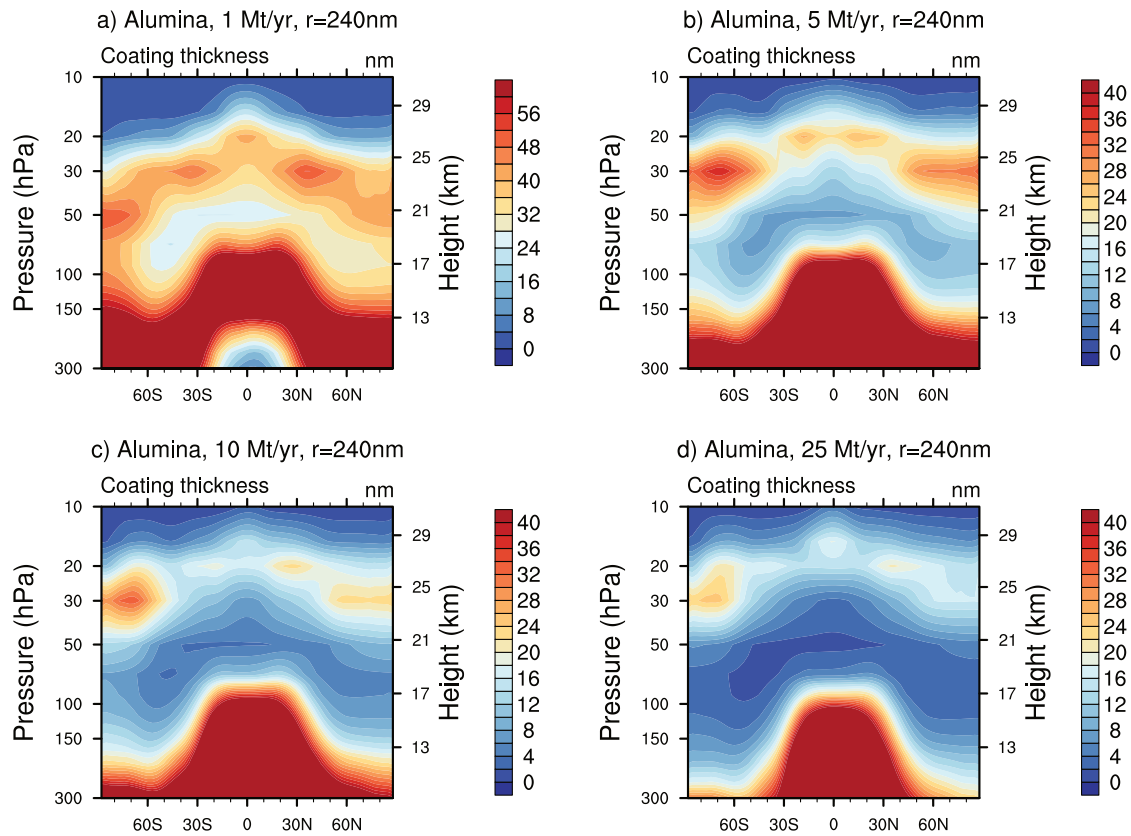


Figure 3.20: The resulting coating thickness when injecting alumina particles with radii of 240 nm at 1 Mt/yr (a), 5 Mt/yr (b), 10 Mt/yr (c) and 25 Mt/yr (d). The values listed above correspond to the average coating thickness of the mass bin with the largest coating thickness, which is at the same time also the mass bin with the largest share of alumina burden (bin 1 for all scenarios). Other mass bin have smaller coating thicknesses.

## F: The stratospheric sulphur cycle under different calcite injection rates

Figure 3.21 shows the response of the stratospheric sulfur cycle to different injection rates of calcite particles. The response of the stratospheric sulfur cycle is proportional to the available solid particle SAD, which increases for larger injection rates. Therefore the response of the stratospheric sulfur cycle when increasing the calcite particle injection rate while keeping the radius constant is the same as for decreasing the particle radius at constant injection rate (see Figure 9 in the main text). The larger the available solid particle SAD the larger the uptake of  $\text{H}_2\text{SO}_4$ ,  $\text{HCl}$  and  $\text{HNO}_3$ .

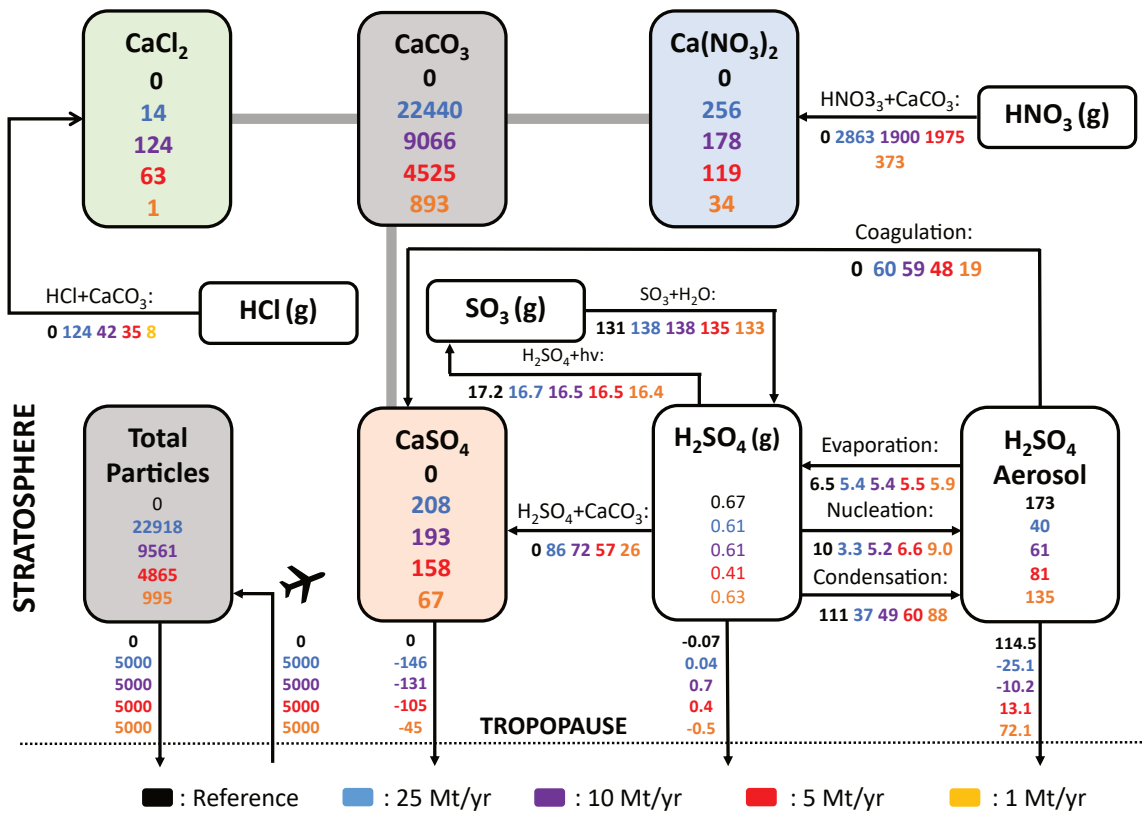


Figure 3.21: The stratospheric sulfur cycle under conditions of SAI of calcite particles with radii of 240nm and injection rates of 25 Mt/yr (blue), 10 Mt/yr (violet), 5 Mt/yr (red) and 1 Mt/yr (orange). All sulfur species (except  $\text{CaSO}_4$ ) are shown in Gg Sulrur for burden (boxes) and Gg Sulrur per year for net fluxes (arrows). The solid species (colored boxes) are given in Gg of the corresponding material. The  $\text{HNO}_3$  and  $\text{HCl}$  flux to  $\text{Ca(NO}_3)_2$  and  $\text{CaCl}_2$  are given in Gg  $\text{HNO}_3$  per year and Gg  $\text{HCl}$  per year. Cross tropopause fluxes are calculated by balancing the mass balance of the individual species.

## G: Number concentrations and surface area densities for calcite particles

Figure 3.22 shows the resulting number concentrations and the resulting calcite SAD for various calcite injection scenarios. As resulting stratospheric aerosol burden for calcite particle injections are about 25% larger for compared to alumina particle injection, also the resulting number concentrations and solid particle SAD are larger. Figure 10 in the main text shows the corresponding figure for alumina particles.

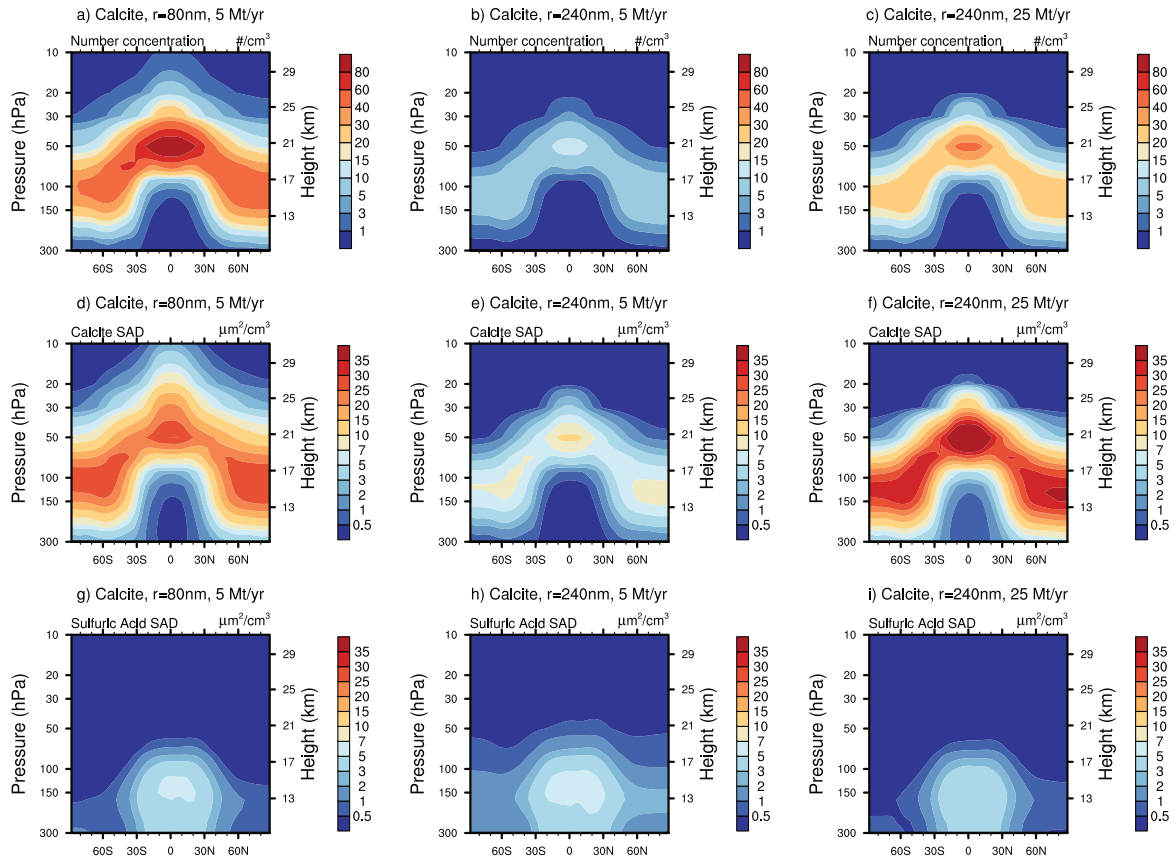


Figure 3.22: The resulting zonal mean number densities (a-c), calcite SAD (d-f) and sulfuric acid SAD (g-i) from injection of 5 Mt/yr of particles with 80 nm (a,d,f), 5 Mt/yr of particles with 240 nm particles (b,e,h) and 25 Mt/yr of particles with 240 nm radius (c,f,i).



## Chapter 4

# Chemical impact of stratospheric alumina particle injection for solar radiation modification and related uncertainties

### Abstract

Compared to stratospheric SO<sub>2</sub> injection for climate intervention, alumina particle injection could reduce stratospheric warming and associated adverse impacts. However, heterogeneous chemistry on alumina particles, especially chlorine activation via ClONO<sub>2</sub> + HCl  $\xrightarrow{\text{surf}}$  Cl<sub>2</sub> + HNO<sub>3</sub>, is poorly constrained under stratospheric conditions, such as low temperature and humidity. This study quantifies the uncertainty in modelling the ozone response to alumina injection. We show that extrapolating the limited experimental data for ClONO<sub>2</sub> + HCl to stratospheric conditions leads to uncertainties in heterogeneous reaction rates of almost two orders of magnitude. Implementation of injection of 5 Mt/yr of particles with 240 nm radius in an aerosol-chemistry-climate model shows that resulting global total ozone depletions range between negligible and as large as 9%, i.e., more than twice the loss caused by chlorofluorocarbons, depending on assumptions on the degree of dissociation and interaction of the acids HCl, HNO<sub>3</sub> and H<sub>2</sub>SO<sub>4</sub> on the alumina surface.

### This chapter was published as a research paper:

Vattioni, S., Luo, B., Feinberg, A., Stenke, A., Vockenhuber, C., Weber, R., Dykema, J. A., Krieger, U. A., Ammann, M., Keutsch, F. N., Peter, T., Chiodo, G. (2023). Chemical impact of stratospheric alumina particle injection for solar radiation modification and related uncertainties. **Geophysical Research Letters**, 50, e2023GL105889. <https://doi.org/10.1029/2023GL105889>

## 4.1 Introduction

Since preindustrial times, atmospheric greenhouse gas (GHG) concentrations have risen to levels never before experienced by humankind, with negative consequences for the environment and society (Arias et al., 2021; Jouzel, 2013). Even if society succeeded in rapidly ceasing emissions, global warming and its impacts would linger for millennia as carbon dioxide removal techniques may not prove efficient or may not be scaled up fast enough (NRC, 2015; Clark et al., 2016). These prospects have motivated proposals for stratospheric aerosol injection (SAI) as an affordable intervention strategy that could provide immediate cooling to counteract some of the impacts of climate change (Budyko, 1977; Crutzen, 2006). SAI could potentially serve as a temporary supplement to measures that actually address the cause of climate change, such as GHG mitigation and adaptation, until society finds solutions on how to remove long-lived GHGs from the atmosphere (MacMartin et al., 2014; Keith and MacMartin, 2015). It has been proposed that SAI might help to limit global warming to 1.5°C, the target set by the Paris Agreement in 2015 (MacMartin et al., 2018). However, despite potential benefits of SAI there are large uncertainties about risks associated with negative side effects, for example its impact on stratospheric chemistry (e.g., Robock, 2008).

Until now, most research on SAI has focused on SO<sub>2</sub> as the injected species, motivated by the observed cooling after explosive volcanic eruptions, such as Mt. Pinatubo in 1991 (Bluth et al., 1992; Wilson et al., 1993). Sulfuric acid aerosols are formed after the oxidation of SO<sub>2</sub> in the stratosphere. However, SAI by sulfuric acid aerosols bears several limitations, including optically inefficient aerosol size distributions (Vattioni et al., 2019), stratospheric ozone depletion (Tilmes et al., 2008; Vattioni et al., 2019; Weisenstein et al., 2022) and stratospheric heating (Aquila et al., 2014; Dykema et al., 2016). This has repercussions for global atmospheric dynamics potentially with additional feedbacks on stratospheric chemistry.

Recent studies have shown that the injection of solid particles, such as alumina (Al<sub>2</sub>O<sub>3</sub>), calcite (CaCO<sub>3</sub>) or diamond (C) particles might reduce some of the limitations of sulfuric acid-based SAI (Ferraro et al., 2011; Pope et al., 2012; Weisenstein et al., 2015; Keith et al., 2016; Dykema et al., 2016). In particular, it has been suggested that the optical properties of some of these materials would result in smaller stratospheric heating because of less absorption of infrared radiation and more efficient backscattering of solar radiation per stratospheric aerosol burden than SAI by sulfuric acid aerosols (Dykema et al., 2016). In addition, it has been suggested that solid particles such as alumina or calcite could result in reduced ozone depletion compared to SAI by sulfuric acid aerosols (Weisenstein et al., 2015; Keith et al., 2016; WMO, 2022). Based on these lines of evidence, the IPCC-AR6 inferred that injection of non-sulphate aerosols is likely to result in less stratospheric heating and ozone loss (Arias et al., 2021). However, previous studies are based on simplifying assumptions about particle reactivity under stratospheric conditions, due to lack of experimental data. Therefore, uncertainties remain high regarding SAI of solid particles, especially concerning their impact on stratospheric ozone.

### 4.1.1 Aging and non-aging solid particles

There is only limited knowledge about the physical chemistry of solid particles under stratospheric conditions, especially with respect to temperature (< 220 K), relative humidity (< 1%), interactions with stratospheric chemical species, and UV irradiation. The

various materials under consideration can be divided into two categories. On the one hand, solids such as calcite ( $\text{CaCO}_3$ ) particles that are expected to undergo “chemical aging” during their stratospheric residence time of about one year (Dai et al., 2020; Huynh and McNeill, 2021). On the other hand, solids such as alumina ( $\text{Al}_2\text{O}_3$ ), which are not expected to undergo significant chemical aging. For example, in the first category, calcite particles could change their composition and crystalline structure upon reaction with the stratospheric acids  $\text{H}_2\text{SO}_4$ ,  $\text{HNO}_3$  or  $\text{HCl}$ , which is likely to affect their optical and chemical properties (Keith et al., 2016). In the second category, alumina will likely not react with stratospheric gases, but a thin  $\text{H}_2\text{SO}_4$ - $\text{H}_2\text{O}$  coating, partially or fully covering the particles, may result from  $\text{H}_2\text{SO}_4$ - $\text{H}_2\text{O}$  co-condensation and coagulation with stratospheric background aerosol particles (see also Weisenstein et al., 2015). While the inertness of alumina significantly reduces uncertainties of particle evolution under stratospheric conditions compared to solid particles with chemical aging, it is at present uncertain whether “non-aging” particle surfaces may host heterogeneous chemistry of trace gases such as  $\text{HCl}$ ,  $\text{ClONO}_2$ ,  $\text{HNO}_3$  and  $\text{H}_2\text{SO}_4$ . The lack of experimental data makes it difficult to quantify surface processes and heterogeneous reactions on solid particles as a function of temperature, relative humidity, and material properties, like hydrophilicity, under stratospheric conditions.

### 4.1.2 Experimental data on heterogeneous chemistry on alumina particles

Molina et al. (1997) demonstrated that alumina may provide the surface for heterogeneous surface reaction 4.1 (reaction 4.1), which contributes to stratospheric chlorine activation:



$\text{HCl}$  and  $\text{ClONO}_2$  are important reservoir species of stratospheric chlorine and nitrogen oxides,  $\text{ClO}_x$  and  $\text{NO}_x$ , which destroy ozone catalytically. Thus, solid particles can provide surfaces for heterogeneous chlorine activation reactions, which may result in significant ozone loss (after  $\text{Cl}_2$  photolysis). Molina et al. (1997) provide the only experimental study investigating reaction 4.1 on alumina surfaces at stratospheric temperatures. They performed flow tube measurements of reaction 4.1 and found a reaction probability  $\gamma_{\text{ClONO}_2} \approx 0.02$  for temperatures ranging from 208 K to 223 K and  $\text{HCl}$  concentrations ranging from  $4.5 \times 10^{-7}$  to  $1.7 \times 10^{-6}$  hPa (corresponding to 9-35 ppb at 50 hPa, i.e., at about 20 km altitude, Figure 4.1). Their study aimed at quantifying the impact of space shuttle exhaust, which contains alumina,  $\text{HCl}$  and water (Potter, 1978). Therefore, Molina et al. (1997) used  $\text{HCl}$  with concentrations one order of magnitude higher than typical stratospheric volume mixing ratios (1-2 ppb at 50 hPa under present day conditions). Appendix 4B provides more details on their measurement conditions. We extrapolate these measured reaction probabilities to  $\text{HCl}$  partial pressures representative of the present-day stratosphere by using a Langmuir-Hinshelwood molecular description of co-adsorption/desorption and reaction (e.g., Tabazadeh and Turco, 1993; Carslaw and Peter, 1997; Aguzzi and Rossi, 2001; Fernandez et al., 2005). This requires knowledge of the temperature dependent second order rate coefficient of reaction 4.1 and the Langmuir constants (i.e., the ratio of forward reaction constant for adsorption over backward reaction constant for desorption) for  $\text{ClONO}_2$  and  $\text{HCl}$  on alumina particles, which cannot be directly retrieved from the Molina et al. (1997) measurements. Therefore, extrapolation

to typical stratospheric partial pressures of HCl is subject to large uncertainty, which we will quantify in this study.

### 4.1.3 Previous modeling studies on SAI of alumina particles

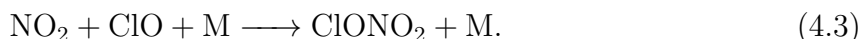
Using a 2D-aerosol chemistry climate model, Weisenstein et al. (2015) were the first to study alumina particles for SAI. In their scenario, which resulted in the smallest ozone depletion in relation to the achieved radiative forcing, 4 Mt/yr of alumina particles with a radius of 240 nm were injected. This simulation resulted in a globally averaged clear sky shortwave radiative forcing of  $-1.2 \text{ W/m}^2$  and globally averaged depletion of the total ozone column of 3.4% with values of up to 7% over the poles assuming present day concentrations of ozone depleting substances (ODS).

Weisenstein et al. (2015) distinguished between bare alumina particles and alumina particles which acquired a sulfuric acid coating due to gaseous  $\text{H}_2\text{SO}_4$  adsorption or coagulation with sulfuric acid particles. They estimated that 70-92% of the alumina surface area density (SAD) would be  $\text{H}_2\text{SO}_4$ -coated and applied the same heterogeneous chemistry as for aqueous  $\text{H}_2\text{SO}_4$  aerosols. Conversely, only 8-30% of the total resulting SAD increase in the lower stratosphere was treated as bare alumina SAD for reaction 4.1 with  $\gamma_{\text{ClONO}_2} = 0.02$ . Extrapolation to HCl partial pressures was done by scaling  $\gamma_{\text{ClONO}_2}$  with the logarithm of the ratio  $[\text{HCl}]/[\text{ClONO}_2]$ , an ad-hoc assumption which quenches reaction 4.1 for very small  $[\text{HCl}]$ , but is hard to justify physically or in view of Molina et al. (1997) measurements (see also Appendix 4C).

On aqueous sulfuric acid aerosol and on the  $\text{H}_2\text{SO}_4$ -coated fraction of the alumina surface, the  $\text{N}_2\text{O}_5$  hydrolysis (reaction 4.2)



is the most important heterogeneous reaction. Reaction 4.2 removes active nitrogen from the  $\text{NO}_x$ -induced ozone-depletion cycle and, thus, also weakens deactivation of  $\text{ClO}_X$  via



Therefore, in the present chlorine-rich stratosphere reaction 4.2 results in increased ozone destruction, albeit to a lesser degree than the direct chlorine activation via reaction 4.1. The estimates of Weisenstein et al. (2015) are subject to large uncertainties, mainly due to two factors, which both, will be addresses in this paper: (i) how they extrapolated the Molina et al. (1997) measurements of reaction 4.1 to present-day stratospheric HCl concentrations; (ii) their assumption on SAD availability of bare vs.  $\text{H}_2\text{SO}_4$ -coated alumina. In reality, the situation is more complex. Bare alumina particles injected into the stratosphere would immediately be subject to adsorption of stratospheric trace gas molecules  $\text{HNO}_3$ ,  $\text{H}_2\text{SO}_{4(\text{g})}$ , HCl,  $\text{ClONO}_2$ , and coagulation with  $\text{H}_2\text{SO}_{4(\text{aq})}$ . Except for  $\text{H}_2\text{SO}_{4(\text{g})}$ , these gases are present at ppb mixing ratios, so their collision frequency with the surfaces would be sufficient to establish a molecular monolayer within a few minutes. However, this neglects desorption and given the low partial pressure of these gases it is unlikely that the coverage would exceed a small fraction of a monolayer. In contrast, even though  $\text{H}_2\text{SO}_4$  has mixing ratios several orders of magnitude lower, it is the only trace



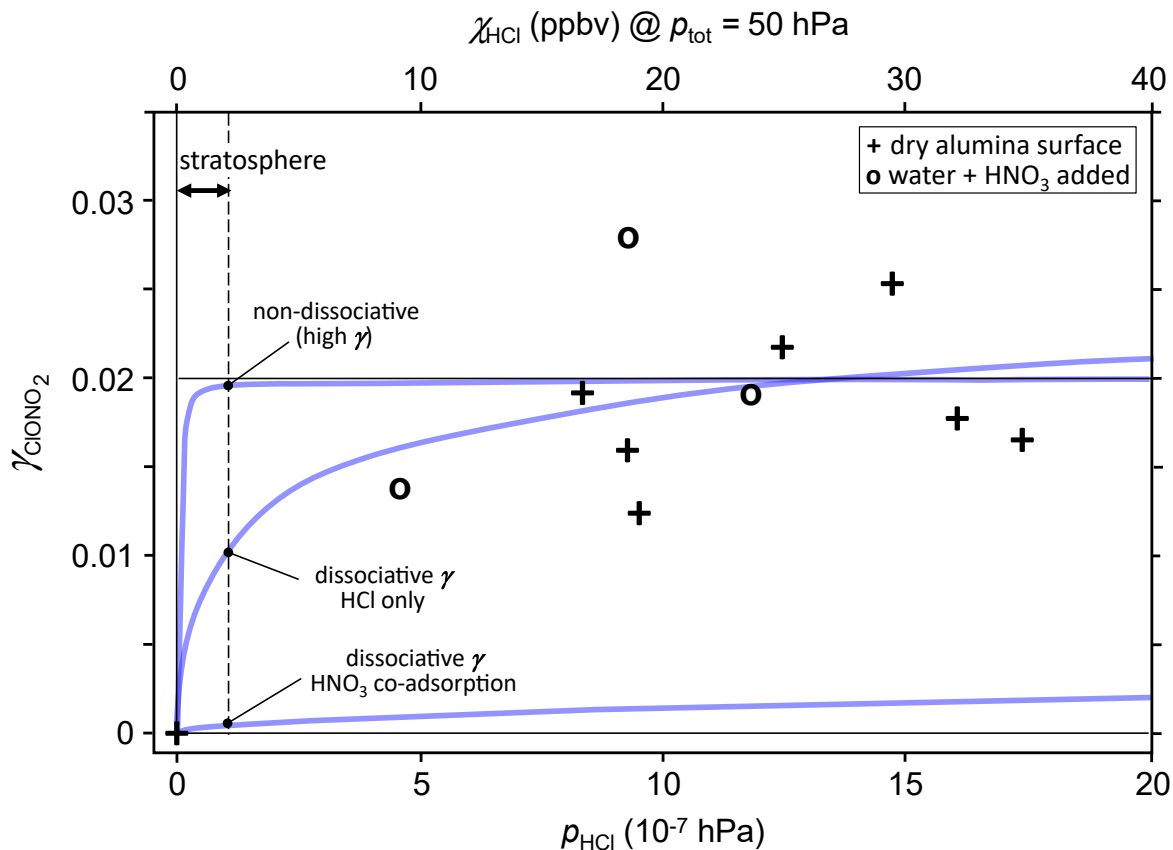


Figure 4.1: Reaction probability  $\gamma_{\text{ClONO}_2}$  for  $\text{ClONO}_2 + \text{HCl}$  on alumina measured by Molina et al. (1997) as a function of  $p_{\text{HCl}}$  (black symbols) in comparison with uptake coefficients calculated from isotherms of adsorption/desorption and reaction rate coefficients (blue curves). Measurements were performed under dry conditions (crosses) or after adding  $2.5 \times 10^{-4}$  hPa water and  $4.5 \times 10^{-7}$  hPa  $\text{HNO}_3$  (circles), see Appendix 4B. The uptake coefficient based on dissociative adsorption of “HCl only” was calculated using  $1/\gamma_{\text{ClONO}_2} = 1/\alpha_{\text{ClONO}_2} + 1/(\beta \sqrt{p_{\text{HCl}}})$  with  $\alpha$  and  $\beta$  fitted to the data, for  $\text{HNO}_3$  co-adsorption using  $1/\gamma_{\text{ClONO}_2} = 1/\alpha_{\text{ClONO}_2} + 1/(33 \beta \sqrt{p_{\text{HCl}}})$ , and for non-dissociative HCl adsorption using  $1/\gamma_{\text{ClONO}_2} = 1/\alpha_{\text{ClONO}_2} + 1/(\beta p_{\text{HCl}})$  with fixed values  $\alpha_{\text{ClONO}_2} = 0.02$  and  $\beta = 2.7 \times 10^7$  hPa, resulting in a “high”  $\gamma_{\text{ClONO}_2}$  of 0.019 at 50 hPa and 1 ppb HCl (see Table 4.1). Typical stratospheric values of  $p_{\text{HCl}}$  are  $1 \times 10^{-7}$  hPa or lower (dashed vertical line). Axis on top shows HCl mixing ratio  $\chi_{\text{HCl}}$  for a total pressure of 50 hPa representative of  $\sim 20$  km altitude in the stratosphere, for reference.

gas whose vapor pressure is low enough to form a stable aqueous solution. This results in co-condensation of  $\text{H}_2\text{SO}_{4(\text{g})}$  and  $\text{H}_2\text{O}_{(\text{g})}$  on available surfaces, while other trace gases adsorb and readily desorb again. Assuming an alumina SAD of  $3 \mu\text{m}^2/\text{cm}^3$  in the lower stratosphere (Appendix 4G), the condensation rate of  $\text{H}_2\text{SO}_{4(\text{g})}$  on the particle surface is roughly one monolayer of  $\text{H}_2\text{SO}_4$  per two weeks (Appendix 4D). In the initial phase after injection, the surface must still be treated as blank alumina with a few adsorbed trace gas molecules, but during the stratospheric residence time the particles could acquire a  $\text{H}_2\text{SO}_4(\text{aq})$ -coating of nominally  $\sim 10$  nm thickness (Appendix 4D).

## 4.2 Methods

We performed Elastic Recoil Detection Analysis (ERDA, Kottler et al., 2006) experiments to test the assumption of alumina being non-aging under stratospheric conditions. Appendix 4E describes the results and provide evidence that alumina is unlikely to change its composition or crystalline structure under exposures to  $\text{HNO}_3$  as in the stratosphere. We further measured the wettability of the alumina surface to determine whether the  $\text{H}_2\text{SO}_4$ - $\text{H}_2\text{O}$  condensate of nominally  $\sim 10$  nm thickness on the alumina particles fully wets the surface or tends to contract and form small islands of liquid. Appendix 4D shows that aqueous  $\text{H}_2\text{SO}_4$  droplets on alumina single crystals have contact angles of around  $30^\circ$  (McLachlan Jr and Cox, 1975; Corti and Krieger, 2007; Thomason and Peter, 2006). If this is also true for the 240-nm particles investigated here, the condensed material would contract and only cover a small fraction of the surface. On the uncovered fraction of the surface HCl can react with  $\text{ClONO}_2$ , but might be impaired by the co-adsorbing  $\text{HNO}_3$ . Therefore, understanding reaction 4.1 on these particle surfaces requires modeling, which we describe subsequently.

### 4.2.1 Reactive uptake on alumina surfaces

Heterogeneous reaction rates  $k$  can be calculated by

$$k = \frac{\gamma \bar{v} \text{SAD}}{4}, \quad (4.4)$$

where SAD is the surface area density,  $\bar{v}$  is the mean molecular speed of the molecules colliding with the surface and  $\gamma$  is the reaction probability, i.e., the probability that such a collision actually results in a reaction. For the reaction  $\text{ClONO}_2 + \text{HCl}$ ,  $\gamma_{\text{ClONO}_2}$  depends on the amount of HCl available. SAD is determined by the injection rate and size of the aerosol particles. For a given injection mass, smaller particles result in larger SAD because of the larger surface-to-mass ratio and because of smaller sedimentation velocities.

The reaction probability,  $\gamma$ , of heterogeneous reactions for reactants with low adsorptivity on alumina surfaces, such as HCl and  $\text{ClONO}_2$  in reaction 4.1, can be described for example by a Eley-Rideal mechanism or a Langmuir-Hinshelwood mechanism for adsorption/desorption and reaction. Some studies found that the Eley-Rideal mechanism is more accurate to represent reaction 4.1 (Fernandez et al., 2005). However, the Langmuir-Hinshelwood mechanism was also successfully used to describe heterogeneous reactions such as reaction 4.1 on polar stratospheric clouds (e.g., Carslaw and Peter, 1997; Aguzzi and Rossi, 2001; Fernandez et al., 2005; Crowley et al., 2010; Ammann et al., 2013; Burkholder et al., 2020). In this study we use the Langmuir-Hinshelwood mechanism to extrapolate the measurements of Molina et al. (1997) to stratospheric HCl concentrations

(i.e.,  $\sim 1$  ppb at 50 hPa). As derived in Appendix 4F, the reaction probability  $\gamma_{\text{ClONO}_2}$  can be described by

$$\frac{1}{\gamma_{\text{ClONO}_2}} = \frac{1}{\alpha_{\text{ClONO}_2}} + \frac{\bar{v} \sigma^2}{4 K_{\text{ClONO}_2} k_B T k^{\text{II}} \theta_{\text{Cl}^-}}, \quad (4.5)$$

where  $\alpha_{\text{ClONO}_2}$  is the surface accommodation coefficient of species  $\text{ClONO}_2$  on alumina,  $\sigma$  is the surface area per adsorption site,  $K_X$  is the Langmuir constant of species X,  $k^{\text{II}}$  the second order surface reaction rate coefficient of reaction 4.1,  $k_B$  the Boltzmann constant and  $T$  the absolute temperature. Under stratospheric conditions, the fractional surface coverage  $\theta_{\text{Cl}^-}$  depends not only on the HCl partial pressure, but also on the competitive  $\text{HNO}_3$  co-adsorption (Appendix 4F):

$$\theta_{\text{Cl}^-} \approx \frac{K_{\text{HCl}} p_{\text{HCl}}}{\theta_{\text{NO}_3^-}} \approx \frac{K_{\text{HCl}} p_{\text{HCl}}}{\sqrt{K_{\text{HNO}_3} p_{\text{HNO}_3}}} \approx \frac{1}{f} \sqrt{K_{\text{HCl}} p_{\text{HCl}}}, \quad (4.6)$$

where the first expression,  $K_{\text{HCl}} p_{\text{HCl}} / \theta_{\text{NO}_3^-}$ , reveals the dissociative nature of adsorption and the competition of HCl and  $\text{HNO}_3$  via  $\text{H}^+$ -concentration on the surface. In equation 4.6 (equation 4.6),  $f$  is the reduction factor by which the adsorption of HCl is diminished due to the presence of  $\text{HNO}_3$  relative to a system without  $\text{HNO}_3$  interaction. In the absence of measurements on alumina, we have estimated  $f$  from a comparison of measurements of the HCl uptake on ice with  $\text{HNO}_3$  (Hynes et al., 2002) and without  $\text{HNO}_3$  (Zimmermann et al., 2016) and find  $f \approx 33$  (Appendix 4F). In equation 4.5 and equation 4.6, we combine the unknown quantities  $K_{\text{ClONO}_2}$ ,  $K_{\text{HCl}}$ , and  $k^{\text{II}}$  as follows:

$$\beta = \frac{4 K_{\text{ClONO}_2} k_B T k^{\text{II}} \sqrt{K_{\text{HCl}}}}{\bar{v} \sigma^2 f}. \quad (4.7)$$

Thus:

$$\frac{1}{\gamma_{\text{ClONO}_2}} = \frac{1}{\alpha_{\text{ClONO}_2}} + \frac{1}{\beta \sqrt{p_{\text{HCl}}}}. \quad (4.8)$$

This allows us to describe the measured  $\gamma_{\text{ClONO}_2}$  by treating the unknown quantities  $\alpha_{\text{ClONO}_2}$  and  $\beta$  as fit parameters. Finally, we use the fit of equation 4.8 to Molina et al. (1997) measurements and scale it down by  $f$  to take into account the HCl- $\text{HNO}_3$  interaction.

Figure 4.1 shows equation 4.8 (blue curves) fitted to Molina et al. (1997) data (black symbols) as a function of HCl partial pressure. The curve labeled “dissociative  $\gamma_{\text{ClONO}_2}$ , HCl only” shows a least-squares best fit of equation 4.8 to the measurements with  $f=1$  for pure HCl uptake (i.e.,  $\text{HNO}_3$  and  $\text{H}_2\text{SO}_4$  absent). The curve labeled “dissociative  $\gamma_{\text{ClONO}_2}$ ,  $\text{HNO}_3$  co-adsorption” is the same, but with  $f = 33$  derived from measurements of HCl uptake in competition with  $\text{HNO}_3$  on ice. Finally, the curve labeled “non-dissociative, high  $\gamma_{\text{ClONO}_2}$ ” assumes HCl molecules not to dissociate on the surface (Carslaw and Peter, 1997), and further assumes a high value of  $\beta$ , to span the full range of possible  $\gamma_{\text{ClONO}_2}$  compatible with the data (Table 4.1 also provides examples with medium and low  $\gamma_{\text{ClONO}_2}$ ).

Besides  $\text{ClONO}_2$  and HCl, Molina et al. (1997) also examined the effects of the presence of stratospheric concentrations of  $\text{H}_2\text{O}$  and  $\text{HNO}_3$ , but found no measurable change in  $\gamma_{\text{ClONO}_2}$  (within the range 0.018 and 0.022), which is seemingly in contradiction with equation 4.6. However, it would be misleading to assume that these two gases have no effect on reaction 4.1 under present-day stratospheric conditions. Because Molina et al.

(1997) applied  $\text{H}_2\text{O}$  and  $\text{HNO}_3$  at stratospheric concentrations, but  $\text{HCl}$  at concentrations more than 10-times higher, the effects of  $\text{H}_2\text{O}$  and  $\text{HNO}_3$  were likely dwarfed by the excess of  $\text{HCl}$ . In addition, the impact of  $\text{H}_2\text{SO}_4$  was not examined by Molina and coworkers. In summary, trace gases, such as  $\text{HNO}_3$ , co-adsorb on the particle surface and  $\text{H}_2\text{SO}_4$  can condense on it (with  $\text{H}_2\text{O}$ ). These acids, besides occupying adsorption sites on the surface, will likely dissociate and lead to a highly acidic environment that reduces the adsorptivity of  $\text{HCl}$  (Appendix 4F). Therefore,  $\gamma_{\text{ClONO}_2}$  measured by Molina et al. (1997) with no  $\text{HNO}_3$  or too little  $\text{HNO}_3$  is likely an overestimate compared to stratospheric conditions.

All curves in Figure 4.1 are plausible representations of the  $\gamma_{\text{ClONO}_2}$  measured by Molina et al. (1997). Obviously, the measured data do not help constraining  $\gamma_{\text{ClONO}_2}$  for low stratospheric  $p_{\text{HCl}}$ , where the Langmuir adsorption isotherms are in the linear, unsaturated regime. At 1 ppb  $\text{HCl}$ ,  $\gamma_{\text{ClONO}_2}$  can be as large as 0.019 (“non-dissociative high  $\gamma$ ”) or as small as 0.0003 ( $\gamma$  with  $\text{HNO}_3$  co-adsorption and dissociation), a ratio of almost two orders of magnitude (Figure 4.1, Table 4.1).

## 4.2.2 Aerosol-Chemistry-Climate Model description

We determined the stratospheric ozone response to injection of alumina particles by means of the aerosol-chemistry-climate model SOCOL-AERv2 (Feinberg et al., 2019), which allows us to represent all relevant aspects of stratospheric chemistry and dynamics. Its dynamical core is ECHAM5.4 (Roeckner et al., 2003), which is interactively coupled to the chemistry module MEZON (Rozanov et al., 2001; Egorova et al., 2003; Stenke et al., 2013) and the sectional aerosol module AER (Weisenstein et al., 1997; Sheng et al., 2015). SOCOL-AERv2 employs a T42 horizontal resolution (i.e., 310 km x 310 km) and 39 vertical sigma pressure levels up to 0.01 hPa (i.e.,  $\sim 80\text{km}$ ). It represents stratospheric chemistry with 40 sulfuric acid aerosol mass bins and 89 gas phase species including all relevant chlorine, nitrogen, carbon, bromine, oxygen, hydrogen and sulfur species which interact with each other through 16 heterogeneous, 58 photolysis and 160 gas phase reactions. The aerosols, the chemistry and the dynamics are fully interactive with each other allowing for accurate representation of stratospheric dynamics and chemistry (e.g., Friedel et al., 2022; Brodowsky et al., 2021).

The aerosol module in SOCOL-AERv2 was extended to include tracers for spherical monomers and agglomerates of alumina particles, assuming a density of  $3.95\text{ g/cm}^3$ . Ten prognostic variables (mass bins) were integrated to represent the injection of monomers with 240 nm and 80 nm radius and their agglomeration, while assuming mass doubling between subsequent mass bins. Self-coagulation of alumina particles follows the description of Weisenstein et al. (2015). SAD is calculated as the sum of the area of the number of monomers per agglomerate assuming the contact between single monomers within an agglomerate to be infinitely small. Their sedimentation as well as wet and dry deposition in the troposphere is treated the same way as for sulfuric acid aerosols (Feinberg et al., 2019). Scattering and absorption of radiation by alumina particles and stratospheric sulfuric acid aerosols were not accounted for in this study to isolate the impact of heterogeneous chemistry on alumina particle surfaces. The alumina particles are assumed not to interact with sulfuric acid aerosols except in the scenarios labeled “ $\text{H}_2\text{SO}_4$  coating”. In these scenarios, alumina particles acquire a sulfuric acid coating through coagulation with sulfuric acid aerosols and  $\text{H}_2\text{SO}_4\text{-H}_2\text{O}$  co-condensation (following Weisenstein et al., 2015), and the heterogeneous chemistry on the entire resulting SAD is assumed to be

identical to sulfuric acid aerosols (see Sheng et al., 2015).

### 4.2.3 Modeling scenarios

Each alumina injection scenario (Table 4.1) assumes an emission of 5 Mt/yr of  $\text{Al}_2\text{O}_3$  particles between  $30^\circ\text{N}$  and  $30^\circ\text{S}$  at all longitudes at the 54 hPa level ( $\sim 20$  km altitude). Particle radius is 240 nm (reference case) or 80 nm (sensitivity analysis). In Weisenstein et al. (2015) injections at particle radius of 240 nm resulted in the best tradeoff between global cooling and ozone depletion per injected aerosol mass (see Section 1.3). A radius of 240 nm is also close to the optimal radius for backscattering solar radiation of 215 nm reported by Dykema et al. (2016). Indeed, other simulations which account for scattering and absorption of radiation show a top-of-atmosphere (TOA) all sky radiative forcing of about  $-0.75 \text{ W/m}^2$  for 5 Mt/yr injection of 240 nm (see Chapter 3, Figure 3.4).

Scenarios were performed with different parameterizations for co-adsorption/desorption and reaction or different assumptions on the partitioning of  $\text{HNO}_3$  and  $\text{H}_2\text{SO}_4$  at the particle surface (blue lines in Figure 4.1 and Table 4.1). For comparison with sulfur-based SAI, a scenario with injections of 5 Mt of  $\text{SO}_2$  per year (i.e., 2.5 Mt of Sulfur per year) was also run. All simulations are time-slices spanning 15 years, with climatological sea surface temperature (SST), sea ice concentrations (SIC), GHG and ODS concentrations set to 2020 or 2090 conditions. The first 5 years of each simulation served as spin-up to equilibrate stratospheric aerosol burdens. Hence, all data shown in this study are 10-year averages. GHG and ODS concentrations were taken from SSP5-8.5 (O’Neill et al., 2015) and WMO (2018), respectively, while SST and SIC were taken from a 10-year average (2011-2020) of the Hadley dataset (Kennedy et al., 2019) for 2020 conditions and CESM5-CAM1 RCP8.5 (2090-2099) for 2090 conditions (Meehl et al., 2013).

## 4.3 Results

The scenarios with injection of 5 Mt per year of particles with radius of 240 nm result in global mean stratospheric alumina burdens of about 3.7 Mt. The corresponding mean stratospheric particle residence times are about 9 months and the resulting alumina SAD is  $3\text{-}5 \mu\text{m}^2/\text{cm}^3$  in the lower stratosphere (Appendix 4G). When applying the different parameterizations for co-adsorption/desorption and reaction for  $\gamma_{\text{ClONO}_2}$  depicted in Figure 4.1, the “non-dissociative high  $\gamma_{\text{ClONO}_2}$ ” scenario for 240-nm particles results in a total ozone column (TOC) decrease of 9% globally, up to 16% over the poles and midlatitudes and about 6% in the tropics for present day ODS (Figure 4.2a). When injecting particles of a radius of 80 nm instead of 240 nm at 5 Mt/yr, the global mean aerosol burden increases to 5.2 Mt (due to reduced sedimentation). In the “non-dissociative high- $\gamma_{\text{ClONO}_2}$ ” case SAD increases to  $5\text{-}16 \mu\text{m}^2/\text{cm}^3$  (Appendix 4G), which enhances global mean TOC depletion to more than 20% (Figure 4.2a).

However, most likely  $\text{HNO}_3$  will co-adsorb on the alumina surface (Appendix 4F). The scenario “ $\gamma_{\text{ClONO}_2}$  with  $\text{HNO}_3$ ”, which accounts for co-adsorption and dissociation of  $\text{HCl}$  and  $\text{HNO}_3$  on the particle surface, yields no substantial ozone loss. Furthermore, gaseous  $\text{H}_2\text{SO}_4$  can co-condense with water, and aqueous  $\text{H}_2\text{SO}_4$  droplets can coagulate with the alumina particles. Therefore, alumina surfaces will be covered partly or fully by sulfuric acid a few weeks after injection. A full coating (core-shell configuration) is not very likely, given the contact angle of  $25\text{-}38^\circ$  for macroscopic  $\text{H}_2\text{SO}_4\text{-H}_2\text{O}$  droplets on alumina

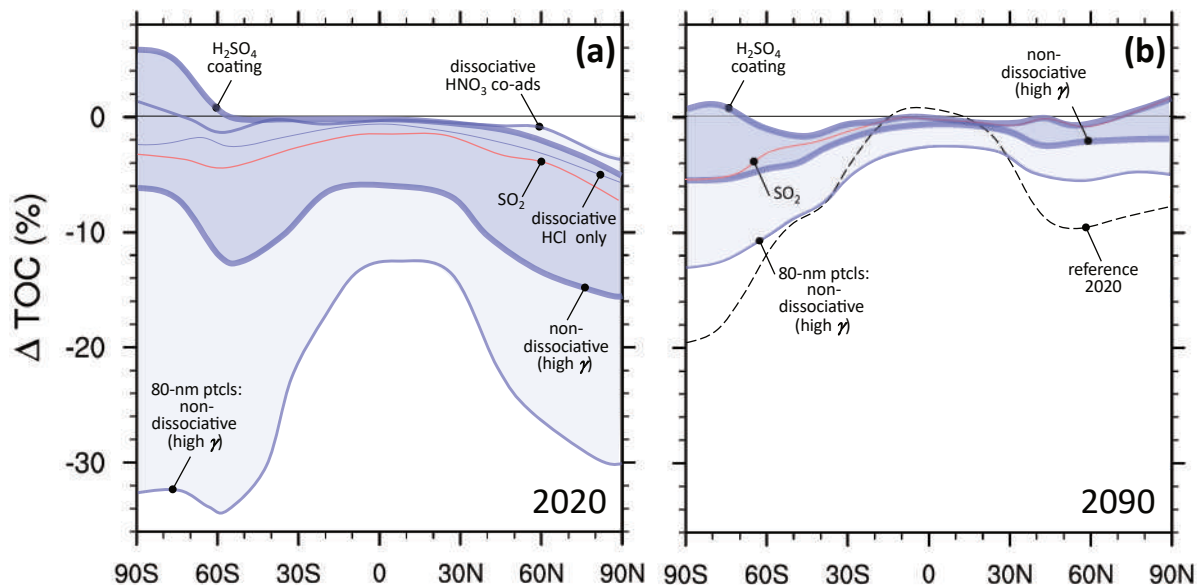


Figure 4.2: Zonal mean of 10 year averaged total ozone column depletion resulting from injection of 5 Mt/yr of alumina particles assuming different parameterizations of reaction 4.1 (Figure 4.1) or alumina particles to be covered with sulfuric acid (“ $\text{H}_2\text{SO}_4$  coating”) simulated with SOCOL-AER under 2020 (a) and 2090 (b) ODS and GHG conditions. For comparison we also show an  $\text{SO}_2$  injection scenario with equal injection rates as for the alumina injection scenarios (i.e., 5 Mt  $\text{SO}_2$  per year).

surfaces (Appendix 4D). However, we analyze the sensitivity of the ozone response to alumina particles by assuming a full coating by sulfuric acid (termed “ $\text{H}_2\text{SO}_4$  coating” in Figure 4.2). In this conservative scenario, the entire resulting SAD (Appendix 4G) hosts the same heterogeneous chemistry as on sulfuric acid aerosols. The impact on ozone in this scenario is small since the absolute sulfuric acid SAD increase in the extratropics is only about 20% (Appendix 4G). The increase from coated sulfuric acid SAD is partially compensated by the decrease in background sulfuric acid aerosol SAD. The TOC increase in the southern polar stratosphere is due to less PSC in the “ $\text{H}_2\text{SO}_4$  coating” simulation, since the number density of sulfuric acid aerosols is significantly reduced, which also explains the strong positive  $\text{HNO}_3$  anomaly over the south polar region (see Appendix 4H,  $\Delta\text{HNO}_3$ ). However, the microphysical interactions of alumina particles with sulfuric acid and PSC in the stratosphere is unknown and subject to large uncertainty.

To put these results into a broader context, we also performed simulations for the year 2090 with much reduced atmospheric chlorine loading using SSP5-8.5 GHG and WMO (2018) ODS boundary conditions. Under these conditions, all SAI scenarios result in substantially less ozone depletion, which also reduces the uncertainty range (gray area in Figure 4.2b). The reduced ozone depletion is mostly due to the much smaller chlorine loadings in these scenarios. Depletion of TOC reaches 6% in the south polar region, but only 1% in the tropics and 3% in the north polar region for the “non-dissociative high  $\gamma_{\text{ClONO}_2}$ ” scenario, which has the strongest depletion of TOC across all scenarios with particle radius 240 nm. The more invasive scenario using particles with 80 nm radius still results in TOC depletion of 13% over the south polar region and 3% in the tropics (Appendix 4H).

The difference between the modeled 2090 and the 2020 TOC levels (Figure 4.2b) is

representing the effect of ozone recovery which is consistent with projections from other models (WMO, 2022). Under 2090 conditions, all scenarios result in significantly higher TOC compared with present day TOC. This means that the projected TOC changes due to future ozone recovery are still much larger than the upper limit TOC depletion in any of the SAI scenarios.

## 4.4 Summary and conclusions

Climate intervention to cool the climate by injecting alumina particles into the lower stratosphere could have advantages over sulfur injection, such as enhanced backscattering of solar radiation and reduced stratospheric heating. However, this study reveals that alumina injection is fraught with significant uncertainties in estimating the chemical impact on the ozone layer. Using 5 Mt/yr of alumina particles with a radius of 240 nm which would result in TOA radiative forcing of about  $-0.75 \text{ W/m}^2$ , we estimate that the global mean ozone loss could be as high as 9% for 2020 conditions. This is about twice the historical peak ozone loss caused by chlorofluorocarbons and other ODS at the end of the last century (WMO, 2022).

These simulations assume that the heterogeneous reaction of  $\text{ClONO}_2$  with  $\text{HCl}$  has a reaction probability  $\gamma_{\text{ClONO}_2} \approx 0.02$ , as suggested by the only available measurement (Molina et al., 1997). However, these measurements were made for conditions in exhaust plumes from solid-fuel rocket motors with  $\text{HCl}$  concentrations more than an order of magnitude higher than in the stratosphere today. We apply a Langmuir-Hinshelwood mechanism for co-adsorption/desorption and reaction to extrapolate to lower concentrations in a physically consistent manner. This shows that  $\gamma_{\text{ClONO}_2}$  is not well constrained due to the sparsity of experimental data, but ranges from  $\gamma_{\text{ClONO}_2} = 0.019$  to  $\gamma_{\text{ClONO}_2} = 0.0003$ , depending on uncertain reaction rate coefficients and Langmuir constants, as well as due to the unknown effect of co-adsorption and dissociation of  $\text{HNO}_3$  and co-condensation of  $\text{H}_2\text{SO}_4$  on resulting  $\text{Cl}^-$  availability. This has massive repercussions for the modeled impacts of SAI by alumina particles. An additional complication is the uncertain wettability and degree of coverage by  $\text{H}_2\text{SO}_4$ - $\text{H}_2\text{O}$  solutions, which may further reduce impact on stratospheric ozone (see Table 4.1 for all scenarios). Other heterogeneous reactions on alumina, such as  $\text{N}_2\text{O}_5$  hydrolysis, are presently unconstrained by experimental data, but likely play a much smaller role than reaction 4.1 (Appendix 4I). Interactions with PSCs represent a further source of uncertainty.

We have identified a number of key processes as sources of uncertainty: (1) extrapolation of measured data for reaction 4.1 to stratospheric trace gas concentrations, (2) lack of detailed knowledge of competitive co-adsorption and interaction with other trace gases on the surface, (3) wettability by co-condensation of  $\text{H}_2\text{SO}_4$  and  $\text{H}_2\text{O}$  on the surface, and (4) the effect of future ODS and GHG concentration changes. The findings of this study call for investigations on heterogeneous chemistry on solid particles that incorporate present and future stratospheric conditions in terms of temperatures, partial pressures of relevant trace gases (e.g.,  $\text{H}_2\text{SO}_4$ ,  $\text{ClONO}_2$ ,  $\text{N}_2\text{O}_5$ ,  $\text{HCl}$  and  $\text{HNO}_3$ ) and relative humidity.

## Data Availability

The modelled data used for this study are available in the ETH research collection via Vattioni (2023a). The model code of SOCOL-AERv2 incorporating the solid particle

microphysics scheme used for data generation is available via Vattioni (2023b).

## Author Contributions

SV developed and implemented the Langmuir-Hinshelwood parameterisation for heterogeneous chemistry on solid particles in the model, performed the simulations, created the figures and wrote the first draft of the manuscript. BL, SV, FK and TP derived the specific scenarios for different assumptions on surface chemistry. TP helped editing the figures and the text. RW and SV performed the contact angle measurements. CV performed the ERDA measurements. AF, AS and BL helped with the model development. All co-authors contributed to discussion of the results and to text editing.

## Acknowledgments

We thank Debra Weisenstein for providing the 2D-AER code, which simplified implementation of solid particles into SOCOL-AER. We also thank her and David Keith for the feedback on our work, Liviana Klein for support with the coating angle measurements and Uwe Weers with the ERDA measurements, Max Döbeli for conducting and analyzing the ERDA measurements together with Christof Vockenhuber. Gabriel Chiodo and Andrea Stenke were supported by the Swiss Science Foundation (grant no. PZ00P2\_180043), Sandro Vattioni by the ETH Research (grant no. ETH-1719-2) and by the Harvard Solar Geoengineering Research Program, which also supported Frank Keutsch, Timofei Sukhodolov by the Swiss National Science Foundation (grant no. 200020-182239) and the Karbacher Fonds, Graubünden, Switzerland.



## Appendix 4: Supplementary information

### A: The different parameterizations assumed in this study

Table 4.1 gives an overview of the different parameterizations of reaction 4.1, which were presented in this study.

Table 4.1: Overview of model scenarios which are the basis of this work. This includes uptake coefficients calculated based on Langmuir isotherms  $1/\gamma_{\text{ClONO}_2} = 1/\alpha_{\text{ClONO}_2} + 1/(\beta p_{\text{HCl}})$  for non-dissociative and  $1/\gamma_{\text{ClONO}_2} = 1/\alpha_{\text{ClONO}_2} + 1/(\beta \sqrt{p_{\text{HCl}}})$  for dissociative adsorption (see Appendix F for a derivation). The parameters  $\alpha_{\text{ClONO}_2}$  and  $\beta$  have been fitted to the  $\gamma_{\text{ClONO}_2}$  measured by Molina et al. (1997) under high HCl conditions, and  $\gamma_{\text{ClONO}_2}$  has then been extrapolated to typical stratospheric conditions (i.e.,  $\sim 1$  ppbv HCl at 50 hPa which is  $\sim 5 \times 10^{-8}$  hPa). Based on simulations with the aerosol-chemistry-climate model SOCOL-AER, the last two columns show results for the reduction of the total ozone column (TOC) in percent. These are 10 year averages of global mean depletions in TOC for 5 Mt/yr injection of alumina particles with radius of 240 nm for time sliced conditions of the years 2020 and 2090 (referring to globally averaged TOCs of 317 and 336 DU, respectively). The alumina scenarios are compared with a 5 Mt/yr  $\text{SO}_2$  injection scenario and with a scenario in which the alumina particles are fully coated by aqueous  $\text{H}_2\text{SO}_4$  and their heterogeneous chemistry is treated like that of  $\text{H}_2\text{SO}_4$ - $\text{H}_2\text{O}$  droplets. Entries marked “n/a” are not applicable (for the case of  $\text{H}_2\text{SO}_4$  coating,  $\text{SO}_2$  injections and the reference simulation) or have not been determined (as some simulations for 2090).

Scenario name	Langmuir Fit		typical $\gamma_{\text{ClONO}_2}$ (1 ppb HCl at 50 hPa)	$\Delta\text{TOC}$ (%)	
	$\alpha_{\text{ClONO}_2}$	$\beta$		2020	2090
Reference ( $\gamma=0$ )	n/a	n/a	n/a	0	0
$\text{SO}_2$	n/a	n/a	n/a	-2.8	-1.4
non-dissociative					
high $\gamma$	0.02	$2.7 \times 10^{-7} \text{ hPa}^{-1}$	0.019	-9.1	-2.0
medium $\gamma$	0.02	$2.7 \times 10^{-6} \text{ hPa}^{-1}$	0.017	-6.1	-1.3
low $\gamma$	0.02	$2.7 \times 10^{-5} \text{ hPa}^{-1}$	0.007	-1.7	n/a
dissociative					
only HCl, best fit $\gamma$	0.03	$59 \text{ hPa}^{-1/2}$	0.008	-2.6	n/a
only HCl, fitted $\gamma$ , $\alpha=0.1$	0.10	$25 \text{ hPa}^{-1/2}$	0.004	-1.3	n/a
$\gamma$ with $\text{HNO}_3$ co-ads.	0.03	$1.79 \text{ hPa}^{-1/2}$	0.0003	-0.03	n/a
$\text{H}_2\text{SO}_4$ coating	n/a	n/a	n/a	-0.5	-0.6

## B: Details and caveats of the Molina et al. 1997 measurements

The measurements by Molina et al. (1997) were performed in a flow tube with Helium as carrier gas (2.5 torr) with a flow velocity of 2800 cm<sup>3</sup>/s. Figures 4.1 and 4.3 show the measurements which were performed under dry conditions (crosses) and in the presence of  $1.9 \times 10^{-4}$  torr H<sub>2</sub>O (open circles), which corresponds to a water vapor mixing ratio  $\chi_{\text{H}_2\text{O}}$  of 3.8 ppm at 50 hPa total pressure (open circles). Molina et al. (1997) indicated that in their measurements on dry alumina surfaces their samples were dry-baked prior to the experiment. However, they also state that between the drying and the measurements the samples were exposed to ambient air. Even this short exposure to ambient air humidity is likely enough to hydroxylate the alumina surfaces again. Although no change in their measurements was observed when adding H<sub>2</sub>O to the carrier gas (Figures 4.1 and 4.3), a dependence on H<sub>2</sub>O adsorption can still not be excluded, since all measurements could have been performed in the presence of at least a few monolayers of water.

Furthermore, Molina et al. (1997) performed some experiments with  $p_{\text{HCl}} = (1 - 10) \times 10^{-7}$  torr,  $p_{\text{H}_2\text{O}} = 3.8 \times 10^{-4}$  torr, and  $p_{\text{HNO}_3} = 3.8 \times 10^{-7}$  torr. While these H<sub>2</sub>O and HNO<sub>3</sub> partial pressures correspond roughly to present-day stratospheric conditions, the HCl partial pressures are higher by 1-2 orders of magnitude than in the stratosphere. This was on purpose, taking account of the HCl-rich conditions in a rocket plume examined by Molina et al. (1997). To estimate the effect of the presence of the HNO<sub>3</sub> concentrations present in Molina et al. (1997) on the HCl uptake, which compared to HCl concentrations are relatively small, we refer to the treatment of competitive co-adsorption in Appendix 4F below (using co-adsorption on ice as a proxy). Instead of using Figure 4.7 for stratospheric conditions indicated by the red double arrow, we apply it to the higher HCl concentrations used by Molina et al. (1997) in their experiments, yielding the gray-shaded area in Figure 4.3. The competitive co-adsorption of HNO<sub>3</sub> in these experiments is expected to have a much weaker effect than HNO<sub>3</sub> under stratospheric conditions. However, the effect should still be discernible, whereas Molina et al. (1997) did not note any effect of their HNO<sub>3</sub> addition. We can only speculate why this is the case. First, Molina and colleagues only provide a range for the HCl concentrations ( $1 \times 10^{-6}$  -  $1 \times 10^{-5}$  torr) and possibly most experiments were performed at the high HCl concentration end, which yields only small effects. Second, we note that the reaction 4.1 itself is a source for HNO<sub>3</sub>, which may remain on the surface and reduce the contrast between their experiments with and without HNO<sub>3</sub>.

In summary, from the experiments of Molina et al. (1997) we cannot exclude an effect of water vapor on the HCl adsorptivity and, hence, on the reaction rate of ClONO<sub>2</sub> + HCl (reaction 4.1). More importantly, the effect of HNO<sub>3</sub>, which quenches the HCl uptake and slows the reaction, is expected to be much smaller in Molina et al.'s experiments than under stratospheric conditions (see Figure 4.1). Thus, a physically consistent approach is required to extrapolate these experimental data to stratospheric conditions (see Appendix 4F).

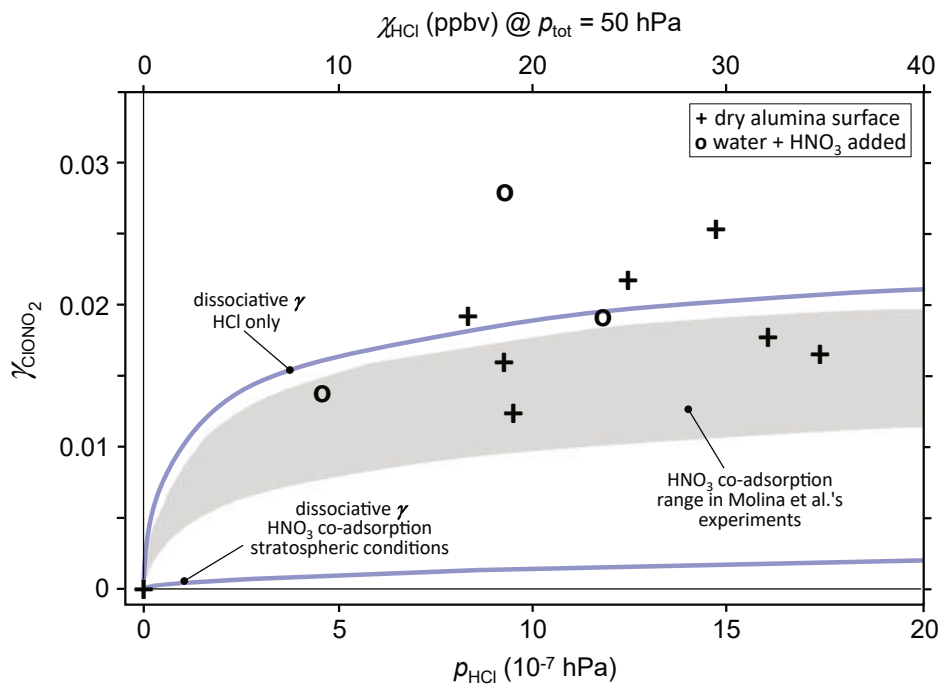


Figure 4.3: Reactive uptake probability  $\gamma_{\text{ClONO}_2}$  of  $\text{ClONO}_2$  on alumina surfaces as function of  $\text{HCl}$  partial pressure. Symbols show data measured by Molina et al. (1997). Blue lines are identical to lines in Figure 4.1, i.e.,  $\gamma_{\text{ClONO}_2}$  in the absence of dissociating gases other than  $\text{HCl}$  (upper curve) and  $\gamma_{\text{ClONO}_2}$  in presence of dissociating  $\text{HNO}_3$  at stratospheric concentrations (lower curve, see also Appendix 4F). Gray area: estimated range of reactive  $\text{ClONO}_2$  uptake as function of  $\text{HCl}$  partial pressure in the presence of the very low  $\text{HNO}_3$  concentrations as in the experiments of Molina et al. (1997), namely  $[\text{HNO}_3]/[\text{HCl}]=0.03\text{-}0.3$ .

### C: Weisenstein et al. (2015) modeling details

For extrapolation to HCl partial pressures relevant for the stratosphere Weisenstein et al. (2015) used the following parameterization:

For  $[\text{HCl}]/[\text{ClONO}_2] > 10$   $\gamma_{\text{ClONO}_2} = 0.02$

For  $[\text{HCl}]/[\text{ClONO}_2] \leq 10$   $\gamma_{\text{ClONO}_2} = \log_{10}([\text{HCl}]/[\text{ClONO}_2]) \cdot 0.02$

For  $[\text{HCl}]/[\text{ClONO}_2] \leq 1$   $\gamma_{\text{ClONO}_2} = 0.00$

Figure 4.4 shows the Molina et al. (1997) data as well as the parameterization used in Weisenstein et al. (2015) as a function of  $[\text{HCl}]/[\text{ClONO}_2]$ . The measurements by Molina et al. (1997) are not well captured by this parameterization. The calculated  $\gamma_{\text{ClONO}_2}$  values from this study are significantly different in magnitude and zonal mean shape compared to the ones applied in Weisenstein et al. (2015), see (Figure 4.10a-f). Furthermore, reaction 4.1 on alumina particles could result in significantly increased  $\text{ClONO}_2$  concentrations (see Appendix 4H and Figure 4.11,  $\Delta\text{ClONO}_2$  of the “non-dissociative medium  $\gamma_{\text{ClONO}_2}$ ” scenario), which would further decrease the resulting  $\gamma_{\text{ClONO}_2}$  proportionally to the increase of  $\text{ClONO}_2$ . The scenario in Weisenstein et al. (2015), which injected 4 Mt per year of 240 nm alumina particles, resulted in about 1-4% less zonal mean TOC depletion than the “non-dissociative low  $\gamma_{\text{ClONO}_2}$ ” scenario in this study, which injected 5 Mt per year of alumina particles at 240 nm radius. However, this could also be influenced due to the very different microphysics between the two studies resulting in very different aerosol burden and surface area densities (SAD).

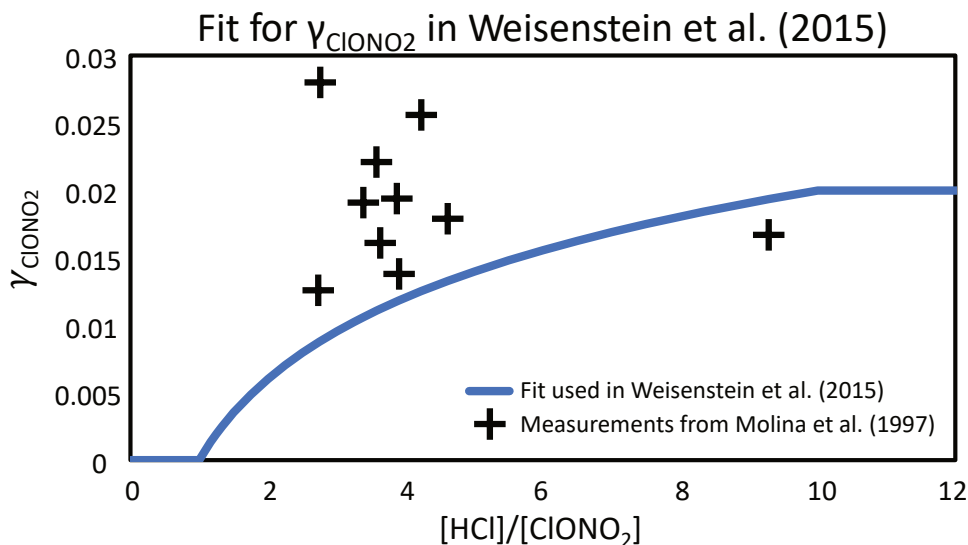


Figure 4.4: The black crosses represent measured values of  $\gamma_{\text{ClONO}_2}$  for reaction 4.1 on alumina surfaces as a function of  $[\text{HCl}]/[\text{ClONO}_2]$  from Molina et al. (1997). The blue line represents the fitting curve which was used to calculate  $\gamma_{\text{ClONO}_2}$  in Weisenstein et al. (1997) assuming a constant  $\text{ClONO}_2$  concentration.

## D: Contact angle measurements of sulfuric acid on alumina particles

The simulations which allowed for uptake of  $\text{H}_2\text{SO}_4$  on alumina particles through coagulation and condensation (see scenarios “ $\text{H}_2\text{SO}_4$ -coating” in Figure 4.2) resulted in an average alumina SAD of about  $3 \mu\text{m}^2/\text{cm}^3$  with a  $\text{H}_2\text{SO}_4$ – $\text{H}_2\text{O}$  layer of about 10 nm thickness in the lower stratosphere when injecting 5 Mt/yr of alumina particles with a radius of 240 nm. In these simulations the  $\text{H}_2\text{SO}_4$ – $\text{H}_2\text{O}$  was assumed to be equally distributed over the whole alumina SAD. Taking the total stratospheric  $\text{H}_2\text{SO}_4$  flux from gas phase to condensed phase from Feinberg et al. (2019, see their Figure 8, sum of condensation and nucleation equals 132 Gg Sulfur/yr in the form of  $\text{H}_2\text{SO}_4$ ), the average time to build up one monolayer can be estimated to be about 17 days (i.e., roughly two weeks). When integrating this over the stratospheric residence time of the particles (i.e., about 9 months, see Section 3, Results), this results in a thickness of roughly 6.5 nm, when not accounting for  $\text{H}_2\text{O}$ . This is in good agreement with the resulting  $\text{H}_2\text{SO}_4$ – $\text{H}_2\text{O}$  coating thickness of 10 nm in SOCOL-AER. However, it is not clear whether the  $\text{H}_2\text{SO}_4$ – $\text{H}_2\text{O}$  on the surface would cover the whole surface or form small accumulated islands on the surface.

We have performed contact angle measurements using the approach of Corti and Krieger (2007) called the “inverted bubble method” (McLachlan Jr and Cox, 1975). In the inverted bubble method, the solid surface (in our case alumina) is immersed in a test solution and the contact angle is measured by means of small gas bubbles, which are created by blowing air into the solution below the sample with a pipette (see Figure 4.5, left). The contact angle is then determined optically (see Figure 4.5, right). The inverted bubble method is less sensitive to ambient conditions such as relative humidity or temperature since the solution has a much larger volume compared to the sessile drop method (see Figure 4.5, left). This is important since small highly concentrated sulfuric acid droplets could dilute relatively fast by uptake of water from ambient air. Typical stratospheric sulfuric acid aerosols have a weight percent of about 70 wt% sulfuric acid (Thomason and Peter, 2006).

The contact angle of sulfuric acid solutions was measured as a function of weight percent of sulfuric acid between 0wt% and 90wt% with steps of 10wt% by analyzing multiple bubbles at every step at multiple samples. We found no significant dependence of the contact angle on the weight percent of sulfuric acid. Measurements between 10wt% and 90wt% resulted in an average contact angle of about  $30^\circ$  with values between  $38^\circ$  for 10wt% and  $25^\circ$  for 90wt%, whereas the contact angle for pure water resulted in  $62^\circ$ .

These measurements are subject to large uncertainties since the contact angle is not only dependent on the solution characteristics, but also on the surface material properties. Morphology, pollution and treatment of the sample surface (e.g. polishing or cleaning with isopropanol or ethanol) could strongly influence the contact angle. Additionally, especially for higher concentrated sulfuric acid solutions water uptake from ambient air could have decreased the effective weight percent of the solutions. Furthermore, the method is limited in accuracy by the simplified optical determination of the contact angle (i.e. through commercial mobile cameras).

Despite these large uncertainties, the result of our measurements is unequivocal: The wetting capability of aqueous sulfuric acid on alumina surfaces is quite limited, leading to the formation of liquid droplets with a contact angle of about  $30^\circ$ , which do not spread over the entire surface. While we cannot be sure that this is also true under stratospheric conditions with microscopic particles, low temperatures and high UV radiation, we take

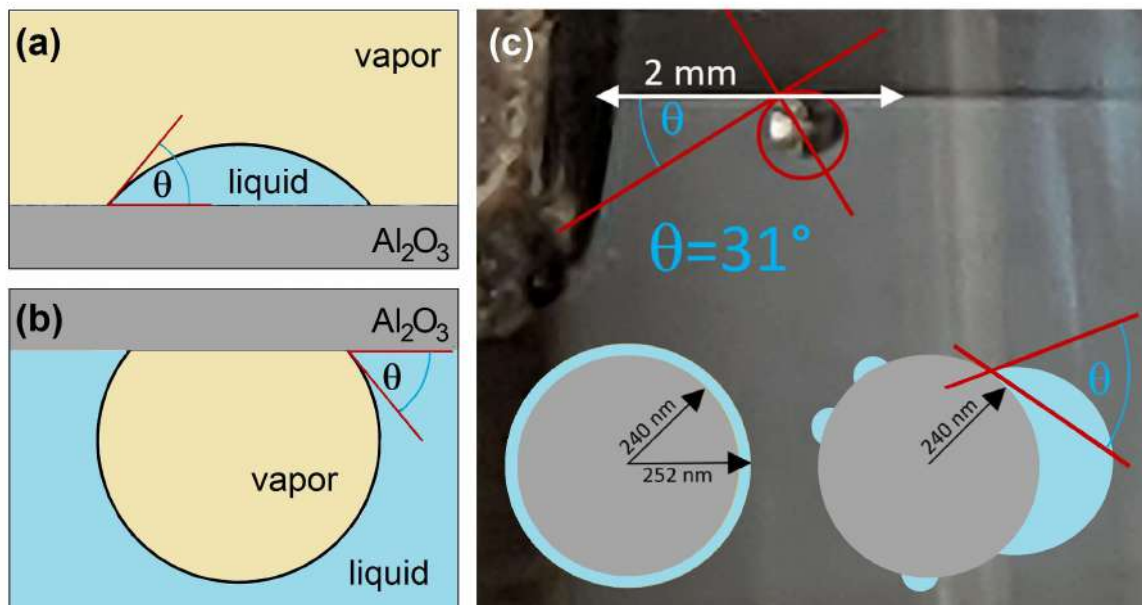


Figure 4.5: Left diagrams show schematics of (a) an  $\text{H}_2\text{SO}_4\text{-H}_2\text{O}$  droplet sitting in the vapor phase supported by an  $\text{Al}_2\text{O}_3$  surface and (b) the inverted bubble method using vapor bubble in  $\text{H}_2\text{SO}_4\text{-H}_2\text{O}$  submersed by an  $\text{Al}_2\text{O}_3$  surface (e.g., Corti and Krieger, 2007, see also Appendix 4D). Both cases develop the same contact angle,  $\theta$ . (c) Measurements of the wettability of  $\text{Al}_2\text{O}_3$  single crystals by 70wt%  $\text{H}_2\text{SO}_4$  solution using the inverted bubble method showed a contact angle of about  $31^\circ (\pm 7^\circ)$ , see Appendix 4D). If this is also true for the 240-nm particles investigated here, the nominal 12-nm layer (left sketch) would contract and only cover a small fraction of the particle surface (e.g. like in right sketch).

this as an indication that there is a high probability that a large fraction of the particle surface remains uncoated and may host the  $\text{ClONO}_2 + \text{HCl}$  reaction.

## E: Experimental evidence for chemically aging and non-aging materials

We performed Elastic Recoil Detection Analysis (ERDA) experiments at the 1.7 MV Tandetron accelerator (Kottler et al., 2006) at Laboratory of Ion Beam Physics at ETH Zurich, Switzerland, to investigate how  $\text{HNO}_3$  interacts with alumina and calcite surfaces. ERDA is based on the detection of elastically scattered recoils from the impact of 13 MeV primary  $^{127}\text{I}$  ions hitting the sample surface under an angle of  $17^\circ$ . Recoiling atoms are identified under a scattering angle of  $34^\circ$  by velocity and energy using a time-of-flight spectrometer in combination with a gas ionization detector. This allows us to calculate the elemental composition of the sample as a function of depth from the surface into a depth of about 180 nm. We have put two samples of alumina ( $\text{Al}_2\text{O}_3$ ) and calcite ( $\text{CaCO}_3$ ) into an excicator above a bath of 65wt%  $\text{H}_2\text{SO}_4$  containing 2wt% of  $\text{HNO}_3$ . The excicator was put into a fridge for 10 days at 253 K which resulted in a  $\text{HNO}_3$  mixing ratio of 80 ppm above the liquid at ambient pressure. Exposing the samples to  $\text{HNO}_3$  like this for 10 days results in a  $\text{HNO}_3$  exposure (i.e., exposure time multiplied by the exposure concentration in  $\text{s}/\text{cm}^3$ ) that is about 1000 times higher than the exposure of a solid particle with a stratospheric residence time of about one year (assuming about 10 ppb  $\text{HNO}_3$  at 50 hPa).

Strong uptake of  $\text{HNO}_3$  throughout the outermost 180 nm can be observed in the calcite sample (Figure 4.6b). However, for alumina we did not detect any counts of nitrogen throughout the accessible sample depth (Figure 4.6a). From this we conclude that the bulk of the alumina particle does not react with the acids in the stratosphere. Thus, the bulk of the alumina particles will likely not undergo any chemical aging in the stratosphere, but may serve as surfaces for adsorption of trace gases as well as condensation and coagulation of  $\text{H}_2\text{SO}_4$  onto the surface.

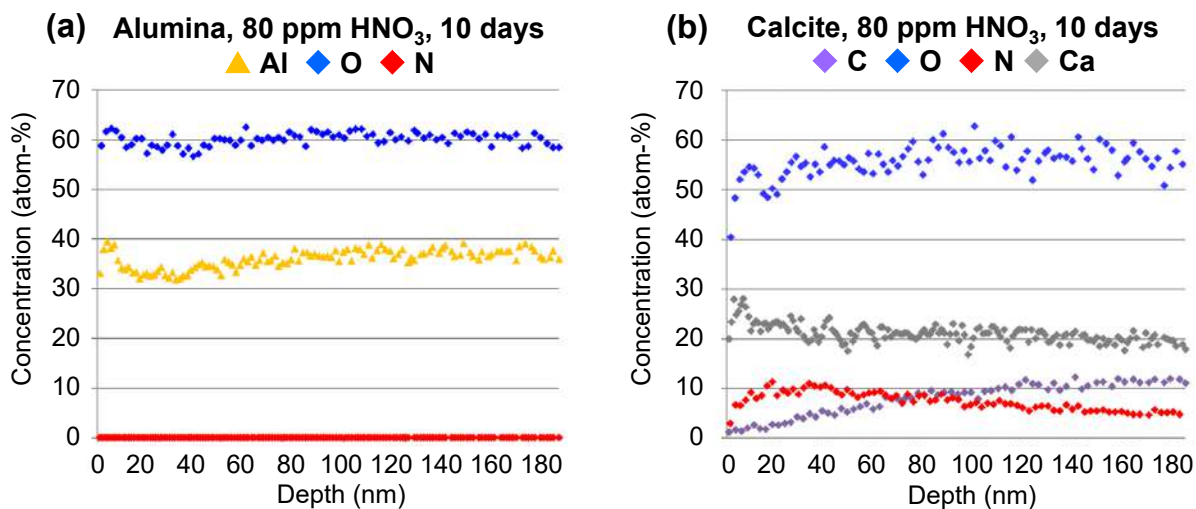
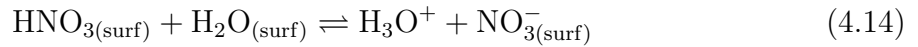
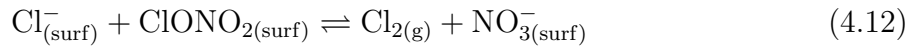
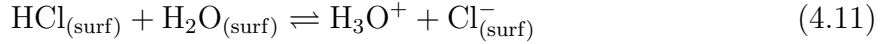
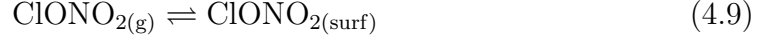


Figure 4.6: Elastic Recoil Detection Analysis (ERDA) of an alumina (a) and a calcite sample (b) after exposure to 80 ppm  $\text{HNO}_3$  at ambient pressure and 253 K for 10 days. Depicted quantities are the elemental compositions of the samples as a function of depth from the surface to 180 nm depth (see also Appendix 4E).

## F: Langmuir-Hinshelwood kinetics of ClONO<sub>2</sub> + HCl on an HNO<sub>3</sub>-dosed surface

We describe the co-adsorption/desorption and reaction mechanisms, while accounting for dissociation of the involved species. We assume that the net reaction ClONO<sub>2</sub> + HCl  $\xrightarrow{\text{surf}}$  Cl<sub>2</sub> + HNO<sub>3</sub> (reaction 4.1) proceeds according to the following steps:



This means:

- HCl and ClONO<sub>2</sub> both adsorb on the surface, where HCl has a much longer residence time (before desorption) than ClONO<sub>2</sub> (reaction 4.9 and reaction 4.10);
- On the surface, HCl is assumed to dissociate immediately and fully to H<sub>3</sub>O<sup>+</sup> and Cl<sup>-</sup> (reaction 4.11);
- Both Cl<sup>-</sup> and ClONO<sub>2</sub> undergo 2D-diffusion on the surface and can interact and react with each other according to reaction 4.1;
- The presence of HNO<sub>3</sub>, which also fully dissociates, acidifies the surface and, thus, reduces the uptake of HCl (reaction 4.13 and 4.14);
- Similar to HNO<sub>3</sub> also H<sub>2</sub>SO<sub>4</sub> may adsorb, dissociate, acidify the surface and reduce the uptake of HCl, but much less because of its lower concentration and tendency to contract into small droplets (see Appendix 4D);

We define:

- X = ClONO<sub>2</sub>, Y = Cl<sup>-</sup>, Z = NO<sub>3</sub><sup>-</sup> or HSO<sub>4</sub><sup>-</sup>;
- N<sub>X</sub>, N<sub>Y</sub>, N<sub>Z</sub> = number of molecules of X, Y, Z adsorbed on surface (molec/cm<sup>2</sup>);
- N<sub>tot</sub> = total number of adsorption sites on the surface (typically 10<sup>14</sup>-10<sup>15</sup>/cm<sup>2</sup>);
- θ<sub>X</sub>, θ<sub>Y</sub>, θ<sub>Z</sub> = fractional surface coverage of adsorption sites by X, Y, Z (dimensionless, θ<sub>X</sub> = N<sub>X</sub> σ etc.);
- σ = 1/N<sub>tot</sub> = surface area per adsorption site (typically 10<sup>-15</sup> cm<sup>2</sup>);
- [X] = molecule number density of molecules X in the gas phase (in cm<sup>-3</sup>);
- p<sub>X</sub> = [X] k<sub>B</sub> T = partial pressure of molecules X in the gas phase (in Pa);



- $k_B$  = Boltzmann constant;
- $T$  = absolute temperature;
- $\bar{v}_X$  = mean thermal speed of molecules X;
- $\gamma_X$  = reaction probability of X in reaction 4.1 (also called “reactive uptake coefficient”);
- $\alpha_X$  = surface accommodation coefficient of X (=ClONO<sub>2</sub>, also called “sticking coefficient”);
- $k^{II}$  = second order surface reaction rate coefficient (in cm<sup>2</sup>/s<sup>2</sup>) for reaction 4.12;
- $k_{\text{abs}}$  = reaction rate of adsorption of X (in Pa<sup>-1</sup>s<sup>-1</sup>) in reaction 4.9;
- $k_{\text{des}}$  = reaction rate of desorption of X (in s<sup>-1</sup>) in reaction 4.9;
- $K = k_{\text{abs}}/k_{\text{des}}$  = Langmuir constant of X (in Pa<sup>-1</sup>) in reaction 4.9;

For the description of the reactive uptake on the surface by adsorption, 2D-diffusion, and then desorption or reaction (i.e., a Langmuir-Hinshelwood scheme), we need the following equations 4.15-4.17.

The reactive flux equation for X:

$$j_X = \frac{1}{4}[X] \bar{v} \gamma_X = \frac{1}{4} \frac{p_X}{k_B T} \bar{v} \gamma_X = k^{II} N_X N_Y = k^{II} \theta_X \theta_Y \sigma^{-2} . \quad (4.15)$$

The mass balance for X on the surface:

$$\begin{aligned} \frac{dN_X}{dt} &= k_{\text{ads}} p_X (N_{\text{tot}} - N_X - N_Y - N_Z) - k_{\text{des}} N_X - k^{II} N_X N_Y \\ &= k_{\text{ads}} p_X (1 - \theta_X - \theta_Y - \theta_Z) \sigma^{-1} - k_{\text{des}} \theta_X \sigma^{-1} - k^{II} \theta_X \theta_Y \sigma^{-2} . \end{aligned} \quad (4.16)$$

Finally, the number of collisions of X with the surface leading to adsorption divided by the number of all collisions as given by the surface accommodation coefficient:

$$\alpha_X = \frac{k_{\text{ads}} p_X (N_{\text{tot}} - N_X - N_Y - N_Z)}{\frac{1}{4} [X] \bar{v}} = \frac{4 k_{\text{ads}} k_B T}{\bar{v} \sigma} (1 - \theta_X - \theta_Y - \theta_Z) . \quad (4.17)$$

Under steady state conditions,  $dN_X/dt = 0$  in equation 4.16. We use equation 4.15 and 4.16 to eliminate  $p_X$ :

$$0 = \frac{4 k_{\text{ads}} k^{II} k_B T}{\bar{v} \gamma_X \sigma^2} \theta_Y (1 - \theta_X - \theta_Y - \theta_Z) - k_{\text{des}} - k^{II} \theta_Y \sigma^{-1} . \quad (4.18)$$

We insert equation 4.17 into equation 4.18, thereby eliminating  $\theta_X$ , and use  $k_{\text{des}} = k_{\text{ads}}/K$ :

$$0 = \frac{k^{II}}{\gamma_X \sigma} \theta_Y \alpha_X - \frac{k_{\text{ads}}}{K} - k^{II} \theta_Y \sigma^{-1} . \quad (4.19)$$

Re-sorting terms in equation 4.19 provides:

$$\frac{1}{\gamma_X} = \frac{1}{\alpha_X} + \frac{\bar{v} \sigma^2}{4 k_B T k^{\text{II}} K \theta_Y (1 - \theta_X - \theta_Y - \theta_Z)} . \quad (4.20)$$

Since  $\theta_Z$  represents nitrate, bisulfate and hydronium ions,  $\theta_Z \gg \theta_X + \theta_Y$ , equation 4.20 simplifies to:

$$\frac{1}{\gamma_X} = \frac{1}{\alpha_X} + \frac{\bar{v} \sigma^2}{4 k_B T k^{\text{II}} K \theta_Y (1 - \theta_Z)} . \quad (4.21)$$

Here,  $\alpha_X$  is the surface accommodation coefficient on the  $\text{HNO}_3$ -dosed surface. When expressing this in terms of the surface accommodation coefficient on  $\text{HNO}_3$ -free and  $\text{H}_2\text{SO}_4$ -free surface,  $\alpha_{X,0} = \alpha_X/(1-\theta_Z)$ , we obtain

$$\frac{1}{\gamma_X} = \frac{1}{\alpha_{X,0} (1 - \theta_Z)} + \frac{\bar{v} \sigma^2}{4 k_B T k^{\text{II}} K \theta_Y (1 - \theta_Z)} , \quad (4.22)$$

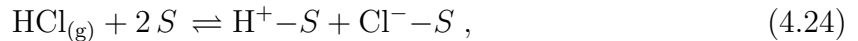
where  $\theta_Z$  is the part not covered by nitrate, bisulfate or hydronium ions. Or explicitly for reaction 4.1:

$$\frac{1}{\gamma_{\text{ClONO}_2}} = \frac{1}{\alpha_{\text{ClONO}_2,0} (1 - \theta_{\text{NO}_3^-} - \theta_{\text{HSO}_4^-} - \theta_{\text{H}^+})} + \frac{\bar{v} \sigma^2}{4 k_B T k^{\text{II}} K \theta_{\text{Cl}^-} (1 - \theta_{\text{NO}_3^-} - \theta_{\text{HSO}_4^-} - \theta_{\text{H}^+})} . \quad (4.23)$$

#### Competitive, dissociative adsorption:

In order to express the term  $\theta_{\text{Cl}^-} (1 - \theta_{\text{NO}_3^-} - \theta_{\text{HSO}_4^-} - \theta_{\text{H}^+})$  in equation 4.23 by the corresponding vapor pressures  $p_{\text{HCl}}$ ,  $p_{\text{HNO}_3}$  and  $p_{\text{H}_2\text{SO}_4}$ , we have to consider that these acids co-adsorb competitively and dissociate after accommodation on the surface.

We first treat this for a binary system, such as adsorption/desorption of  $\text{HCl}$  on a pure material layer (e.g., alumina) and formulate the adsorption by the following reaction:



where  $S$  marks an adsorption site on the surface and  $\text{H}^+ - S$  and  $\text{Cl}^- - S$  are the adsorbed species (where we use  $\text{H}^+$  as short form for  $\text{H}_3\text{O}^+$ ). With  $N_{\text{H}^+}$  and  $N_{\text{Cl}^-}$  being the numbers of adsorbed ions, the number of vacant sites is  $N_{\text{tot}} - N_{\text{H}^+} - N_{\text{Cl}^-}$ , and the rate equation for adsorption/desorption reads:

$$\frac{dN_{\text{Cl}^-}}{dt} = k_{\text{ads}} p_{\text{HCl}} (N_{\text{tot}} - N_{\text{H}^+} - N_{\text{Cl}^-})^2 - k_{\text{des}} N_{\text{H}^+} N_{\text{Cl}^-} , \quad (4.25)$$

In equation 4.25, the adsorption term depends on the square of vacant sites, because two such sites are required to accommodate the anion and cation. In steady-state,  $dN_{\text{Cl}^-}/dt = 0$ , and dividing by  $\sigma^2$ , yields

$$k_{\text{ads}} p_{\text{HCl}} (1 - \theta_{\text{H}^+} - \theta_{\text{Cl}^-})^2 = k_{\text{des}} \theta_{\text{H}^+} \theta_{\text{Cl}^-} . \quad (4.26)$$

For binary  $\text{HCl}$ - $\text{H}_2\text{O}$  adsorption, we have  $\theta_{\text{H}^+} = \theta_{\text{Cl}^-}$ , and with  $K_{\text{HCl}} = k_{\text{ads}}/k_{\text{des}}$ :

$$K_{\text{HCl}} = p_{\text{HCl}} (1 - 2 \theta_{\text{Cl}^-})^2 = \theta_{\text{Cl}^-}^2 , \quad (4.27)$$

or

$$\theta_{\text{Cl}^-} = \frac{\sqrt{K_{\text{HCl}} p_{\text{HCl}}}}{1 + 2 \sqrt{K_{\text{HCl}} p_{\text{HCl}}}} . \quad (4.28)$$

In equation 4.28,  $\theta_{\text{Cl}^-}$  ranges between 0 and a maximum surface coverage of 0.5, when the other half of sites is covered by  $\text{H}^+$ . This adsorption isotherm replaces the common Langmuir isotherm  $\theta_{\text{X}} = K_{\text{X}} p_{\text{X}} / (1 + K_{\text{X}} p_{\text{X}})$  for non-dissociating species. It is important to note that the square root dependence is simply a consequence of the binary nature of the system with  $\theta_{\text{H}^+} = \theta_{\text{Cl}^-}$ , which reverts back to a linear  $K_{\text{X}} p_{\text{X}}$  -dependence when other species control  $\theta_{\text{H}^+}$  (such as  $\text{HNO}_3$ , which is of interest here). For the ternary  $\text{HCl-HNO}_3\text{-H}_2\text{O}$  co-adsorption on a surface, equation 4.26 is replaced by

$$k_{\text{ads}} p_{\text{HCl}} (1 - \theta_{\text{H}^+} - \theta_{\text{NO}_3^-} - \theta_{\text{Cl}^-})^2 = k_{\text{des}} \theta_{\text{H}^+} \theta_{\text{Cl}^-} . \quad (4.29)$$

In the stratosphere,  $\text{HNO}_3$  concentrations are typically one order of magnitude higher than those of  $\text{HCl}$ . Therefore,  $\text{HNO}_3$  dominates in this competitive adsorption process, i.e.,  $\theta_{\text{NO}_3^-} \gg \theta_{\text{Cl}^-}$ , and equation 4.29 simplifies to

$$k_{\text{ads}} p_{\text{HCl}} (1 - 2 \theta_{\text{NO}_3^-})^2 \approx k_{\text{des}} \theta_{\text{NO}_3^-} \theta_{\text{Cl}^-} . \quad (4.30)$$

The resulting co-adsorption isotherm for  $\text{HCl}$  on the  $\text{HNO}_3$ -dominated surface reads then:

$$\theta_{\text{Cl}^-} = K_{\text{HCl}} p_{\text{HCl}} \frac{(1 - 2 \theta_{\text{NO}_3^-})^2}{\theta_{\text{NO}_3^-}} . \quad (4.31)$$

where

$$\theta_{\text{NO}_3^-} = \frac{\sqrt{K_{\text{HNO}_3} p_{\text{HNO}_3}}}{1 + 2 \sqrt{K_{\text{HNO}_3} p_{\text{HNO}_3}}} . \quad (4.32)$$

In the stratosphere, where  $\text{HCl}$  and  $\text{HNO}_3$  concentrations are generally low, we assume the fractional coverages  $\theta_{\text{H}^+}$ ,  $\theta_{\text{NO}_3^-}$  and  $\theta_{\text{Cl}^-}$  to be low. We further assume the ratio of both species,  $R = p_{\text{HNO}_3} / p_{\text{HCl}}$ , to stay roughly constant, which is the case for instance in adiabatic air motion. Hence, equation 4.31 and 4.32 result in:

$$\theta_{\text{Cl}^-} \approx \frac{K_{\text{HCl}} p_{\text{HCl}}}{\sqrt{K_{\text{HNO}_3} p_{\text{HNO}_3}}} \approx \frac{\sqrt{K_{\text{HCl}}}}{\sqrt{K_{\text{HNO}_3} \text{reaction}} / K_{\text{HCl}}} \sqrt{p_{\text{HCl}}} , \quad (4.33)$$

Finally, introducing  $f = \sqrt{K_{\text{HNO}_3} R} / K_{\text{HCl}}$ , we obtain

$$\theta_{\text{Cl}^-} \approx \frac{1}{f} \sqrt{K_{\text{HCl}} p_{\text{HCl}}} . \quad (4.34)$$

Note that the square root dependence on  $p_{\text{HCl}}$  results from the competitive co-adsorption and dissociation of  $\text{HNO}_3$  on the surface (or of  $\text{H}_2\text{SO}_4$ , albeit to a much lower degree because of the much lower partial pressure). Here,  $f$  is the reduction factor, by which the adsorption of  $\text{HCl}$  is reduced through the presence of  $\text{HNO}_3$  relative to a system without  $\text{HNO}_3$  interaction. In the absence of measurements on alumina, we have estimated  $f$  from measurements the  $\text{HCl}$  uptake on ice under conditions characteristic for the lower stratosphere, with  $\text{HNO}_3$  (Hynes et al., 2002) and without  $\text{HNO}_3$  (Zimmermann

et al., 2016). From this we find  $f \approx 33$  (see Figure 4.7). The equations 4.31 and 4.32 should be used if the condition  $\theta_{\text{NO}_3^-} \ll 0.5$  is not satisfied. From equation 4.23 and 4.34 we obtain

$$\frac{1}{\gamma_{\text{ClONO}_2}} = \frac{1}{\alpha_{\text{ClONO}_2}} + \frac{1}{\beta \sqrt{p_{\text{HCl}}}}, \quad (4.35)$$

which is identical to equation 5 in the main text with  $\beta$  given by equation 4 and assuming  $\theta_{\text{NO}_3^-} + \theta_{\text{HSO}_4^-} \ll 1$ .

We performed a least square fit of equation 4.35 to the data of Molina et al. (1997) and obtained values for  $\alpha_{\text{ClONO}_2} = 0.03$  and  $\beta = 59 \text{ torr}^{-0.5}$  (see curve labeled “dissociative  $\gamma_{\text{ClONO}_2}$ , HCl only” in Figure 4.1 and Table 4.1). However, when comparing with uptake coefficients of  $\text{ClONO}_2$  on other materials (e.g., on water or aqueous sulfuric acid, Ammann et al., 2013; Burkholder et al., 2020), a value of  $\alpha_{\text{ClONO}_2} \approx 0.1$  might be more realistic, which would further decrease estimates of  $\gamma_{\text{ClONO}_2}$  at stratospheric partial pressures of HCl (see gray fit in Figure 4.8 and Table 4.1).

If other acids such as  $\text{HNO}_3$  or  $\text{H}_2\text{SO}_4$  co-adsorb ( $\sim 10$  ppb  $\text{HNO}_3$  at 50 hPa in the stratosphere), they will influence the concentration of protons on the surface. We need to distinguish between stratospheric and laboratory conditions of Molina et al. (1997) with  $[\text{HNO}_3] \ll [\text{HCl}]$ , i.e.,  $\theta_{\text{Cl}^-}^0 \approx \theta_{\text{H}^+}^0$ . Under stratospheric conditions, when accounting for the partitioning, co-adsorption and dissociation of  $\text{HNO}_3$  with  $f = 33$ , we obtain  $\gamma_{\text{ClONO}_2} = 0.003$ , i.e. about an order of magnitude less than the nominal 0.02 measured under other conditions by Molina et al. (1997, see Figure 4.8).

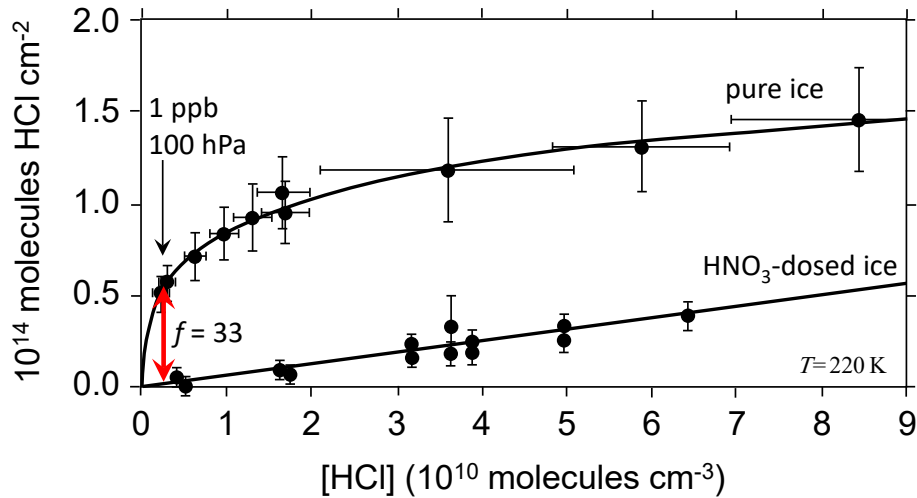


Figure 4.7: Uptake of HCl on ice under near-stratospheric conditions. Data and curves: adsorption isotherms for HCl on ice surfaces at  $\sim 220$  K measured in coated-wall flow-tubes. Upper dataset: HCl on pure ice measured by Zimmermann et al. (2016). Lower dataset: HCl on  $\text{HNO}_3$ -dosed ice measured by Hynes et al. (2002) with  $p_{\text{HNO}_3}$  held at  $\sim 1.3 \times 10^{-6}$  hPa  $\text{HNO}_3$  ( $\sim 4.4 \times 10^{10}$  molecules  $\text{cm}^3$ ) in all experiments measured in the same temperature range as Zimmermann et al. (2016). The vertical red arrow shows the reduction factor  $f=33$  by which the presence of  $\text{HNO}_3$  reduces the uptake of HCl.

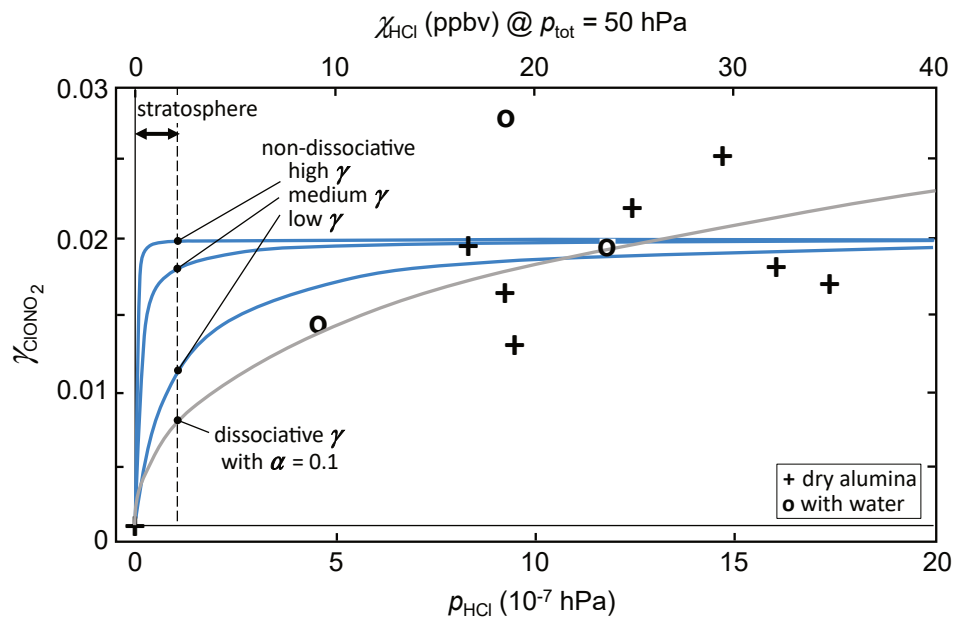


Figure 4.8: Reaction probability  $\gamma_{\text{ClONO}_2}$  for  $\text{ClONO}_2 + \text{HCl}$  on alumina measured by Molina et al. (1997) as a function of  $p_{\text{HCl}}$  (black symbols, see also Appendix 4B) in comparison with uptake coefficients calculated from isotherms of adsorption/desorption and reaction rate coefficients (blue curves). The uptake coefficient based on dissociative adsorption of “HCl only” was calculated using  $1/\gamma_{\text{ClONO}_2} = 1/\alpha_{\text{ClONO}_2} + 1/(\beta\sqrt{p_{\text{HCl}}})$  assuming  $\alpha = 0.1$  and  $\beta$  fitted to the data and for non-dissociative HCl adsorption using  $1/\gamma_{\text{ClONO}_2} = 1/\alpha_{\text{ClONO}_2} + 1/(\beta p_{\text{HCl}})$  with fixed values  $\alpha_{\text{ClONO}_2} = 0.02$  and varying  $\beta$  by three orders of magnitude (see Table 4.1). Typical stratospheric values of  $p_{\text{HCl}}$  are below  $\sim 1 \times 10^{-7}$  hPa (below dashed vertical line).

## **G: Sensitivity to injected particle size and surface area availability**

When injecting particles with a radius of 80 nm instead of 240 nm at 5 Mt/yr, the globally averaged aerosol burden is 5.2 Mt with a SAD of up to  $16 \mu\text{m}^2/\text{cm}^3$  (see Figure 4.9c). Compared to injecting particles with radius of 240 nm SAD is increased about 4 times. This significantly increases zonally averaged ozone column depletion to 35% in the south polar region and 13% in the tropics for 80 nm particle injection using the “non-dissociative high  $\gamma_{\text{ClONO}_2}$ ” parameterization. When injecting 80 nm particles, also the lower estimate scenario, “non-dissociative low  $\gamma_{\text{ClONO}_2}$ ” results in significant total ozone column depletion of up to 15% over the polar regions. This shows that the availability of SAD is a critical factor for heterogeneous chlorine activation on alumina particles (see also Equation 1 in the main text). Injecting particles with a small radius or injecting fractals of larger particles must be avoided since this results in significantly larger SAD while also reducing the scattering efficiency of the particles (Dykema et al., 2016, e.g.).

Injecting the same rate of  $\text{SO}_2$  instead of alumina particles with radius of 240 nm also results in a much larger SAD (i.e.,  $16\text{-}20 \mu\text{m}^2/\text{cm}^3$ , see Figure 4.9), which is partially due to the much larger particle size of the alumina particles compared to the average aerosol size of the sulfuric acid aerosols. This results in larger SAD per mass unit for sulfuric acid aerosols. However, the sulfuric acid aerosols also have a smaller density, which together with the smaller particle size results in much lower sedimentation velocities and thus, in larger stratospheric aerosol burden ( $\sim 10 \text{ Mt H}_2\text{SO}_4\text{-H}_2\text{O}$ ) compared to alumina injections with a radius of 240 nm ( $\sim 3.7 \text{ Mt alumina}$ ). The resulting total top of the atmosphere radiative forcing is about  $1.0 \text{ W/m}^2$  for  $\text{SO}_2$  injections compared to  $0.75 \text{ W/m}^2$  for alumina injections at 240 nm radius when injecting 5 Mt/yr of material.

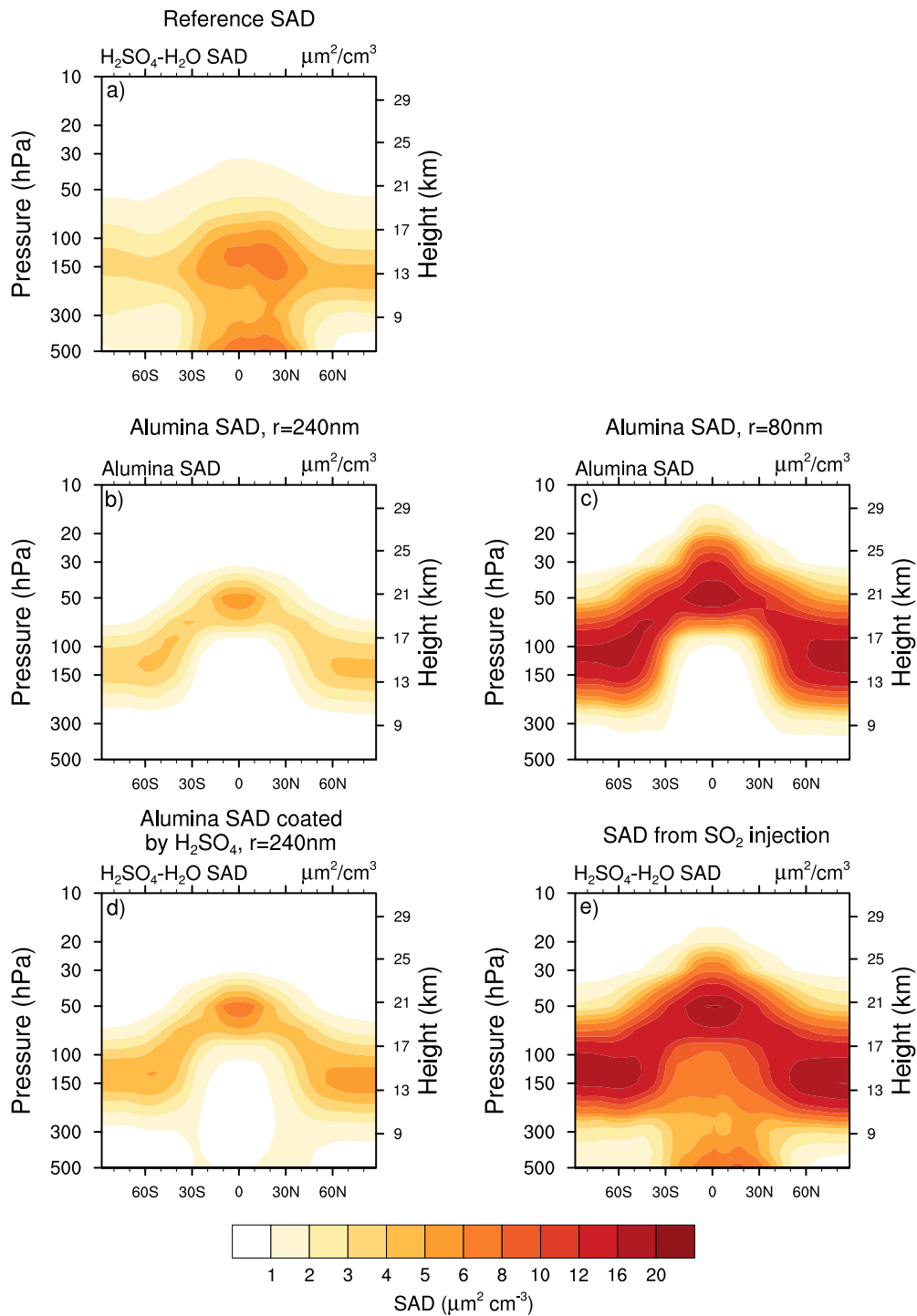


Figure 4.9: Zonal mean of resulting total SAD of different model scenarios averaged over 10 years. Panel a) and e) show only sulfuric acid aerosol SAD of the reference and the  $\text{SO}_2$  injection scenario, respectively. Panel b) and c) show only bare alumina SAD resulting from 5 Mt/yr injection of particles at radius of 240 nm and 80 nm, respectively. Panel d) shows the sum of  $\text{H}_2\text{SO}_4\text{-H}_2\text{O}$  coated alumina SAD and sulfuric acid aerosol SAD for the “ $\text{H}_2\text{SO}_4$  coating” scenario (see scenarios in Table 4.1).

## H: Composition changes

HCl and ClONO<sub>2</sub> represent two important reservoir species of stratospheric ozone chemistry. When injecting 5 Mt/yr of alumina particles with radius of 240 nm assuming the “non-dissociative medium  $\gamma_{\text{ClONO}_2}$ ” parameterization results in up to 70% HCl loss in the lower stratosphere as a result of reaction 4.1 (Figure 4.11, left column). However, for ClONO<sub>2</sub> we observe an increase in concentrations of up to 90% (Figure 4.11, left column) which is due to the much faster reformation of ClONO<sub>2</sub> via reaction 4.3 compared to destruction via R1. The significantly increased ClONO<sub>2</sub> concentration would additionally lower the calculated  $\gamma_{\text{ClONO}_2}$  used in the parameterization from Weisenstein et al. (2015, see Appendix 4C, and Figures 4.4, 4.10a and 4.10b), whereas our parameterization is not dependent on  $p_{\text{ClONO}_2}$ .

When assuming the alumina particles to be coated by sulfuric acid (Figure 4.11, middle column) or when injecting SO<sub>2</sub> (Figure 4.11, right column) the increased sulfuric acid aerosol SAD (Figure 4.9) provides surface for N<sub>2</sub>O<sub>5</sub> hydrolysis (Reaction 4.36). This results in TOC depletion due to less availability of NO<sub>x</sub> and thus reduced deactivation of ClO<sub>x</sub> via reaction 4.3 under present day concentrations of ozone depleting substances (ODS, see Figure 4.11, middle and right column). However, due to the lower SAD availability in the “H<sub>2</sub>SO<sub>4</sub> coating” alumina injection scenario (see Appendix 4G), which assumes the particles to be coated by H<sub>2</sub>SO<sub>4</sub>–H<sub>2</sub>O (Figure 4.11, middle column) the ozone alteration is much smaller compared to ozone alteration from SO<sub>2</sub> injections.

Under 2090 conditions, when ODS concentrations are lower again, we still observe the same effects on stratospheric composition changes, but with much smaller anomalies, which is mainly due to the lower stratospheric chlorine concentrations (Figure 4.12). However, the reduction in stratospheric chlorine by the year 2090 is not yet large enough in SOCOL-AER to turn the ozone depletion in an ozone increase due to deactivation of NO<sub>x</sub>.



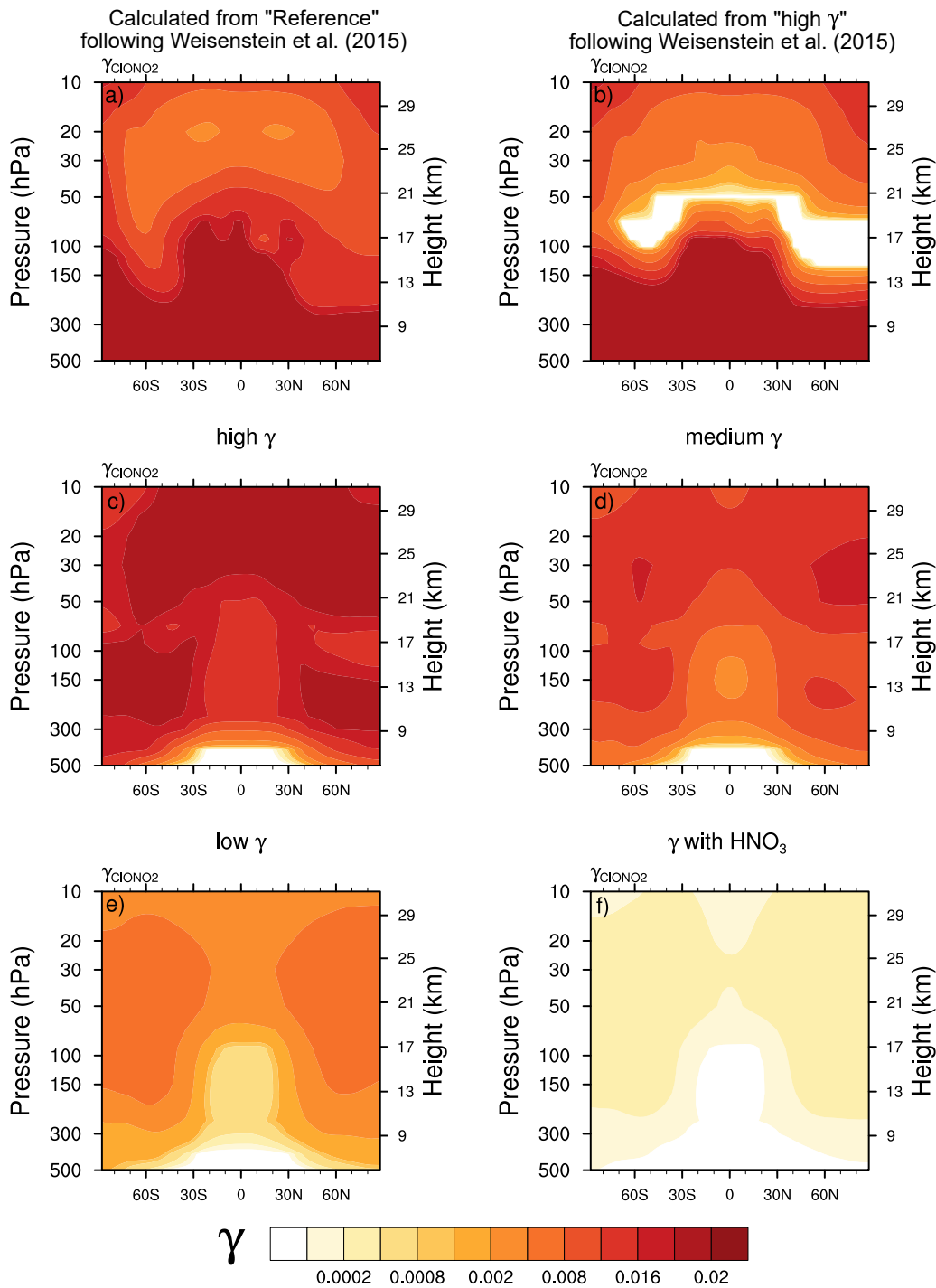


Figure 4.10: Panels a) and b) show the resulting  $\gamma_{\text{ClONO}_2}$  when calculating following the method used in Weisenstein et al. (2015, i.e. scaling with  $[\text{HCl}]/[\text{ClONO}_2]$ , see Appendix 4B and Figure 4.4) with HCl and ClONO<sub>2</sub> concentrations resulting from a) our reference simulation and b) the “non-dissociative high  $\gamma_{\text{ClONO}_2}$ ” scenario. Panels c) to f) show the resulting  $\gamma_{\text{ClONO}_2}$  when applying our own “non-dissociative, HCl-only” parameterizations derived in this paper (see Figure 4.1, Figure 4.8 and Table 4.1).

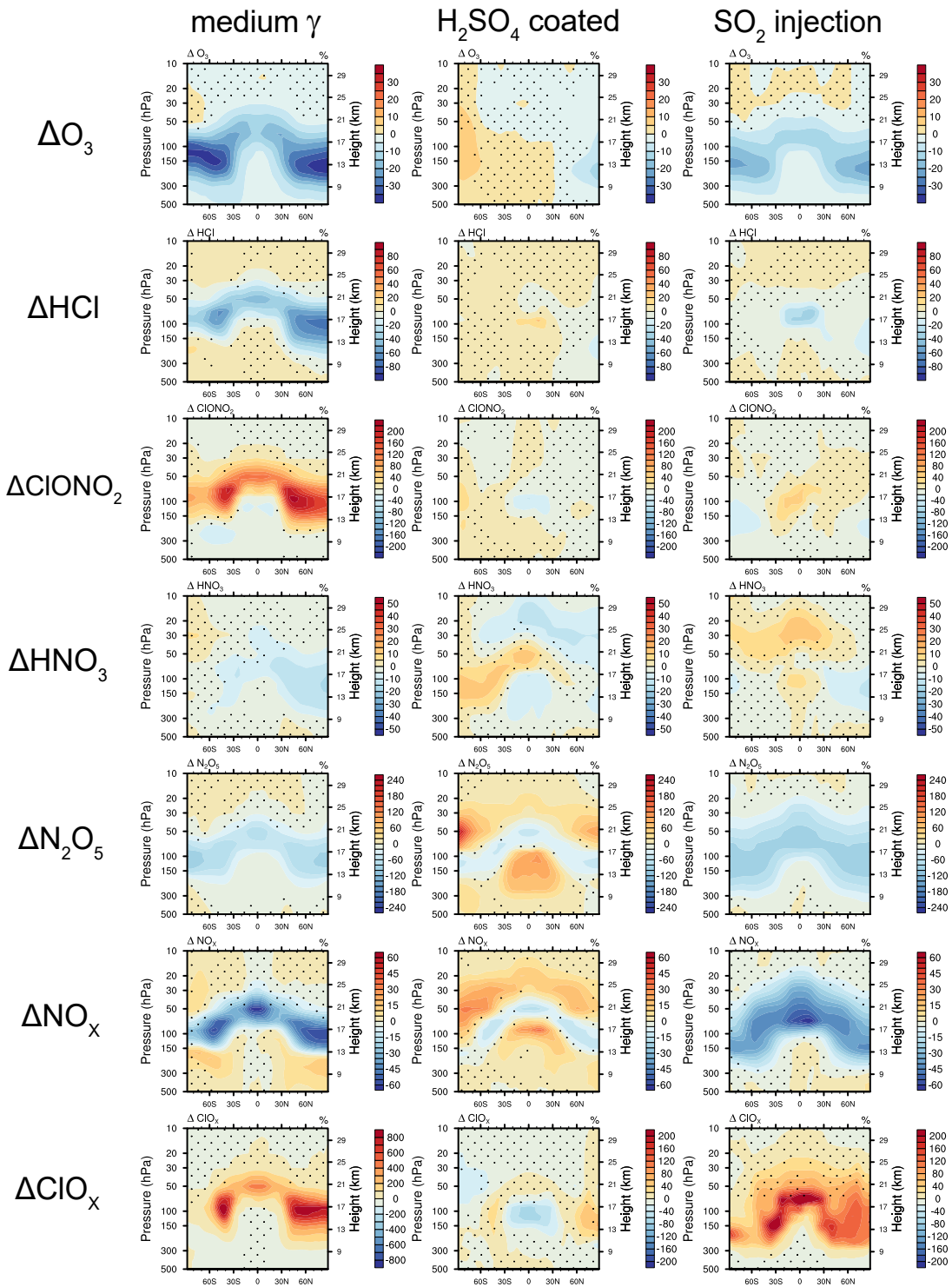


Figure 4.11: The resulting  $O_3$ , HCl,  $ClONO_2$ ,  $HNO_3$ ,  $N_2O_5$ ,  $NO_x$  and  $ClO_x$  anomalies from the “non-dissociative, HCl only, medium  $\gamma_{ClONO_2}$ ” and the “ $H_2SO_4$  coated” scenarios (see also Table 4.1) with injection radius of 240 nm as well as the  $SO_2$  injection scenarios for 2020 ODS and green house gas (GHG) conditions. Dotted areas represent statistically insignificant values on the 95% t-test interval.

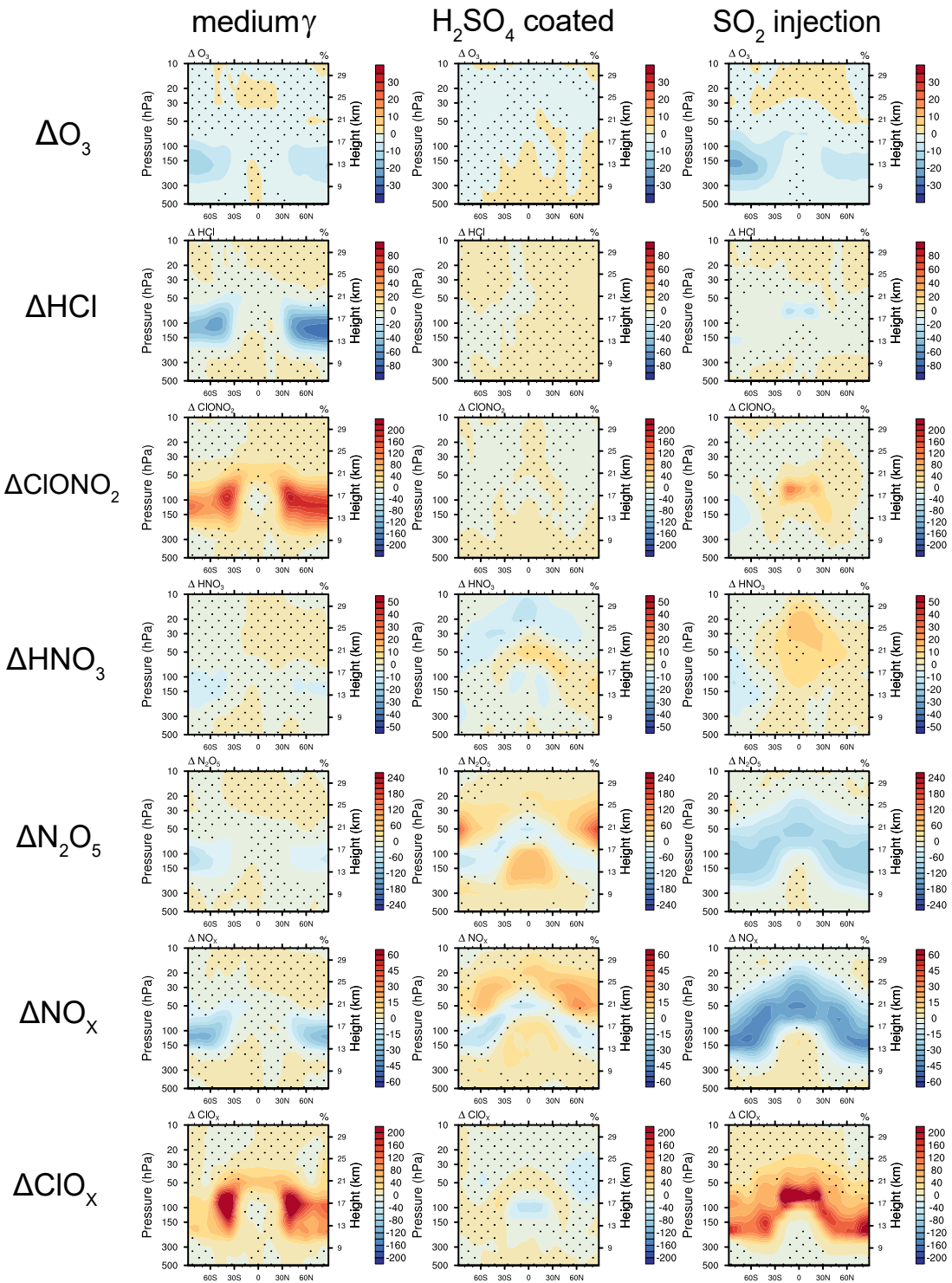
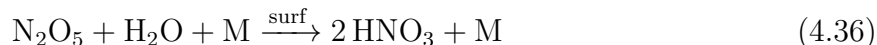


Figure 4.12: The resulting  $O_3$ ,  $HCl$ ,  $ClONO_2$ ,  $HNO_3$ ,  $N_2O_5$ ,  $NO_x$  and  $ClO_x$  anomalies from the “non-dissociative,  $HCl$  only, medium  $\gamma_{ClONO_2}$ ” and the “ $H_2SO_4$  coated” scenarios (see also Table 4.1) with injection radius of 240 nm as well as the  $SO_2$  injection scenarios for 2090 ODS and GHG conditions. Dotted areas represent statistically insignificant values on the 95% t-test interval.

## I: Sensitivity to injection altitude and to other heterogeneous reactions on solid particles

Injection at 25 km ( $\sim 20$  hPa) instead of 20 km ( $\sim 54$  hPa) increases the stratospheric alumina burden by 41% from 3.67 Mt to 5.19 Mt. SAD increases correspondingly and leads to a decrease in zonal mean TOC across all latitudes (see Figure 4.12).

In addition to simulations representing the various parameters used for parameterizations of reaction 4.1, we also performed simulations which account for heterogeneous reactions 4.36 and 4.37 on alumina surfaces.



In view of the lack of experimental data, we assume the same  $\gamma$  as for heterogeneous reactions on sulfuric acid aerosols for reactions 4.36 and 4.37 (Sheng et al., 2015). This is likely an upper limit estimate, since the real  $\gamma$  of these reactions on solid particles is possibly smaller due to larger availability of  $\text{H}_2\text{O}$  on sulfuric acid aerosols compared to solid particles.

Under conditions with present day stratospheric chlorine concentrations, reactions 4.36 and 4.37 are both expected to increase ozone depletion due to additional chlorine activation (4.37) and decreased chlorine deactivation due to removal of  $\text{NO}_x$  (reaction 4.3). However, the resulting TOC anomalies from taking into account these two reactions only result in about 1-2% more ozone depletion compared to scenarios which do not take these reactions into account (Figure 4.13). Therefore, we conclude that reaction 4.1 is the most important heterogeneous reaction impacting stratospheric ozone under present day chlorine conditions.

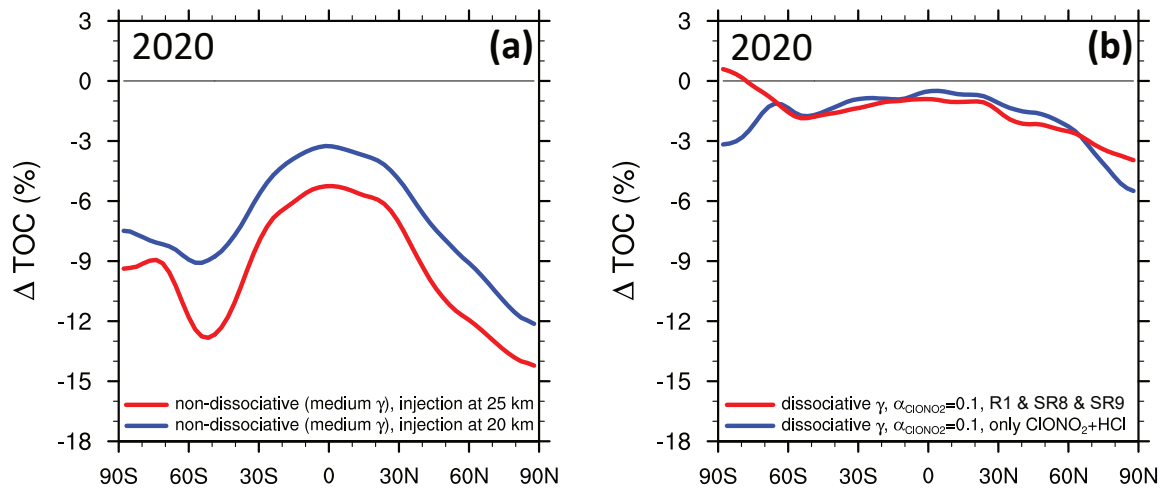


Figure 4.13: Zonal mean of 10 year averaged TOC depletion resulting from injection of 5 Mt per year of alumina particles simulated with SOCOL-AER under 2020 conditions. Panel (a) shows TOC depletion resulting when applying the "non-dissociative medium  $\gamma_{\text{ClONO}_2}$ " scenario (see Appendix 4A and 4F) when injecting at 25 km altitude (red) instead of 20 km altitude (blue). Panel (b) shows TOC depletion when applying the "best fit dissociative  $\gamma_{\text{ClONO}_2}$ " scenario with  $\alpha_{\text{ClONO}_2}$  set to 0.1 (see Appendix 4A and 4F), when only accounting for reaction 4.1 (blue) and when additionally accounting for reactions 4.36 and 4.37 (red) with same heterogeneous reaction rates as for sulfuric acid aerosols.



## Chapter 5

# X-ray photoelectron spectroscopy and elastic recoil detection analysis to quantify uptake of HCl and HNO<sub>3</sub> on calcite surfaces

### Abstract

Stratospheric aerosol injection (SAI) has been proposed as a means for climate intervention, for example by emitting SO<sub>2</sub>, which is oxidized and forms aqueous sulfuric acid aerosols that scatter some of the incoming solar radiation back to space and cool the planet. Recent studies have indicated that injecting calcite particles instead of SO<sub>2</sub> could reduce some of the adverse side effects of SAI, such as ozone depletion, if the uptake of stratospheric HCl and HNO<sub>3</sub> by calcite reduces the concentrations of ozone-depleting chlorine and nitrogen species (ClO<sub>x</sub> and NO<sub>x</sub>). However, heterogeneous chemistry on calcite particles in the stratosphere is subject to large uncertainties. Using in situ X-ray photoelectron spectroscopy (XPS) and elastic recoil detection analysis (ERDA), we measured the uptake of HNO<sub>3</sub> and HCl on calcite under near-stratospheric conditions, and determined their penetration into deeper layers below the surface and the chemical transformation of calcite into calcium chlorides and nitrates. We find uptake coefficients  $\gamma_{\text{HNO}_3} = 10^{-5}$  to  $10^{-4}$  for HNO<sub>3</sub> measured with XPS and  $\gamma_{\text{HNO}_3, \text{HCl}} = 10^{-6}$  to  $10^{-5}$  for both HNO<sub>3</sub> and HCl measured with ERDA. The XPS measurements were carried out under stratospheric conditions in terms of temperature, relative humidity and HNO<sub>3</sub> concentrations and lasted up to 20 hours. They show that nitrate penetrates to sample depths of a few nanometers within the first hours of exposure, followed by a progressive slowdown of the uptake process at later times. In comparison, elemental analysis with ERDA on samples exposed for 10 days to HNO<sub>3</sub> or HCl concentrations 2-3 orders of magnitude higher than in the stratosphere indicates a diffusion-like penetration of nitrogenous species to depths greater than 250 nm. Putting our results into context of SAI, we conclude that the uptake coefficient of HCl and HNO<sub>3</sub> decreases with stratospheric exposure time. The reason for this is a layer that is increasingly enriched with nitrogen- and chlorine-containing reaction products (likely Ca(NO<sub>3</sub>)<sub>2</sub> and CaCl<sub>2</sub> hydrates), whose depth increases with exposure, as evidenced by the ERDA depth profiles. This, in turn, leads to an increasing protection of the underlying CaCO<sub>3</sub> core. The measurements indicate that exposure of these particles to typically 5 ppb HNO<sub>3</sub> and 1 ppb HCl over stratospheric residence times of about 1 year leads to mean uptake coefficients  $< 10^{-4}$ , which represents a strong constraint on uptake. However, a burden of 5 Mt CaCO<sub>3</sub> particles with an initial radius of 240 nm could still reduce the gas phase of HNO<sub>3</sub> and HCl by about 50% each and convert half of the calcite mass to nitrates and chlorides. Owing to the limited gas uptakes, the effects on ozone may be much smaller than previously thought.

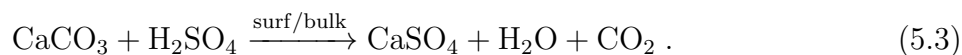
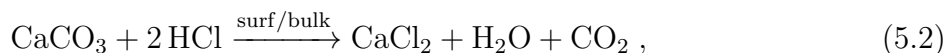
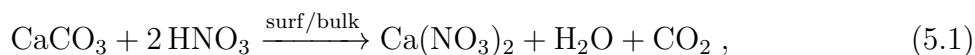
**This chapter will be submitted as:**

**Vattioni, S.**, Telliou, P., Klaus, O., Vockenhuber, C, Döbeli, M., Longetti, L., Artiglia, L., Yang, H., Manoharan, Y., Gabathuler, J.-P., Bartels-Rausch, T., Luo, B., Krieger, U., Keutsch, F., Ammann, F., Peter, T., Chiodo, G. (2024). X-ray photoelectron spectroscopy and elastic recoil detection analysis to quantify uptake of HCl and HNO<sub>3</sub> on calcite surfaces **American Chemical Society (ACS), Earth and Space Chemistry**

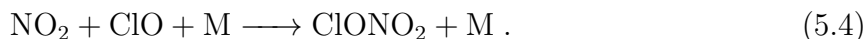


## 5.1 Introduction

Stratospheric aerosol injection (SAI) is a proposed technique designed to reduce risks of climate change by injecting aerosol particles into the lower stratosphere to increase the Earth's albedo and cool the climate. In measures against climate change, SAI has the potential to serve as temporary supplement to mitigation and adaptation, until society finds solutions how to remove long-lived greenhouse gases from the atmosphere (MacMartin et al., 2014; Keith and MacMartin, 2015). This motivates research on the risks and benefits of SAI. A research focus has been on SAI applying sulfuric acid aerosols based on the natural analogue of volcanic eruptions (Budyko, 1974; Crutzen, 2006). However, sulfur-based SAI is associated with a number of adverse side effects, including stratospheric warming (e.g., Aquila et al., 2014; Dykema et al., 2016) and depletion of the stratospheric ozone layer (e.g., Tilmes et al., 2008; Weisenstein et al., 2022). Recent modeling studies suggest that using solid particles such as calcite particles instead of sulfate aerosols would result in more effective cooling per stratospheric aerosol burden due to better optical properties and at the same time reduce the impact on stratospheric ozone (Weisenstein et al., 2015; Dykema et al., 2016; Keith et al., 2016; Dai et al., 2020). Keith et al. (2016) suggested that calcite particles could react with stratospheric acids such as HNO<sub>3</sub>, HCl and H<sub>2</sub>SO<sub>4</sub> (in the sequence of the abundance of these acidic gases in the stratosphere) by generating calcium salts and releasing CO<sub>2</sub> and H<sub>2</sub>O:



These chemical reactions are well-known, but their importance under stratospheric conditions is uncertain. They can lead to significant removal of HNO<sub>3</sub> and HCl, two reservoir species of nitrogen and chlorine oxides (NO<sub>x</sub> and ClO<sub>x</sub>), via irreversible uptake by the calcite particles (reactions 5.1-5.2) and subsequent removal of these particles from the stratosphere via the atmospheric circulation and gravitational settling. On the one hand, strong uptake of HNO<sub>3</sub> may lead to increased ozone depletion under present day conditions due to reduction of NO<sub>2</sub> concentrations, which is important for the deactivation of ClO:



On the other hand, strong uptake of HCl would result in removal of reactive chlorine from the stratosphere, which might accelerate the recovery of the stratospheric ozone layer (Keith et al., 2016). However, the efficiency of the reactive uptake of HNO<sub>3</sub>, HCl and H<sub>2</sub>SO<sub>4</sub> on the calcite surfaces is highly uncertain, because the formation of a thin shell of Ca(NO<sub>3</sub>)<sub>2</sub>, CaCl<sub>2</sub> and CaSO<sub>4</sub> could limit the diffusion of NO<sub>3</sub><sup>-</sup> ions into the solid particles and passivate the calcite core, which remains unprocessed (Cziczo et al., 2019). In this case the particles would largely maintain the optical properties of calcite and reduce their impact on stratospheric ozone via uptake of HCl, HCl and H<sub>2</sub>SO<sub>4</sub>. Conversely, depending on the particle type (Huynh and McNeill, 2020) and size and on the injection rate persistent uptake could potentially lead to complete transformation of the particle to Ca(NO<sub>3</sub>)<sub>2</sub>, CaCl<sub>2</sub> and CaSO<sub>4</sub>, which could significantly alter the optical and chemical properties of the particles. While Huynh and McNeill (2020, 2021) measured uptake

coefficients larger than  $7.6 \times 10^{-3}$  for HNO<sub>3</sub> and HCl, Dai et al. (2020) showed an increasing passivisation effect with longer exposure times.

For reaction 5.3, an uptake coefficient ( $\gamma_{\text{H}_2\text{SO}_4}$ ) of 1.0 can be assumed since the equilibrium vapor pressure of aqueous H<sub>2</sub>SO<sub>4</sub> is very low in the stratosphere leading to very efficient condensation of H<sub>2</sub>SO<sub>4</sub>, together with H<sub>2</sub>O on any available surfaces. In contrast, under stratospheric conditions  $p_{\text{HNO}_3}$  and  $p_{\text{HCl}}$  are far below the equilibrium vapor pressure of their aqueous solutions. However, concentrations of both species are high enough to allow for a monolayer coverage within minutes when assuming  $\gamma = 1$  (Vattioni et al., 2023a). Various experimental studies used aerosol flow tube reactors or Knudsen cell reactors and quantified the uptake coefficient of HNO<sub>3</sub> and to a smaller extent of HCl at wide ranges of relative humidities (RH), temperature and concentrations of HCl and HNO<sub>3</sub> (summarized in Tables S1 and S2), for example by means of Fourier transform infrared spectroscopy. The uptake coefficients of HNO<sub>3</sub> ( $\gamma_{\text{HNO}_3}$ ) and HCl ( $\gamma_{\text{HCl}}$ ) resulting from these studies range between  $1 \times 10^{-5}$  and  $1 \times 10^{-1}$  for  $\gamma_{\text{HNO}_3}$  (Fenter et al., 1995; Underwood et al., 2000; Goodman, 2000; Johnson et al., 2005; Vlasenko et al., 2006; Liu et al., 2008; Santschi and Rossi, 2006; Dai et al., 2020; Huynh and McNeill, 2020) and between  $1 \times 10^{-12}$  and  $1 \times 10^{-1}$  for  $\gamma_{\text{HCl}}$  (Santschi and Rossi, 2006; Dai et al., 2020; Huynh and McNeill, 2020, 2021).

### 5.1.1 Factors influencing uptake coefficient measurements

In reviewing these studies, we identified several key processes which determine the uptake coefficients reported in these studies (see Table and 5.3 and 5.4 in the Appendix 5A).

**Exposition.** Importantly, most of the measured uptake coefficients decrease with increasing exposure (= reactant concentration times duration of exposition) suggesting passivation with increasing uptake, which might be caused by a solid-state diffusion limitation becoming stronger over time (Dai et al., 2020). Except for the measurements of Huynh and McNeill (2020), the exposure dependence is particularly evident in the values for the uptake of HCl (see Table 5.3 and Table 5.4). The reported uptake coefficients depend on whether the long-term uptake or only the initial uptake was examined, with lower  $\gamma$  or higher  $\gamma$  being preferred. The initial high uptake can be described by an adsorption-reaction mechanism, which is important as long as surface sites are available. Beyond this initial phase, further uptake of these acids depends on their solid-phase diffusivity and reactivity in the CaCO<sub>3</sub> matrix (see Section S2).

**Temperature.** Another major source of uncertainty of experimental work are the temperature at which the measurements were carried out. Most experimental work reported in Table 5.3 and 5.3 was performed at room temperature (except for Dai et al., 2020; Huynh and McNeill, 2021), while the temperatures in the stratosphere can be 210 K and lower. On the one hand, lower temperatures lead to a decrease of the rate of thermally activated reactions as well as of diffusion in the solid phase. On the other hand the equilibrium coverage of adsorbed trace gases on the surface would increase with decreasing temperature due to the change in adsorption enthalpy (Vlasenko et al., 2009). While it is unclear, which of these two aspects dominates for reactions 5.1-5.2 in the surface mode, the negative temperature dependence of the reactivity and diffusivity will dominate in the bulk mode.

**Relative humidity.** In addition, the availability of water at the sample surface can influence the initial uptake. On the reaction time scale of minutes, Fenter et al. (1995) measured a decrease in  $\gamma_{\text{HNO}_3}$  by factors 2-3 when calcite pellets were dried after

compression (see Table 5.4). On reaction time scale of 2 s, an increase of  $\gamma_{\text{HNO}_3}$  by a factor 5 when increasing RH from 10% to 80% occurred on Arizona test dust aerosol particles, whose reactivity was assumed to be dominated by the presence of CaCO<sub>3</sub> (Vlasenko et al., 2006).

Accounting for stratospheric temperature and humidity during experiments is especially important since CaCl<sub>2</sub> and Ca(NO<sub>3</sub>)<sub>2</sub> form highly concentrated solutions at low relative humidity (Zhu et al., 2018; Cziczko et al., 2019). Several studies have reported a deliquescence RH (DRH) as low as 7% and 11% for Ca(NO<sub>3</sub>)<sub>2</sub> at room temperature (Liu et al., 2008; Al-Hosney and Grassian, 2005; Prince et al., 2007; Sullivan et al., 2009) and even lower efflorescence RH. Uptake experiments conducted above this DRH measure another uptake reaction mechanism than those with effloresced salts (see Section S2). The DRH depends on temperature (Stahlbuhk, 2016) and is larger at lower temperatures. Under stratospheric conditions Ca(NO<sub>3</sub>)<sub>2</sub> as well as CaCl<sub>2</sub> might also form hydrates (Stahlbuhk, 2016; Steiger et al., 2011) due to the strong hygroscopicity of these salts. Several studies have shown that under ambient atmospheric conditions calcite surfaces show a termination layer with OH groups that will remain attached even under dry and ultrahigh vacuum conditions at room temperature (Santschi and Rossi, 2006; Huynh and McNeill, 2020, 2021). This Ca(OH)(HCO<sub>3</sub>) termination layer forms by dissociative chemisorption of water. This hydroxyl terminated surface attracts additional reversibly adsorbed water and allows an overall increased mobility of ions and thus uptake efficiency of acids with increasing relative humidity (Dai et al., 2020). This may lead to stabilization of liquid-like layers on the calcite surface that would allow diffusional exchange of hydrated acids and the calcite underneath. Thus, information on the existence, the thickness, the structure, the morphology and the hydration state of the CaCl<sub>2</sub>, Ca(NO<sub>3</sub>)<sub>2</sub> or CaSO<sub>4</sub> products at the particle surface as well as their development in time is important for impact analysis on stratospheric chemistry of potential calcite SAI scenarios.

**Surface roughness.** Santschi and Rossi (2006) found  $\gamma_{\text{HNO}_3}$  to be lower by a factor of 4 on polished calcite compared with freshly cut, rough calcite. This difference could be explained from the expected lower concentration of defect sites on the surface in case of polished sample, which in return leads to less water absorbance and ultimately to less Ca(OH)(HCO<sub>3</sub>) at the surface. For uptake of HCl, the polishing of the marble disks (limestone, consisting chiefly of calcite) resulted in a reduction of HCl uptake below the detection limit of their setup, which excludes bias of the uptake coefficients by taking the geometric area and thus, omitting changes in available surface area in the calculations of  $\gamma$ .

**Surface area.** Finally, there is an ongoing debate about the method how uptake coefficients are calculated from experimental data. Measurement techniques, which derive the uptake coefficients from differences between upstream and downstream gas phase concentrations (e.g., in Knudsen cells or coated or aerosol flow tubes) require accurate information about the available surface area of their samples. On the one hand, some studies reasoned that the BET-surface is not the appropriate reactive surface to calculate  $\gamma$ , since they found  $\gamma$  values to be independent of the grain size (Hanisch and Crowley, 2001) or of the sample type (powder vs. pellet, Fenter et al., 1995). However, the measured uptake coefficient in Hanisch and Crowley (2001) decreased by a factor of 10 when going from a CaCO<sub>3</sub> powder to an unpolished calcite crystal. Therefore, this decrease can only be explained by a decrease in reactive sites per geometric area. On the other hand, all publications by the Grassian Group argue that the internal surface area is to be accounted for when determining number of collisions for the initial uptake coefficient (Underwood

et al., 2000; Goodman, 2000; Johnson et al., 2005; Liu et al., 2008). This correction can lead to differences in reported uptake coefficients spanning more than one order of magnitude as reported by (Johnson et al., 2005, see Table 5.3). However, using the entire BET surface as available for collision might also be an overestimate and the reported uptake coefficient might be too low. This further complicates comparison of experimental results across publications. Related to the uncertainties associated with the accessible surface area, aerosol flow tube studies are considered more reliable (Crowley et al., 2010).

**Comparison of these factors.** Tendencies of the uptake coefficient include: (i) a decrease in the bulk mode of (5.1-5.2) when temperature decreases; (ii) a decrease when decreasing RH or drying the sample before the measurement; (iii) a decrease when going from a powder sample to a rough surface pellet to a smooth single crystal surface; (iv) a decrease when accounting for the BET correction; (v) a decrease when increasing the exposure. While there is some preliminary evidence that (i)-(iv) affect  $\gamma_{\text{HNO}_3}$  and  $\gamma_{\text{HCl}}$  on calcite typically by less than a factor of 10, (v) affects the  $\gamma$ 's very strongly, i.e., different exposures may change the  $\gamma$ 's by 3-12 orders of magnitude, see below. Therefore, the influence of exposure on  $\gamma_{\text{HNO}_3}$  and  $\gamma_{\text{HCl}}$  is the main subject of this investigation.

### 5.1.2 The importance of "long-term" depth-resolving experiments under stratospheric conditions

Experimental methods are required that probe the first few monolayers directly below the surface and also to enable monitoring the slow diffusion-like exchange processes at greater depth scales for calcite. Ambient Pressure X-ray Photoelectron Spectroscopy (AP-XPS) and Heavy Ion Elastic Recoil Detection Analysis (HI-ERDA) are perfectly suited to provide the required chemical and physical information (see Figure 5.1 for details).

XPS is based on photoionization of core electrons of elements in a sample by X-rays and measurement of the kinetic energy distribution of the escaping photoelectrons. Photoelectrons from atoms in the outermost monolayer, which do not undergo inelastic scattering, appear in well defined peaks at a kinetic energy ( $E_k$ ) corresponding to the difference between the exciting X-ray photon energy ( $E_{h\nu}$ ) and the binding energy ( $E_B$ ) of the core level of the different elements of a sample.  $E_B$  is characteristic for the element and its chemical state (oxidation state, bonding, environment). Hence, XPS not only shows what elements are present, but also what other elements they are bonded to, i.e. provides molecular information. For photoelectrons emerging from deeper levels, strong inelastic scattering occurs with an  $E_k$ -dependent characteristic inelastic mean free path (IMFP) of 1 to 3 nm in the range of  $100 \text{ eV} < E_k < 1000 \text{ eV}$ . This enables XPS to provide chemical composition information from within the outermost few nanometers of a sample. While traditionally performed in ultra-high vacuum, recent developments of AP-XPS allows performing XPS analysis at pressures up to a few hectopascals (Frank Ogletree et al., 2009). Thus, in-situ experiments under stratospheric conditions with respect to trace gas concentrations, temperature and RH have become possible (Orlando et al., 2016).

HI-ERDA is an ion beam detection method which allows analyzing the depth-resolved elemental composition of the upper few 100 nm of a sample. While it makes a much deeper layer accessible than XPS, it provides only elemental composition and requires offline sampling with long periods of up to months, to assess long term solid-phase diffusion of ions deep into the matrix of samples. HI-ERDA is based on the bombardment of samples with heavy ions (in our case <sup>127</sup>I), which hit the surface at high, predefined energies

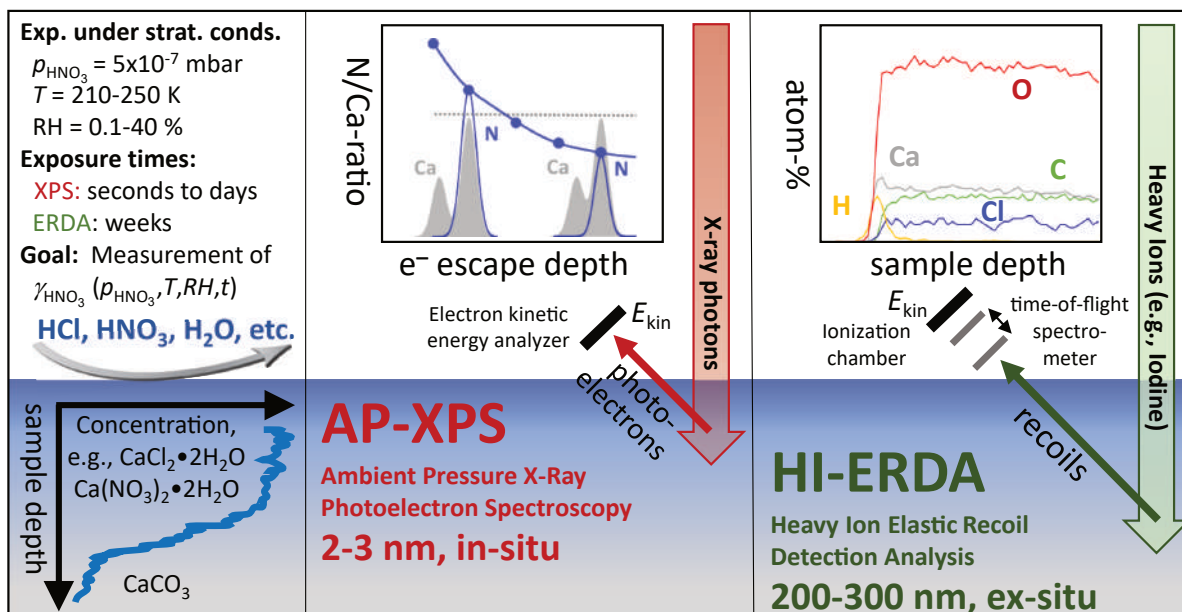


Figure 5.1: Schematic overview of the experimental techniques applied in this study. XPS detects the kinetic energy ( $E_k$ ) of photoelectrons during X-ray irradiation, allowing the atomic density and chemical state of the sample in the upper 2-3 nm to be determined in-situ under stratospheric conditions in terms of temperature, relative humidity and trace gas partial pressures. In contrast, HI-ERDA is an ex-situ measurement technique based on the scattering of MeV ions to measure elemental composition depth profiles to a few hundred nanometers. In this work we use 13 MeV iodine ions under 17° glancing incidence to determine the elemental composition as a function of depth.

between 1.5 and 100 MeV, determining the penetration depth of the ions (L’Ecuyer et al., 1976; Assmann et al., 1994). These heavy ions collide with the nuclei of the atoms in the sample, which subsequently are elastically recoiled. Some of the recoiled atoms eventually leave the sample. Their energies can be measured under a predefined scattering angle, which allows us to determine the mass of the recoiled atoms and thus, the exact elemental composition as a function of depth.

Combining these two techniques addresses the evolution of the surface composition and the diffusion of ions ( $\text{NO}_3^-$  and  $\text{Cl}^-$  in this study) into the bulk of the calcite samples and thus, they allow quantifying time dependent uptake coefficients  $\gamma_{\text{HNO}_2}$  and  $\gamma_{\text{HCl}}$  over relevant time and spatial scales (see Figure 5.1). The physico-chemical and kinetic parameters obtained from the two methods are the backbone of understanding chemical aging processes and their representation in numerical models.

## 5.2 Methods

This section describes first the AP-XPS method as well as the experimental AP-XPS set-up and the attenuation model used to calculate the depth profiles measured with AP-XPS. Subsequently a description of the HI-ERDA method as well as the experimental setup applied in this study is provided.

### 5.2.1 Ambient Pressure X-ray Photoelectron Spectroscopy (AP-XPS)

XPS is a spectroscopic technique based on photo-emission of electrons due to ionising radiation that impinges on the sample. With the use of monochromatic radiation with specific energy  $E(h\nu)$ , one can retrieve the binding energy  $E_B$  of the photoemitted electrons in force of the energy conservation, as from the following equation (equation 5.5):

$$E_B = E(h\nu) - E_k - W , \quad (5.5)$$

where  $W$  is the work function and  $E_k$  is the measured kinetic energy of photoelectrons (see also Figure 5.2). Electrostatic charging of a non-conducting sample leads to an additional variable shift. The extent of shift due to charging and  $W$  can be taken into account by calibrating the  $E_B$  scale using an element with known  $E_k$  (see below).

In this work we exploit the elemental selectivity of XPS to investigate the relative abundance of chemical species as a function of depth from the sample surface. This is possible thanks to the specific binding energies of core-level electrons of different elements and by exploitation of the electron mean free path of photoelectrons to tune the probing depth by varying their kinetic energy (Matthew, 2004; Greczynski and Hultman, 2022). The measured photo electron (PE) signal intensity ( $I_X$ ) related to a specific elemental core level is the integral of the signal from all corresponding atoms from the surface to infinite depth ( $z$ ) below the sample, with the contribution from an atom at a given depth to the measured signal decreasing exponentially with increasing depth (see equation 5.6 and also Figure 5.2), where  $\theta$  is the acceptance angle of the spectrometer, which is 30° in our setup:

$$I_{X, \text{norm}}(E_k) = \frac{I_X}{\phi(h\nu, X) T(E_k) \sigma_{X, \text{tot}}(h\nu, \psi)} = \int_0^\infty n_{X(z)} e^{-\frac{z}{\lambda_s(E_k) \cos(\theta)}} dz , \quad (5.6)$$

Commonly,  $I_X$  of a specific core level X (e.g., O 1s) is normalized according to equation 5.6.  $\phi(h\nu, X)$  is the excitation photon flux (number of photons per second) with photon energy  $h\nu$  used for the measurement of X.  $\sigma_{X, \text{tot}}(h\nu, \psi)$  for linearly horizontally polarized light is the total differential photoionization cross section, which can be expressed with equation 5.7:

$$\sigma_{X, \text{tot}}(h\nu, \psi) = \sigma_X(h\nu) \frac{1 + \beta_X(h\nu)}{4\pi} , \quad (5.7)$$

where  $\sigma_X(h\nu)$  is the photo-ionization cross section of the core level X under consideration and  $\beta_X(h\nu)$  is the asymmetry parameter of the core-level electronic orbital under consideration, which are both a function of the excitation energy (i.e., photon energy  $h\nu$ ). Both, values for  $\beta_X(h\nu)$  and  $\sigma_X(h\nu)$  were taken from Yeh and Lindau (1985) and Yeh (1993).  $T$  includes the electron detection efficiency ( $D_0(h\nu)$ ) and the acceptance angle ( $\Omega_0$ ) of the electron spectrometer as well as the effectively analyzed area ( $A_0$ ), which is a few  $\mu\text{m}^2$ :

$$T(E_k) = \Omega_0 A_0 D_0(E_k) . \quad (5.8)$$

These quantities are assumed to be only slightly dependant on  $E_k$ . Therefore, they can be assumed to be the same for measurements at the same  $E_k$  and when determining PE

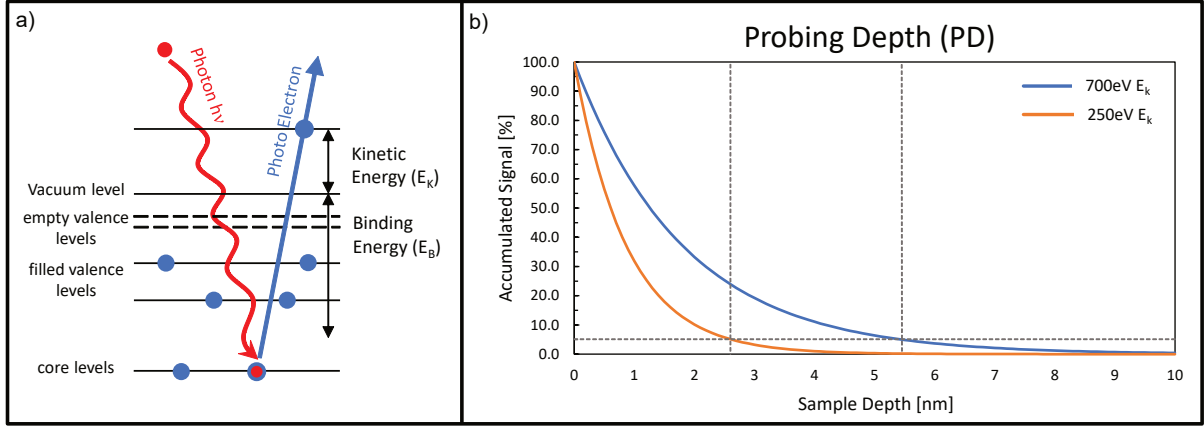


Figure 5.2: Schematic illustration of XPS (panel a). Photons hit the core level electrons of an element with energy  $h\nu$  and eject the core level electrons at  $E_K$  if the energy  $h\nu$  of the photons are larger than  $E_B$  of the core level under consideration, which is needed to overcome the vacuum energy level of an atom. The larger the  $E_K$  of the emitted photo electrons the larger their inelastic mean free path, which also increases the probing depth. Panel b) shows the surface sensitivity of XPS when assuming an inelastic mean free paths ( $\lambda$ ) of 2.1 nm and 1.0 nm at  $E_K$  of 700 eV and 250 eV, respectively. At  $E_K$  of 250 eV 95% of the signal originates from the uppermost 2.7 nm of the sample (black lines), whereas at  $E_K$  of 700 eV 95% of the signal originates from the uppermost 5.5 nm. Therefore, the probing depth (defined as  $3 \times \lambda \cos(\theta)$ ) of CaCO<sub>3</sub> in our setup varies between 2.7 nm for  $E_K$  of 250 eV and 5.5 nm for  $E_K$  of 750 eV.

signal intensity ratios for two different elements (e.g., X and Y) at same  $E_k$ ,  $T$  will cancel out according to the following equation:

$$\frac{I_{X, \text{norm}}(E_k)}{I_{Y, \text{norm}}(E_k)} = \frac{\int_0^\infty n_X e^{-\frac{z}{\lambda_s(E_k) \cos(\theta)}} dz}{\int_0^\infty n_Y e^{-\frac{z}{\lambda_s(E_k) \cos(\theta)}} dz}. \quad (5.9)$$

Given the exponentially decreasing contribution with depth, the surface sensitivity of XPS is characterized either by the mean escape depth (MED) of electrons,  $\lambda \cos(\theta)$ , from which 63% of the signal originates (i.e., a fraction of  $1-1/e$ ), or the probing depth (PD),  $3 \times \lambda \cos(\theta)$ , constituting 95% of the signal according to equation 5.6 (Greczynski and Hultman, 2022, see also Figure 5.2). For  $E_k$  above 100 eV the electron IMFP, and thus the PD, increases almost linearly with  $E_k$ . When using tunable synchrotron radiation, the different elements of interest can be probed by exciting their core-level electrons such that the resulting photoelectrons appear at the same kinetic energy and thus the same PD. By systematically varying the  $E_K$  for each element between 250 eV and 700 eV, the sample can be investigated with a PD between 2.7 nm and 5.5 nm (see Figure 5.2). Therefore, XPS can be used to obtain quantitative elemental ratios for different MED values. Note that these ratios are not directly related to the atomic density profiles of the elements as a function of depth due to the nature of the integration described in equation 5.6.

### 5.2.1.1 Experimental details on AP-XPS

XPS measurements were carried out at the Swiss Light Source (SLS) at the in-situ spectroscopy (ISS) beamline. The solid-gas interface chamber, described in Orlando et al.

(2016), Kong et al. (2017), Orlando et al. (2019) and Yang et al. (2021), allowed us to perform experiments at pressures in the mbar range with tunable partial pressures of gases of choice admitted by two leakvalves. One of the leakvalves was directly connected to a perfluor alkoxy (PFA) co-polymer tube downstream of the valve that directly extended to just 12 mm above the sample substrate, which facilitates the admission of sticky gases. The temperature at the surface of the cryo sample holder was adjusted to 210 K from the backside by an adjustable flow of N<sub>2</sub> that passed through a coil immersed in liquid N<sub>2</sub> outside the chamber system. The substrate temperature was measured a few mm away from the coldest spot in the center of the substrate by means of a thermocouple spot-welded to its side. Note that the XPS analysis cell itself remained at ambient temperature. The temperature offset between the sample surface and the thermocouple was routinely calibrated by determining the frost point as a function of the water vapor partial pressure. The frost point appears as a sudden drop in the water vapor partial pressure due to condensation of ice. This offset was typically between 1.0 and 1.5 K. We measured the O 1s, Ca 2p, C 1s and N 1s core level photo electron spectra through two different approaches: 1) We measured the core levels at a constant photon energy of 730eV, which corresponds to different kinetic energies for each element core level and thus different MED for each element, to track and quantify the uptake of nitrogen at the sample surface as a function of time. 2) We measured the same core levels at different photon energies (only for experiments A, B and C) such that each elemental core level was measured at the same 4 kinetic energies (i.e, 250 eV, 400 eV, 550 eV and 700 eV, see also Figure 5.2), corresponding to 4 different MED. Since measuring all the core levels at 4 different kinetic energies (i.e., approach 2) with sufficient quality takes about 4 hours, the depth profiles were only measured when no additional uptake of nitrogen could be observed anymore and steady state conditions at the surface were reached on timescales relevant for the experiment.

$\phi(h\nu, X)$  is measured for each photon energy ( $h\nu$ ) with a diode. The photon flux was corrected for the fraction of second order light (Raabe et al., 2008). The  $E_B$  scale was calibrated by using the main C 1s peak of adventitious carbon. The samples analyzed consist of calcite particles with a radius of 40 nm, which were first plasma-cleaned with oxygen and argon and then exposed to a ultra sonic bath for 5 minutes prior to the experiment to remove any contaminants and also to remove any agglomeration of particles prior to dispersion to prohibit differential charging of the sample surface. The particles were subsequently dispersed in ethanol, grinded and drop casted onto the cryo-sample holder leaving a thin homogeneous layer of particles on the sample holder. The cryo-sample holder temperature was set to 210 K for all our experiments.

To dose HNO<sub>3</sub> in the chamber we made use of N<sub>2</sub>O<sub>5</sub> hydrolysis. N<sub>2</sub>O<sub>5</sub> will immediately hydrolyse upon contact with surfaces exhibiting adsorbed water leading to the formation of HNO<sub>3</sub> (see reaction 5.11).



Figure 5.13 in the Appendix 5C presents a sketch of the dosing scheme applied in this experiment. The N<sub>2</sub>O<sub>5</sub> was generated via reaction 5.10 within a reactor of 50 cm<sup>3</sup> following the approach described in Gržinić et al. (2014). O<sub>3</sub> was produced upstream via an O<sub>2</sub> flow through an O<sub>3</sub>-generator at  $T = 50$  K, while NO was dosed from a NO/N<sub>2</sub> gas bottle with a fixed NO to N<sub>2</sub> mixing ratio. A detailed sketch of the dosing setup, which also includes several dilution steps with N<sub>2</sub> to reach the low stratospheric HNO<sub>3</sub>



Table 5.1: Experimental conditions of sample A to E investigated in this study at a temperature of 210K. Shown are the volume mixing ratio of HNO<sub>3</sub>, the total pressure, ratio of the resulting experimental partial pressure to the stratospheric partial pressure (equivalent stratospheric concentration), as well as the exposure time of the experiment and the resulting  $\gamma$ .

Sample	vmr	$p_{tot}$	equiv. strat. Conc.	RH	Time	$\gamma$
A	0.6/8.8 ppm	1 mbar	1.2/17.6	4%	10h/10h	$(2.50 \pm 1.25) \times 10^{-5}$
B	8.6 ppm	1 mbar	17.2	4%	14h	$(4.5 \pm 1.0) \times 10^{-5}$
C	1.4 ppm	1 mbar	2.8	4%	15h	$(1.0 \pm 0.8) \times 10^{-4}$
D	0.3 ppm	1 mbar	0.6	4%	14h	$(1.0 \pm 0.8) \times 10^{-4}$
E	6.1 ppm	1 mbar	12.2	0%	4.5h	$(6.5 \pm 4.5) \times 10^{-5}$

concentrations, is depicted and described in Figure 5.13 in the Appendix 5C. All mass flows were controlled via mass flow controllers. Controlling the NO/N<sub>2</sub> flow into the N<sub>2</sub>O<sub>5</sub> generator allowed tuning the N<sub>2</sub>O<sub>5</sub> concentration in the chamber. Downstream of the chamber a NO<sub>x</sub> and an O<sub>3</sub> analyzer determined the exact N<sub>2</sub>O<sub>5</sub> concentration in the chamber. The gas flow was dosed to 1 mbar total pressure in the chamber via the leak valve connected to the PFA tube mentioned above directly delivering this flow to the region just above the sample. Detailed experimental conditions of experiments A to E can be found in Table 5.1.

Water was dosed via Argon flowing above a liquid bath of water held at 24°C corresponding to a equilibrium vapour pressure of 0.029 mbar of H<sub>2</sub>O above the liquid. This humidified argon was then dosed to 0.01 mbar within the chamber via the second leak valve. This humidified flow passed around the PFA tube containing the N<sub>2</sub>O<sub>5</sub> flow and only mixed with the latter just above the sample. These dosing conditions for H<sub>2</sub>O resulted in a H<sub>2</sub>O partial pressure of  $2.9 \times 10^{-4}$  mbar of H<sub>2</sub>O. This corresponds to a volume mixing ratio of 5.8 ppm H<sub>2</sub>O at 50 hPa altitude, which is the upper limit of observed water volume mixing ratios in the stratosphere between 100 and 10 hPa (Wang et al., 2017) and corresponds to about 4% RH at 210 K.

Using nitrogen as carrier gas for dosing N<sub>2</sub>O<sub>5</sub> and argon for dosing water vapor allowed using the residual gas analyzer attached to the 2<sup>nd</sup> differential pumping stage of the electron analyzer to monitor the Ar/N<sub>2</sub> ratio. This allowed us to quantify and monitor the water and vapor pressure without the need to measure N<sub>2</sub>O<sub>5</sub> and H<sub>2</sub>O directly, which were beyond the detection limit of the mass spectrometer.

### 5.2.1.2 Attenuation model

The signal intensity ratios obtained as a function of  $E_k$  described above, which represent the ratios of exponentially weighted integrated density profiles, cannot directly be inverted to obtain the density profiles of the atoms involved. Therefore, we developed an attenuation model (see Figure 5.14 in the Appendix 5D) to calculate signal intensity ratios based on different scenarios of the structure of the sample and its change upon reaction. The model allows us to quantify the expected PE signal intensity ratios relative to the Ca 2p PE signal intensity for specific sample compositions from the surface to about 13 nm depth below the surface based on equation 5.12. For simplicity we applied the same IMFP ( $\lambda$ ) of CaCO<sub>3</sub> taken from (Jablonski and Powell, 2010) as a function of kinetic energy independent of sample composition and location within the sample. The

inelastic mean free path of Ca(NO<sub>3</sub>)<sub>2</sub> in the kinetic energy range of 250 eV and 700 eV deviates between 7% and 8% from that of CaCO<sub>3</sub> whereas for pure water  $\lambda$  would be longer by 40 to 50%.

$$\frac{I_{X, \text{norm}}(E_k)}{I_{Y, \text{norm}}(E_k)} = \frac{\sum_{z=0}^d n_X(z) e^{-\frac{z}{\lambda_s(E_k) \cos(\theta)}}}{\sum_{z=0}^d n_Y(z) e^{-\frac{z}{\lambda_s(E_k) \cos(\theta)}}}, \quad (5.12)$$

We applied a depth resolution of 0.01 nm, and elemental densities ( $n_X$ ) were calculated based on material densities of 2.7 g/cm<sup>3</sup> for CaCO<sub>3</sub>, 2.5 g/cm<sup>3</sup> for Ca(NO<sub>3</sub>)<sub>2</sub>, 2.0 g/cm<sup>3</sup> for Ca(NO<sub>3</sub>)<sub>2</sub> · 3H<sub>2</sub>O, 1.6 g/cm<sup>3</sup> for adventitious carbon and 1.0 g/cm<sup>3</sup> for H<sub>2</sub>O. The model assumes a top layer of adventitious carbon, followed by water containing adsorbed HNO<sub>3</sub>. Subsequently the model assumes a Ca(NO<sub>3</sub>)<sub>2</sub> layer with a CaCO<sub>3</sub> bulk layer below. This allows for 6 degrees of freedom to represent the measured PE signal ratio: (1) the thickness of the adventitious carbon layer, (2) the thickness of the adsorbed water layer, (3) the concentration of adsorbed HNO<sub>3</sub> in the water layer, (4) the thickness of the Ca(NO<sub>3</sub>)<sub>2</sub> layer, (5) accounting either for pure Ca(NO<sub>3</sub>)<sub>2</sub> or Ca(NO<sub>3</sub>)<sub>2</sub> · 3H<sub>2</sub>O and (6) accounting for either a homogeneous Ca(NO<sub>3</sub>)<sub>2</sub> layer or a Ca(NO<sub>3</sub>)<sub>2</sub> layer with a linear decrease in Ca(NO<sub>3</sub>)<sub>2</sub> content from 100% to 0% and a corresponding increase of CaCO<sub>3</sub> with sample depth.

## 5.2.2 Heavy Ion Elastic Recoil Detection Analysis (HI-ERDA)

Elastic Recoil Detection Analysis (ERDA) is an ion beam analysis technique to analyze quantitatively the composition of a sample surface region. It was first introduced by L'Ecuyer et al. (1976) and is nowadays a valuable tool to complement classical Rutherford Backscattering Spectrometry (RBS) in particular for the analysis of light elements in thin films. Projectile ions in the several MeV range have enough energy to penetrate the electron shell of a sample atom. If a projectile ion comes close to the nucleus of a sample atom it scatters elastically on the Coulomb potential of the nucleus. In this process energy and momentum is transferred from the projectile ion to the sample atom and the recoiling atom moves forward under a scattering angle  $\theta$  depending on the impact parameter (Assmann et al., 1994). The ratio of the energy of the recoiled atom ( $E_r$ ) to the energy of the projectile ion ( $E_{p,0}$ ) can then be calculated using the masses of recoil  $m_r$  and projectile ion  $m_p$ :

$$k_r = \frac{E_r}{E_{p,0}} = \frac{4 m_r m_p}{(m_r + m_p)^2} \cos^2 \theta. \quad (5.13)$$

The final kinetic energy of the recoils depends on the depth  $x$ , where the elastic collision in the sample appeared, since the projectile ions lose energy on their way into the sample ( $\Delta E_p(x)$ ) and the recoiled atoms lose energy on their way out of the sample ( $\Delta E_r(x)$ ). Thus the detected energy of the recoil depends on  $x$  and is

$$E_{r, \text{det}}(x) = k_r (E_{p,0} - \Delta E_p(x)) - \Delta E_r(x). \quad (5.14)$$

These energy losses are zero at the surface ( $x = 0$ ) and increase with depth  $x$ , which gives rise to the mass curves in Figure 5.4. The energy losses can be calculated based on the specific energy loss rate of the projectile  $|dE/dx|_{p, \text{in}}$  and the recoiling atom  $|dE/dx|_{r, \text{out}}$

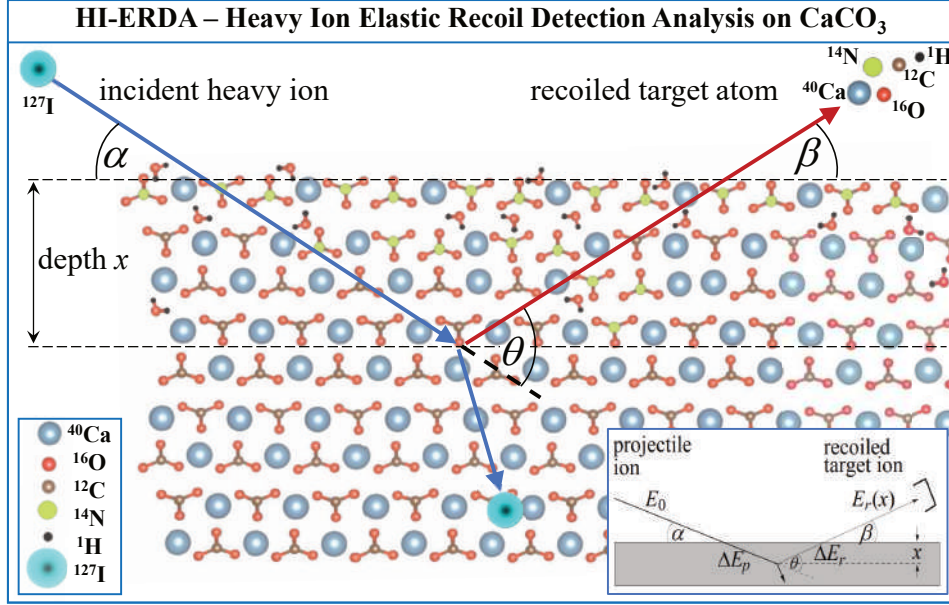


Figure 5.3: Schematic illustration of Heavy Ion-Elastic Recoil Detection Analysis. Incident heavy ions hit the surface under an angle  $\alpha$  of 17° at  $E_{0,p}$ . Within the sample the incident ion loses energy ( $\Delta E_p$ ) until it collides with an atom within the sample. In an elastic collision energy from the incident ion is transferred to the recoiling atom. The recoiling atom loses again energy ( $\Delta E_r$ ) on the way out of the sample. The detected recoil mass can then be reconstructed via a combined measurement of the velocity and the energy ( $E_r$ ) with a time-of-flight detector and a gas ionization chamber, respectively (see Figure 5.4). From the energy profile of each mass a depth profile can be calculated.

within the matter under consideration and the incident and exit angle under the assumption of small and thus constant energy loss rates:

$$\Delta E_p(x) = \left| \frac{dE}{dx} \right|_{p,in} \cdot \frac{x}{\sin \alpha} \quad (5.15)$$

and

$$\Delta E_r(x) = \left| \frac{dE}{dx} \right|_{r,out} \cdot \frac{x}{\sin \beta} \quad (5.16)$$

The detected rate depends on the cross section, the solid angle of the detection system and the mass-dependent efficiency. For several MeV ions the conditions for Rutherford scattering are still valid and the differential recoil cross section can be calculated as

$$\left( \frac{d\sigma}{d\Omega} \right)_r = \left( \frac{z_p z_r e^2}{2E_{p,0}} \right)^2 \left( 1 + \frac{m_p}{m_r} \right) \frac{1}{\cos^3 \theta} \quad (5.17)$$

with  $z_p$  and  $z_r$  the atomic numbers of projectile and recoil, respectively, and  $e^2 = 1.44$  eV nm. The strong dependence on projectile mass and atomic number gives a high yield for the detection of light elements for heavy projectiles.

Specifically, in heavy-ion ERDA (HI-ERDA), an energetic heavy ion beam in the MeV energy range (e.g., <sup>127</sup>I ions at 13 MeV in this setup) is hitting the sample under a small angle of incidence  $\alpha$  of 17° (see Figure 5.3 and Döbeli et al., 2005). The mass of the

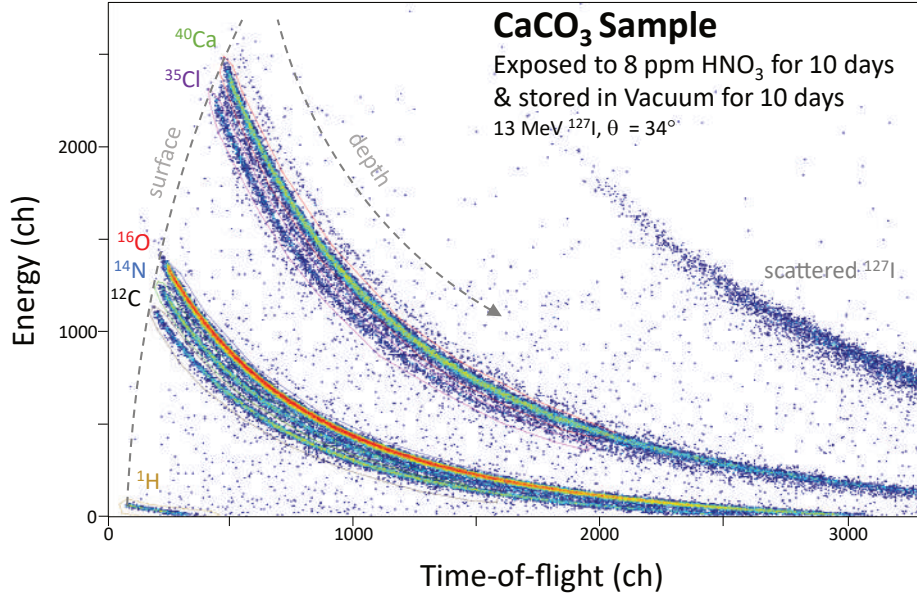


Figure 5.4: A typical 2D spectrum of a HI-ERDA measurement of a calcite sample which was previously exposed to HNO<sub>3</sub>. The atomic mass of the detected recoils can be derived from the energy and time-of-flight measurement via the relationship in equation 5.18. The depth scale for each mass is calculated via the specific energy loss as a function of depth into the sample of the matter under consideration. Note: the chlorine measured in this sample is an artefact of the sample preparation, showing that care must be taken in subtracting sample artefacts from measured signals after exposure to HCl.

recoiled particles and the collision depth is then identified by a combined measurement of the recoil velocity  $v_r$  in a time-of-flight spectrometer and the kinetic energy ( $E_r$ ) in a gas ionization chamber under a scattering angle  $\theta=34^\circ$  (see Figure 5.4). The mass of each detected recoil is derived from its combined velocity and energy measurement via

$$E_{r\text{det}} = \frac{m_r v_r^2}{2} \quad (5.18)$$

For each detected element (defined by its mass) the depth distribution is calculated from the measured kinetic energy distribution and the respective energy-loss rate in the sample material. The maximum sampling depth is in the order of hundreds of nm depending on the energy of the projectile ion. In the measurements presented here the maximal sampling depth, in which masses are still well resolved is about 240 nm for C, N, Ca and O, and about 120 nm for H because of the lower recoil energy. The depth profiles can then be calculated by creating mass spectra slices along the depth scale (i.e. grey arrow in Figure 5.4) based on the measured counts, the recoil cross section (equation 5.17) and a mass-dependent efficiency which is determined with calibration standards. The depth resolution which is 12 nm in this study needs to be large enough to have enough counts for reliable statistics.

Alternatively, for H detection He ions (typically with an energy of 2 MeV as used for standard RBS measurements) can be used in a dedicated ERDA setup (called He-ERD). The sample is rotated with respect to the incoming beam allowing for recoils to be detected under a scattering angle of  $30^\circ$ . Due to the lower mass of the projectile only H recoils gain sufficient energy to reach the detector which is here a solid state detector measuring

the kinetic energy. Additionally forward scattered He projectiles reach the detector, but are stopped in a 8  $\mu\text{m}$  Mylar absorber foil due to the higher energy-loss rate. From the measured energy the depth profile can be calculated. Since only H is measured in He-ERDA the H concentration profiles are normalized to the internal H standard.

### 5.2.2.1 Experimental details on HI-ERDA

HI-ERDA experiments were performed at the 1.7 MV Tandetron accelerator (Döbeli et al., 2005; Kottler et al., 2006) at Laboratory of Ion Beam Physics at ETH Zurich, Switzerland to quantify the uptake of HNO<sub>3</sub> and HCl on calcite samples, which were previously exposed to those gases. We put single crystal samples of CaCO<sub>3</sub> (polished single crystal calcite sample, c-axis vertical to the polished plate, 15 x 10 x 1 mm, from Korth Kristalle GMBH, Kiel, D) into an desiccators containing either a H<sub>2</sub>SO<sub>4</sub>–HNO<sub>3</sub> or a H<sub>2</sub>SO<sub>4</sub>–HCl solution to get the desired HNO<sub>3</sub> and HCl vapor concentration above the solution at -20°C (253 K, see Figure 5.15). The desiccators were sealed by grease and stored in a commercial fridge for cooling during the exposure. We used a combined 65wt% H<sub>2</sub>SO<sub>4</sub> and 2 wt% HNO<sub>3</sub> as well as a 65 wt% H<sub>2</sub>SO<sub>4</sub> and 0.2 wt% HNO<sub>3</sub> bath to get HNO<sub>3</sub> volume mixing ratios of 8 ppm and 0.8 ppm, respectively (see Table 5.4). For HCl we used a 35 wt% H<sub>2</sub>SO<sub>4</sub> bath containing 1 wt% HCl as well as a 35 wt% H<sub>2</sub>SO<sub>4</sub> bath containing 0.15 wt% HCl to get HCl volume mixing ratios of 1.2 ppm and 0.12 ppm, respectively (see Table 5.3). These concentrations are about 2 to 3 orders of magnitude larger compared to the stratosphere and conditions during the AP-XPS measurements. Lower concentrations cannot be dosed with high enough accuracy in this setup. However, this setup allowed us to expose the samples to much longer exposure times, compared to the AP-XPS measurements, which is important to investigate slow diffusion processes. After exposure times of 10 days and 5 days for HNO<sub>3</sub> and HCl, respectively, the samples were put into the measurement chamber for Elastic Recoil Detection Analysis (ERDA), in which they were measured immediately after evacuating the chamber. During the transport from the fridge to the measurement chamber, the samples were exposed to ambient lab air (with ambient RH and temperature) for about 1-2 minutes, which might be enough to dissolve some of the reaction products at the surface. However, there is no mass loss, which allows us to quantify the share of N and Cl atoms of the upper 240 nm of the CaCO<sub>3</sub> sample, which is used to estimate the uptake coefficient of HCl and HNO<sub>3</sub> on our calcite samples by dividing the integrated amount of N and Cl molecules throughout the sample depths (reacted HNO<sub>3</sub> and HCl) by the total collisions of HNO<sub>3</sub> and HCl molecules with the surface integrated over the exposure time (see Table 5.3 and 5.4 in the Appendix 5A).

## 5.3 Results

In this section we discuss first the results of the AP-XPS experiments and then the results of the ERDA experiments.

### 5.3.1 AP-XPS results

Representative examples of the O 1s, N 1s, Ca 2p and C 1s spectral regions measured for sample A (see Figure 5.5) show PE peaks at binding energies at around 531.5 eV, 406.0 eV, 346.5 eV and 288.5 eV, respectively (see Figure 5.16 in Appendix 5F for the full survey spectra). This corresponds to kinetic energies of 198.5 eV, 324.0 eV, 383.5 eV and

441.5 eV, respectively. The small kinetic energy for O 1s required measuring at lower pass energy (20 eV) whereas the other measurements were measured with higher pass energy (50 eV), which is why O 1s shows the smallest PE count rate of all elements in this overview, despite having the largest atomic density. For the spectra shown a background was subtracted. The  $E_B$  scale was corrected for charging relative to the adventitious C 1s peak at 284.8 eV  $E_B$ . The charging was between 10 eV and 18 eV across measurements in spite of the total gas pressure of 1 mbar in the chamber, that generally helps to reduce charging of insulating samples. Charging is not always exactly homogeneous within the field of view of the electron analyzer, which leads to some peak broadening. This makes quantification of the exact binding energies challenging. But this is not of further relevance for this study, since we are mainly interested in the total PE peak areas. While the O 1s PE peak consists of the total signal contributed by oxygen within carbonate, nitrate and water and the Ca 2p peak contains the combined signals of CaCO<sub>3</sub> and Ca(NO<sub>3</sub>)<sub>2</sub>, the N 1s nitrate peak and the C 1s carbonate peak are clearly distinguishable from other N 1s and C 1s peaks. The other measured N 1s and C 1s peaks originate from adventitious carbon and nitrogen species resulting from the effect of X-rays and secondary electrons as well as from the contribution of the N<sub>2</sub> carrier gas in the chamber in the acceptance volume of the analyzer also hit by X-rays. The black curves show the Gaussian fits of the spectra, from which the peak area is calculated (i.e.,  $I_X$ ). While the 1s peaks are represented by single Gaussian peaks, the 2p peak shows the typical spin-orbit splitting with a binding energy difference of about 3.55 eV between the 2p<sub>3/2</sub> and the 2p<sub>1/2</sub> peak (e.g., Ni and Ratner, 2008).

The black fitting curve shows the fit to the data at the end of experiment A after 20h of exposure and after a distinct N 1s nitrate peak has built up indicating the formation of Ca(NO<sub>3</sub>)<sub>2</sub> (see Figure 5.5). The pink line shows the fit to the data in the beginning of the experiment when the N 1s nitrate peak was not present yet. The Ca 2p and C 1s carbonate peaks both show a decrease with time, since the densities of these two atoms decrease with increasing formation of Ca(NO<sub>3</sub>)<sub>2</sub> (see also Figure 5.6).

Across all peaks the standard deviation from the fitting curve to the data is below 5% of the total fitted peak area, except for the fit of the C 1s peak of carbonate, where the standard deviation is higher (below 10%) due to the overlap with the adventitious carbon peak. Therefore, the uncertainty from the peak fitting is relatively small compared to other sources of uncertainty such as uncertainty from the subsequent corrections applied to normalize the different peak areas to each other. These uncertainties include the higher order light correction ( $\pm \sim 20\%$ ), the cross section values (unknown) or the measurement of the photon flux with the diode ( $\pm \sim 10\%$ ). Therefore we assumed an uncertainty range of about  $\pm 20\%$  for all the measured normalized PE signals (see Figure 5.6).

The normalized PEI evolution of Sample C shows a decrease in PE signal of C1s of almost 75%, while the one of Ca 2p decreases about 33% (Figure 5.6). The PE intensities of adventitious carbon C 1s and O 1s are very stable with time, since C 1s is not participating in reactions and O 1s might be dominated by the O 1s of water. The N 1s nitrate signal increases from below the detection limit to a signal strength about equal to the one of Ca 2p. PE signal evolution of experiments A, B, D and E can be found in Figure 5.17 in Appendix 5F. We have also tested the stability of the N 1s peak when switching off the N<sub>2</sub>O<sub>5</sub> dosing and found no decrease in PE peak area (see Figure 5.17 in the Appendix 5F, Sample B). Additionally, we also found the different peaks to be very stable with respect to beam damage since the peaks are very stable over time also when switching measurement spot on the sample (see Figure 5.17 in the Appendix 5F, Sample

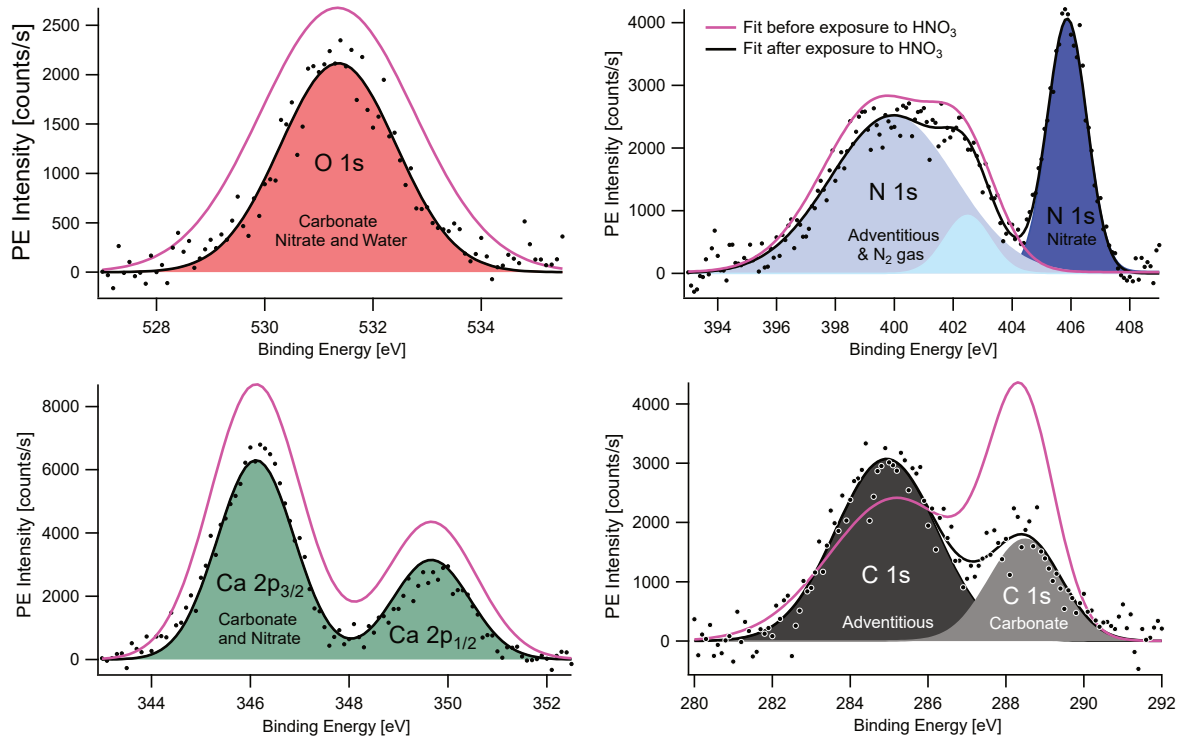


Figure 5.5: The photoelectron intensity (PEI) of O 1s, Ca 2p, N 1s and C1s for sample A measured at 730 eV photon energy as a function of binding energy corrected only for charging and background counts. Black dots represent measurements at the end of the experiment after about 20 h of exposure and the black line the corresponding Gaussian peak fitting curve, whereas the pink line represents the fitting curve of the measurement at the beginning of the experiment after about 1h of dosing.

B).

For sample A, B and C also the PE signal intensities, representing exponentially weighted integrated density profiles (equation 5.6), were measured at kinetic energies of 250 eV, 400 eV, 550 eV and 700 eV (see Figure 5.7), once the N 1s peak in these experiments has stabilized on timescales relevant to the experiment as shown above in conjunction with Figure 5.6. The relatively flat N 1s gradient apparent in Figure 5.7 from lower to larger kinetic energies, which can be observed in all three samples indicates that after the exposure to HNO<sub>3</sub> during the several hours of these experiments nitrate can not only be located at the very surface but also further inside the sample to depths below more than 4 nm, which is the MED at 700 eV. Ca(NO<sub>3</sub>)<sub>2</sub> has a N/Ca ratio of 2, whereas CaCO<sub>3</sub> has a N/Ca ratio of 0. Therefore, ratios observed in the measurements for the lowest Ek and thus lowest MED indicate almost complete transformation of CaCO<sub>3</sub> to Ca(NO<sub>3</sub>)<sub>2</sub> at the surface where measured N 1s/Ca 2p ratios are about 2. With increasing Ek and thus more contributions to the signal from deeper in the bulk the N 1s/Ca 2p decreases to values between 1 and 1.5 across all three samples, while the C1s carbonate to Ca 2p ratio is at about 0.5 throughout all kinetic energy levels. To adequately simulate these measured PE signal intensity ratios with the attenuation model (see Section 5.2.1.2), it was necessary to account first, for a thin layer of adventitious carbon on top; second, an adsorbed H<sub>2</sub>O/HNO<sub>3</sub> layer; and third for a layer containing Ca(NO<sub>3</sub>)<sub>2</sub> in form of its tetrahydrate (i.e, Ca(NO<sub>3</sub>)<sub>2</sub> · 4H<sub>2</sub>O) and therein for a linear gradient from 100% Ca(NO<sub>3</sub>)<sub>2</sub> · 4H<sub>2</sub>O at



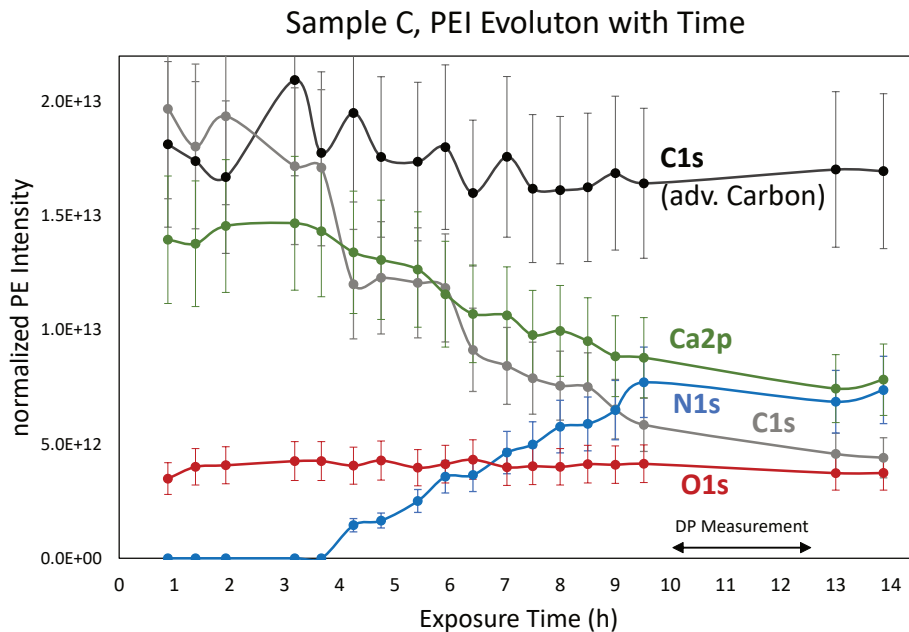


Figure 5.6: The normalized PEI of all peaks measured at 730 eV photon energy for sample C as a function of time. The lack of measurement points between 10 and 13 h is due to the measurement of the depth profile (see Figure 5.12). The uncertainty bars all include values  $\pm 20\%$ . The PEI evolution of the other 4 samples can be found in Figure 5.17 in the Appendix 5F.

the top of this layer to 0% tetra hydrate at the bottom of the layer (see Figure 5.14 in Appendix 5D). The resulting thickness of this third layer are 8 nm, 7 nm and 5 nm for sample A, sample B and sample C, respectively. The amount of Ca(NO<sub>3</sub>)<sub>2</sub> contained in this mixed layer would correspond to an effective pure Ca(NO<sub>3</sub>)<sub>2</sub> layer of 3 nm, 2.7 nm and 1.9 nm thickness, respectively. The modelled HNO<sub>3</sub> to H<sub>2</sub>O ratio within the adsorbed water layer was assumed to be 1:3, 1:3 and 1:6, respectively. The modelled sample layer composition for Sample A, B, and C can be found in Figure 5.14 in Appendix 5D. Only modelling a pure Ca(NO<sub>3</sub>)<sub>2</sub> layer of this effective thickness without gradient would result in an overestimation of the N1s/Ca 2p ratio and in an underestimation of the C1s carbonate/Ca 2p ratio. However, the uncertainty of the model is likely as large as  $\pm 50\%$ , since 1) the model does not agree with the measured profiles with absolute accuracy (e.g., assumes a constant inelastic mean free path of CaCO<sub>3</sub>, independent of the actually evolving composition, 2) there are many degrees of freedom such as for example accounting for a tetra hydrate (and not a mono- or di-hydrate), the linear gradient of the Ca(NO<sub>3</sub>)<sub>2</sub> · 4H<sub>2</sub>O profile as well as 3) the amount of HNO<sub>3</sub> within the adsorbed water layer, which are all not well constrained, but chosen to plausibly represent the conceivable structure.

We also attempted at estimating the effective Ca(NO<sub>3</sub>)<sub>2</sub> layer thicknesses for the measurements of the PE signal intensities at constant photon energy, but different kinetic energy and thus, different surface sensitivities for all elements (see Figure 5.8). However, compared to the simulation of the signal intensity ratios measured at constant MED discussed above, it was more challenging to reproduce the measured data with the model due to the different MED values of the measurement of each element as well as due to the O 1s peak being measured at lower pass energy compared to the other peaks. Therefore,



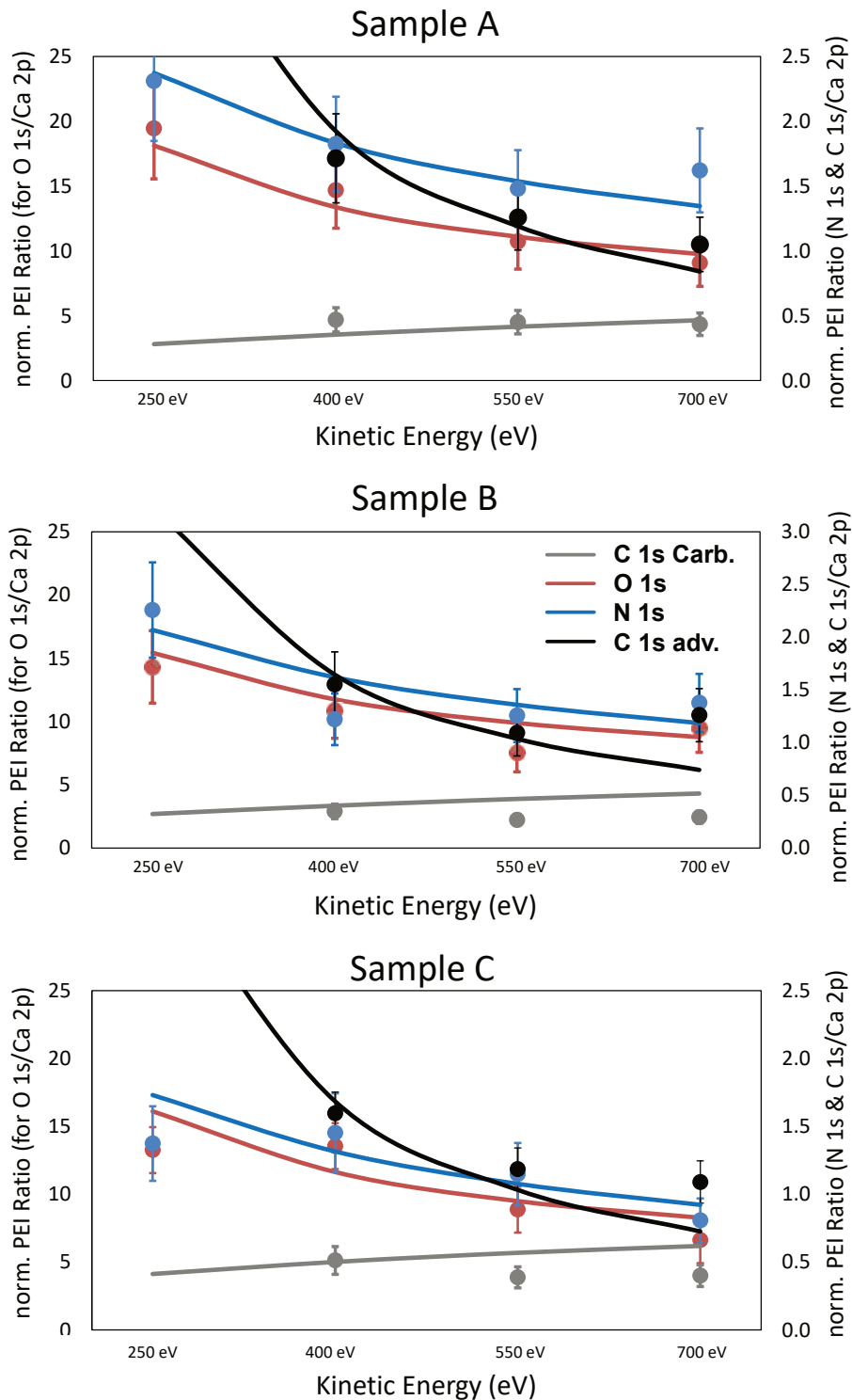


Figure 5.7: Measured values of the PE signal intensity ratios as a function of kinetic energy are represented with dots, while the lines show the values simulated with the attenuation model (see Section 5.2.1.2), which result in elemental compositions shown in Figure 5.14. The depth profile was measured at 250 eV, 400 eV, 550 eV and 700 eV kinetic Energy. While the left Y-axis shows the ratio of O 1s/Ca 2p, the right Y-axis is for the ratios is N 1s/Ca 2p, C 1s/Ca 2p. The error bars of the measurement points indicate a ~20% range.

we only simulated the N 1s and the C 1s carbonate peaks with a simplified model version which only assumes layers of pure Ca(NO<sub>3</sub>)<sub>2</sub> without gradient, without considering hydrates and without considering adsorbed HNO<sub>3</sub>. This allowed estimation of the growth of the Ca(NO<sub>3</sub>)<sub>2</sub> layer with time (see figure 5.8). The resulting layer thicknesses at the end of the measurements are about 33% to 50% smaller than the effective layer thicknesses modelled for the depth profiles for samples A, B and C, which is within the range of uncertainty for the modelling. However, if we also accounted for adsorbed HNO<sub>3</sub>, a Ca(NO<sub>3</sub>)<sub>2</sub> gradient as well as hydrates in these modelling results, the effective layer thicknesses would likely be higher by up to a factor of 2.

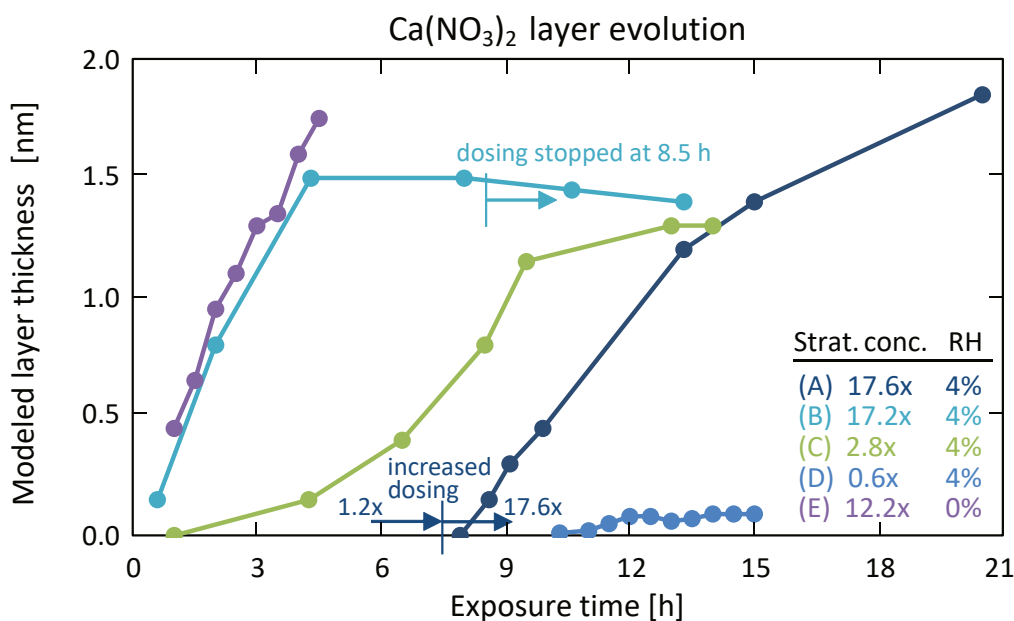


Figure 5.8: The Ca(NO<sub>3</sub>)<sub>2</sub> layer thickness evolution as a function of time based on adjusting the attenuation model to the measured PE intensities at 730 eV photon energy for all peaks for samples A, B, C, D and E. The model assumed a pure Ca(CO<sub>3</sub>)<sub>2</sub> layer at the surface without gradient and hydrates, such that the C 1s carbonate/Ca 2p and the N 1s/Ca 2p ratio of each measurement was reproduced (see 5.14 in the Appendix 5A). The legend within the figure indicates the ratio of the HNO<sub>3</sub> partial pressure relative to the one in the stratosphere (i.e., about  $5 \times 10^{-7}$  mbar) labeled with "Stat. conc." as well as the RH applied during the experiment.

The Ca(NO<sub>3</sub>)<sub>2</sub> evolution of the thickness of the nitrate layer in Figure 5.8 derived from adjusting the attenuation model are in good correspondence with the measurement conditions applied. Sample A, the first sample we measured, was first exposed to very low stratospheric HNO<sub>3</sub> concentrations. After not detecting a N 1s nitrate signal for 7.5 hours the concentration was increased to 17.6 fold stratospheric concentrations. From that time we could observe a constant increase in the effective layer thickness. With sample B we reproduced experiment A under same conditions. The slightly steeper PE signal increase in experiment B, compared to experiment A could be a result of sample A having already been exposed to lower HNO<sub>3</sub> partial pressures beforehand. The chamber walls may become a source of HNO<sub>3</sub> after continued exposure to N<sub>2</sub>O<sub>5</sub> during the previous experiments. The resulting layer thickness reaches similar levels in peaks A, B and E,

whereupon switching off H<sub>2</sub>O dosing at similar HNO<sub>3</sub> partial pressures (sample E) did not result in a significantly different PE signal evolution than for sample B. However, even though the H<sub>2</sub>O partial pressure during the measurement of sample E was switched off, there were still some counts of H<sub>2</sub>O measured by the RGA which analyzed the residual gas composition downstream of the chamber. The two samples, which were the closest to stratospheric concentrations (sample C and D), were exposed to 280% and 60% stratospheric HNO<sub>3</sub> concentrations, respectively. For the very low concentration (sample D) it took more than 10 hours to detect a N 1s nitrate signal. The time it takes to detect a N 1s signal could also be influenced by N<sub>2</sub>O<sub>5</sub> loss on walls as well as the stickiness of HNO<sub>3</sub> on all surfaces. The sensitivity to this artefact increases the smaller the partial pressure of N<sub>2</sub>O<sub>5</sub> is, even though this loss was minimized by reducing the PVA tubing between the N<sub>2</sub>O<sub>5</sub> generator and the chamber to a minimal level (i.e., below 40 cm). However, in contradiction to this, we must note that the time between the individual experiments was less than one hour, and walls were likely saturated after the measurement of each sample. However, we observed clean nitrate free conditions at the beginning of every measurement. Furthermore, we want to point to the C 1s carbonate signal decrease in Figure 5.6 and Figure 5.17 in the Appendix 5F (Sample D as well as Sample A), which already starts before the detection of the N 1s nitrate signal indicating some changes in the sample composition before any N 1s could be detected. The detection of the N 1s peak at low nitrate coverages is somewhat challenging: with a binding energy of 406 eV, when excited with E(hν) of 730 eV, its peak appears at a kinetic energy of 324 eV, which is on the substantial inelastic scattering background of the O KLL Auger electrons appearing with a primary kinetic energy of around 510 eV, which leads to a lower signal to noise ratio. Additionally nitrates are very sensitive to radiolysis by X-rays and secondary electrons. While changing sample spots at already substantial nitrate coverages did not indicate beam damage, at very low coverage, a reduction of the steady state surface coverage could lead to a delay until the N 1s peaks becomes detectable, while the change in the carbonate C 1s is already apparent.

The modelled effective Ca(NO<sub>3</sub>)<sub>2</sub> layer thicknesses were used to calculate uptake coefficients from these measurements by dividing the integrated amounts of HNO<sub>3</sub> collisions over time with the amount of nitrogen molecules in the effective Ca(NO<sub>3</sub>)<sub>2</sub> layer accumulating over a certain period of time. The resulting uptake coefficients fall in the range between 10<sup>-4</sup> and 10<sup>-5</sup> and are listed in Table 5.1. These uptake coefficients are significantly lower compared to most previous measurements (see Tables 5.3 and 5.4 in the Appendix 5A). This is related to the exposures and degree of conversion reached during the present experiment. Note that a layer thickness of 1 nm corresponds to around 4.8 × 10<sup>15</sup> and 1.6 × 10<sup>15</sup> molecules per cm<sup>-2</sup> and thus, 1.7 and 2.5 formal monolayers for Ca(NO<sub>3</sub>)<sub>2</sub> and CaCO<sub>3</sub>, respectively. This will be discussed later in the discussion section.

### 5.3.2 HI-ERDA results

Figure 5.10 shows mass spectra of the forward recoil scattered nuclei of a CaCO<sub>3</sub> sample, which was exposed to 0.8 ppm HNO<sub>3</sub> for 10 days, i.e., an exposure of about four times stratospheric values (assuming such particles to stay for about one year in the stratosphere). The two spectra clearly show the penetration of N and H atoms, most likely as NO<sub>3</sub><sup>-</sup> and H<sub>2</sub>O, into the depth of the calcite matrix, with high concentrations in the 6-9 nm slab and much lower concentrations in the 36-39 nm slab. With count numbers of 10 and more, ERDA represents a highly accurate spectrometry, which enables to obtain

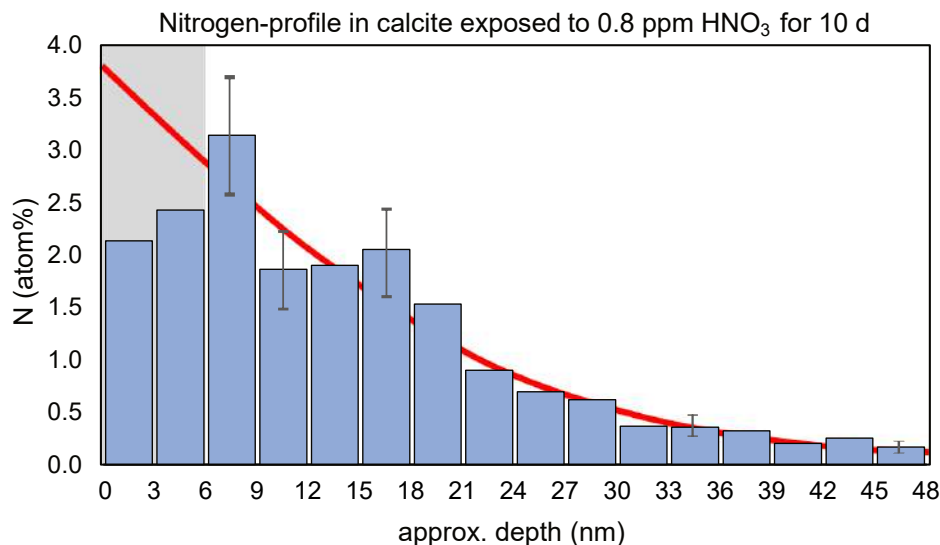


Figure 5.9: The nitrogen gradient from the surface to the interior of the sample exposed for 10 days to 0.8 ppm HNO<sub>3</sub> with a depth resolution of 1 nm. The profile shows a high correlation with a diffusion profile (red line, erfc-function with an effective solid-state diffusion constant  $D = 10^{-18}$  cm<sup>2</sup>/s) from the surface to the interior of the sample. Artifacts and uncertainties are as follows: the outermost 2 nm are depleted in N by beam damage, marked by gray shading (counts decrease after starting irradiation, then stay constant); uncertainties are mainly given by counting statistics and background subtraction; typically, there are 10-30 counts per 1-nm depth slice; thus, statistical uncertainties are roughly  $\pm 20$  %; systematic errors are small, as we conclude from the expected stoichiometry for pristine calcite.

depth profiles as the one shown in Figure 5.9.

The profile in Figure 5.9 reveals a decrease of the N concentration with increasing depth, which is well correlated with a complementary error function,  $\text{erfc}(x/\sqrt{Dt}) = 1 - \text{erf}(x/\sqrt{Dt})$ , with  $x$  being the depth in the CaCO<sub>3</sub> sample. This is characteristic for the profile of a species diffusing from one halfspace (here HNO<sub>3</sub> in the gas phase) into the other halfspace (here NO<sub>3</sub><sup>-</sup> in the solid CaCO<sub>3</sub>/Ca(NO<sub>3</sub>)<sub>2</sub> matrix) with an effective solid-state diffusion constant  $D = 10^{-17}$  cm<sup>2</sup>/s) (shown by the red line).

Figure 5.11 shows depth profiles of various elements in CaCO<sub>3</sub> samples exposed to different conditions (reference, 0.8 ppm HNO<sub>3</sub> and 8 ppm HNO<sub>3</sub> for ten days). The ERDA measurement of a reference sample (Figure 5.11a), which was only exposed to ambient air, shows an almost constant depth profile with the expected elemental composition of CaCO<sub>3</sub> of 20% Ca, 20% C and 60% O in the entire accessible depth to 240 nm below the interface with the gas phase. The uppermost 0-12 nm of the depicted profiles are subject to larger uncertainty due to challenges in clearly defining the surface onset of different elements in our analysis method (gray shaded area in depth profiles in Figure 5.11). The experiment in which the sample was exposed to 8 ppm HNO<sub>3</sub> for 10 days at 1000 mbar which equals about 40 times stratospheric exposure (Figure 5.11c) shows almost complete transformation of calcium carbonate throughout the whole depth profile, since almost no carbon is left in the accessible depth range. Instead, significant amounts of hydrogen and nitrogen (both at about 16%) are present indicating reaction to calcium

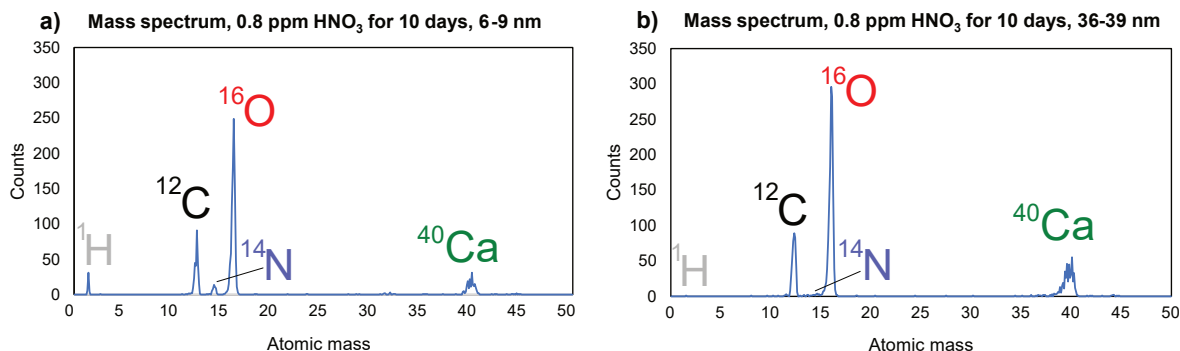


Figure 5.10: Resulting HI-ERDA mass spectra of the sample, which was exposed to 0.8 ppm HNO<sub>3</sub> for 10 days with measured counts between 12 and 15 nm depth (a), in which a clear H and N peak was measured as well as between 42 and 45 nm depth (b) in which no H and N peak was measured anymore.

nitrate in presence of hydrates. Santschi and Rossi (2006) reasonably postulated that the OH group of the reactive intermediate Ca(OH)(HCO<sub>3</sub>) will react first since it is more reactive towards acid uptake. They also experimentally ruled out the spontaneous conversion of Ca(OH)(HCO<sub>3</sub>) to Ca(OH)<sub>2</sub>. Composition must thus be in the form of Ca(OH)(HCO<sub>3</sub>) and Ca(NO<sub>3</sub>)<sub>2</sub> · nH<sub>2</sub>O. This composition can then be derived by fitting the shares of three species Ca(NO<sub>3</sub>)<sub>2</sub>, CaCO<sub>3</sub> and H<sub>2</sub>O to match the composition of the depth profile assuming that the water would then either be in the form of Ca(OH)(HCO<sub>3</sub>) or Ca(NO<sub>3</sub>)<sub>2</sub> · nH<sub>2</sub>O. The composition which represents the depth profile in Figure 5.11c most accurately is 68% Ca(NO<sub>3</sub>)<sub>2</sub>, 9% CaCO<sub>3</sub> and 23% H<sub>2</sub>O resulting in an elemental composition of about 9% Ca, 2% C, 58% O, 15% N, and 15% H. The same setup in which a sample was exposed to a concentration of 0.8 ppm for 10 days (about 4 times stratospheric exposure) still showed a considerable portion of carbon atoms while only detecting nitrogen to a depth of about 36 nm (Figure 5.11b). In the uppermost 36 nm, this corresponds to a molecular composition of 9% Ca(NO<sub>3</sub>)<sub>2</sub> and 91% CaCO<sub>3</sub> resulting in an elemental composition of 19% Ca, 18% C, 61% O and 2% N leading to HNO<sub>3</sub> uptake coefficients of about  $3.2 \times 10^{-6}$  and at least  $> 2.4 \times 10^{-5}$  for the experiment at 4 times and 40 times stratospheric exposure, respectively. The uptake coefficient of the experiment with the 40 times stratospheric exposure could also be much larger since nitrate penetrated the crystal to depths beyond the detection limit of HI-ERDA. These resulting uptake coefficients are non-intuitive since lowering the concentration in an uptake experiment while not changing anything else should result in either no change or increased uptake coefficients. Therefore, also other factors such for example RH could have influenced the uptake of HNO<sub>3</sub>. The RH during the experiment was about 6% and 4.5% for the experiment at 4 times and 40 times stratospheric exposure, respectively. At 253 K, both of these RH are below DRH, which is 73% at this temperature (according to the phase diagram for calcium nitrate in Steiger et al., 2011, see their Figure 4.25). Between 3% and 8% RH, the most stable hydrate form is Ca(NO<sub>3</sub>)<sub>2</sub> · 2H<sub>2</sub>O, whereas below and above these RH thresholds the mono-hydrate and the tetra-hydrate form are stable (Steiger et al., 2011). Ion diffusion and thus the uptake coefficient is much faster the more water is available, and thus the more hydrated the Ca(NO<sub>3</sub>)<sub>2</sub> is. However, also contrary to this the uptake experiment at 8 ppm HNO<sub>3</sub> and 4.5% RH resulted in a larger uptake coefficient compared to the one at at 0.8 ppm HNO<sub>3</sub> and 6% RH (see also Section 5.1.1).

Subsequently, after the initial HI-ERDA measurement, the sample was stored in vac-

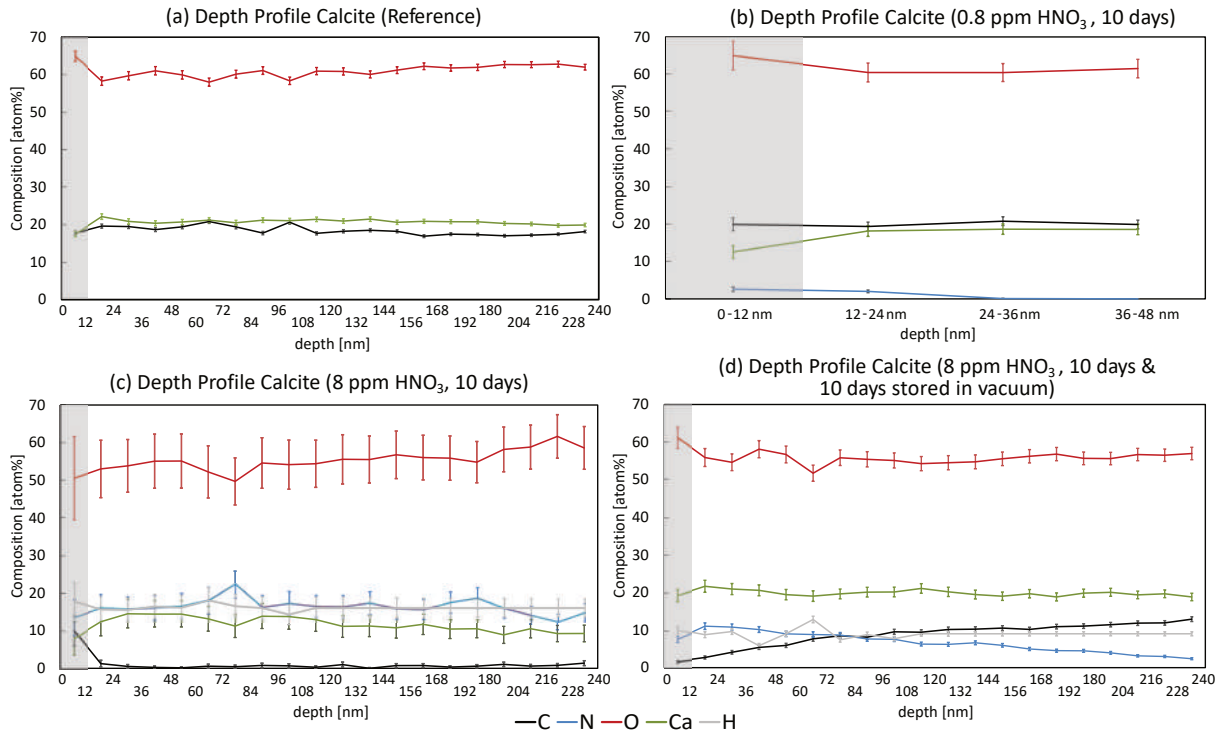


Figure 5.11: Elemental composition as a function of depth measured with HI-ERDA from the surface to 240 nm depth. (a) Reference CaCO<sub>3</sub> sample with an elemental Ca:C:O ratio of 1:1:3. (b) Elemental depth profile of a sample that was exposed to 0.8 ppm of HNO<sub>3</sub> for 10 days (4 times stratospheric exposure), resulting in  $\gamma_{\text{HNO}_3} = 10^{-6}$ . (c) Sample that was exposed to 8 ppm HNO<sub>3</sub> for 10 days (40 times stratospheric exposure,  $\gamma_{\text{HNO}_3} = 3 \times 10^{-5}$ ). (d) Same sample as in (c) after a further two weeks of storage in vacuum. The elemental composition in the uppermost surface sensitive data points (gray shaded area) are subject to large uncertainty since the surface cannot be accurately defined in HI-ERDA. The error bars refer to  $\pm 2\sigma$  statistical error. (Note that the hydrogen concentration was not measured in (a) and (b) and was assumed to be constant between 120 nm and 240 nm in (c) and (d), since the maximum detection depth of the H measurement is only about half as large compared to the sensitivity of the other elements, but it can be assumed that H does not change significantly up to a depth of 240 nm).

uum for 10 days at room temperature and was then measured again (see Figure 5.11d). The resulting depth profile shows that the nitrogen concentration in the sample decreased and carbon was detected again. The gradients of the two species as a function of depth indicate that carbon is diffusing from inside the sample to the surface, whereas nitrogen continues diffusing into the sample interior. This shows that ion diffusion plays an important role in the uptake of HNO<sub>3</sub> during time scales of days to weeks.

The exposure to HCl only resulted in very little formation of CaCl<sub>2</sub> (not shown). The profile only contained at most 2% of CaCl<sub>2</sub> in the uppermost 40-50 nm (not shown). This would correspond to uptake coefficients of  $1.3 \times 10^{-8}$  and  $1.3 \times 10^{-7}$  for the experiment exposed to 1.2 ppm and 0.12 ppm HCl (i.e., 329 and 32.9 times stratospheric exposure), respectively. However, since the H<sub>2</sub>SO<sub>4</sub>-HCl solution had a much larger water weight percent, compared to the HNO<sub>3</sub> uptake experiments, the RH in these experiments was much larger ( $\sim 70\%$ ), which is above DRH. It could well be that no CaCl<sub>2</sub> was formed since it immediately dissolved in a liquid layer at the surface.

## 5.4 Discussion

In most previous experimental studies, the initial uptake coefficient of HCl and HNO<sub>3</sub> was measured using techniques that are not suitable for observing further uptake after the reactive surface sites have been converted to Ca(NO<sub>3</sub>)<sub>2</sub> or CaCl<sub>2</sub>. The high  $\gamma$ -values last only for minutes or even seconds (depending on the applied gaseous concentrations). Hence, these experiments investigated mostly an adsorption-reaction mechanism on the calcite surface as compared to the reacto-diffusive mechanism deeper in the calcite matrix, as it is relevant for the long-time exposure to HCl and HNO<sub>3</sub> in the stratosphere (see also Section S2.2 on diffusion mechanisms).

The AP-XPS uptake experiments presented in this study are the first allowing us to observe the uptake of HNO<sub>3</sub> at stratospheric conditions with respect to temperature, RH and HNO<sub>3</sub> concentrations in-situ over timescales of several hours. The measured uptake coefficients fall in the lower range of uptake coefficients measured in previous studies (see Figure 5.12). The experiments showed a slowdown in the uptake of nitrate after several hours, which could either be a result of saturation of the surface sites in conjunction with a subsequent limitation by ion diffusion or a limitation in sensitivity to larger sample depths of the measurement technique (see Figure 5.2). It is also possible that it is a combination of both factors, as carbonate was still detected at the very end of the experiments. However, our measurements also detected nitrate to sample depths of up to 8 nm within a few hours, which indicates strong ion diffusion. Significant ion diffusion was also detected in the HI-ERDA measurements presented in this study on timescales of weeks through sample depths of more than 250 nm.

The importance of ion diffusion becomes clear when considering the timescales relevant to cover one monolayer with HNO<sub>3</sub> and HCl in the stratosphere (see Table 5.2), which even for small  $\gamma$ 's is only a small fraction of the total exposure time of the calcite particles (typically 1/2 year for particles with radius 240 nm). These values were derived by calculating the collision rate ( $J$ ) of molecules with a surface,

$$J = k[X], \quad (5.19)$$

where X is the gaseous species (i.e., HNO<sub>3</sub> or HCl) colliding with the surface. The reaction

coefficient  $k$  can be determined from

$$k = \frac{\gamma \bar{v} \text{SAD}}{4}, \quad (5.20)$$

where  $\bar{v}$  is the mean thermal velocity. This allows us to calculate time required to reach monolayer-coverage in dependence of  $\gamma$ .

Table 5.2: Time required to cover a surface with one monolayer of HCl and HNO<sub>3</sub> assuming a total pressure of 50 hPa (about 21 km altitude), a temperature of 240 K and typical stratospheric volume mixing ratios of HCl and HNO<sub>3</sub> of 1 ppb and 5 ppb, respectively. The molecule size was derived using densities of 1.49 g/cm<sup>3</sup> and 1.51 g/cm<sup>3</sup>, yielding 8.5 and  $6.0 \times 10^{14}$  molecules per cm<sup>2</sup> for HCl and HNO<sub>3</sub> respectively.

$\gamma$	$t_{\text{HCl}}$	$t_{\text{HNO}_3}$
$10^0$	2 min	18 s
$10^{-1}$	20 min	2.8 min
$10^{-2}$	2.3 h	28 min
$10^{-3}$	1.5 d	4.6 h
$10^{-4}$	14 d	2 d
$10^{-5}$	138 d	20 d
$10^{-6}$	3.8 yr	200 d
$10^{-7}$	38 yr	5.2 yr

The timescales in Table 5.2 indicate that high uptake coefficients larger than  $10^{-4}$  for HCl and  $10^{-5}$  for HNO<sub>3</sub> cannot be maintained for much longer than a few days if the uptake mechanism consists only of adsorption and immediate reaction. After that, free reactive surface sites will deplete quickly and a diffusion-based mechanism must take effect. Given the realization from (Dai et al., 2020) that the products do not cover the surface uniformly, the transition to a diffusion-based mechanism would occur even sooner. Conversely, extremely low uptake coefficients, e.g., below  $10^{-6}$  for HCl and below  $10^{-7}$  for HNO<sub>3</sub>, would be unimportant for stratospheric chemistry on timescales relevant for SRM.

#### 5.4.1 Uptake coefficients representative for calcite particles throughout their stratospheric residence time

We now determine uptake coefficients for HNO<sub>3</sub> and HCl that are representative for the injection of calcite particles into the stratosphere, which requires some aspects to be considered. Although some researchers found that their  $\gamma$  values were independent of gas phase concentration of the acid (Fenter et al., 1995; Huynh and McNeill, 2020), Tables S1 and S2 suggest correlations between the measured uptake coefficient and the exposure (= reactant concentration times duration of exposition applied in the experiment). This correlation is depicted in Figure 5.12. A double logarithmic least-square fit function was derived (see equation 5.21 and 5.22), resulting in correlation coefficients of 0.807 and 0.0034 for HCl and HNO<sub>3</sub>, respectively (see black line in Figure 5.12). While the correlation for HNO<sub>3</sub> is very poor, the HCl fit to the data is very good (which could be a coincidence since the total amount of measurements is much smaller for HCl).

$$\log(\gamma_{\text{HCl}}) = 9.845 - 0.878 \times \log(\text{Exposure}) \quad (5.21)$$



$$\log(\gamma_{\text{HNO}_3}) = 0.548 - 0.242 \times \log(\text{Exposure}) \quad (5.22)$$

For calculation the corresponding stratospheric exposure of a calcite particle to HCl and HNO<sub>3</sub> we assumed the average stratospheric residence time of a particle to be 9 months when assuming a particle radius of 240 nm (see Chapter 3) and a total molecule number concentrations of  $1.25 \times 10^{18}$  molecules/cm<sup>3</sup> at 50 hPa (i.e. 20 km altitude) with corresponding HCl and HNO<sub>3</sub> mixing ratios of around 1 ppb and 10 ppb, respectively. This results in a estimated exposures of  $2.3 \times 10^{16}$  s/cm<sup>3</sup> and  $2.3 \times 10^{17}$  s/cm<sup>3</sup> for HCl and HNO<sub>3</sub>, respectively. Using the fit derived above, the uptake coefficients of these exposures would result in an average uptake coefficient of  $2 \times 10^{-5}$  and  $2 \times 10^{-4}$  for HCl and HNO<sub>3</sub>, respectively. However, this simplistic approximation disregards any dependence on other factors such as those listed in 5.1.1 as well as temperature, which vary significantly across all studies represented in Figure 5.12. Furthermore, the derived fits (E5.21 and E5.22) used in this approximation are also flawed as they would lead to an illogical uptake coefficient larger than 1 for very low exposure inputs. Therefore, it is difficult to indicate any reliable uncertainty range. For the HCl fit, we indicated the uncertainty with plus minus one standard deviation of the slope of the fit (gray lines). Due to the very small correlation coefficient this is not possible for the HNO<sub>3</sub> fit, since the uncertainty range would cover the whole plot area. Therefore, we simply give the uncertainty as plus minus 1.5 orders of magnitude. This results in an uncertainty range of uptake coefficients representative for stratospheric exposures between  $1 \times 10^{-2}$  and  $1 \times 10^{-7}$  for HCl and between  $7 \times 10^{-2}$  and  $7 \times 10^{-6}$  for HNO<sub>3</sub>, respectively (see Figure 5.12). This does not further constrain the uncertainty range of uptake coefficients derived based on Table 5.2.

Even considering all this information, it is still not possible to determine an uptake coefficient, representative for the stratosphere with any relevant certainty. Our AP-XPS results show an uptake coefficients of up to  $1 \times 10^{-4}$  for HNO<sub>3</sub> during the first hours of exposure, which is likely an upper limit. The upper limit for HCl might be slightly lower (see Figure 5.12). The open question remains whether or not these uptake coefficients can be sustained in the stratosphere, which is likely a question of ion diffusion efficiency. The diffusion efficiency is strongly dependent on the availability of water and thus, the stable hydrate form of the Ca(NO<sub>3</sub>)<sub>2</sub> and CaCl<sub>2</sub> products at the particle surface, which is a function of RH and thus, temperature. The ERDA results point at very strong diffusion processes. Even though the ERDA measurements were performed at higher temperatures compared to the stratosphere, it can not be excluded that diffusion is very efficient at stratospheric temperatures too.

#### 5.4.2 Estimate of gas phase HNO<sub>3</sub> depletion through uptake by calcite particles

With an emission of 5 Mt/yr of calcite particles with an initial radius of 240 nm, an approximate residence time of these particles of one year in a 10 km thick layer ensheathing Earth, the particle number density will be  $\approx 6/\text{cm}^3$  and the surface area density in this aerosol layer will be  $\text{SAD} \approx 5 \mu\text{m}^2/\text{cm}^3$ . With  $\gamma = 10^{-4}$  as derived above, the buildup of a monolayer of Ca(NO<sub>3</sub>)<sub>2</sub> is then about one day. When ignoring the stratospheric HNO<sub>3</sub> source from the N<sub>2</sub>O reaction with O(<sup>1</sup>D), the loss of HNO<sub>3</sub> through uptake by calcite has an e-folding time of  $\tau = (\gamma \bar{v} \text{SAD}/4)^{-1}$ . Again, with  $\gamma = 10^{-4}$  we find  $\tau \approx 1$  yr, i.e. it takes roughly one year to reduce the stratospheric HNO<sub>3</sub> to 35 % of its initial value. Given the residence time of one year, stratospheric HNO<sub>3</sub> will be reduced to about 1/3 of its value without the calcite aerosol. Bear in mind that this is a very rough back-of-the-

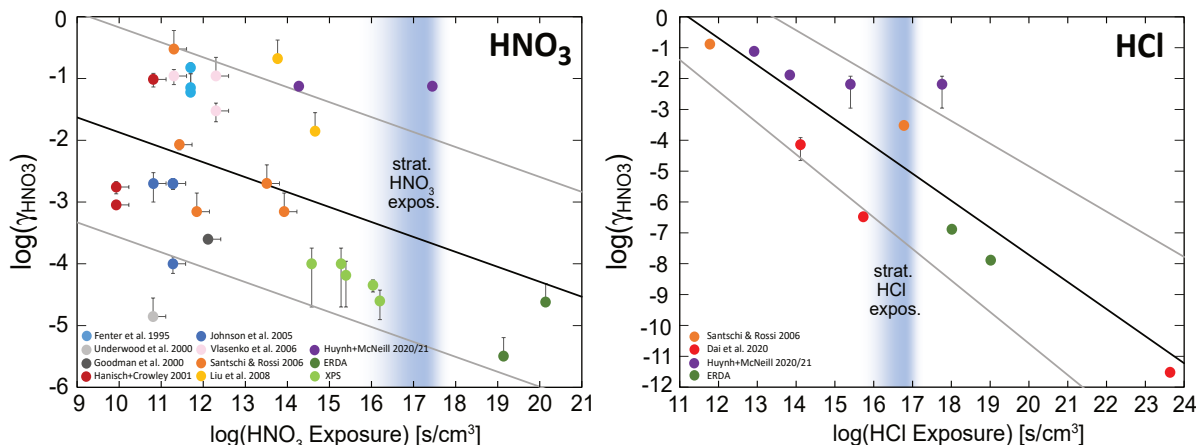


Figure 5.12: Uptake coefficients of HNO<sub>3</sub> (left) and HCl (right) measured by different studies ((see Tables 5.3 and 5.4 in the Appendix 5A) as a function of exposure (i.e., concentrations during the experiment multiplied with the exposure time). The thick black lines represents a logarithmic least square fits to the experimental data. The thin gray lines indicate for HCl  $\pm$  the standard deviation of the slope of the fit and for HNO<sub>3</sub> we simply indicate the error to be  $\pm 1.5$  orders of magnitude, which includes most data points (whereas the standard deviation of the slope would be even larger). The blue shaded ranges indicate the maximum stratospheric exposures of calcite particles injected into stratosphere assuming a characteristic residence times and concentrations in the lower stratosphere (e.g., about one year at 50 hPa with 5 ppb HNO<sub>3</sub> and 1 ppb HCl).

envelope estimate, which requires confirmation by means of an aerosol-chemistry-climate model.

## 5.5 Conclusions and outlook

We have performed HI-ERDA and AP-XPS experiments to quantify the uptake of HNO<sub>3</sub> as well as HI-ERDA experiments to additionally quantify the uptake of HCl on calcite surfaces. The AP-XPS experiments allowed for the first time to monitor the uptake of HNO<sub>3</sub> in-situ during up to 20 hours under stratospheric conditions with respect to temperature (210 K), RH ( $\sim 4\%$ ) and HNO<sub>3</sub> concentrations ( $\sim 10^{-7}$  hPa). The resulting Ca(NO<sub>3</sub>)<sub>2</sub> layer reached an effective thickness at least 0.1 nm after 15 hours which corresponds to an uptake coefficient of about  $(6.5 \pm 4.5) \times 10^{-5}$  (see Figure 5.8 and Table 5.1). This is good agreement with Dai et al. (2020), who found uptake coefficients of  $(2.5 \pm 1.5) \times 10^{-4}$  with flow tube measurements under similar conditions. The HI-ERDA experiments were performed at HNO<sub>3</sub> and HCl concentration of 2-3 orders of magnitude larger than stratospheric concentrations at -20°K and at RH larger than in the stratosphere, but at much longer exposure times of up to 10 days. The measured uptake coefficients for HNO<sub>3</sub> are at least  $2.4 \times 10^{-5}$  and about  $(4.5 \pm 1.0) \times 10^{-5}$  when exposed to concentrations 2 and 3 orders of magnitudes larger compared to the stratosphere and for the uptake of HCl they are  $1.3 \times 10^{-7}$  and  $2 \times 10^{-8}$  when exposed to concentrations 2 and 3 orders of magnitudes larger compared to the stratosphere, respectively. The sample exposed to 3 orders of magnitude larger HNO<sub>3</sub> concentrations compared to the stratosphere showed complete transformation of HNO<sub>3</sub> to Ca(NO<sub>3</sub>)<sub>2</sub> · n H<sub>2</sub>O, indicating the formation of hydrates. Mea-

asuring the same sample again after two weeks of storage indicated diffusion of CO<sub>3</sub><sup>2-</sup> ions from the bulk towards the surface and of NO<sub>3</sub><sup>-</sup> in the other direction, indicating strong diffusion processes within the sample, even after exposure.

As already shown in previous studies (e.g., Cziczo et al., 2019; Dai et al., 2020) it is likely that the particle surfaces would passivate with time due to depletion of reaction sites at the surface and increasing limitation of the uptake by diffusion. Comparing measured uptake coefficients versus the applied exposure during the experiment, we show that uptake coefficients representative for the average stratospheric residence time of a calcite particles are around  $2 \times 10^{-4}$  for HNO<sub>3</sub> and  $2 \times 10^{-5}$  for HCl (see Figure 5.12). However, this estimate also contains measurements performed at room temperature, larger RH and under significantly larger HNO<sub>3</sub> and HCl concentrations. As shown by Dai et al. (2020) as well as our own measurements the uptake coefficient is likely smaller when measuring under stratospheric conditions.

Even with all this information in mind, it is not possible to determine an uptake coefficient representative for stratospheric residence time of a calcite particle with any relevant certainty. Using the reasoning and the calculations derived in the previous section regarding 1) duration until monolayer coverage, 2) decrease of uptake coefficient with increasing exposure, and 3) depletion of reactants with time it is reasonable to narrow down the range of probable  $\gamma$ -values as it excludes unreasonable fast and slow uptake coefficients. On the one hand, all Knudsen cell studies had various degrees of fast initial uptakes with  $\gamma$ -values in the range of approximately 0.5 to 0.001 (see Table 5.3 and 5.4 in the Appendix 5A). After this fast uptake, further reactive uptake dropped below the detection limit for this setup. Any uptake coefficient larger than  $10^{-3}$  for HNO<sub>3</sub> and  $10^{-4}$  will therefore not be sustained over the entire exposure duration and will more likely saturate the initial reactivity in a matter of hours. On the other hand, starting off with an uptake coefficient at the lower end of literature values would only lead to enough reactive uptake to cover a monolayer after years in the stratosphere. Therefore values smaller than  $10^{-6}$  are not altering the stratospheric reservoirs of HNO<sub>3</sub> and HCl and neither the calcite particles significantly.

From the present information, the limiting factor in the long-term uptake of gaseous acids on the surface of calcite is the diffusion from and into the bulk. Additional ERDA experiments spanning exposures across different timescales of up to several months at stratospheric temperatures (i.e., lower than the -20°C in this study), while keeping the exposure concentration constant would allow us to estimate diffusion coefficients. However, most importantly it would be necessary to determine the stable hydrate forms of mixtures of CaCO<sub>3</sub>, Ca(NO<sub>3</sub>)<sub>2</sub>, CaCl<sub>2</sub> and CaSO<sub>4</sub> at stratospheric temperature and RH. It would also be important to determine the exact diffusion or ion exchange mechanisms within this system, which could for example be addressed by using models such as the kinetic multi-layer model for gas-particle interactions in aerosols and clouds (Shiraiwa et al., 2012). For now the uptake of acids on calcite particles in the stratosphere is likely smaller than  $10^{-4}$ .

## Author contributions

SV wrote the initial paper draft and created most of the figures. PT, SV, LL, LA, MA, TBR, HY, JG PT measured the XPS data. PT did most of the XPS data analysis with support from LL, MA and SV. MD, CV conducted the ERDA measurement, which were setup and prepared by SV. TP and CV also created some of the figures. Substantial

editing and commenting on the paper draft was done by TP, MA and CV, while all co-authors provided feedback for the final draft.

## Acknowledgments

This work was performed at the Soft X-Ray in-situ ambient pressure photoelectron spectroscopy beamline (X07DB) of the Swiss Light Source (SLS) at Paul Scherrer Institute in Villigen, Switzerland. We thank the SLS operators for granting us beamtime at the AP-XPS beamline (X07DB). Support for Sandro Vattioni was provided by the ETH Research grant no. ETH-1719-2 as well as by the Harvard Geoengineering Research Program. Support for PT was provided by the research group of TP at ETH Zürich. Support for Gabriel Chiodo was provided by the Swiss Science Foundation within the Ambizione grant no. PZ00P2\_180043.

## Appendix 5: Supplementary information

### A: Uptake of HCl and HNO<sub>3</sub> on calcite

The following tables provides uptake coefficients of gaseous HCl (Table 5.3) and HNO<sub>3</sub> (Table 5.4) and on various forms of calcite, which were experimentally determined by different studies including this one. Table 5.4 shows experimental results from studies which measured  $\gamma_{\text{HNO}_3}$  (Fenter et al., 1995; Underwood et al., 2000; Goodman, 2000; Hanisch and Crowley, 2001; Johnson et al., 2005; Vlasenko et al., 2006; Liu et al., 2008; Huynh and McNeill, 2020) and Table 5.3 shows results from studies which looked at  $\gamma_{\text{HCl}}$  (Santschi and Rossi, 2006; Dai et al., 2020; Huynh and McNeill, 2020, 2021). These values have been determined through vastly differing procedures, measurement techniques and measurement conditions which are elaborated on below.

### Studies on the uptake of HCl on calcite:

Table 5.3: Various  $\gamma_{\text{HCl}}$  measured in previous studies as well as the current study. Different columns indicate the lead author of the study, the equivalent stratospheric exposure time (see \*), the duration, as well conditions such as time, RH, temperature and information about the sample, the measurement technique applied (method), the calculation applied to get  $\gamma_{\text{HCl}}$  as well as the resulting  $\gamma_{\text{HCl}}$ -Value. A relative humidity stated as "dry" is assumed to be around 0% but was not measured during the experiment. Entries on which no information was found are marked with N.A., i.e., not applicable

Lead Author	eq. exp.*	Conc. [ $\text{cm}^{-3}$ ]	time	RH	temp.	Sample	Method	Calculated	$\gamma_{\text{HCl}}$ -Value
A) Santschi2006	N.A.	$10^{14}$	10min	dry	RT	cut marble disk	Knudsen Cell	geom. area	$3 \times 10^{-4}$
B)	10min	$6 \times 10^{11}$	1 s			CaCO <sub>3</sub> powder			$1.3 \times 10^{-1}$
C)						CaCO <sub>3</sub> powder			$6 \times 10^{-2}$
A) Dai 2020	36h	$7.2 \times 10^{11}$	3min	~ 0%	215K	depos.ptc.	flow tube	semi ss	$(7.2 \pm 5.0) \times 10^{-5}$
B)	62.5d	$5.4 \times 10^{14}$	10 s	dry	200K	depos.ptc.	gasflow flask		$(3.3 \pm 0.6) \times 10^{-7}$
C)	$1.4 \times 10^7$ a	$3.6 \times 10^{17}$	14d						$(3.0 \pm 0.6) \times 10^{-12}$
A) Huynh 2020	N.A.	$7.0 \times 10^{11}$ $1.6 \times 10^{14}$	–	<5%	RT	depos.ptc.	flow tube	geom. area	$(6.5 \pm 5.4) \times 10^{-3}$
B)	19h	$5.3 \times 10^{12}$	13s			dry disp. ptc.		SAD	$(1.3 \pm 0.1) \times 10^{-2}$
Huynh 2021	13h	$3.6 \times 10^{12}$	2.3s		207K				$(7.6 \pm 0.9) \times 10^{-2}$
A) this study	329yr	$2.4 \times 10^{13}$	5d	~ 70%	253K	sgl. crst. slab	isolated flask	geom. area	$1.3 \times 10^{-8}$
B) HI-ERDA	32.9yr	$2.4 \times 10^{12}$							$1.3 \times 10^{-7}$
A) this study	14h	$10^9$	220K				AP-XPS	geom. area	$2 \times 10^{-8}$
B) AP-XPS	14h	$10^9$	220K				AP-XPS	geom. area	$2 \times 10^{-8}$

\* "eq. exp." refers to the corresponding time of exposure to stratospheric HCl concentrations of each experiment. For the stratosphere, a number density of air equal to  $10^{18}$  molecules  $\text{cm}^{-3}$  and a HCl volume mixing ratio of 1 ppb at a total pressure of 50 hPa was assumed. The duration was then calculated from the ratio of the gas phase concentration used in the experiment to the stratospheric concentration multiplied by the duration of the laboratory experiment

**Santschi and Rossi (2006):**

This study conducted experiments similarly to the previously explained nitric acid uptake; using a Knudsen Cell (Golden et al., 1973).

**Material and Preparation:** Carrara marble was cut into 5 mm disks with a radius of 50 mm and then heated at 330 K for 24 h. Using their experimental set up on polished marble disks, it did neither provide any detectable uptake of HCl nor resulted in any detectable product. The marble disk was therefore used unpolished A in Table 5.3. For values B and C, they used precipitated CaCO<sub>3</sub> powder crystals with a measured  $S_{\text{BET}}$  of 3.7 m<sup>2</sup> g<sup>-1</sup>, a side length of 2 μm (determined via SEM) and density of 1.3 g cm<sup>-3</sup>

**Reaction Conditions:** The reaction on the unpolished marble (experiment A) used an HCl concentration of 10<sup>14</sup> molecules cm<sup>-3</sup>; albeit table 4 in their publication states this as concentration of HCl<sub>3</sub> in molecules cm<sup>3</sup>. The experiments on the calcite powder used a gas phase concentration of 6 × 10<sup>11</sup> molecules cm<sup>-3</sup>. All experiments were conducted at 300 K and can be assumed to have dry conditions as usual for a Knudsen Cell.

**Measurement and Calculations:** A mass spectrometer was coupled to the reactor to determine the uptake coefficients  $\gamma_0$  which was determined from the net loss of the gas phase reactant HCl. Values B and C are referring to initial uptake coefficients whereas the experiment on the marble disk measured a longer uptake. Unfortunately no mention of a exposure time was found. **Note:** It is unclear what exactly the difference between values B and C is supposed to be. In cases when a saturated sample was pumped or left to regenerate before additional uptake experiments, this has been clearly stated in the paper. The terms "first" and "third" uptake might just be them numbering their experiments. So there is not really an explanation for the factor of two difference in  $\gamma_0$ .

**Dai et al. (2020):**

They used two methods to determine the uptake coefficient for this reaction.

**Material and Preparation:** Both methods used calcite particles with a stated average diameter of 200 nm and a BET surface area of 14.8 ± 0.5 m<sup>2</sup> g<sup>-1</sup>. For value A in Table 5.3, the calcite sample was deposited from an isopropanol solution on the walls of the insert. The insert was subsequently heated in an oven to 250 °C for roughly 30 min. It is stated that the insert was covered with around 2.5 layers of particle. The sample inserts are then placed into the flow tube and pumped for 2 h down to 60 mTorr to remove any physisorbed water. For the flask experiments (values B and C) 0.1 g of the calcite particles were simply deposited on the bottom of the reaction vessel.

**Reaction Conditions:** The flow tube experiment was conducted at 215 K and 1.7 Torr. Values 2.2 & 2.3 resulted from flask experiments using a glass vessel at 200 K and ambient pressure. The cooling was done with dry ice. A flow of HCl and N<sub>2</sub> was used as a reactant gas and the glass vessel was flushed with pure N<sub>2</sub> before and after the exposure to HCl. For the reaction leading to value A, it is stated that the semi steady-state occurs after around 3 min and this time period was thus used as a reaction time. The experiment with which value B was determined had a reaction time of 10 s whereas value C was determined from an experiment with a reaction time of approximately 10<sup>6</sup> s or 14 days.

**Measurement and Calculations:** The uptake coefficient in experiment A was calculated from a decrease in reactant flow determined with a coupled mass spectrometer. The amount of reacted CaCO<sub>3</sub> reacted to CaCl<sub>2</sub> in the flask experiments was determined from dissolved Cl<sup>-</sup> ions after the reaction.

**Huynh and McNeill (2020) and Huynh and McNeill (2021):**

They determined the uptake coefficient of this reaction using two different methods. A flow reactor with deposited CaCO<sub>3</sub> particles was used for value A in Table 5.3 and the other values were determined in an aerosol flow tube reactor.

**Material and Preparation:** The aerosols were generated from dry dispersing calcite powder with an initial particle size of 200 nm. The aerosols had a size distribution peaking around 1 μm. For value A these aerosols were then deposited on a ZnSe window.

**Reaction Conditions:** The deposited particle experiment was conducted similarly to the HNO<sub>3</sub> uptake experiment in the same paper (Table 5.4). Values A & B in Table 5.3 were obtained at room temperature (296 K) and C was obtained from a later study at a temperature of 207 ± 3 K. The flow rate and dimensions in these experiments resulted in a reaction time of 13 s for values B & C. All experiments were conducted at ambient pressure and the relative humidity was measured to be below 5%.

**Measurement and Calculations:** Value A was quantified by observing the change in the absorbance intensity via IR of the asymmetric stretching of CO<sub>3</sub><sup>2-</sup>. The calculation is elaborated in the description of the experiment with nitric acid above. The uptake in the flow reactor was quantified by measuring the change in the HCl concentration during the experiment using a chemical ionisation mass spectrometer (CIMS) using SF<sub>6</sub><sup>-</sup>. The change was monitored on the SF<sub>5</sub>Cl<sup>-</sup> ion which was determined to linearly correlate to the HCl concentration. The uptake coefficient was then calculated from the surface area density determined via SPMS.

**HI-ERDA (this study):**

We determined the uptake coefficient on single crystal calcite with a long term experiment at -20 °C.

**Material and Preparation:** We used single-crystal calcite slabs of dimension (15 × 10 × 1) mm<sup>3</sup> with polished surfaces.

**Reaction Conditions:** The experiment was conducted in a desiccator at -20 °C and ambient pressure. The calcite sample was left in the desiccator for 5 days with an H<sub>2</sub>SO<sub>4</sub> solution (30wt%) containing the required amount of HCl to provide a gas phase concentration of 8 ppm in the case of experiment A in Table 5.3 and 0.8 ppm for experiment B. The relative humidity was measured at around 70% which is far above the deliquescence relative humidity for CaCl<sub>2</sub> at -20 °C which was found by M. Steiger (unpublished) to be 52.5%.

**Measurement and Calculations:** The uptake coefficient was calculated from the geometric surface area of the crystal to determine the number of collisions, and the elemental composition measured using ERDA measurements.

### Studies on the uptake of HNO<sub>3</sub> on calcite:

Santschi and Rossi (2006) clearly differentiated value A from their other uptake experiments with HCl as not being an initial uptake or  $\gamma_0$ , while not indicating any reaction time for that experiment. To observe any uptake at all, they had used a HCl concentration of a factor of 20 larger than for any of the other experiments. Due to the complete lack of reaction time, no equivalent time in the stratosphere could be deduced nor could this value be included in Figure 12. The value is nevertheless included in the table, as it provides a comparison to the uptake on the powder sample.

Dai et al. (2020) stated uptake coefficients depending on the product layer thickness. The range given for these values, determined using the flask setup, span five orders of magnitude. Those values were determined from reactions with product layers of different thickness. It is intuitive that the reactive uptake becomes lower if the reactive CaCO<sub>3</sub> core is behind a thicker layer of product. Those values of different product layer thickness also correspond to longer reaction time. Value B was determined from a reaction with a 0.05 Å product layer. This seems odd as 5 pm is over 36 times smaller than the radius of a single chloride ion (around 181 pm). The product layer thickness for value C (3.3 nm) would correspond to approximately 15 monolayers of product. This is in contrast to the several 100 nm depth at which we found chlorine atoms in our ERDA experiments.

Dai et al. (2020) calculated the product thickness from the total amount of Cl<sup>-</sup> ions and the BET surface area. Hence, it describes an average distribution assuming even surface coverage. The difference shown in the previous paragraph shows that the product layer of CaCl<sub>2</sub> · xH<sub>2</sub>O is not an even distribution over the sample surface even after a reaction time of 14 days (value C). The depth resolved ERDA measurements performed in this study do not contradict this as carbon atoms were still present throughout the measured range at both concentrations, unlike for the uptake of HNO<sub>3</sub>.

All in all, the four publications on this reaction can be put into two different categories: measurements determining the initial surface uptake (short-term) and measurements which also observed reaction in the bulk through a form of diffusion (long-term). Short-term would include values from Santschi and Rossi (2006), Huynh and McNeill (2020) and Huynh and McNeill (2021).



Table 5.4: Various  $\gamma_{\text{HNO}_3}$  measured in previous studies. Different columns indicate the lead author of the study, the equivalent stratospheric exposure, i.e., the time which a sample exposed to the same concentrations as in the specific experiment would require to reach stratospheric exposure, the HCl concentration applied in the, measurement, the duration, as well conditions such as time, RH, temperature and information about the sample, the measurement technique applied (method), the calculation applied to get  $\gamma_{\text{HNO}_3}$  as well as the resulting  $\gamma_{\text{HNO}_3}$ -Value. A relative humidity stated as "dry" is assumed to be around 0% but was not measured during the experiment. Entries on which no information was found are marked with N.A., i.e., not applicable

Lead Author	eq.exp.*	Conc. [cm <sup>-3</sup> ]	time	RH	T	Sample	Method	Calculated	$\gamma_{\text{HNO}_3}$ -Value
A) Fenter1995	1 s to	(0.1–100) × 10 <sup>11</sup>	1 s	dry	RT	dried powder	KnudsenCell	geom. area	7.1 × 10 <sup>-2</sup>
B)	16.67 min					pellets ("humid")			(1.5 ± 0.3) × 10 <sup>-1</sup>
C)						pellets ("dried")			6.0 × 10 <sup>-2</sup>
Underwood2000	6.4 s	6.4 × 10 <sup>10</sup>	1 s	dry	RT	powder	KnudsenCell	BET corr.	1.4 × 10 <sup>-5</sup>
Goodman2000	130 s	1.3 × 10 <sup>12</sup>	1 s	~ 0%	RT	powder	KnudsenCell	BET corr.	(2.5 ± 0.1) × 10 <sup>-4</sup>
A) Hanish2001	6.5 s	6.5 × 10 <sup>10</sup>	1 s	dry	RT	"dry" powder	KnudsenCell	geom. area	(9.7 ± 2.4) × 10 <sup>-2</sup>
B)	0.85 s	8.5 × 10 <sup>9</sup>	1 s			sgl. crst. unpol.			(1.75 ± 0.39) × 10 <sup>-3</sup>
C)						sgl. crst. pol.			(0.90 ± 0.12) × 10 <sup>-3</sup>
A) Johnson2005	6.5 s	6.5 × 10 <sup>10</sup>	1 s	dry	RT	multp. ptc. lys	KnudsenCell	BET corr.	(2.0 ± 1.0) × 10 <sup>-3</sup>
B)	19 s	1.9 × 10 <sup>11</sup>	1 s			fract. ptc. layer		$\gamma_{\text{obs}}$	(2.0 ± 0.4) × 10 <sup>-3</sup>
C)								BET corr.	(1.0 ± 0.3) × 10 <sup>-4</sup>
D)								Hoffmann	(2.0 ± 0.4) × 10 <sup>-3</sup>
A) Vlasenko2006	N.A.	(10 ± 1) × 10 <sup>11</sup>	2s	33%	RT	CaCO <sub>3</sub> aerosol	aerosolFT	SPMS	11 × 10 <sup>-2</sup>
B)		(10 ± 5) × 10 <sup>10</sup>	2s	33%		ATD			(11 ± 3) × 10 <sup>-2</sup>
C)		(10 ± 1) × 10 <sup>11</sup>	2s	33%		ATD			(3 ± 1) × 10 <sup>-2</sup>

Table: (continued)

Lead Author	eq. exp. *	Conc. [cm <sup>-3</sup> ]	time	RH	T	Sample	Method	Calculated	γ-Value
A) Santschi2006	27 s	$2.7 \times 10^{11}$	1 s	dry	RT	pm disk	KnudsenCell	geom.area	$(8.5 \pm 1.5) \times 10^{-3}$
B)	70 s	$7.0 \times 10^{11}$	1 s			pm			$7 \times 10^{-4}$
C)	54 min	$2.7 \times 10^{11}$	2 min			pm, steady-state			$2 \times 10^{-3}$
D)	2.33 h	$7 \times 10^{11}$				pm, steady state			$7 \times 10^{-4}$
E)	~20 s	$\sim 2.0 \times 10^{11}$	1 s			CaCO <sub>3</sub> powder			0.3
A) Liu 2008	23–73h	$(5.5\text{--}8.8) \times 10^{11}$	various	10%	RT	depos.powder	stagnat.flow	N.A.	$3.2 \times 10^{-3}$
B)	11–14h	$(4.1\text{--}5.4) \times 10^{11}$	16 min	20%					$1.4 \times 10^{-2}$
C)	1.6–1.7h	$(1.9\text{--}2.0) \times 10^{11}$	5 min	80%					$21 \times 10^{-2}$
Dai 2020				~0%	215 K	depos.ptc	flow tube	semi ss	$(2.5 \pm 1.8) \times 10^{-4}$
Huynh 2020	5.2 h– 325 d	$5.2 \times 10^{10}$ $7.8 \times 10^{13}$	to 1 h	<5%	RT	depos.ptc	flow reactor	N.A.	$(7.5 \pm 6.5) \times 10^{-2}$
A) this study	44 yr	$1.6 \times 10^{14}$	10 d	6%	253 K	single crystal	flask	geom.area	$>2.4 \times 10^{-5}$
B) HI-ERDA	4.4 yr	$1.6 \times 10^{13}$		4.5%			(HI-ERDA)		$3.2 \times 10^{-6}$
A) this study	14.7 d	$2.2 \times 10^{11}$	20 h	4%	210 K	CaCO <sub>3</sub> powder	AP-XPS	Atm. Mod.	$(2.50 \pm 1.25) \times 10^{-5}$
B) AP-XPS	10 d	$2.15 \times 10^{11}$	14 h	4%	210 K				$(4.5 \pm 1.0) \times 10^{-5}$
C)	1.75 d	$3.5 \times 10^{10}$	15 h	4%	210 K				$(1.0 \pm 0.8) \times 10^{-4}$
D)	8.4 h	$7.5 \times 10^9$	14 h	4%	210 K				$(1.0 \pm 0.8) \times 10^{-4}$
E)	2.3 d	$1.525 \times 10^{11}$	4.5 h	0%	210 K				$(6.5 \pm 4.5) \times 10^{-5}$

\* "eq. exp." refers to the corresponding time of exposure to stratospheric HCl concentrations of each experiment. For the stratosphere, a number density of air equal to  $10^{18}$  molecules cm<sup>-3</sup> and a HNO<sub>3</sub> volume mixing ratio of 10 ppb at a total pressure of 50 hPa was assumed. The duration was then calculated from the ratio of the gas phase concentration used in the experiment to the stratospheric concentration multiplied by the duration of the laboratory experiment.

**Fenter et al. (1995):**

They used a Knudsen Cell with a low-pressure flow reactor, and measured the initial uptake on various materials. The values herein stem from experiments on calcite powder and two kinds of calcite pellets.

**Material and preparation:** Calcite powder samples were prepared by grinding the material with a "Wig-L-Bug" amalgamator. The powder density was determined to be 0.6 g cm<sup>-3</sup>. Grain size was determined to be between 5 μm and 100 μm using scanning electron microscopy. Powders were dried in the evacuated Knudsen cell at around 10<sup>-7</sup> mbar for 10 - 48 hours prior to the experiments. The calcite pellets used for measurements B and C (see Table 5.4) were formed by compressing 500–700 mg of undried CaCO<sub>3</sub> powder into disks of approximately 2 mm thickness and a diameter of 13 mm. Density of the pellets was found to be 2.1 g cm<sup>-3</sup>, so a factor of 3.5 denser. The "humid" pellets were used freshly after being compressed whereas the "dried" pellets had been pumped in the reactor until the desorption of water reached background levels.

**Reaction Conditions:** Fenter et al. (1995) did not provide any temperature under which the experiment was conducted, but it can be assumed from other similar experiments conducted in Knudsen Cells that the reaction proceeded at room temperature. No pressure in the reaction chamber was stated either but Knudsen Cell flow reactors are characteristically operated at very low pressure in order to have a mean free path of the molecules larger than the vessel diameter Golden et al. (1973). The reaction on the calcite powder (measurement A) was conducted once. It used the smaller of the two reactors which had a stated surface area of the powder sample of 10.8 cm<sup>2</sup>. The number density in both of the reactors could be varied between (0.1–00) × 10<sup>11</sup> cm<sup>3</sup>. Some other specifications of the two reactors are summarised in a table in the original paper. The values provided above were obtained from a table stating the "low-dose experimental results" but it is not further specified what exactly a "low-dose" means.

**Measurement and Calculation:** The Knudsen Cell flow reactor was coupled to a quadrupole mass spectrometer (MS). The MS signal was characterised as a function of pressure change which could then be related to the mass flow. To determine the collision frequency, Fenter et al. (1995) used the surface of the sample without regard to any interior surfaces or reactive sites. The uptake coefficient  $\gamma$  was then calculated from the collision frequency  $\omega$  via  $\gamma = k_{\text{uni}}/\omega$  where  $k_{\text{uni}}$  is the first-order uptake of HNO<sub>3</sub> which was calculated via  $k_{\text{uni}} = (S_i/S_f - 1) \cdot k_{\text{esc}}$ . In this,  $S_i$  and  $S_f$  are the the MS signal at  $m/e = 46$  before and after the establishment of a steady-state respectively.

**Underwood et al. (2000):**

This study used a passivated Knudsen Cell reactor and investigated the diffusion into underlying layers. Alongside a variety of other reactions, the initial uptake of HNO<sub>3</sub> on CaCO<sub>3</sub> into a powder sample was investigated.

**Material and Preparation:** For the uptake coefficient values provided in this summary, Underwood et al. (2000) used CaCO<sub>3</sub> powder with a bulk density of 0.96 g cm<sup>-3</sup> and with a  $S_{\text{BET}}$  of 1.4 m<sup>2</sup> g<sup>-1</sup> corresponding to 0.22 particle layers per mg of powder. The graph illustrating the results in their paper shows three experimental measurements with different masses of the powder in the same sample area resulting in different layers of the samples. They appear to be around 20, 65 and 150 mg respectively. This powder was applied to the sample holder evenly using an atomiser.

**Reaction Conditions:** In the Knudsen Cell, 2 μTorr of nitric acid was dosed to react

with the CaCO<sub>3</sub> powder and the data acquisition time spanned around half a second. Using this pressure and the given reactor volume of 765 cm<sup>3</sup>, a number density of  $6.4 \times 10^{10}$  molecules cm<sup>-3</sup> was approximated for the concentration of nitric acid using the ideal gas law. The experiments were conducted at 298 K. Prior to the reaction, the reactor was passivated by flowing the reactant gas through it for at least 90 min.

**Measurement and Calculation:** The uptake was measured using a quadrupole mass spectrometer coupled to the reactor. The observed uptake  $\gamma_{\text{obs}}$  was determined from the MS signal according to the following equation:  $\gamma_{\text{obs}} = \frac{A_{\text{h}}}{A_{\text{s}}} \cdot \left(\frac{I_{\text{o}} - I}{I}\right)$ . In this,  $A_{\text{h}}$  and  $A_{\text{s}}$  are the area of the escape aperture and of the sample holder respectively, and  $I$  is the MS signal. Using the three experimentally observed uptake coefficients  $\gamma_{\text{obs}}$  with different sample masses, Underwood et al. (2000) calculated a "true" initial uptake coefficient  $\gamma_{\text{t}}$  to correct for diffusion into underlying layers and account for the entire reactive area. This was done with the BET surface area and the slope of a linear fit through the three  $\gamma_{\text{obs}}$  values according to the following equation:  $\gamma_{\text{t}} = \text{slope} \cdot (A_{\text{s}}/S_{\text{BET}})$  where  $A_{\text{s}}$  is equal to the sum of the top layer surface and the area of the voids of the sample.

### Goodman (2000):

This study used a Tefal passivated Knudsen Cell to determine the initial uptake coefficient on calcite powder and further looked at the dependence on relative humidity with an FTIR study.

**Material and Preparation:** For the uptake experiments, CaCO<sub>3</sub> powder was used as bought in two different sizes. The smaller particle size measured an average diameter of 3.5  $\mu\text{m}$  and a  $S_{\text{BET}}$  of 0.59 m<sup>2</sup> mg<sup>-1</sup> whereas the larger particles measured an average diameter of 7.4  $\mu\text{m}$  and a  $S_{\text{BET}}$  of 0.27 m<sup>2</sup> mg<sup>-1</sup>. The results of the two powder sizes varied only slightly, so the value listed in Table 5.4 is the average.

**Reaction Conditions:** The uptake coefficient was determined from an experiment at a low pressure of around 40  $\mu\text{Torr}$  which resulted in a gas phase concentration of  $1.3 \times 10^{12}$  molecules cm<sup>-3</sup>, and at 295 K. The relative humidity was stated to be "near 0%".

**Measurement and Calculation:** The initial uptake was measured with a coupled quadrupole mass spectrometer which observed the NO<sub>2</sub><sup>+</sup> signal at  $m/e = 46$ . The calculation of  $\gamma_{\text{obs}}$  was done in the same fashion as explained in the section above on Underwood et al. (2000). This uptake coefficient was again corrected for contribution of underlying layers. This was done using a slightly adapted version of the KML-model (Keyser et al., 1991) to correct uptake coefficients for the effect of gas diffusion into the bulk. This resulted in the  $\gamma$ -value listed in the table.

### Hanisch and Crowley (2001):

This study measured the uptake coefficient in 22 slightly varying experiments on calcite powder as well as on polished and unpolished single crystal samples using a Knudsen Cell.

**Material and Preparation:** The three values (A, B and C in Table 5.4) were determined from different sample materials. For the sample experiments leading to value A, 60 mg of a CaCO<sub>3</sub> powder with a particle diameter of less than 10  $\mu\text{m}$  was used which was dispersed onto the surface from an ethanol paste. In total the paper provides 22 measured initial uptake coefficients for the powder sample with varying experimental

conditions. Values B and C used a single crystal calcite sample along the 104 surface in its polished and unpolished state respectively. It had a size of (10 × 10 × 0.5) mm<sup>3</sup>. Both the powder and the single crystal were dried for these experiments prior to the reaction by heating them to 363 K for 5 h under a vacuum (2 × 10<sup>-6</sup> Torr).

**Reaction Conditions:** The total pressure in the Knudsen Cell was 0.4 mTorr and the reactions were conducted at 298 K. Value A was determined with a low gas phase concentration of 6.5 × 10<sup>10</sup> molecules cm<sup>-2</sup> and an approximate HNO<sub>3</sub> flow of 9 × 10<sup>13</sup> s<sup>-1</sup>. The single crystal experiment used an HNO<sub>3</sub> flow of 2.6 × 10<sup>13</sup> s<sup>-1</sup>. The number density was calculated from this to be 8.5 × 10<sup>9</sup> molecules cm<sup>-3</sup> via the equation  $n/V = 4F/(A_h\bar{c})$ . The average molecular velocity  $\bar{c}$  was calculated as  $\bar{c} = 1.46 \cdot 10^4 \sqrt{T/M}$ .

**Measurement and Calculation:** The reactor was coupled to a quadrupole mass spectrometer and to quantify the uptake, the decrease in HNO<sub>3</sub> flow was again determined from the NO<sub>2</sub><sup>+</sup> signal at m/e = 46. The signal was integrated over a period of 0.8 s to observe the initial uptake. The initial uptake coefficient was then calculated in a comparable manner to Fenter et al. (1995) using  $\gamma = k_{\text{uni}}/\omega$ .

### Johnson et al. (2005):

This study used a Teflon coated Knudsen Cell to measure the initial uptake of the reaction at varying particle layer quantities and correcting them with different models.

**Material and Preparation:** CaCO<sub>3</sub> was used in these experiments in the form of two different powders - as received - with a  $S_{\text{BET}}$  of 0.2 m<sup>2</sup> mg<sup>-1</sup> and 1.4 m<sup>2</sup> mg<sup>-1</sup> respectively. The uptake on multi-layer sample was determined with both types of powder and the fractional layer experiments used the finer powder and used 0.08, 0.09 and 0.18 monolayers of the powder.

**Reaction Conditions:** Prior to all experiments, a flow of nitric acid was used to further passivate the reactor until a steady flow was obtained. The experiments determining the uptake coefficient for a multi-layer sample A used a nitric acid concentration of 6.5 × 10<sup>10</sup> molecules cm<sup>-3</sup> which corresponded to a partial pressure of 2 μTorr when using the larger particle powder and a nitric acid concentration of 1.9 × 10<sup>11</sup> molecules cm<sup>-3</sup> corresponding to a partial pressure of 6 μTorr for the finer powder. The experiments leading to values B to D were conducted using a gas phase concentration of 6.5 × 10<sup>10</sup> molecules cm<sup>-3</sup>. Similar to all other Knudsen Cell measurements, these measurements were done at room temperature (296 K) and under dry conditions.

**Measurement and Calculation:** The uptake was measured with a coupled quadrupole mass spectrometer.  $\gamma_{\text{obs}}$  was calculated in the same way as explained in the section above on Underwood et al. (2000). This measured value was then corrected for the multi-layer experiment by using the KML model as well as by assuming a slope for a linear mass-dependent region (see section on Underwood et al., 2000). Both corrections lead to the same initial uptake coefficient listed as value A in Table 5.4. The  $\gamma_{\text{obs}}$  for fractional layers of particles is provided as value B and it was once corrected using the same method as for A but as it yielded a much smaller uptake coefficient, it was also corrected using the model described by Hoffman et al. (2003). These corrected values correspond to C and D in Table 5.4.

**Vlasenko et al. (2006):**

This study measured the uptake of HNO<sub>3</sub> on airborne, dry-dispersed calcite aerosol as well as on Arizona Test Dust (ATD) aerosol in a flow reactor.

**Material and Preparation:** The calcite aerosols were generated by nebulising a saturated aqueous CaCO<sub>3</sub> solution which was then dried in a diffusion dryer. The ATD aerosols were generated using a solid aerosol generated which provided submicron particles from the dust.

**Reaction Conditions:** The flow tube experiments were conducted at atmospheric pressure and room temperature. The reaction on CaCO<sub>3</sub> was measured at a nitric acid concentration of  $10 \pm 1 \times 10^{11}$  molecules cm<sup>-3</sup>. Values B and C in Table 5.4) for ATD were measured at two different nitric acid concentrations of  $10 \pm 5 \times 10^{10}$  molecules cm<sup>-3</sup> and  $10 \pm 1 \times 10^{11}$  molecules cm<sup>-3</sup>, respectively. All three values were determined at a relative humidity of  $(33 \pm 1)\%$  which was measured downstream of the flow reactor.

**Measurement and Calculation:** The uptake of nitric acid onto the aerosols was derived by measuring the decay of <sup>13</sup>N isotopes which were included in the reactant flow with a known ratio in the form of H<sup>13</sup>NO<sub>3</sub>. Vlasenko et al. (2006) clearly state that the uptake obtained through their measurement only accounts for irreversibly absorbed nitric acid which is still in the particulate phase when it reaches the aerosol filter, the initial loss of gas phase nitric acid could well be higher. The total aerosol surface area was measured using a Scanning Mobility Particle Sizer (SPMS).

**Santschi and Rossi (2006):**

This study used a Knudsen Cell and determined the initial uptake and a steady-state uptake on marble disks and CaCO<sub>3</sub> powder.

**Material and Preparation:** The polished marble disk (pm) used to obtain values A to D in Table 5.4 were cut from Carrara marble with a thickness of 5 mm and a diameter of 50 mm resulting in total exposed geometric surface of 27.4 cm<sup>2</sup>. These disks were heated at 330 K for 24 h and polished to a roughness of 6 μm. An additional experiment E used powdered CaCO<sub>3</sub> crystals with a measured  $S_{\text{BET}}$  of 3.7 m<sup>2</sup> g<sup>-1</sup>, a side length of 2 μm (determined via SEM) and density of 1.3 g cm<sup>-3</sup>.

**Reaction Conditions:** Two uptake experiments on the polished marble disk used a concentration of nitric acid of  $2.7 \times 10^{11}$  molecules cm<sup>-3</sup> resulting from a flow rate of  $5.5 \times 10^{14}$  molecules s<sup>-1</sup>. A third uptake experiment on the same substrate used a nitric acid concentration of  $7 \times 10^{11}$  molecules cm<sup>-3</sup>. The reaction on the CaCO<sub>3</sub> powder (value E in Table 5.4) as well as value A & B, measured the initial uptake coefficient  $\gamma_0$ . Value A provided in the table above states the average  $\gamma_0$  of the two experiments and the stated error is simply the range of results. The steady-states values (values C & D) were obtained after "an apparent saturation [...] after 2 min or so" which is thus treated as the reaction time. In steady-state conditions, the two measurements leading to value C provided an identical uptake coefficient. All experiments were conducted at 300 K and can be assumed to have dry conditions as usual for a Knudsen Cell. The authors did not provide a HNO<sub>3</sub> concentration for the measurement of value E. Compared to similar setups in this study it would most likely be in the range of  $2 \times 10^{11}$  molecules cm<sup>-3</sup> as well.

**Measurement and Calculation:** The Knudsen Cell was coupled to a mass spectrometer and The uptake coefficients were then calculated in a comparable manner to Fenter et al. (1995) using  $\gamma = k_{\text{uni}}/\omega$ . The collision frequency  $\omega$  was calculated from the

average molecular speed  $\bar{c}$  and the sample area  $A_s$  and the reactor volume according to  $\omega = (\bar{c}/4V) \cdot A_s$ .

**Liu et al. (2008):**

They used a stagnation flow reactor at determined the uptake coefficients on deposited calcite at various relative humidities.

**Material and Preparation:** The deposited CaCO<sub>3</sub> particles for the uptake experiments were generated by atomising a suspension of calcite powder in water. These particles were then dried and deposited. A size selective deposition impactor (MOUDI) and subsequent SEM imaging provided particles with a median diameter of 0.85  $\mu\text{m}$ .

**Reaction Conditions:** The stagnation flow reactor used a laminar flow of premixed N<sub>2</sub>/H<sub>2</sub>O/HNO<sub>3</sub> gases in desired ratios. The reactor was passivated with a flow of this gas mixture for 2 h before each experiment. The gas phase concentration of nitric acid was between  $(1.7\text{--}7.3) \times 10^{11}$  molecules cm<sup>-3</sup>. This range can be narrowed down by using the experimental conditions table for the specific relative humidity. The concentrations there were stated in terms of parts per billion from which the concentration was calculated with an assumed air density of  $2.55 \times 10^{19}$  molecules cm<sup>-3</sup> Brasseur and Solomon (1984). These concentration ranges at the respective relative humidity can be found in the table above. This overview includes measurements at 10 %, 20 % and 80% RH corresponding to values A, B and C in Table 5.4, respectively. All experiments were conducted at room temperature and at atmospheric pressure. A range of reaction time can also be found in the experimental conditions table in the original paper. For value A it included one measurement at 25 min and four each at 40 min and 50 min. Value B had a reaction time of 16 min and C of 5 min. Liu et al. (2008) provide further values for the uptake coefficient at varying relative humidities ranging in 10 % intervals from 10 % to 80% which was measured in line.

**Measurement and Calculation:** HNO<sub>3</sub> at the exit of the reactor was measured using a chemiluminescence NO<sub>y</sub> analyser. The extent of the reaction from CaCO<sub>3</sub> to Ca(NO<sub>3</sub>)<sub>2</sub> and the uptake coefficient was determined using the O/Ca ratio which was determined using energy-dispersed X-ray spectrometry and quantified with reference values for conversion at 0% and 100%.

**Dai et al. (2020):**

They determined the uptake coefficient using a flow tube reactor at stratospherically relevant temperature.

**Material and Preparation:** Purchased calcite particles with a declared average diameter of 200 nm and a measured BET surface area of  $14.8 \pm 0.5$  m<sup>2</sup> g<sup>-1</sup> were used throughout the study. The desired amount of CaCO<sub>3</sub> was deposited from an isopropanol solution evenly on the walls of the insert. The insert was subsequently heated in an oven to 250 °C for roughly 30 min. It is stated that the insert was covered with around 2.5 layers of particle. The sample inserts are then placed into the flow tube and pumped for 2 h down to 60 mTorr to remove any physisorbed water.

**Reaction Conditions:** The reaction was conducted at 1.7 Torr pressure and 215 K, which was achieved using a cooling jacket with a circulating dry ice/ethanol mixture. Dai et al. (2020) stated that the RH in the reactor could be treated to be 0. No HNO<sub>3</sub>

concentration was found in the publication.

**Measurement and Calculation:** The uptake coefficient was calculated from a decrease in reactant flow determined with a coupled mass spectrometer. They provided a semi steady-state uptake coefficient which occurred after about 3 min.

#### Huynh and McNeill (2020):

This study used a flow tube experiment to determine the uptake coefficient on impacted CaCO<sub>3</sub> aerosols.

**Material and Preparation:** Calcite powder with an initial particle size of 200 nm was deposited on to a ZnSe window from dry dispersed aerosols which were size selected to an average diameter of 1 μm. The mass density and surface density of the aerosols was observed using a scanning mobility particle sizer.

**Reaction Conditions:** The flow reactor was operated at 296 K and ambient pressure (760 Torr). The carrier gas used was N<sub>2</sub> and the HNO<sub>3</sub> reactant gas was varied in concentration from  $5.2 \times 10^{10}$  to  $7.8 \times 10^{13}$  cm<sup>-3</sup> or from approximately 3 to 267 parts per billion respectively. Independent of the concentration used, all experimental runs used a reaction time of 1 h. The relative humidity in the reactor was measured to be below 5%.

**Measurement and Calculation:** The reaction of CaCO<sub>3</sub> to Ca(NO<sub>3</sub>)<sub>2</sub> was quantified by observing the absorbance intensity  $S$  of the asymmetric stretching of CO<sub>3</sub><sup>2-</sup> at 876 cm<sup>-1</sup>. The uptake coefficient  $\gamma$  was then calculated using the formula,

$$(S - S_0) \frac{N_d}{[A]_0} = -\frac{1}{4} \gamma \omega [A]_0 SA \times t \quad , \quad (5.23)$$

where the left side is the normalised absorbance,  $SA$  is the surface area of impacted CaCO<sub>3</sub> available for reaction (although it is not elaborated how this surface area was determined),  $\omega$  is the molecular velocity and  $t$  is the reaction time of 1 h.

#### HI-ERDA (this study):

We measured the uptake from a 10-day long exposure to nitric acid of single crystal calcite at stratospherically relevant temperature.

**Material and Preparation:** A single crystal calcite slab was used with the dimensions (15 × 10 × 1) mm<sup>3</sup>.

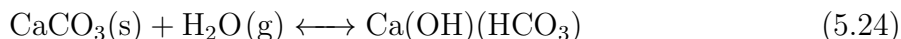
**Reaction Conditions:** The experiment was conducted in a desiccator at -20 °C and ambient pressure. The calcite sample was left in the desiccator for 10 days with an H<sub>2</sub>SO<sub>4</sub> solution (65wt%) containing the required amount of HNO<sub>3</sub> to provide a gas phase concentration of 8 ppm in the case of experiment A and 0.8 ppm for experiment B. The relative humidity at these conditions corresponds to about 6 % and 4.5% for experiment A and B in Table 5.4, respectively.

**Measurement and Calculation:** The uptake coefficient was calculated from the geometric surface area of the crystal to determine the number of collisions, and the elemental composition measured using ERDA measurements. This method only managed to observe the first 180 nm or so, which means the uptake coefficient determined with this method is a lower boundary.

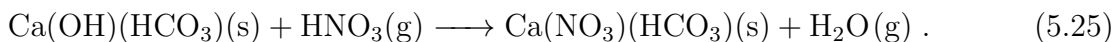


## B: Proposed Mechanisms

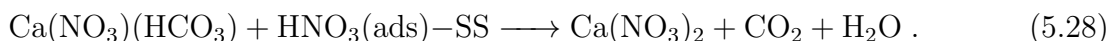
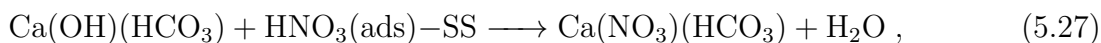
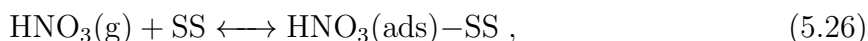
Various publications have postulated that the intermediate Ca(OH)(HCO<sub>3</sub>) is the reactive species during surface reaction of calcite with gaseous reactants (Santschi and Rossi, 2006; Al-Hosney and Grassian, 2005; Huynh and McNeill, 2020). The presence of surface species SS–OH and SS–HCO<sub>3</sub> was confirmed by Stipp and Hochella (1991) using X-Ray Photoelectron Spectroscopy (XPS) and low-energy electron diffraction (LEED) to analyse the binding energy. The Ca(OH)(HCO<sub>3</sub>) intermediate is formed through a number of reactions pathways, but once formed is not easily reversed even under conditions using ultra-high vacuum and/or heat (Stipp and Hochella, 1991). While the overall reaction



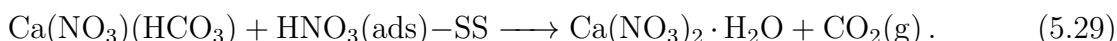
shows only the H<sub>2</sub>O stoichiometrically needed for the chemisorbed water, the proposed mechanism includes CO<sub>2</sub> necessary in the process (Santschi and Rossi, 2006). Formation of this reactive surface intermediate can be considered a result of the high charge density at the surface of calcium carbonate (Al-Hosney and Grassian, 2005). This surface intermediate indicates that the gaseous acid can react with either anionic group. Using the most simple overall reactions, reaction with the SS–OH will lead to HO product formation whereas reaction with SS–HCO<sub>3</sub> yields H<sub>2</sub>O and CO<sub>2</sub> products. The flow reactor study by Santschi and Rossi (2006) investigated the formation of these products in relation to the uptake of HNO<sub>3</sub> indicated by a loss in the reactant flow. They showed an approximate 1:1 relation of HNO<sub>3</sub> reacted and H<sub>2</sub>O released while at first no formation of CO<sub>2</sub> was detected. This suggests the initial reaction of the calcite surface with HNO<sub>3</sub> to be,



After halting the inflow of HNO<sub>3</sub> (Santschi and Rossi, 2006) observed a recovery of around 20% of the previously adsorbed or absorbed HNO<sub>3</sub>. This indicates a reversible adsorption to the surface before reaction. Taking the delayed formation of the product CO<sub>2</sub> into account they suggest the following reaction mechanism for the surface reaction of HNO<sub>3</sub> with CaCO<sub>3</sub> where SS indicates a reactive surface site:



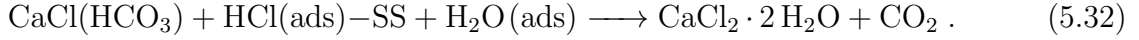
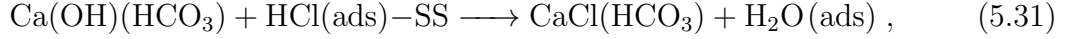
Yet, the absence of the chemisorbed water in the product while only one equivalent H<sub>2</sub>O was detected requires this water to be accounted for elsewhere. At a very low relative humidity, as prevalent in a Knudsen Cell, the prevailing hydrate form of calcium nitrate would be Ca(NO<sub>3</sub>)<sub>2</sub> · H<sub>2</sub>O according to (Steiger et al., 2011). Equation 5.28 should therefore rather be written as:



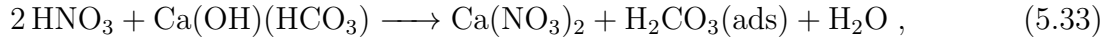
This would also align with findings on the ERDA measurements in this study that at a slightly higher RH the atomic composition of the bulk indicated a hydrate form somewhere between mono- and dihydrate.

Santschi and Rossi (2006) also observed a similar behaviour for the uptake of HCl. There was a slight delay in observed CO<sub>2</sub> formation and HCl desorption was measured after

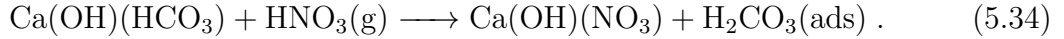
halting the flow. The same behaviour was again observed in Dai et al. (2020). However, Santschi and Rossi (2006) did not detect any H<sub>2</sub>O product. They proposed that the two equivalent of water are incorporated in a dihydrate form due to the high hygroscopicity of calcium chloride. Therefore, a similar reaction mechanism for the initial uptake of HCl on calcite was proposed as:



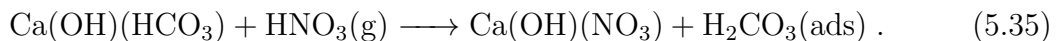
Unlike the delayed formation presented by Santschi and Rossi (2006), Prince et al. (2007) observed formation of CO<sub>2</sub> closely correlating to the loss in HNO<sub>3</sub>. This is likely due to the different experimental setups used. Prince et al. (2007) operated at much higher overall pressure as well as higher relative humidity. Especially the influence of the higher relative humidity is relevant to these differing observations. Huynh and McNeill (2020) noted the overall reaction of the uptake as



where the adsorbed H<sub>2</sub>CO<sub>3</sub> readily dissociates to H<sub>2</sub>O and CO<sub>2</sub> in the "presence of water". Under dry conditions, Al-Hosney and Grassian (2005) identified H<sub>2</sub>CO<sub>3</sub> and proposed the surface reaction of calcite with nitric acid as follow:



Similarly, Fenter et al. (1995) stated that humidity is required to release gaseous CO<sub>2</sub> product and (Hanisch and Crowley, 2001) found that it takes 2.7 and 3.4 equivalents of nitric acid to react in order to release one equivalent of CO<sub>2</sub> for a "damp" and "dry" sample, respectively. In their study on the uptake of H<sub>2</sub>O, SO<sub>2</sub> and HNO<sub>3</sub> on CaCO<sub>3</sub> (Al-Hosney and Grassian, 2005) used IR spectroscopy to observe the different surface groups. After exposure of the calcite to HNO<sub>3</sub>, H<sub>2</sub>CO<sub>3</sub> and adsorbed nitrate were observed. The produced carbonic acid would passivate the surface for further uptake if it would not dissociate. Adsorbed carbonic acid is stable under high-vacuum conditions (Al-Hosney and Grassian, 2005) but it only needs very small quantities of water to dissociate. This could be a reason why Santschi and Rossi (2006) observed a delayed formation of CO<sub>2</sub> in their Knudsen Cell experiment (very low pressure and near 0 RH). In their publication, Al-Hosney and Grassian (2005) proposed a reaction equation for the initial uptake that is contrasting to the one later suggested by Santschi and Rossi (2006) in which the HCO<sub>3</sub><sup>-</sup> group reacts in the first step:



This was reasoned from the observed presence of IR-bands corresponding to carbonic acid and nitrate respectively. Without any remarks on the IR-bands of the hydroxy group, this observation could also be explained with the mechanism formulated by Santschi and Rossi (2006). Unfortunately, the selection of the spectrum presented in the publication does not show the energy region which would be relevant for OH absorbance.

### 5.5.0.1 Surface Water

The IR study by Al-Hosney and Grassian (2005) on CaCO<sub>3</sub> showed an increase in the O–H stretch signal with increasing RH as would be expected. They further showed a broadening of the signal at around 50% RH when increasing the RH and at around 30% RH when decreasing the RH. This transition corresponds to the change from two-dimensional, more ice-like water "islands" on the surface at low RH to more liquid-like 3D clusters of surface adsorbed water at RH >50% (Al-Hosney and Grassian, 2005). The difference of the behaviour of adsorbed water on the surface is also dependent on the hydrophilicity of the surface. A rather hydrophilic surface can accommodate the water either in an ordered ice-like state, a liquid-like state or a co-existence of the two, whereas adsorbed water on an hydrophobic crystal surface assumes a liquid-like structure (Xiao et al., 2019). Santschi and Rossi (2006) determined a molecularly bound and rather mobile physisorbed waterlayer above the chemisorbed water in the form of Ca(OH)(HCO<sub>3</sub>). They experimentally determined that this strongly bound, chemisorbed water represents only about 0.4% of all adsorbed water at ambient conditions.

### 5.5.0.2 Diffusion

Most early studies into reactions (1) and (2) claimed a surface saturation after a few minutes and never observed uptake into the bulk of the sample. However with the longer exposure times in the measurements by ERDA in this study, the recoil signal of nitrogen nuclei, most likely from NO<sub>3</sub><sup>-</sup> ions, was found all the way to the detection limit of the measurement system at a depth of around 240 nm. There are two basic mechanisms of how the deeper sample layers can react: either the reactant gas molecules or ions diffuse through the product layer to the sample core; or CO<sub>3</sub><sup>2-</sup> ions (and HCO<sub>3</sub><sup>-</sup> in the presence of H<sub>2</sub>O) migrate from the solid core through the product layer to the surface, where they then react with the gaseous acids.

The ionic diffusion can occur through different modes to preserve local charge neutrality. In a so-called inward diffusion mechanism, anionic groups, such as NO<sub>3</sub><sup>-</sup> or Cl<sup>-</sup>, diffuse inwards through the bulk while the CO<sub>3</sub><sup>2-</sup> ions diffuse to the surface, whereas an outward diffusion mechanism sees the cation Ca<sup>2+</sup> diffusing to the surface alongside the anionic CO<sub>3</sub><sup>2-</sup>. Sun et al. (2012) experimentally analysed the diffusion mechanism for the reaction CaO + CO<sub>2</sub> → CaCO<sub>3</sub> and found an inward diffusion mechanism. This means that the reacting O<sup>2-</sup> diffuses outwards while the product CO<sub>3</sub><sup>2-</sup> diffuses inwards. Conversely, the outward diffusion mechanism would see Ca<sup>2+</sup> diffuse outwards alongside O<sup>2-</sup>. Due to its larger size, CO<sub>3</sub><sup>2-</sup> has a higher diffusion energy barrier, hence the inward diffusion mechanism is favoured. Co-diffusion in the outward mechanism requires a neighbouring cation and anion vacancy, which are only present at very low concentrations, if at all (Sun et al., 2012). This experimental finding might well not be applicable to reactions 5.1-5.3 as the product and reactant anion not only differ in size but also carry different charges compared to the experiment by Sun et al. (2012). An inward diffusion mechanism would require two NO<sub>3</sub><sup>-</sup> ions to diffuse to the CaCO<sub>3</sub>/Ca(NO<sub>3</sub>)<sub>2</sub> transition zone, while one CO<sub>3</sub><sup>2-</sup> migrates through the product to the surface to conserve charge neutrality. Putting aside the exact method of ionic diffusion, it is likely a shrinking-core of the reactant CaCO<sub>3</sub> and a layer of product from which CO<sub>3</sub><sup>2-</sup> diffuses to the surface to further react with the acids replenished from the gas phase.

Xiaoyu et al. (2011) observed "island formation" on the surface of a polished singly-crystal calcite sample after it has been heated in the presence of CO<sub>2</sub> to decompose and

then reform CaCO<sub>3</sub>. This indicated diffusion through the reactant to specific reactive sites. The investigated reaction of CaCO<sub>3</sub> with SO<sub>2</sub>(g) to form CaSO<sub>4</sub> was also shown to form "mound-like islands". They observed the islands to grow until they coalesced eventually, covering the entire surface. It has to be noted, that this sulfation experiment was conducted at 600 °C.

While adsorption of gas molecules at the surface increases with decreasing temperature, the diffusion through the solid decreases with decreasing temperature. The temperature dependence of the diffusivity  $D$  behaves Arrhenius-like (Heitjans and Kärger, 2005):

$$D = D_0 \cdot \exp\left(-\frac{\Delta H}{RT}\right), \quad (5.36)$$

where  $T$  is the absolute temperature,  $\Delta H$  is the activation enthalpy of diffusion and  $R$  is the universal gas constant. The diffusion through the solid is further heavily influenced by the exact structure of the solid including all kind of defects. The abundance of defects however again increases with increasing temperature. In any case, it is very likely that the solid diffusion is the limiting step for long-term uptake as the surface reaction is much faster.

## C: AP-XPS experimental setup

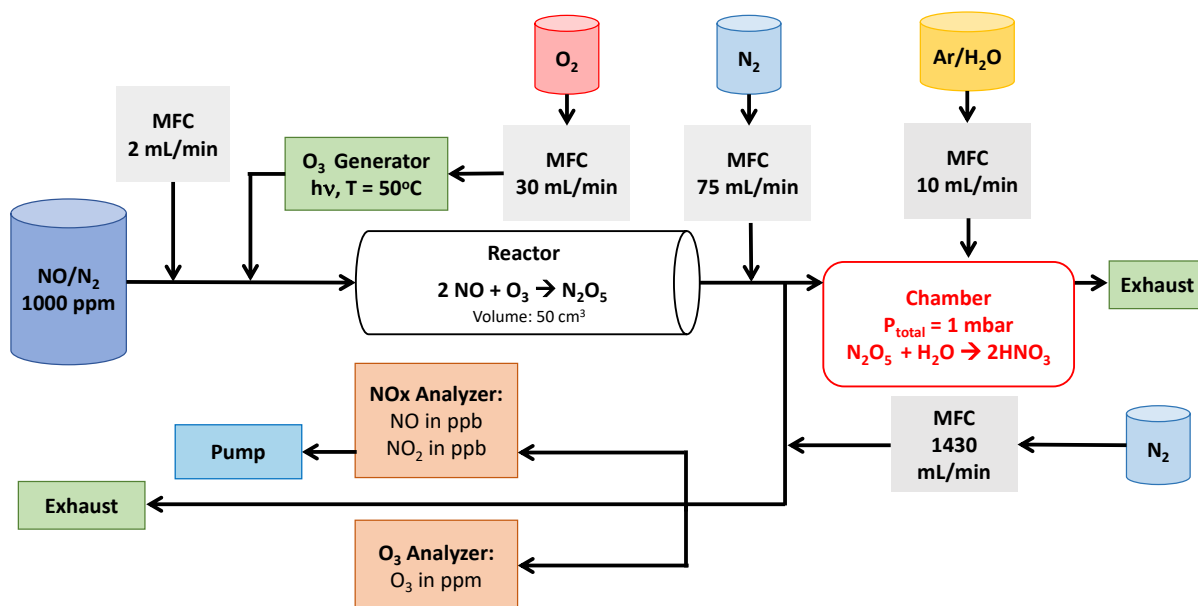


Figure 5.13: The dosing setup applied in this study. N<sub>2</sub>O<sub>5</sub> was generated within a reactor through reaction of NO + O<sub>3</sub>. O<sub>3</sub> was generated via photolysis in a O<sub>3</sub> generator at 50°C. O<sub>2</sub> and NO were dosed with mass flow controllers in order to meet desired concentrations of N<sub>2</sub>O<sub>5</sub> downstream the reactor. The tubing between reactor and the chamber was reduced to a minimum (about 20-30 cm) to minimize N<sub>2</sub>O<sub>5</sub> losses during transport. The desired N<sub>2</sub>O<sub>5</sub> concentration could be dosed via control of the NO flow to the reactor as well as via a N<sub>2</sub> dilution step after the reactor. The N<sub>2</sub>O<sub>5</sub>/O<sub>3</sub>/N<sub>2</sub> flow was dosed in the chamber via a leak valve and kept at 1 mbar total pressure. The excess flow was further diluted by N<sub>2</sub> to reach detectable concentrations in the NO<sub>x</sub> and the O<sub>3</sub> analyzers before the flow was released to the exhaust. Water was dosed via an Argon flow taking up water second leak valve.

## D: Attenuation model

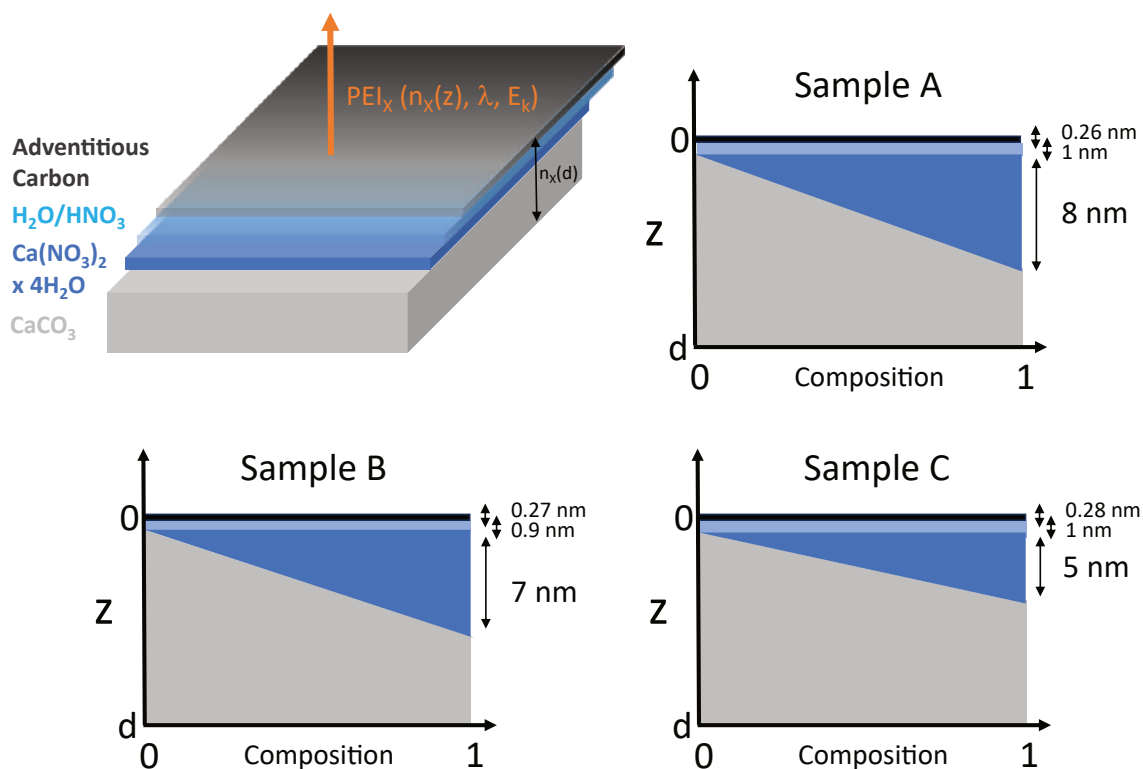


Figure 5.14: The upper left Figure illustrates a schematic overview of the attenuation model used in this study to model the photoelectron intensity (PEI) ratios relative to the Ca 2p PEI signal. The model assumes elemental concentrations ( $n_x$ ) as a function of depth ( $z$ ) with a depth resolution of 0.01 nm to a depth of  $d = 13$ . The model assumes a topmost adventitious carbon layer, followed by a H<sub>2</sub>O layer, which can contain a variable amount of adsorbed HNO<sub>3</sub> and a Ca(NO<sub>3</sub>)<sub>2</sub> x H<sub>2</sub>O layer with a linear gradient from 100% Ca(NO<sub>3</sub>)<sub>2</sub> x H<sub>2</sub>O at the surface to 0% Ca(NO<sub>3</sub>)<sub>2</sub> x H<sub>2</sub>O at the lower end of the layer as well as a bulk CaCO<sub>3</sub> layer. Other Figures represent the best fit configuration for the depth profiles of samples A, B, and C. The resulting Ca(NO<sub>3</sub>)<sub>2</sub> x H<sub>2</sub>O model thickness was 8 nm, 7 nm and 5 nm for samples A, B, and C, respectively. The modelled HNO<sub>3</sub> to H<sub>2</sub>O ratio within the adsorbed water layer was assumed to be 1:3, 1:3 and 1:6 for samples A, B and C, respectively.

## E: HI-ERDA experimental setup

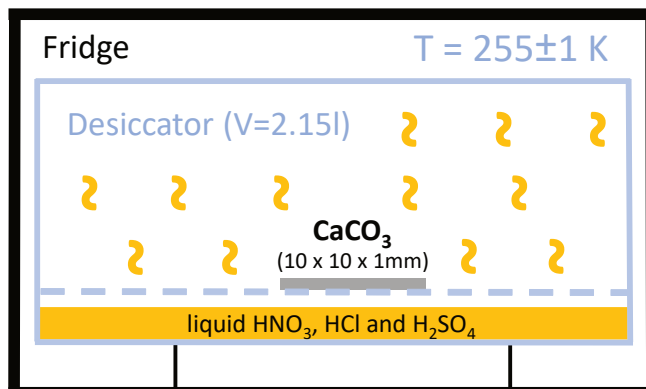


Figure 5.15: The experimental setup of the ERDA measurements. The calcite samples were stored within an desiccator within a fridge at 255K. H<sub>2</sub>SO<sub>4</sub>–HNO<sub>3</sub> and H<sub>2</sub>SO<sub>4</sub>–HCl solutions resulted in corresponding vapour pressures of HNO<sub>3</sub> and HCl above the liquid and thus within the desiccator.

## F: AP-XPS results

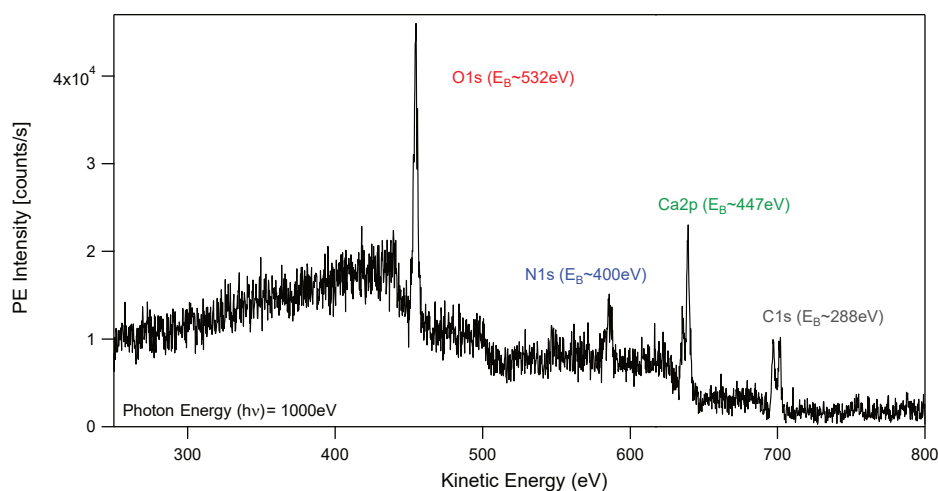


Figure 5.16: An overview spectra showing the entire Kinetic Energy range between 270 eV and 800 eV measured at 1000 eV photon energy. The spectra is clearly dominated by the O 1s peak, the N 1s peak, the Ca 2p peak as well as the adventitious and carbonate C1s peaks, whereas other peaks (e.g., trace elements or Auger peaks) are not distinguishable from background.

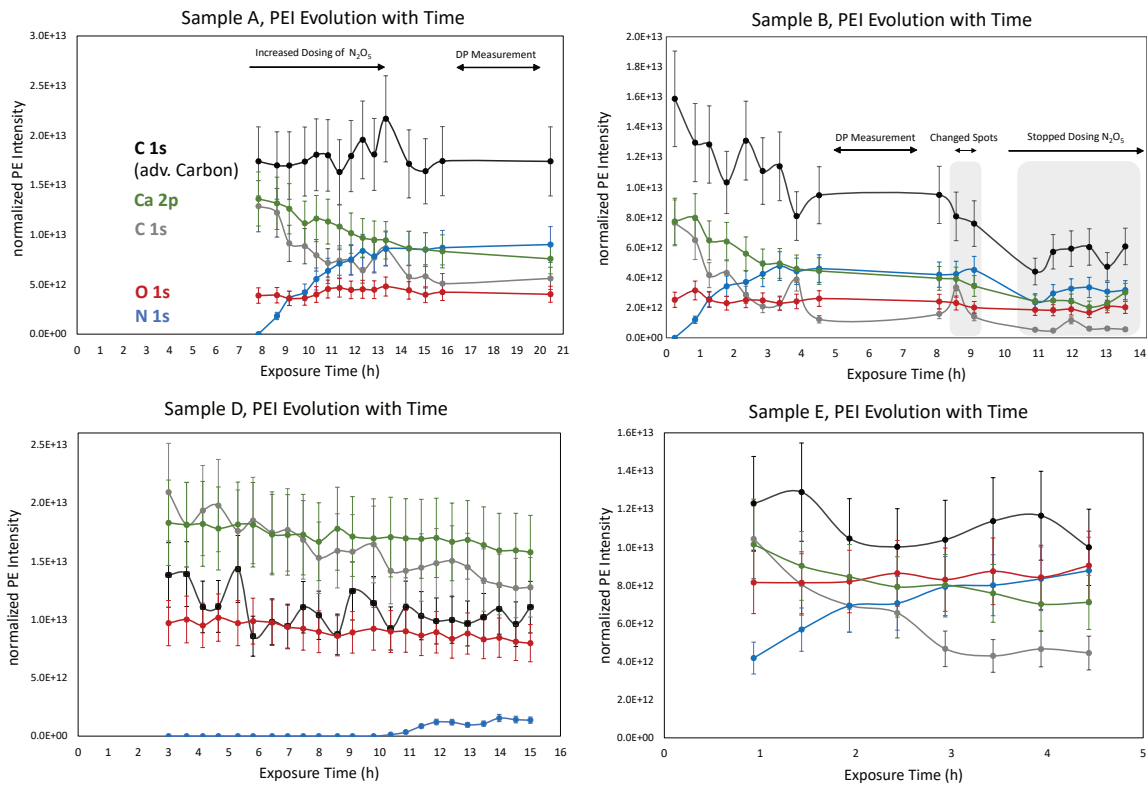


Figure 5.17: The normalized PEI signal of all peaks of samples A, B, D and E as a function of time. The lack of measurement points between 16 and 20 h in sample A and between 5 and 8 h in Sample B is due to the measurement of the depth profile (see Figure 7 in the main text). The gray shaded area in sample B indicate measurements at different spots of the samples to check for beam damage effects as well as a period of measurements for which we stopped the N<sub>2</sub>O<sub>5</sub> dosing to check for stability of the products. The uncertainty bars all include values  $\pm 20\%$ . The PEI evolution with time of sample C can be seen in Figure 6 in the main text.



# Chapter 6

## Concluding Perspectives

### Abstract

Recent studies have suggested that stratospheric aerosol injections (SAI) of solid particles instead of gaseous  $\text{SO}_2$  could reduce some of the related environmental side effects, such as ozone depletion and stratospheric heating. We use a global aerosol-chemistry-climate model (ACCM), which interactively couples microphysical interaction of alumina and calcite particle with the stratospheric sulfur cycle to the models heterogeneous chemistry and radiation schemes. In contrast with previous studies, we find that SAI of alumina and calcite particles only achieves a bigger effective radiative forcing (RF) per unit of aerosol burden compared to sulfuric acid aerosols, but not per unit of injected mass. Reduced warming of the tropical lower stratosphere remains a major advantage of SAI of alumina and calcite particles over  $\text{SO}_2$  injections. Our results also reveal that, when normalised per unit of RF, calcite and alumina particles would lead to a smaller increase in diffuse radiation and reduced ozone depletion compared to the injection of  $\text{SO}_2$ . However, the effects on stratospheric composition are largely dependent on the assumptions made concerning the heterogeneous chemistry on the solid particles. Constraining this structural uncertainty in models requires dedicated laboratory experiments. Sulfur-based SAI appears to carry smaller uncertainties than solid particles, and could thus be deemed as potentially safer. Conversely, SAI via solid particles has more potential for reduced side effects, but also bigger uncertainties, which can only be reduced with a concerted laboratory effort and small scale field experiments.

### This chapter will be submitted as:

**Vattioni, S.,** Weber, R., Dykema, J.-A., Luo, B., Stenke., A., Feinberg, A., Ammann, M., Vockenhuber, C., Döbeli, M., Kelesidis, G.A., Krieger, U., Sukhodolov, T., Keutsch, F., N., Peter, T., Chiodo G. (2024). Risks and benefits of stratospheric solar climate intervention via solid particle injections. **Nature Climate Change**.

## 6.1 Introduction

Climate intervention by stratospheric aerosol intervention has been proposed as a technique, which could rapidly, and at relatively low cost (Smith, 2020), mitigate some of the adverse effects of climate change, especially in an overshoot management approach (Budyko, 1974; Crutzen, 2006; Keith and MacMartin, 2015). This approach could potentially help meeting the Paris agreement by keeping global warming below 1.5 K, until we have reached net-zero green-house gas (GHG) injections and until GHG removal techniques are developed and scaled up (Keith and MacMartin, 2015; MacMartin et al., 2018). The idea mainly developed from observations of the cooling effect of explosive volcanic eruptions, which also helps explain that research on SAI has so far focused on the injection of SO<sub>2</sub>, the main precursor of volcanic sulfuric acid particles in the stratosphere (Mills et al., 2016; Sukhodolov et al., 2018; Feinberg et al., 2019). Due to their natural relevance, the microphysics, optical properties, and heterogeneous chemistry of stratospheric aqueous sulfuric acid particles are relatively well-studied and understood (Mills et al., 2016; Sukhodolov et al., 2018; Timmreck et al., 2018; Quaglia et al., 2023). Nevertheless, model intercomparison studies of SAI through SO<sub>2</sub> injection have showed substantial uncertainties in the resulting stratospheric sulfuric acid aerosol burden, the concomitant RF and ozone depletion, most likely due to differences in the representation of various processes in ACCMs (e.g. microphysics, transport or heterogeneous chemistry) as well as differences in their interaction with each other and their spatial and temporal resolution (e.g., Weisenstein et al., 2022; Jones et al., 2022; Tilmes et al., 2022; Vattioni et al., 2023b).

The latter study (i.e., Chapter 2) highlights the importance of the microphysical settings for quantifying the climate forcing from stratospheric SO<sub>2</sub> injection in the sectional ACCM SOCOL-AERv2. Compared to short-duration volcanic SO<sub>2</sub> emission, the continuous SO<sub>2</sub> injections in climate intervention scenarios pose a greater challenge to the numerical implementation of microphysical processes such as nucleation, condensation, and coagulation. At high sulfur loadings reached in the scenarios injecting 25 Mt/yr of sulfur with a default microphysical timestep of 6 min, changing the call sequence from the default "condensation first" to "nucleation first" leads to a massive increase in the number densities of particles in the nucleation mode ( $r < 0.01 \mu\text{m}$ ) and a small decrease in coarse mode particles ( $r > 1 \mu\text{m}$ ), resulting in much larger stratospheric aerosol burden. This is mostly due to the strong non-linearity of the nucleation rate as a function of H<sub>2</sub>SO<sub>4</sub> supersaturation. Depending on the microphysical timestep and the sequencing of condensation and nucleation, the net global RF ranges from  $-2.3 \text{ W m}^{-2}$  to  $-5.3 \text{ W m}^{-2}$  for injection rates of 25 Tg Sulfur per year. The results suggest that a reasonably short microphysical time step of 2 minutes or less must be applied to accurately capture the magnitude of the H<sub>2</sub>SO<sub>4</sub> supersaturation resulting from SO<sub>2</sub> injection scenarios or volcanic eruptions. Taken together these results underscore how structural aspects of model representation of aerosol microphysical processes become important under conditions of elevated stratospheric sulfur in determining atmospheric chemistry and climate impacts. Furthermore, the results highlight that aerosol microphysics and the resulting aerosol size distributions under continuous stratospheric SO<sub>2</sub> injections for climate intervention are different compared to the one resulting from volcanic eruption plumes, which are the ones ACCMs are usually validated with (e.g. Quaglia et al., 2023). Thus, volcanoes are not a perfect analogue for stratospheric solar climate intervention scenarios with SO<sub>2</sub>; thus, validation against observations from volcanic eruptions is not entirely possible, which introduces uncertainty.

Despite these uncertainties, there is agreement that SAI by sulfuric acid particles can lead to some adverse side effects such as (1) unfavourable size distributions caused by continuous nucleation and condensation, which makes aerosols sediment faster while reducing their backscatter efficiency (English et al., 2011; Niemeier et al., 2011; Heckendorn et al., 2009; Vattioni et al., 2019, 2023b), (2) increased surface area density, potentially enhancing chlorine activation and thus ozone depletion (Weisenstein et al., 2022; Tilmes et al., 2022), (3) stratospheric warming perturbing atmospheric dynamics (impacting e.g., the quasi-biennial oscillation (Jones et al., 2022; Richter et al., 2017; Aquila et al., 2014), stratosphere-troposphere coupling (Banerjee et al., 2021), the North Atlantic oscillation (Jones et al., 2022) or tropical precipitation (Niemeier et al., 2013; Simpson et al., 2019)), (4) increased diffuse visible radiation whitening the sky and altering the net primary production (Kravitz et al., 2012b; Xia et al., 2016; Zarnetske et al., 2021) or (5) feedbacks from aerosol-cloud interactions (Kuebbeler et al., 2012; Cirisan et al., 2013; Vioni et al., 2018) and altered GHG lifetimes (Vioni et al., 2017).

Recent studies suggest that compared to SAI by sulfuric acid aerosols the injection of solid particles such as alumina ( $\text{Al}_2\text{O}_3$ ) or calcite ( $\text{CaCO}_3$ ) may result in more effective negative RF, while simultaneously reducing some of the negative side effects (1)-(4) due to more optimal optical, chemical and microphysical aerosol properties (Weisenstein et al., 2015; Dykema et al., 2016; Ferraro et al., 2011, 2015; Jones et al., 2016; Dai et al., 2020, e.g.). Most of these studies highlighted the reduced stratospheric warming from these materials, but prescribed solid aerosol distributions (Dykema et al., 2016; Ferraro et al., 2011, 2015) and neglected particle interactions with stratospheric chemistry (Dykema et al., 2016; Ferraro et al., 2011, 2015; Jones et al., 2016). Other modelling studies have calculated radiative feedbacks offline, but explicitly simulated solid particle microphysics and heterogeneous chemistry (Keith et al., 2016; Weisenstein et al., 2015) building on only few, idealised laboratory experiments (Molina et al., 1997; Dai et al., 2020; Huynh and McNeill, 2020, 2021; Tang et al., 2014, 2016). In spite of the large uncertainties from solid particle interaction with stratospheric chemistry, IPCC AR6 concludes that “Injection of non-sulphate aerosols is likely to result in less stratospheric heating and ozone loss” (Arias et al., 2021).

## 6.2 The interactive solid particle microphysics scheme in SOCOL-AERv2

This thesis presents the first global ACCM (i.e., SOCOL-AERv2 Feinberg et al., 2019), which simulates the injection of solid particles and their microphysical interactions such as agglomeration via self-coagulation, coagulation with sulfuric acid aerosols, condensation of  $\text{H}_2\text{SO}_4$  on the particle surface and sedimentation interactively coupled to the model’s radiation and heterogeneous chemistry schemes (see Chapter 3). While the model allows for representation of heterogeneous chemistry on the solid particles (see Chapter 3, Section 3.2.3.4 and 3.2.4.1), the solid particles are also coupled to the models longwave and shortwave radiation code via their scattering and absorption properties (see Chapter 3, Section 3.2.2.4). These unprecedented model capabilities make it possible to conduct a comprehensive assessment of the risks and benefits of SAI by solid particles compared to sulfur-based SAI, meeting the target set by the WMO 2022 concerning the need of comprehensive climate model simulations for SAI using alternative materials (WMO, 2022).

The focus of this thesis is on alumina and calcite particles since these are the only potential injection candidates for which some experimental data on heterogeneous chemistry in the stratosphere is available (e.g. Molina et al., 1997; Dai et al., 2020; Huynh and McNeill, 2020, 2021). The model treats alumina and calcite particles as very different representatives of solid particles concerning their interaction with stratospheric chemistry.

On the one hand, alumina is thought to be largely unreactive and the bulk of the particles (i.e.,  $\text{Al}_2\text{O}_3$ ) will most likely not undergo chemical reactions in the stratosphere (see Section 4.4 and Figure 4.6), whereas calcite is a base and is thus expected to readily react with most of the acidic molecules available in stratospheric air (i.e., mainly  $\text{HNO}_3$ ,  $\text{HCl}$  and  $\text{H}_2\text{SO}_4$ ). However, alumina particles still provide surfaces, which allow for adsorption of  $\text{HCl}$  and  $\text{HNO}_3$  as well as for condensation of  $\text{H}_2\text{SO}_4$ . Thus, the solid particle microphysics model takes into account coagulation of solid particles with  $\text{H}_2\text{SO}_4$ – $\text{H}_2\text{O}$  aerosols as well as condensation of gaseous  $\text{H}_2\text{SO}_4$  on alumina surfaces, while the condensed  $\text{H}_2\text{SO}_4$ – $\text{H}_2\text{O}$  is represented on the alumina particles taking into account the contact angle of  $\text{H}_2\text{SO}_4$ – $\text{H}_2\text{O}$  on alumina particles of about  $30^\circ$  (see Chapter 2.2.1, Section 2.2.2). This leaves parts of the alumina surface uncovered and available for hosting for example the heterogeneous reaction  $\text{HCl} + \text{ClONO}_2 \longrightarrow \text{Cl}_2 + \text{HNO}_3$ , whose rate constant on alumina surfaces has been measured in a study which explored chlorine activation on alumina containing space shuttle exhaust (Molina et al., 1997).

On the other hand, calcite particles are thought to react with  $\text{HNO}_3$ ,  $\text{HCl}$  and  $\text{HNO}_3$  thereby altering the composition of the particles. Therefore, calcite is an example of a material which is expected to undergo chemical ageing in the stratosphere, thereby altering its chemical and optical properties over the course of its stratospheric residence time. In case of SAI of calcite, the model thus allows for particle composition changes via uptake of  $\text{HNO}_3$ ,  $\text{HCl}$  and  $\text{H}_2\text{SO}_4$  resulting in particle mixtures of  $\text{CaCO}_3$ ,  $\text{CaSO}_4$ ,  $\text{Ca}(\text{NO}_3)_2$  and  $\text{CaCl}_2$  (see Section 3.2.4). With the XPS and ERDA measurements in presented in Chapter 5 we have shown that the uptake coefficients of  $\text{HCl}$  and  $\text{HNO}_3$  are likely below  $10^{-4}$  on timescales relevant for the stratosphere. Even though other studies have measured much larger uptake coefficients (Huynh and McNeill, 2020, 2021) we showed that these uptake coefficient can not be maintained for relevant timescales due to increased passivisation of the surface with reaction products with time.

### 6.3 Experimental setup

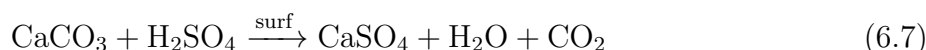
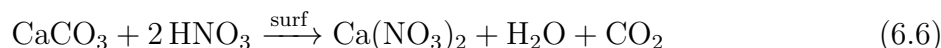
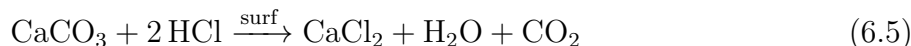
To discuss and illustrate the main findings of this thesis, the baseline scenarios described in Chapter 3, Section 3.3 were extended to an ensemble of three members each to get a more robust estimate of the effective RF. Thus, a total of 5 ensembles were performed including an ensemble for the reference run and four perturbation experiments with injections of 5 Mt/yr  $\text{Al}_2\text{O}_3$ ,  $\text{CaCO}_3$ ,  $\text{SO}_2$  and direct injections of accumulation mode (AM, i.e.,  $r = 0.095 \mu\text{m}$ ) sulfuric acid aerosols. The latter scenario assumes that an optimised aerosol size distribution with a mean radius of  $0.095 \mu\text{m}$  can be produced by injecting gaseous  $\text{H}_2\text{SO}_4$  into an aircraft plume Pierce et al. (2010); Benduhn et al. (2016); Vattioni et al. (2019); Weisenstein et al. (2022). We assumed injection rates of absolute masses and not sulfur equivalent masses since injection of elemental sulfur as proposed in Smith et al. (2018) might not be technically feasible. Each perturbation experiment emitted 5 Mt of material per year at 50 hPa ( $\sim 20$  km altitude) between  $30^\circ\text{N}$  and  $30^\circ\text{S}$  with particle radii of 240 nm for alumina and calcite injections. In addition to the baseline experiments with timeslice boundary conditions with climatological sea surface temperature (SST), sea ice

concentrations (SIC), GHG and ODS concentrations set to 2020 the five ensembles were also simulated for timeslice 2090 boundary conditions. GHG and ODS concentrations were taken from SSP5-8.5 O'Neill et al. (2015) and WMO (2018), respectively, while SST and SIC were taken from a 10-year average (2011-2020) of the Hadley dataset (Kennedy et al., 2019) for 2020 conditions and CESM5-CAM1 RCP8.5 (2090-2099) for 2090 conditions (Meehl et al., 2013). In the following, these boundary conditions will be referred to as "2020 conditions" and "2090 conditions". Each ensemble member was simulated spanning 20 years, of which the first 5 years served as spin-up to equilibrate stratospheric aerosol burdens. Hence, the five ensembles shown in this study are averages of  $3 \times 15$ -years (i.e., 45 years).

For heterogeneous chemistry on alumina particles, we applied the "dissociative HCl only" extrapolation for reaction 6.1 with  $\gamma_{\text{ClONO}_2}$  fitted to the Molina et al. (1997) data assuming  $\alpha=0.1$  (see Table 4.1 in Chapter 4) as well as the same reaction rate as for sulfuric acid aerosols for reaction 6.2 and 6.3 (see section 6.5).



For calcite particles we applied uptake coefficients of  $\gamma_{\text{HCl}} = 10^{-5}$ ,  $\gamma_{\text{HNO}_3} = 10^{-4}$ ,  $\gamma_{\text{H}_2\text{SO}_4} = 1$  which are realistic assumptions for the stratosphere, when taking into account the dependence of the uptake coefficient on exposure, which was found with the XPS and ERDA experiments conducted in Chapter 5 (see Figure 5.12).



## 6.4 Different perspectives on RF efficiency

Most previous studies investigating SAI of solid particles have compared sulfur equivalent injection rates in the form of e.g.,  $\text{SO}_2$  and resulting sulfur equivalent stratospheric aerosol burden to absolute injection rates and burden of solid particles. This effectively resulted in an underestimation of the resulting sulfuric acid burden and RF efficiency compared to solid particles (e.g., Weisenstein et al., 2015). Therefore, in this study we emitted 5 Mt/yr of calcite particles, alumina particles,  $\text{SO}_{2(\text{g})}$  and  $\text{AM-H}_2\text{SO}_{4(\text{aq})}$  and we also provide the resulting wet stratospheric sulfuric acid aerosol burden in Mt  $\text{H}_2\text{SO}_4\text{-H}_2\text{O}$  (see Figure 6.1) instead of the commonly used sulfur equivalent burden (Mt S). This allows for a direct comparison of injection rates, resulting stratospheric aerosol burden and RF between SAI with sulfur and solid particles (see Figure 6.1).

Injecting 5 Mt of material per year resulted in stratospheric particle burdens of 3.8 Mt alumina, 4.8 Mt calcite, and about 10 Mt  $\text{H}_2\text{SO}_4\text{-H}_2\text{O}$  for 2020 conditions (see Figure 6.1

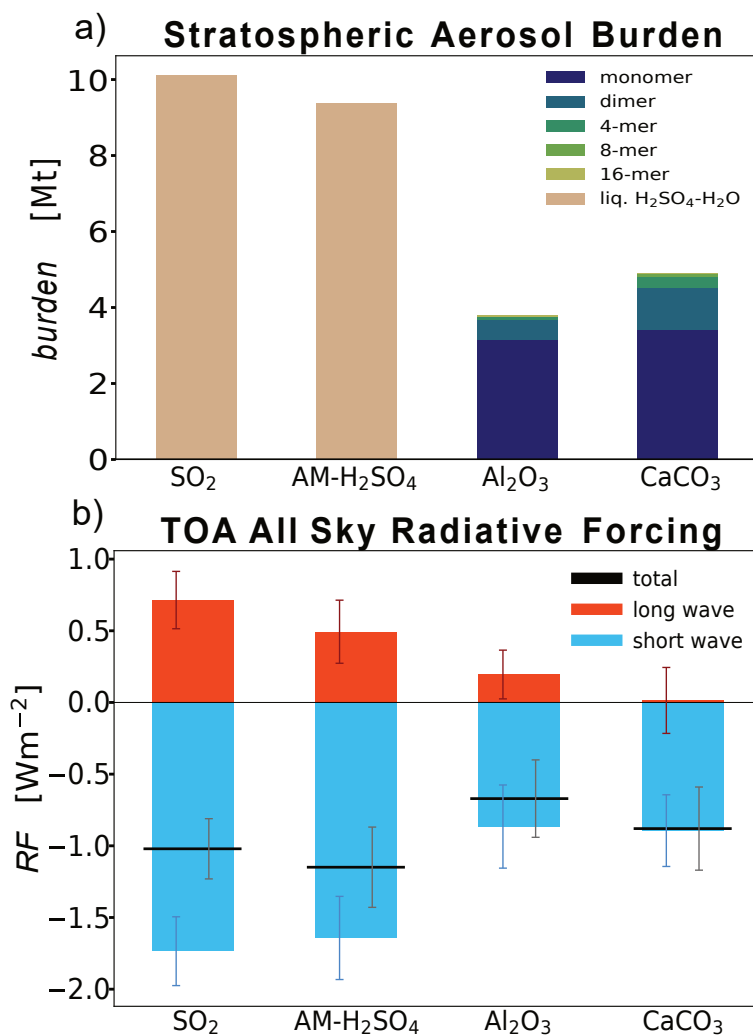


Figure 6.1: Resulting globally averaged stratospheric aerosol burden resolved per agglomerate for solid particles (a) and top of the atmosphere (ToA) LW (red), SW (blue), and total (black lines) all sky RF from 5 Mt/yr injection of each material (b) for 2020 conditions. Uncertainty bars for RF represent the inter-annual standard deviation (see also Table 6.1 for exact values).

and Table 6.1 in appendix A as well as Figure 6.8 with resulting number concentrations for all bins in Appendix B). According to these results, the sulfur-based injection scenarios result in about two times larger stratospheric aerosol burden compared to calcite and alumina particle injections with radius of 240 nm. This is due to the higher density and the larger particle radius of the alumina and calcite particles compared to sulfuric acid aerosols, which results in much faster sedimentation velocities. According to these results, stratospheric particle residence times are 0.82 years, 0.94 years, and about 2 years for alumina, calcite and sulfur-based injections, respectively. Therefore, a correspondingly larger injection rate would be necessary for alumina ( $1.3 \text{ (Mtyr}^{-1})/\text{Mt}$ ) and calcite ( $1.0 \text{ ((Mtyr}^{-1})/\text{Mt)}$ ) particles with radii of 240 nm to maintain the same stratospheric aerosol burden as for SAI by sulfuric acid aerosols ( $0.5 \text{ (Mtyr}^{-1})/\text{Mt}$ , see Figure 6.9b in Appendix C).

As a result of SAI, the top of the atmosphere (ToA) shortwave (SW) RF for 5 Mt/yr SO<sub>2</sub> and AM-H<sub>2</sub>SO<sub>4</sub> injections are  $-1.72 \text{ W/m}^2$  and  $-1.74 \text{ W/m}^2$ , respectively, whereas

## Normalized by Radiative Forcing, 2020

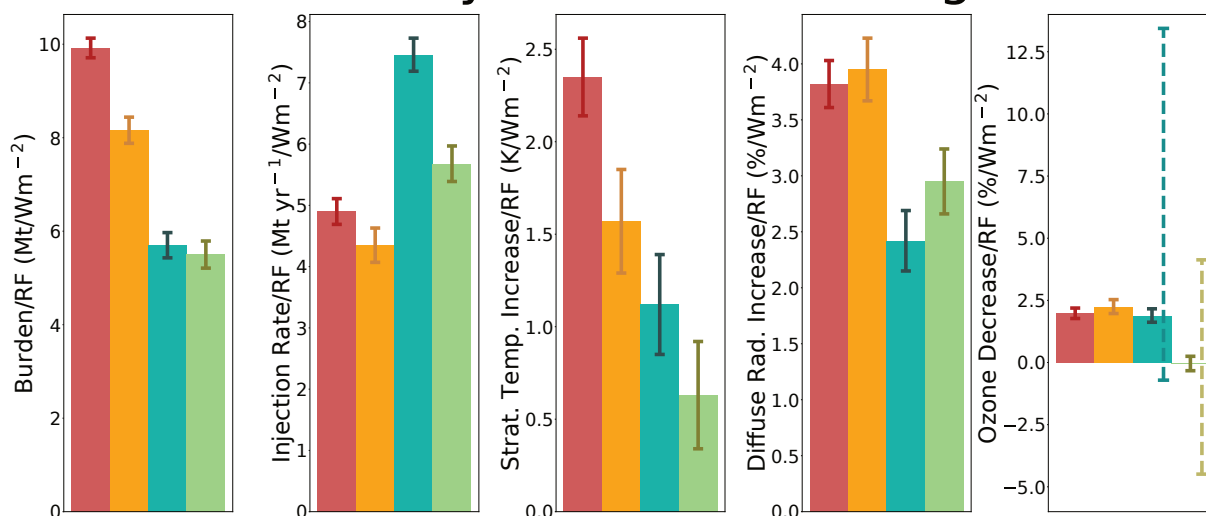


Figure 6.2: Resulting globally averaged stratospheric aerosol burden (see Figure 6.1), injection rate, total ozone column decrease, peak stratospheric heating and diffuse radiation increase normalized by total all sky ToA RF, for SO<sub>2</sub> (red), AM-H<sub>2</sub>SO<sub>4</sub> (orange), alumina (dark green,  $r=240$  nm) and calcite particles (blue,  $r=240$  nm). The standard deviation of inter-annual variability is shown with continuous bars. Dashed uncertainty bars for the ozone response indicate upper and lower sensitivity estimates for the ozone responses (see Section 6.5 and Figure 6.3). Quantities normalized to resulting stratospheric aerosol burden and injection rate are shown in Figure 6.9.

alumina and calcite injection result in  $-0.91$  W/m<sup>2</sup> and  $-1.02$  W/m<sup>2</sup>, respectively (6.1). However, the total ToA RF of the sulfur-based scenarios gets significantly reduced by strong longwave (LW) absorption, whereas alumina and especially calcite are nearly non-absorbing in the LW. The slightly stronger LW absorption of alumina is due to an absorption peak in the wavenumber range  $700\text{--}800$  cm<sup>-1</sup>, which is at the edge of the atmospheric window. The calcite injection scenario almost results in a negative ToA LW RF due to significant depletion of the background stratospheric sulfuric acid layer through H<sub>2</sub>SO<sub>4</sub> uptake on the calcite particle surface (Figure 6.1).

In the case of alumina and calcite injections, the faster sedimentation rates cannot be compensated by the better scattering properties (i.e. larger scattering cross sections, see Figure 3.16), leading to more efficient RF for SO<sub>2</sub> injections ( $4.9$  Mtyr<sup>-1</sup>/Wm<sup>-2</sup>) compared to alumina ( $7.5$  Mtyr<sup>-1</sup>/Wm<sup>-2</sup>) and calcite injections ( $5.7$  Mtyr<sup>-1</sup>/Wm<sup>-2</sup>, see Figure 6.2). Other solid particle species, which have been considered as a potential SAI injection species (e.g., TiO<sub>2</sub>, C, ZrO<sub>2</sub>, SiC, SiO<sub>2</sub> Dykema et al., 2016), are expected to behave similarly, when injected at the same rate and radius. Reducing the radius of the injected particles would increase their stratospheric residence time and in some cases also the RF efficiency. However, this would come at the cost of larger SAD availability for heterogeneous reactions (see Chapter 4, Figure 4.2). Also, the RF efficiency per injection rate of sulfur-based scenarios could be further increased by a factor of two when assuming the lifting of liquid elemental sulfur ( $M=32$  g/mol) with subsequent in-situ oxidation as proposed by Smith et al. (2018). However, the feasibility of such an injection strategy is subject to large uncertainty.

We confirm findings from previous studies, which showed that many materials such as

calcite and alumina scatter more solar radiation per resulting stratospheric aerosol burden while simultaneously absorbing less outgoing LW radiation compared to sulfuric acid aerosols (see Figure 6.1 and 6.9b). However, when inter-comparing SAI across different particle types, the normalization per stratospheric aerosol burden is less meaningful since many of the effects of SAI such as impacts on heterogeneous chemistry, stratospheric warming, diffuse radiation or the scattering efficiency are strong function of the material properties, which are not necessarily proportional to the resulting burden in the same way for different materials. Therefore, we propose to assess the impacts of SAI, by normalizing the metrics that characterise the environmental effects of SAI of different particle types by the resulting RF (see Figure 6.2) and not to stratospheric aerosol burden (see Figure 6.9b). While Table 6.1 in Appendix A shows absolute global mean values resulting from 5 Mt/yr injection for 2020 and 2090 conditions, the additional Figures 6.9 and 6.10 in Appendix C show the quantities normalised per injection rate and per resulting stratospheric burden for 2020 and 2090 conditions respectively.

Given that sulfur-based injections lead to larger RF compared to alumina and calcite injections (see Figure 6.9a), the potential benefits from alumina and calcite particles mostly come from reduced side effects compared to sulfuric acid aerosols; these are, for example, reduced stratospheric warming, reduced ozone depletion, or reduced diffuse versus direct radiation normalised to the resulting RF (see Figure 6.2). These side effects are discussed in detail in the subsequent sections.

## 6.5 Stratospheric chemistry

One metric of concern when it comes to environmental side-effects of SAI is the total ozone column (TOC); changes in this metric can have first-order impacts on UV exposure and are thus of great societal relevance. The TOC changes of the 4 perturbation ensembles, representing realistic estimates of heterogeneous chemistry (see Section 6.3), are shown with thick lines in Figure 6.3 for 5 Mt/yr injection. The resulting global mean TOC depletion for 2020 GHG and ODS boundary conditions are -2.0%, -2.6%, -1.3% and 0.0% for injection of  $\text{SO}_2$ , AM- $\text{H}_2\text{SO}_4$ ,  $\text{Al}_2\text{O}_3$  and  $\text{CaCO}_3$ , respectively. Therefore, the best estimate from current knowledge on heterogeneous chemistry on alumina and calcite particles would result in smaller TOC depletion compared to the sulfur based scenarios. Most crucially, the impact on stratospheric chemistry would decrease significantly in the future, when considering future ozone recovery from decreasing stratospheric chlorine loadings. In 2090, the alumina and calcite injection scenarios result in almost no change of TOC across all latitudes, whereas injection of  $\text{SO}_2$  and AM- $\text{H}_2\text{SO}_4$  would still result in about 5% lower TOC in the south polar region (see Figure 6.3). The resulting sulfuric acid SAD, alumina SAD and calcite SAD of all five ensembles are shown in Appendix D, Figure 6.11, which also highlights the substantial depletion of the background stratospheric sulfuric acid aerosol layer for the alumina and calcite injection scenarios. In the case of calcite particles, the depletion of sulfuric acid aerosols could explain part of the TOC increase in the southern polar region, due to reduced polar stratospheric cloud (PSC) abundance.

However, the interaction of calcite and alumina with stratospheric acidity (i.e., HCl,  $\text{HNO}_3$  and  $\text{H}_2\text{SO}_{4(\text{aq})}$ ) at stratospheric temperatures ( $< 220\text{K}$ ), relative humidity ( $< 1\%$ ) and strong UV irradiance is still poorly constrained, resulting in large uncertainties in modelled responses on stratospheric chemistry and in particular the stratospheric ozone layer. Therefore, additional simulations to estimate the upper and lower limit of potential TOC responses were performed for alumina, calcite and  $\text{SO}_2$  injections.



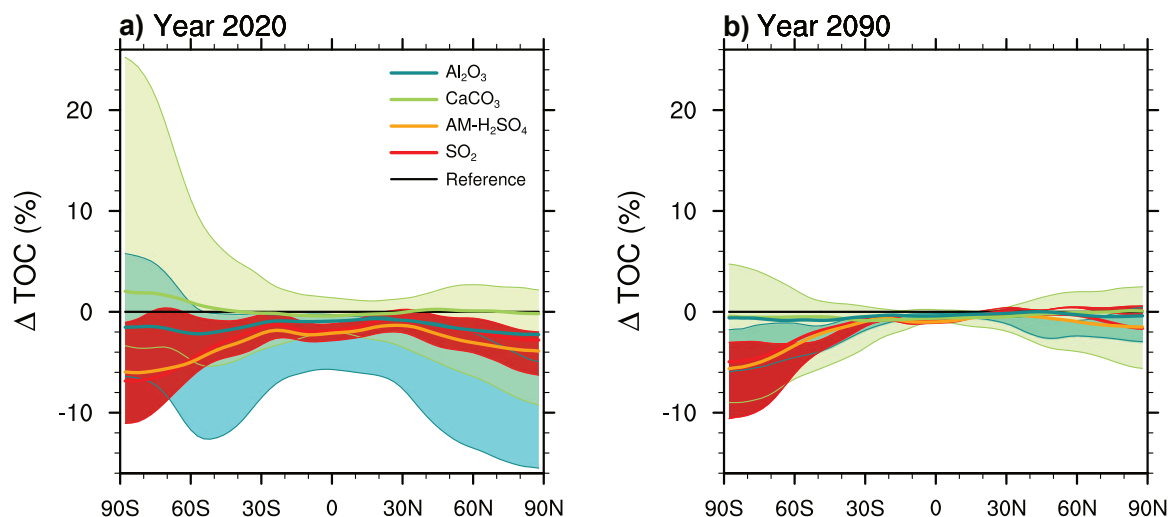
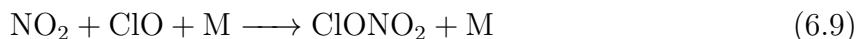


Figure 6.3: Zonally averaged TOC for the SO<sub>2</sub> (red), AM-H<sub>2</sub>SO<sub>4</sub> (orange), alumina (blue,  $r=240$  nm), and calcite (green,  $r=240$  nm) injections of 5 Mt/yr. Areas marked in blue indicates the upper and lower TOC estimate which are assuming the alumina particles to be covered by H<sub>2</sub>SO<sub>4</sub>-H<sub>2</sub>O and assuming the non-dissociative HCl-only scenario without co-adsorption of H<sub>2</sub>SO<sub>4</sub> and HNO<sub>3</sub>, respectively (see Chapter 4, Table 4.1). Area marked in green indicates uncertainty range for calcite based on the uptake of HNO<sub>3</sub> and HCl. The upper estimate was simulated assuming  $\gamma_{\text{HNO}_3}=10^{-5}$  and  $\gamma_{\text{HCl}}=10^{-3}$  and the lower estimate was simulated assuming  $\gamma_{\text{HNO}_3}=10^{-3}$  and  $\gamma_{\text{HCl}}=10^{-5}$ , respectively. The red shading indicates the range comprised between the upper and lower estimates of the TOC response for SO<sub>2</sub> injections, by assuming all heterogeneous reaction rates on sulphuric acid aerosols and PSC to be a factor 5 increased and decreased. Similar as for calcite and alumina particles we think this is a realistic upper and lower uncertainty estimate resulting from SO<sub>2</sub> injection. Panel a) shows scenarios for 2020 boundary conditions and panel b) for 2090 conditions.

The upper and lower TOC estimate of alumina particles is based on reaction 6.1. We have chosen the same scenarios as shown in Chapter 4, which is on the lower end the "non-dissociative HCl only" scenario, which assumes extrapolation to stratospheric HCl partial pressures based on a Langmuir-Hinshelwood parameterisation of the measured uptake coefficients of ClONO<sub>2</sub> for reaction 6.1 by Molina et al. (1997) without any co-adsorption of HNO<sub>3</sub> and without participation of H<sub>2</sub>SO<sub>4</sub> at the surface (see Chapter 4, Figure 4.1). While co-adsorption of HNO<sub>3</sub> would likely significantly decrease the degree of HCl dissociation at the surface, condensed H<sub>2</sub>SO<sub>4</sub>-H<sub>2</sub>O on alumina particles could displace HNO<sub>3</sub> and HCl from the surface. Therefore, for the upper TOC estimate we assume that all alumina particles are covered with a H<sub>2</sub>SO<sub>4</sub>-H<sub>2</sub>O coating allowing the same heterogeneous chemistry as on sulfuric acid aerosols. Both, the lower and the upper estimate are not very likely, since HNO<sub>3</sub> will co-adsorb at the alumina surface and also, H<sub>2</sub>SO<sub>4</sub> will condense on the surface, but it will likely not cover the whole alumina surface if alumina SAD is large enough (e.g., resulting from injection 5 Mt/yr alumina particle with  $r=240$  nm) since the available H<sub>2</sub>SO<sub>4</sub>-H<sub>2</sub>O is likely not enough to cover the whole surface when accounting for the contact angle of 30° of H<sub>2</sub>SO<sub>4</sub> on alumina surfaces (see Chapter 4, Figure 4.5). The resulting uncertainty range for the TOC response from alumina particles is shown in figure 6.3 and reaches from -9.1% to -0.5% in a global mean.

For calcite particles, we assumed the uptake of  $\text{HNO}_3$  (reaction 6.6) and  $\text{HCl}$  (reaction 6.5) of  $10^{-3}$  as the upper limit estimate. This is two and one order of magnitude larger than the exposure dependent uptake coefficient for stratospheric exposure postulated in Figure 5.12 for  $\text{HCl}$  and  $\text{HNO}_3$ , respectively. It is also significantly lower than the measured initial uptake coefficient of 0.076 for  $\text{HCl}$  reported by Huynh and McNeill (2020), but still larger than what was measured by Dai et al. (2020) and in this study (i.e., in HI-ERDA and in AP-XPS) at stratospheric conditions in respect to temperature and  $\text{HCl}$  and  $\text{HNO}_3$  partial pressures. However, with uptake coefficients of  $10^{-3}$  it would take several days to form a product layer of the corresponding salts. Larger uptake coefficients can likely not be maintained for a sufficiently long time due to increasing uptake limitation by diffusive processes. Thus, we have performed additional simulations with uptake coefficients of  $10^{-3}$  and  $10^{-5}$  for  $\text{HCl}$  and  $\text{HNO}_3$ , respectively to estimate the upper limit in the TOC response, as well as a simulation with uptake coefficients of  $10^{-5}$  and  $10^{-3}$ , respectively as the lower sensitivity estimate for the TOC response to ozone alteration for 2020 and 2090 conditions (see green range in Figure 6.3). Conversely, the uptake coefficient for  $\text{H}_2\text{SO}_4$  was kept at 1.0 for all calcite simulations, since  $\text{H}_2\text{SO}_4$  has a very low equilibrium vapour pressure.

On the one hand, assuming  $\gamma_{\text{HCl}} = 10^{-3}$  would result in healing of the ozone hole like already shown by Keith et al. (2016) and Dai et al. (2020) with a TOC increase of up to 25% in the southern hemisphere due to removal of chlorine from the stratosphere. On the other hand, assuming  $\gamma_{\text{HNO}_3} = 10^{-3}$  with a low  $\gamma_{\text{HCl}}$  of  $10^{-5}$  could result in global mean TOC depletion of 3.9%, a potential scenario which was not considered by previous studies. This is mostly due to the removal of  $\text{NO}_x$  from the stratosphere and thus, less availability of  $\text{NO}_2$  for the deactivation of  $\text{ClO}_x$  via reaction 6.9.



To estimate the upper and lower limit for the TOC response from the  $\text{SO}_2$  injection scenarios, we uniformly multiplied and divided all heterogeneous reaction rates on sulfuric acid aerosols and polar stratospheric clouds (reactions 6.1-6.4) by a factor of 5, except for reaction 6.2, which was multiplied and divided by a factor of 2 due to the lower uncertainty of this reaction Burkholder et al. (2020); Ammann et al. (2013). These factors were chosen based on the uncertainty of measured reaction rates in the stratospheric temperature and trace gas concentration range Burkholder et al. (2020); Ammann et al. (2013). Furthermore, uncertainties in available SAD, which for example result from uncertainties in the aerosol microphysics modules applied (see Chapter 2) scale the same way as the reaction rates (see Equation 4.4 in Chapter 4). Thus, these factors also partly reflect uncertainty from the lack of observations or experimental data on resulting aerosol size distributions from continuous large  $\text{SO}_2$  injection rates into the stratosphere, which are known to be different from the ones resulting from volcanic eruptions (Heckendorn et al., 2009; Vattioni et al., 2019, 2023b). Furthermore, (Weisenstein et al., 2022) showed inter-model differences of stratospheric aerosol burden of more than a factor of 2 from the same injection scenario, which subsequently would also translate to very different stratospheric SAD. Therefore, these factors are a valid range for estimating the uncertainty of the TOC response to  $\text{SO}_2$  injection in SOCOL-AERv2. This results in TOC depletion between -0.5% and -3.7% for present day GHG and ODS conditions, which is a much smaller range compared to the same injection rate of alumina and calcite particles at radii of 240 nm.

In summary, based on present day knowledge, calcite and alumina particles are ex-

pected to result in less depletion of TOC compared to  $\text{SO}_2$  and  $\text{AM-H}_2\text{SO}_4$  injection, but at the same time they are subject to substantially larger uncertainty, under present-day stratospheric halogen abundances. While the the heterogeneous chemistry on sulfuric acid aerosols is relatively well constrained (e.g., Burkholder et al., 2020), only relatively little is known about heterogeneous chemistry on solid particles under stratospheric conditions in respect to temperature, trace gas concentrations and relative humidity. It is important to point out that the uncertainty ranges presented for solid particle injections are only based on reaction 6.2 for alumina and reactions 6.5 and 6.6 for calcite injections, while no experimental data is available for other reactions on these particle types.

Furthermore, the impact on stratospheric ozone is a strong function of the available SAD and thus the particle size (see Chapter, 4, Figure 4.2), which provides further uncertainty if particles were injected not exactly monodisperse. For example, when injecting 5 Mt/yr of alumina particles with 80 nm the global mean TOC depletion is more than 20% assuming the "non-dissociative, HCl only" scenario (see Table 4.1 and Figure 4.2). For calcite particles, which undergo chemical ageing in the stratosphere, further uncertainty results from changes of the surface properties with time.  $\text{CaSO}_4$ ,  $\text{CaCl}_2$  and  $\text{Ca}(\text{NO}_3)_2$  as well as their hydrates (see Chapter 5) might host different heterogeneous reactions at different reaction rates compared to calcite particles, which significantly alter heterogeneous chemistry hosted on the calcite particles with time.

However, compared to present day global mean TOC conditions the 2090 reference scenario results in 6.1% TOC increase, which is a significantly larger change than resulting from any of our perturbation experiments. This reflects the TOC changes resulting from decreased future halogen concentrations and well as from dynamical impacts of climate change, which are based on the extreme business as usual SSP5-8.5 scenario.

## 6.6 Stratospheric warming and dynamical response

The major benefit of SAI by solid particles compared to sulfuric acid aerosols is reduced stratospheric warming due to the low LW absorption of alumina and especially calcite particles. Calcite injections leads to a tropical stratospheric warming of at most 0.8 K, for  $\text{SO}_2$  injections warm this region by up to 2.5 K, when injecting 5 Mt/yr of material (see Figure 6.4a and g). As a consequence, solid particles generally lead to smaller perturbations in the stratospheric climate. The SAI scenario in which the stratospheric age of air (AoA), defined as average time since an air parcel has passed the tropopause, shows the smallest changes in the calcite injection scenario, indicating a negligible impact on the Brewer-Dobson circulation (BDC, see Figure 6.4h). Most remarkably, the effects of solid particles on the BDC are dwarfed by the impacts of  $\text{SO}_2$  injections, in which the AoA in the upper stratosphere is up to 3 months younger compared to the reference experiment 6.4b, indicating a much faster overturning, and enhanced mixing of tropical and extra-tropical stratospheric air masses.

Stratospheric warming also increases the tropical cold point temperature at the tropopause, which would also increase  $\text{H}_2\text{O}$  concentrations in the stratosphere (Dessler et al., 2013). Since  $\text{H}_2\text{O}$  is an important GHG, increasing stratospheric  $\text{H}_2\text{O}$  concentrations would not only alter stratospheric chemistry and composition via an increase stratospheric  $\text{HO}_x$  ozone depletion cycle, but also it would perturb the radiative balance of the stratosphere. For 5 Mt/yr injections a  $\text{H}_2\text{O}$  increase of 0.75 ppm (+18.0%) was found in the lower stratosphere for  $\text{SO}_2$  injections, whereas the  $\text{H}_2\text{O}$  increase is only increased by 0.12 ppm and 0.10 ppm for alumina and calcite injections, respectively (+3%

and +2.5%, Figure 6.13).

We show that stratospheric warming and its impacts such as stratospheric water vapour increase, alteration of the BDC as well as zonal winds can substantially be reduced by calcite and to a slightly smaller degree by alumina particle injection compared to sulfur-based SAI (see also Figure 6.13 and 6.12). However, it has to be noted, that these effects are particularly strong in the equatorial injection scenario which was applied in this study. Other studies have shown that impacts from stratospheric warming by sulfuric acid aerosols can be reduced by injecting outside the tropical pipe (e.g., at 15° and 30° north and south Tilmes et al., 2017; MacMartin et al., 2017; Richter et al., 2017; Bednarz et al., 2023), which also would apply to solid particle injections. Furthermore, the calcite injection scenario results in 0.88 W/m<sup>2</sup> RF whereas the SO<sub>2</sub> injection scenario results in 1.04 W/m<sup>2</sup>, which means that the the benefits on dynamical impacts would be slightly reduced when normalising to the same RF.

The dynamical response of SAI is also dependant on the background climate. The AoA (AoA) of the 2090 reference simulation is decreased by about 20-30% compared to the 2020 reference simulation. This change in AoA is the result of faster overturning (i.e. faster BDC), stronger and more efficient mixing (Eichinger et al., 2019) and faster stratosphere-to-troposphere transport (Abalos et al., 2020), effectively decreasing the residence time and thus speeding up the removal of any artificial material used for SAI applications. Therefore, the same scenarios under 2090 conditions result in about 5-20% smaller aerosol burdens under 2090 conditions (see also Figure 6.13 and Figure 6.12).

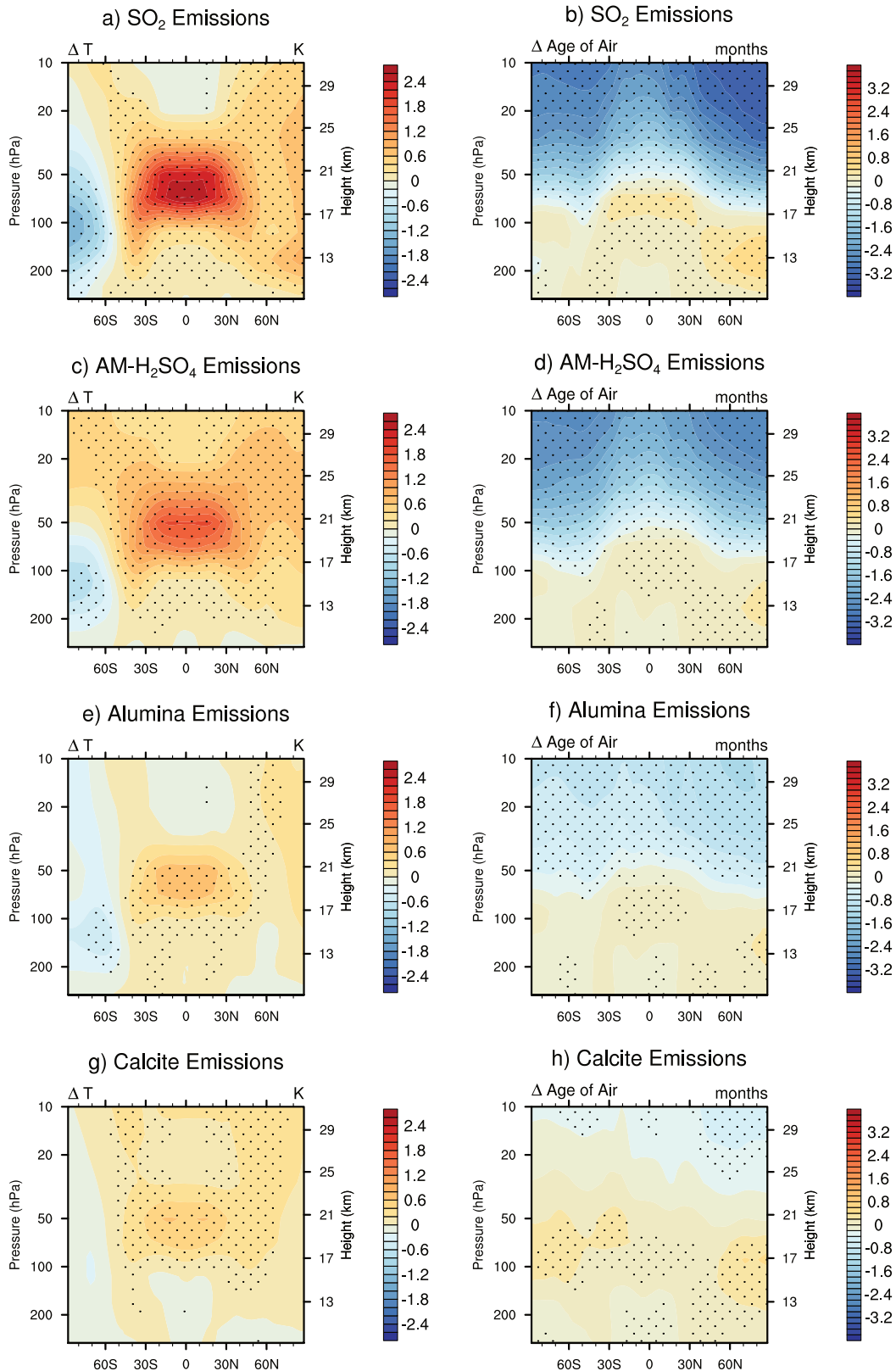


Figure 6.4: The left column shows the zonally averaged temperature anomaly compared to the reference run for all scenarios for 2020 boundary conditions. The right column shows the corresponding anomaly of the AoA in months. Dotted area indicates statistically significant data on the 95% significance interval (t-test). See Figure 6.13 for zonal mean zonal wind, H<sub>2</sub>O and ozone anomalies for 2020 conditions and Figure 6.12 for all quantities for 2090 conditions.

## 6.7 Ecological impacts

Potential ecological impacts from SAI include among others effects from reduced tropospheric temperatures, changes in moisture, increased UV irradiation, increased diffuse radiation and changes in precipitation patterns (e.g., Dagon and Schrag, 2019). Changes in diffuse radiation can alter ecosystems and crop yields and the net primary production rates significantly (Xia et al., 2016), but the effects differ depending on the specific plant species and ecosystem under consideration. Generally, more diffuse radiation is favourable for plant growth and CO<sub>2</sub> uptake (Robock et al., 2009; Gu et al., 2002). Additional factors such as temperature, moisture and nutrient availability also play an important role (Dagon and Schrag, 2019). This makes quantification of effects of increased diffuse radiation on ecosystems from SAI difficult. However, reduced alteration of diffuse radiation would likely decrease the risk of unanticipated impacts on ecosystems. Additionally, more diffuse radiation would whiten the skies with unknown psychological effects (Kravitz et al., 2012a; Robock, 2015). The diffuse radiation increase from SAI is proportional to the mass of aerosols in the stratosphere. Therefore, sulfur-based SAI results in much larger increase of diffuse radiation normalised to the resulting RF (<10% increase per W/m<sup>2</sup> in the tropics) compared to injections of alumina and calcite particle injection with radius of 240 nm (< 6% increase per W/m<sup>2</sup> RF in the tropics, see Figure 6.5 a-d, and Figure 6.2).

Additionally, for sulfur-based SAI increased acid rain from increased sulfuric acid deposition could decrease the soil pH (see Figure 6.5e and f). Vioni et al. (2020) have quantified the effect of increased soil pH and found that the effect would be compensated by the projected future reductions in anthropologically emitted SO<sub>2</sub> from other sources. However deposition patterns would change away from populated areas to more rural regions in high latitudes, where the smaller stratospheric sulfuric acid aerosols would get primarily deposited. For comparison, we show the change in sulfuric acid deposition fluxes from the sulphur-based scenario compared to the reference run (Figure 6.5 e and f). The change in deposition flux is only a small fraction of the total sulfuric acid deposition flux and significant mostly in high latitudes, which is in agreement with conclusions on changes in deposition patterns from Vioni et al. (2020).

The ecological impacts from alumina and calcite particle deposition at the surface are expected to be small, since both materials are naturally abundant and in the case of calcite even in large quantities. Furthermore, the proposed injection rates are orders of magnitude smaller compared to natural dust injection (e.g., from deserts Laurent et al., 2008). However, as in the case of SO<sub>2</sub> injections, the deposition patterns of these materials is different when injected to the stratosphere compared to natural injections in the troposphere (see Figure 6.5g and h).

The calcite and alumina particle deposition fluxes follow the pattern of global precipitation patterns since more than 98% of the injected alumina and calcite particles are deposited via wet deposition (Figure 6.5 g and h). This solid particle deposition pattern is different from the one found for TiO<sub>2</sub> and black carbon particles from Jones et al. (2016) since in that study particles were injected at much smaller radii (<50 nm), which were transported to higher latitudes much more efficiently via the BDC. There are no studies yet which have quantified the effect of deposition of these materials on ecosystems. However, other than sulfuric acid aerosols alumina and calcite particles would not result in increased acidification of the soils. In the case of calcite particle injection, soils may get more alkaline, with unknown effects on ecosystems.

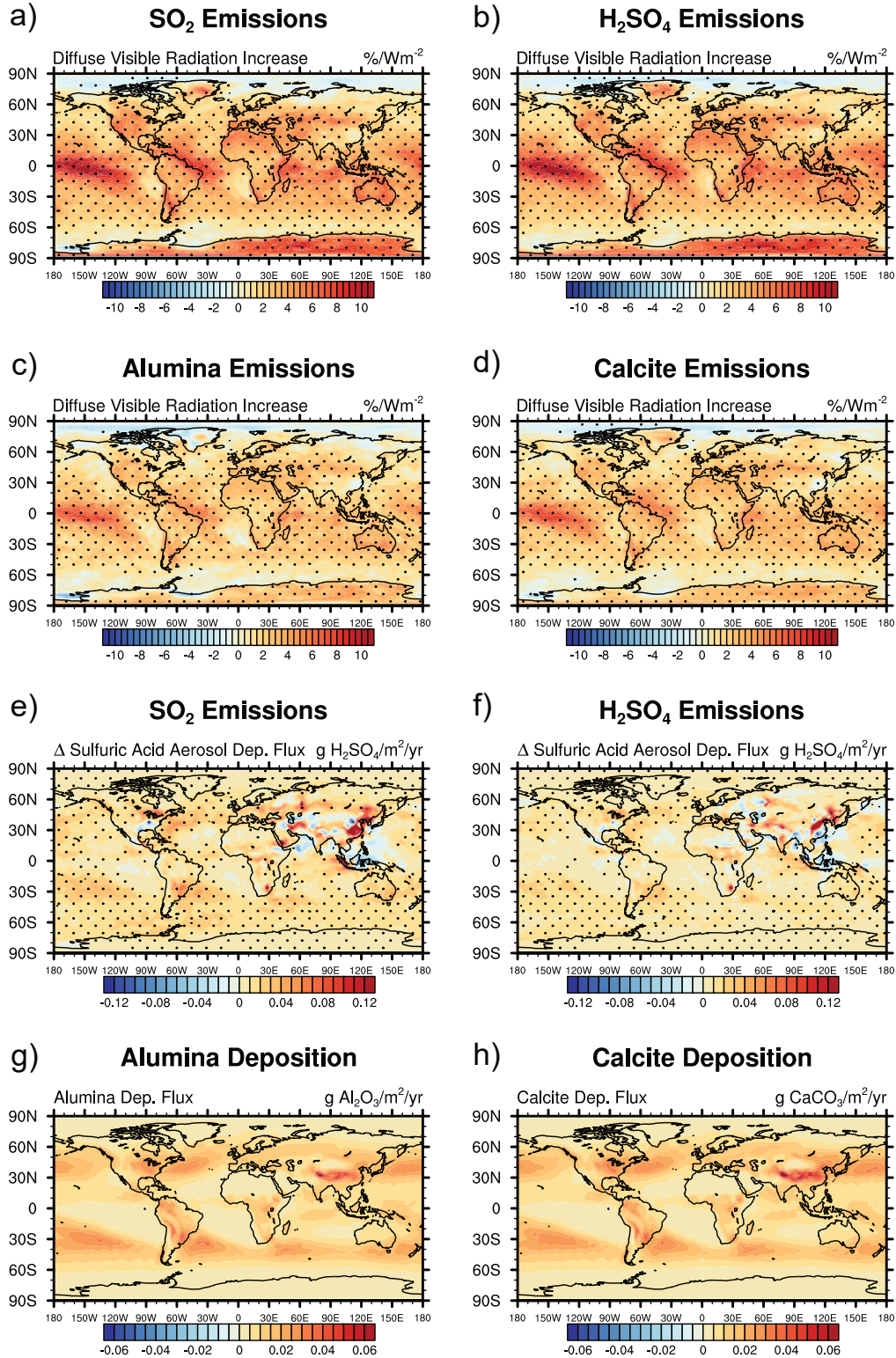


Figure 6.5: Upper four panels (a-d) show changes in diffuse ultraviolet and visible radiation (250 nm - 680 nm) normalized per resulting ToA all sky RF for all scenarios. The lower four panels show the deposition fluxes (wet and dry deposition) of aerosol mass. For SO<sub>2</sub> and AM-H<sub>2</sub>SO<sub>4</sub> deposition fluxes the difference to the reference run is shown. For calcite and alumina particles absolute deposition fluxes are shown. Dotted area indicates statistically significant data on the 95% significance interval (student-t-test), except for solid particle deposition where the reference is zero deposition.



## 6.8 Conclusion and Discussion

This thesis reveals that despite the higher real refractive indices of alumina and calcite particles compared to sulfuric acid particles, they do not result in more efficient radiative cooling, defined in terms of negative RF per units of injected aerosol mass. This is due primarily to their higher densities as well as their larger particle size and thus, larger sedimentation velocities compared to sulfuric acid particles. This reduces stratospheric residence times of solid particles and correspondingly larger injection rates would be needed to sustain the same stratospheric aerosol burden of solid particles compared to sulfuric acid aerosols. Figure 6.6 summarises our main results indicating the stratospheric aerosol burden as well as injection rates required to achieve  $-1 \text{ W/m}^2$  total all sky ToA RF for 2020 and 2090 ODS and GHG concentrations. Compared to  $\text{SO}_2$  injections, larger injection rates are required, but a smaller stratospheric aerosol burden can achieve  $-1 \text{ W/m}^2$  RF, which is due to their smaller average stratospheric residence time (see Figure 6.6). Compared to 2020 conditions, the injection rates and stratospheric aerosol burden required to achieve  $-1 \text{ W/m}^2$  RF are larger in 2090 due to a faster BDC in a much warmer future climate and thus, faster removal of aerosols from the stratosphere.

The main advantage of SAI by alumina and especially calcite particles is the significantly reduced stratospheric warming, which is  $< 0.7 \text{ K/Wm}^{-2}$  for calcite injections. This results in substantially smaller alterations of stratospheric climate, such as in changes of the BDC, zonal winds as well as stratospheric water vapour (see Figures 6.13 and 6.12). This is a major limitation of SAI by sulfuric acid aerosols, which could be significantly reduced by injection of alternative materials. We also show that the injection of solid particles results in reduced diffusive radiation increase compared to the injection of  $\text{SO}_2$  per resulting RF. Further solid particle injection does not result in acid rain and thus, in potentially smaller ecological impact upon deposition.

The results presented in this thesis highlight that calcite and alumina particles could potentially reduce ozone depletion compared to sulfuric acid aerosols. However, due to only little experimental data on heterogeneous chemistry on solid particles under stratospheric conditions the modelled ozone response is largely dependant on the underlying assumptions. Therefore, the uncertainties on modelled ozone are very large with potential for both, substantial ozone depletion or, in the case of calcite particles, even a thickening of the ozone layer, depending on underlying assumptions. Constraining this structural uncertainty in models requires dedicated laboratory experiments on solid particle microphysics and heterogeneous chemistry under stratospheric conditions. While sulfur-based SAI appears to carry smaller uncertainties than solid particles, and could thus be deemed as potentially safer, SAI via solid particles have more potential for reduced side effects but also bigger uncertainties that can only be reduced with a concerted laboratory effort and small scale field experiments.

However, the modelling presented in this thesis has two major limitations. First, model injections were released constantly over time and equally distributed into the grid boxes of SOCOL-AERv2 which has a horizontal resolution of  $325 \text{ km} \times 325 \text{ km} \times 1.5 \text{ km}$  at 50 hPa in the equatorial region. Therefore, it does not resolve the temporal and spatial scale of microphysical processes as they would occur in the injection plume of an aircraft. No solution was presented yet on how to disperse solid particles with sizes blow  $1 \mu\text{m}$ . This is a major limitation, since they are subject to strong Van der Waals forces, which make them stick together (Blackstock et al., 2009), which would decrease their scattering efficiency per mass and increase their sedimentation velocity. Most likely, a carrier gas



or liquid would be necessary for dispersion, which could result in additional perturbation of stratospheric composition. This is an uncertainty of SAI of solid particles, which does not apply for SAI via injection of gaseous  $\text{SO}_2$ .

Second, the ACCM used in this study does not account for aerosol-cloud interactions. It is unclear how alumina or calcite particles alter cirrus cloud coverage by potentially serving as cloud condensation nuclei for heterogeneous ice nucleation. While for sulfur-based SAI Cirisan et al. (2013) have shown that the cirrus cloud thinning effect in regions with cirrus clouds was canceled out by a cirrus cloud thickening effect in cirrus cloud free regions, Vioni et al. (2017) found a net cirrus cloud thinning effect, which strengthened the RF from  $\text{SO}_2$  injections. For calcite particles it has been shown that they are very good ice nucleation particles, which could increase cirrus cloud coverage and thus weaken RF from calcite particles (Cziczo et al., 2019). However, due to the large uncertainties resulting from aerosol-cloud interactions, it remains uncertain how solid particles would alter RF from SAI of solid particles.

Bearing in mind the large process uncertainties, our main simulations with alumina and calcite injections conducted with most reasonable assumptions on heterogeneous reaction rates based on present day knowledge result in slightly reduced ozone depletion compared to sulfur-based scenarios. However, consideration of SAI of solid particles as an alternative to sulfuric acid particles requires coordinated, inter-institutional and substantial laboratory research campaigns to investigate heterogeneous reaction pathways and rates on solid particles at stratospheric temperatures, partial pressures of relevant trace gases, relative humidity and stratospheric UV irradiation to address uncertainties of impacts on stratospheric composition. To quantify the real risks and benefits of SAI of solid particles this research is inevitably needed for a robust assessment of SAI by alternative materials compared to sulfur-based SAI. Given the large potential of reducing stratospheric warming and possibly reducing alteration of stratospheric composition compared to sulfuric acid aerosols, we encourage conducting this research. However, from a present day perspective we conclude that sulfur-based SAI may result in more efficient RF per injection rate at significantly lower risk due to substantial uncertainty of the impact on stratospheric composition by SAI of solid particles.

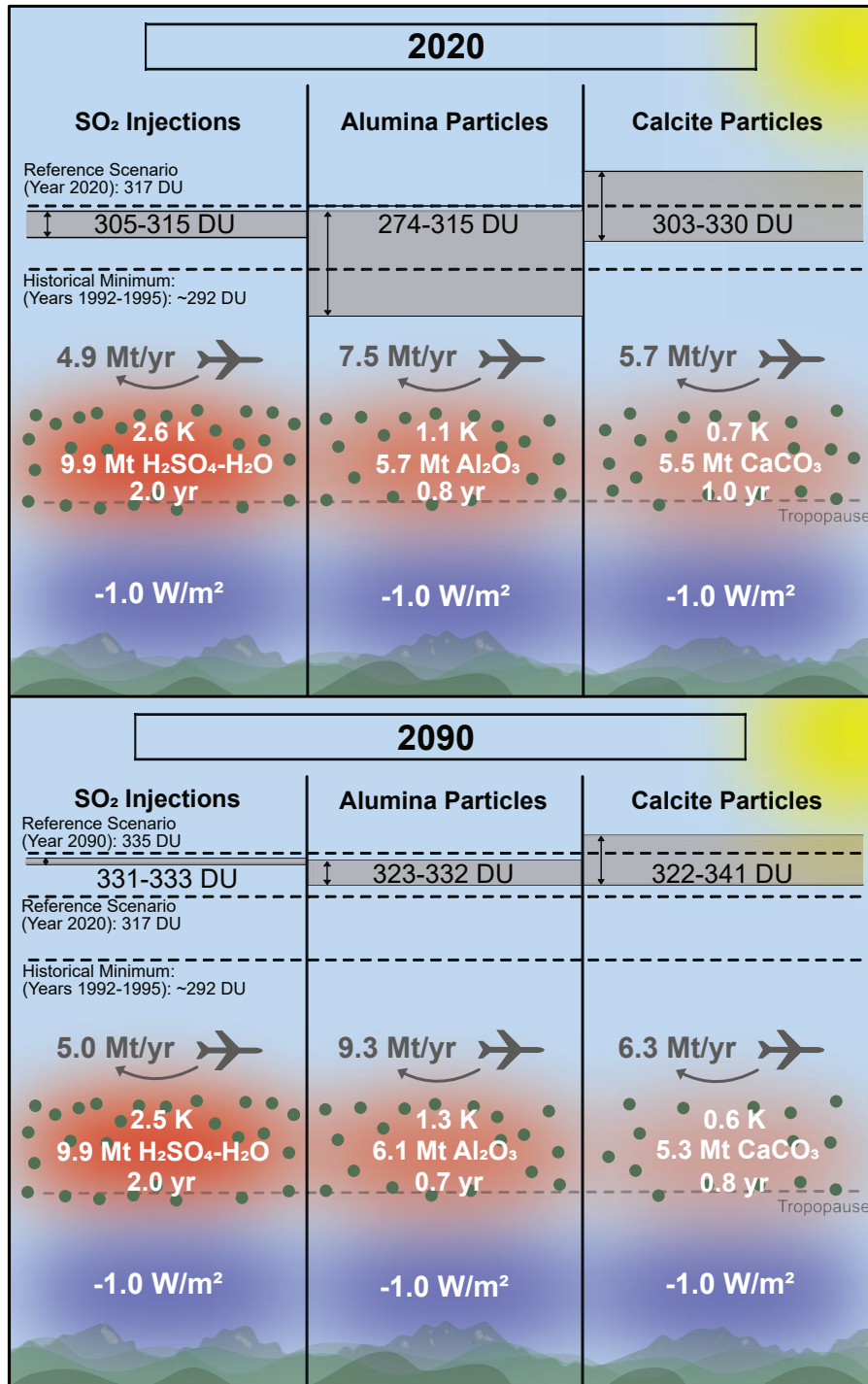


Figure 6.6: Schematic overview of globally averaged quantities linearly normalised to  $-1 \text{ W/m}^2$  total all sky ToA RF under 2020 boundary conditions in respect to GHG, SST, SIC and ODS concentrations when injecting SO<sub>2</sub> (left), alumina (middle) and calcite (right) particles at radius of 240 nm. Shown are required stratospheric aerosol burden, the injection rate, the resulting global average stratospheric residence time of the particles, the resulting stratospheric heating and the resulting TOC. For comparison the TOC of the reference scenario, the historical minimum in the years 1993-1997 (modelled by SOCOL-AERv2) as well as the uncertainty ranges for the resulting TOC (grey areas) are shown (see Section 2.3.3 for details on the uncertainty ranges). For 2090 conditions also the 2090 reference TOC is shown.

## Data Availability

The data is available on a online repository (Vattioni, 2024b) or on request from the corresponding author. The model code is available on a online repository (Vattioni, 2023b) or on request from the corresponding author.

## Author contributions

SV wrote the paper draft, created most of the figures, developed the model, tested the model and did the data analysis. RW performed some of the simulations, provided support with data analysis and created some of the figures. AF and AS contributed to model development as well as debugging and sanity checking of the model code. JAD performed the Mie-calculations to get the optical properties for alumina and calcite particles and their agglomerates. BL helped with the implementation of microphysics such as the contact angle on solid particles as well as implementation of optical properties. GAK and CAB performed discrete element model simulations to determine the mobility radius of alumina and calcite particles and all authors contributed to the discussion of the results.

## Acknowledgements

We especially thank Debra Weisenstein for discussions about her original solid particle AER code as well as David Keith for valuable discussion of our results. Support for Gabriel Chiodo and Andrea Stenke was provided by the Swiss Science Foundation within the Ambizione grant no. PZ00P2\_180043. Support for Sandro Vattioni was provided by the ETH Research grant no. ETH-1719-2 as well as by the Harvard Geoengineering Research Program. JD was also supported by the Harvard Solar Geoengineering Research Program. Timofei Sukhodolov acknowledges the support from the Swiss National Science Foundation (grant no. 200020-182239) and the Karbacher Fonds, Graubünden, Switzerland. GAK and CAB acknowledge the support from the Particle Technology Laboratory, ETH Zurich and, in part, the Swiss National Science Foundation (grant no. 200020\_182668, 250320\_163243 and 206021\_170729).

## Appendix 6: Supplementary information

### A: Absolute global mean quantities

Table 6.1 shows the resulting globally averaged RF, the resulting stratospheric aerosol burden, the resulting diffuse radiation as well as the resulting globally averaged TOC for all scenarios simulated in for this chapter. Each simulation consists of 3 ensemble members of 20 year-simulations of which the first 5 years served as a spin-up. Thus, all ensembles consist of 3 times 15 years. Figure 6.7 yearly averages of RF and burden as a function of time to provide a visualisation of inter-annual variability.

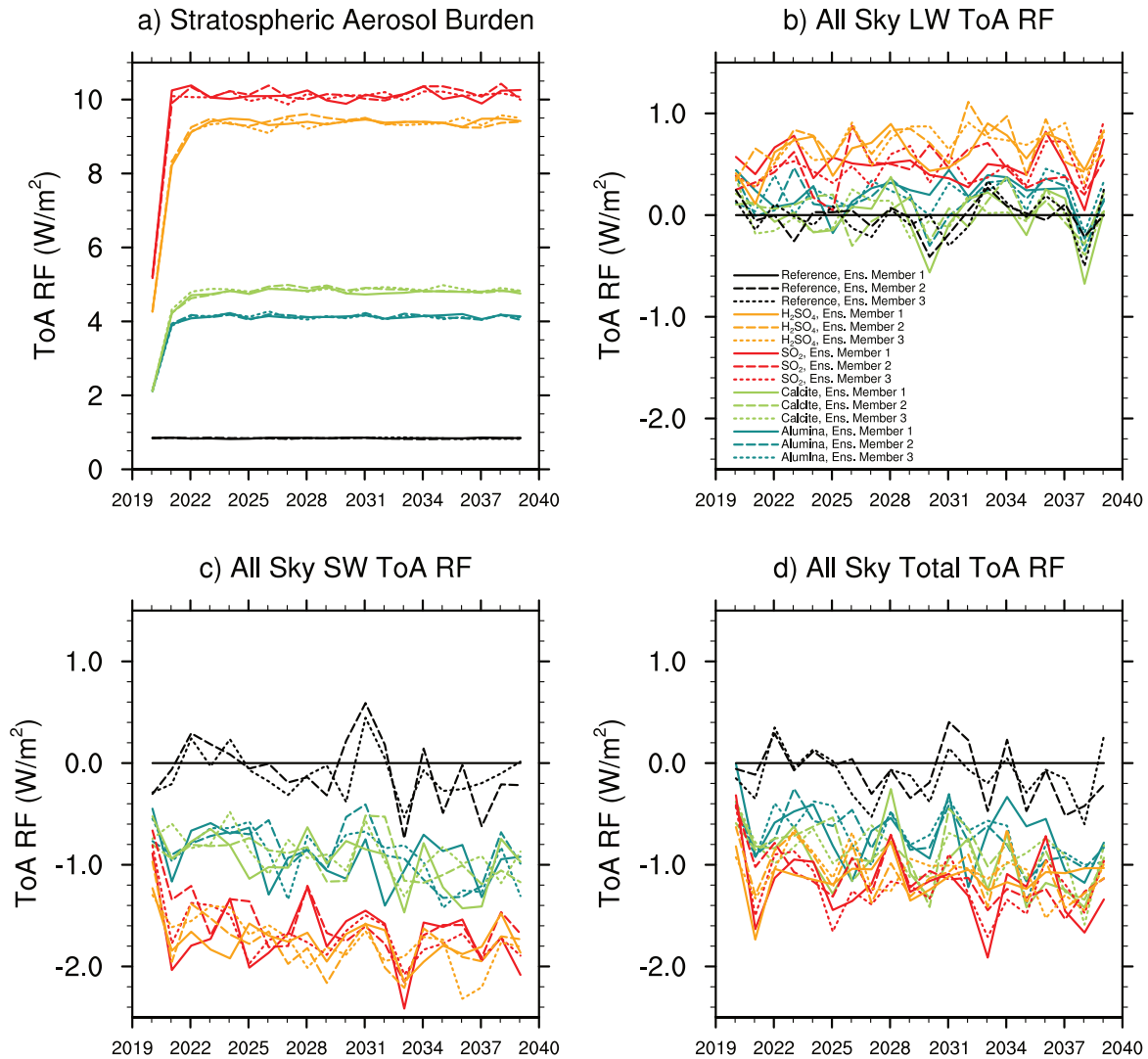


Figure 6.7: Evolution of global annual mean values for Stratospheric aerosol burden (a), all sky LW ToA RF (b), all sky SW ToA RF (c) and all sky total ToA RF (d) of all three ensemble members for injection of 5 Mt/yr SO<sub>2</sub> (red), AM-H<sub>2</sub>SO<sub>4</sub> (orange), alumina (dark green,  $r=240$  nm) and calcite particles (light green,  $r=240$  nm). Data shown in this paper show averages over the last 15 years of each ensemble member.

Table 6.1: Globally averaged all sky (AS), LW ToA RF, AS SW RF, AS total RF, clear sky (CS) LW ToA RF, CS SW RF, CS total RF, stratospheric aerosol Burden (in Mt alumina, calcite and  $\text{H}_2\text{SO}_4\text{-H}_2\text{O}$ ), diffuse radiation, and TOC for 2020 boundary conditions (upper part) and 2090 boundary conditions (lower part).

2020 Boundary Cond.	Reference	$\text{SO}_2$	$\text{AM-H}_2\text{SO}_4$	$\text{Al}_2\text{O}_3$	$\text{CaCO}_3$
AS LW RF ( $\text{W/m}^2$ )	n/a	$0.71 \pm 0.15$	$0.49 \pm 0.16$	$0.19 \pm 0.13$	$0.01 \pm 0.17$
AS SW RF ( $\text{W/m}^2$ )	n/a	$-1.73 \pm 0.17$	$-1.64 \pm 0.18$	$-0.87 \pm 0.24$	$-0.89 \pm 0.19$
AS tot RF ( $\text{W/m}^2$ )	n/a	$-1.02 \pm 0.19$	$-1.15 \pm 0.21$	$-0.67 \pm 0.21$	$-0.88 \pm 0.21$
CS LW RF ( $\text{W/m}^2$ )	n/a	$0.95 \pm 0.11$	$0.66 \pm 0.13$	$0.27 \pm 0.10$	$0.01 \pm 0.11$
CS SW RF ( $\text{W/m}^2$ )	n/a	$-2.49 \pm 0.08$	$-2.48 \pm 0.09$	$-1.28 \pm 0.08$	$-1.40 \pm 0.11$
CS tot RF ( $\text{W/m}^2$ )	n/a	$-1.55 \pm 0.12$	$-1.82 \pm 0.13$	$-1.01 \pm 0.10$	$-1.39 \pm 0.11$
Strat. Burden (Mt)	$0.84 \pm 0.01$	$10.12 \pm 0.01$	$9.38 \pm 0.13$	$3.82 \pm 0.05$	$4.84 \pm 0.06$
Diff. Rad. ( $\text{W/m}^2$ )	$30.8 \pm 0.1$	$32.0 \pm 0.2$	$32.2 \pm 0.1$	$31.3 \pm 0.1$	$31.6 \pm 0.1$
TOC (DU)	$316.5 \pm 1.5$	$310.1 \pm 1.3$	$308.3 \pm 1.5$	$312.5 \pm 1.6$	$316.6 \pm 1.3$
2090 Boundary Cond.	Reference	$\text{SO}_2$	$\text{AM-H}_2\text{SO}_4$	$\text{Al}_2\text{O}_3$	$\text{CaCO}_3$
AS LW RF ( $\text{W/m}^2$ )	n/a	$0.72 \pm 0.18$	$0.52 \pm 0.15$	$0.26 \pm 0.15$	$0.01 \pm 0.12$
AS SW RF ( $\text{W/m}^2$ )	n/a	$-1.72 \pm 0.19$	$-1.56 \pm 0.17$	$-0.80 \pm 0.19$	$-0.81 \pm 0.17$
AS tot RF ( $\text{W/m}^2$ )	n/a	$-1.00 \pm 0.20$	$-1.04 \pm 0.18$	$-0.54 \pm 0.21$	$-0.80 \pm 0.19$
CS LW RF ( $\text{W/m}^2$ )	n/a	$0.99 \pm 0.15$	$0.69 \pm 0.13$	$0.32 \pm 0.06$	$-0.02 \pm 0.10$
CS SW RF ( $\text{W/m}^2$ )	n/a	$-2.54 \pm 0.06$	$-2.33 \pm 0.06$	$-1.15 \pm 0.06$	$-1.28 \pm 0.05$
CS tot RF ( $\text{W/m}^2$ )	n/a	$-1.56 \pm 0.14$	$-1.64 \pm 0.11$	$-0.83 \pm 0.12$	$-1.30 \pm 0.10$
Strat. Burden (Mt)	$0.69 \pm 0.01$	$9.85 \pm 0.14$	$8.48 \pm 0.12$	$3.30 \pm 0.07$	$4.20 \pm 0.05$
Diff. Rad. ( $\text{W/m}^2$ )	$29.6 \pm 0.1$	$31.0 \pm 0.1$	$31.0 \pm 0.1$	$30.3 \pm 0.2$	$30.1 \pm 0.1$
TOC (DU)	$335.7 \pm 1.7$	$332.3 \pm 2.0$	$331.5 \pm 1.6$	$334.2 \pm 1.7$	$333.9 \pm 1.6$

## B: Zonal mean particle number densities

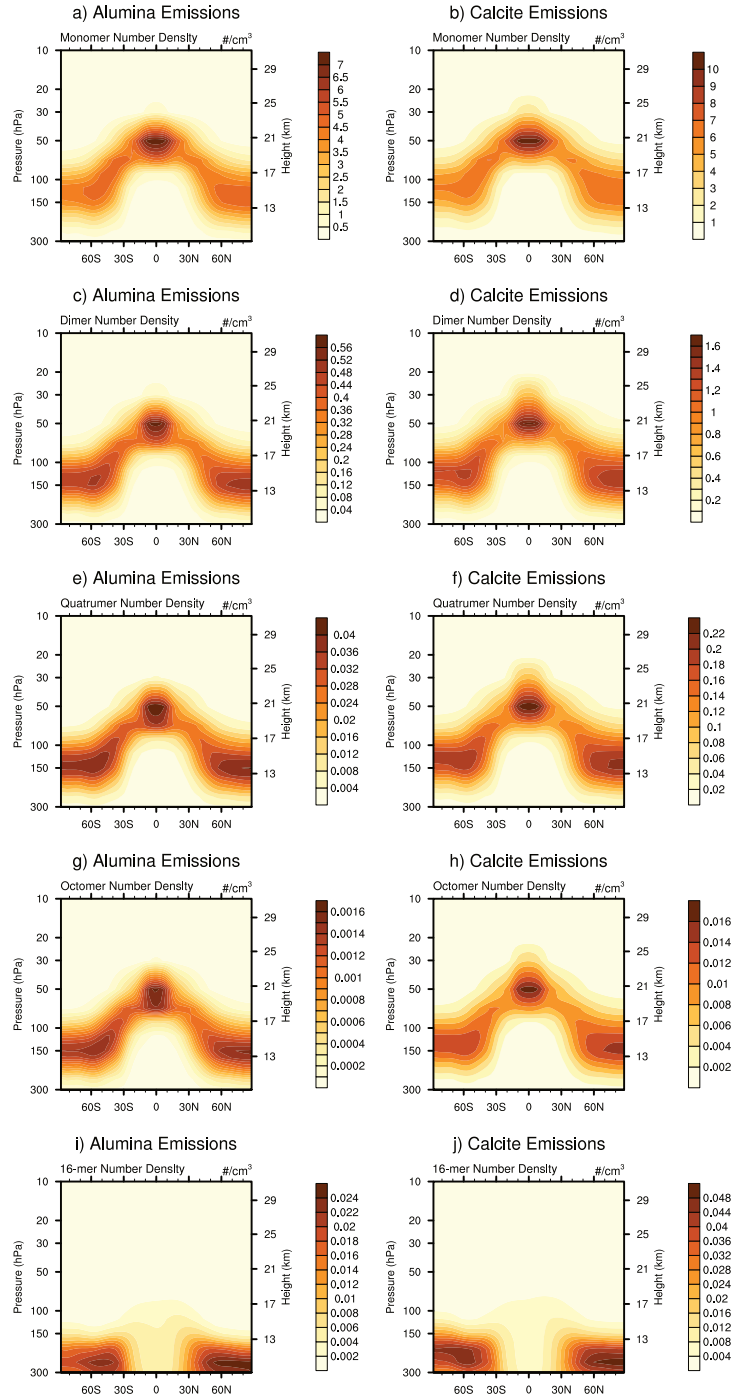


Figure 6.8: Particle number concentrations for 5 Mt/yr injection of alumina particles with radius of 240 nm (left column), of alumina particles with radius of 240 nm (right column). Panel (a) and (b) show monomers, panel (c) and (d) dimers, panel (e) and (f) 4-mers, panel (g) and (h) 8-mers, and panel (i) and (j) 16-mers.

**C: Global mean quantities normalised per injection rate and per resulting stratospheric aerosol burden**

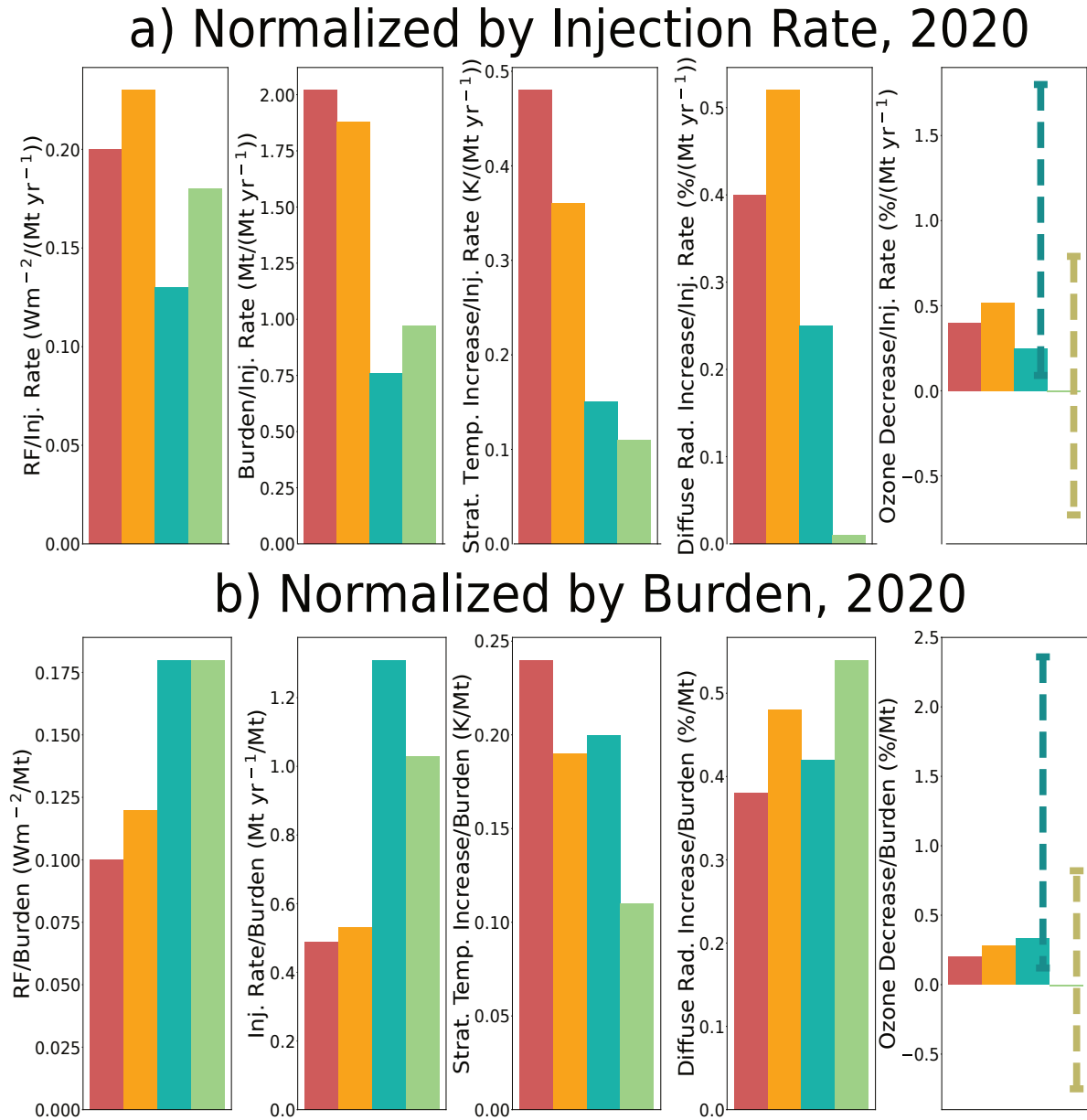


Figure 6.9: Resulting globally averaged stratospheric aerosol burden (see Figure 6.1), injection rate, ToA all sky RF, total ozone column decrease, peak stratospheric heating and diffuse radiation increase for SO<sub>2</sub> (red), AM-H<sub>2</sub>SO<sub>4</sub> (orange), alumina (blue, r=240 nm) and calcite particles (light green, r=240 nm) normalized by injection rate in (a) and by resulting stratospheric aerosol burden in (b). Quantities normalised to RF are shown in Figure 6.2 for 2020 conditions

## D: Zonal mean SAD

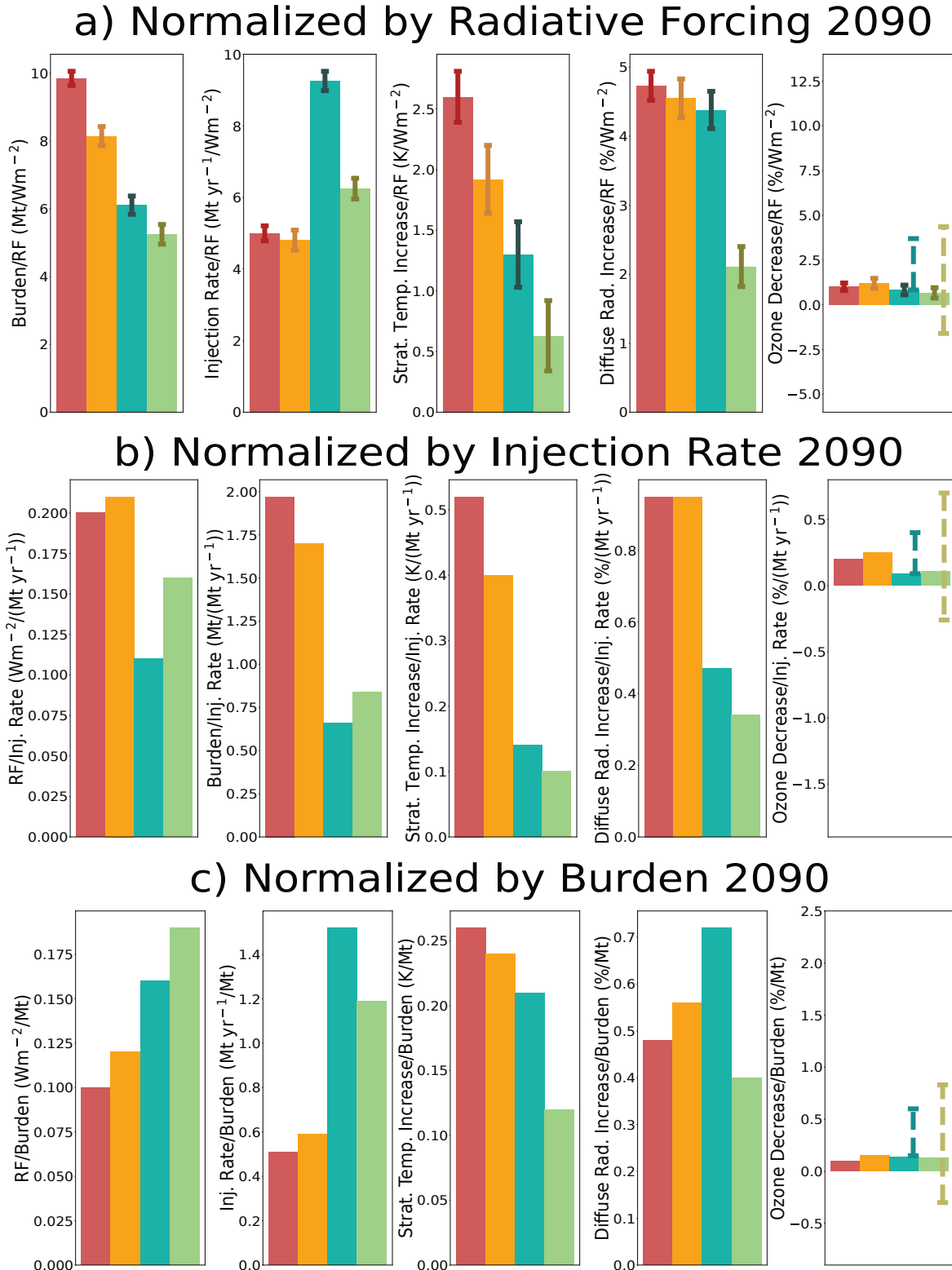


Figure 6.10: Resulting globally averaged stratospheric aerosol burden (see Figure 6.1), injection rate, ToA all sky RF, total ozone column decrease, peak stratospheric heating and diffuse radiation increase for  $\text{SO}_2$  (red),  $\text{AM-H}_2\text{SO}_4$  (orange), alumina (blue,  $r=240$  nm) and calcite particles (light green,  $r=240$  nm) normalised by injection rate in (a) and by resulting stratospheric aerosol burden in (b). Quantities normalised to RF are shown in Figure 6.2



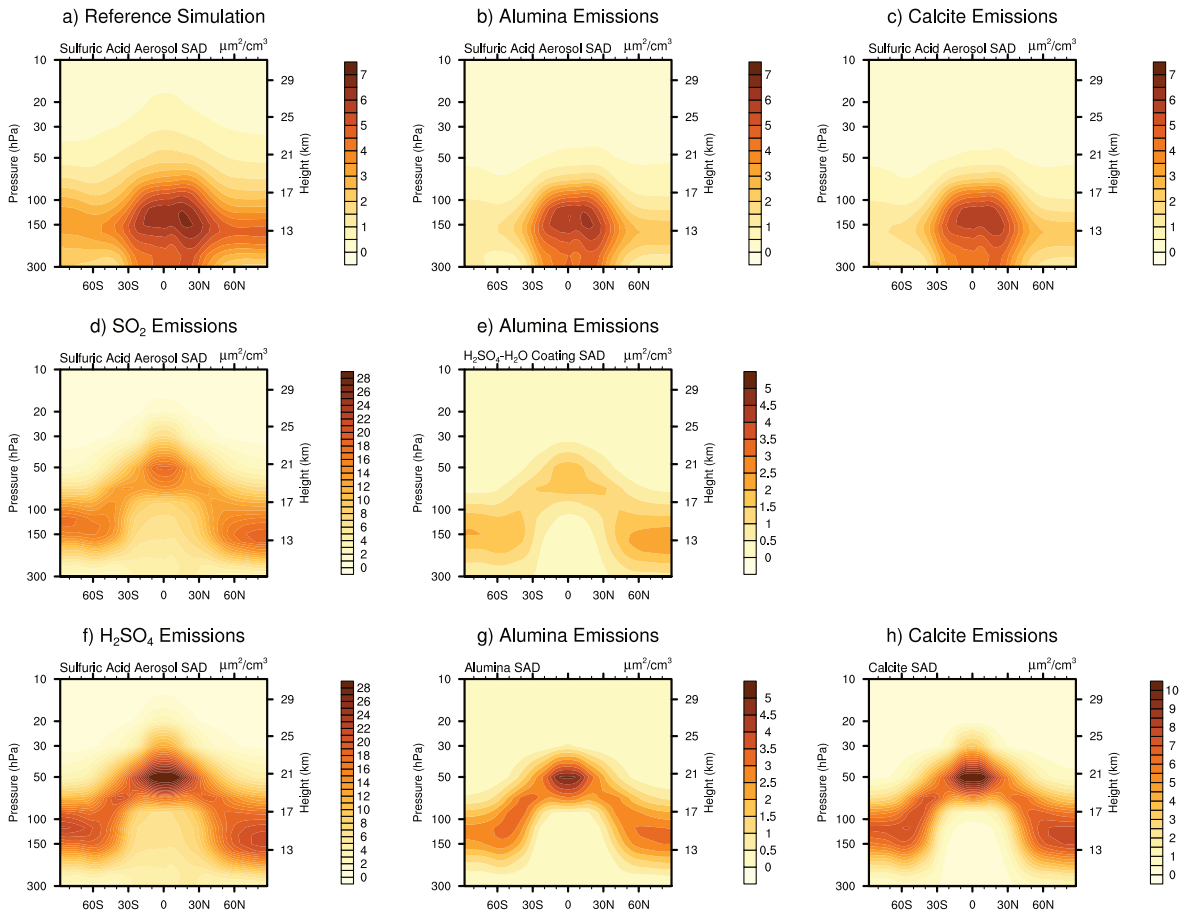


Figure 6.11: The resulting SAD of all scenarios simulated in this chapter. The upper row shows the the background sulfuric acid SAD of the reference run (a), when injecting alumina particles (b) and when injecting calcite particles (c). The sulfuric acid SAD resulting from  $\text{SO}_2$  injections and AM- $\text{H}_2\text{SO}_4$  injections are shown in (d) and (f). The middle column shows resulting sulfuric acid coating SAD (e) and alumina SAD (g) for alumina injections and resulting calcite SAD is shown in (h).

## E: Zonal mean dynamical impacts for 2020 and 2090 conditions

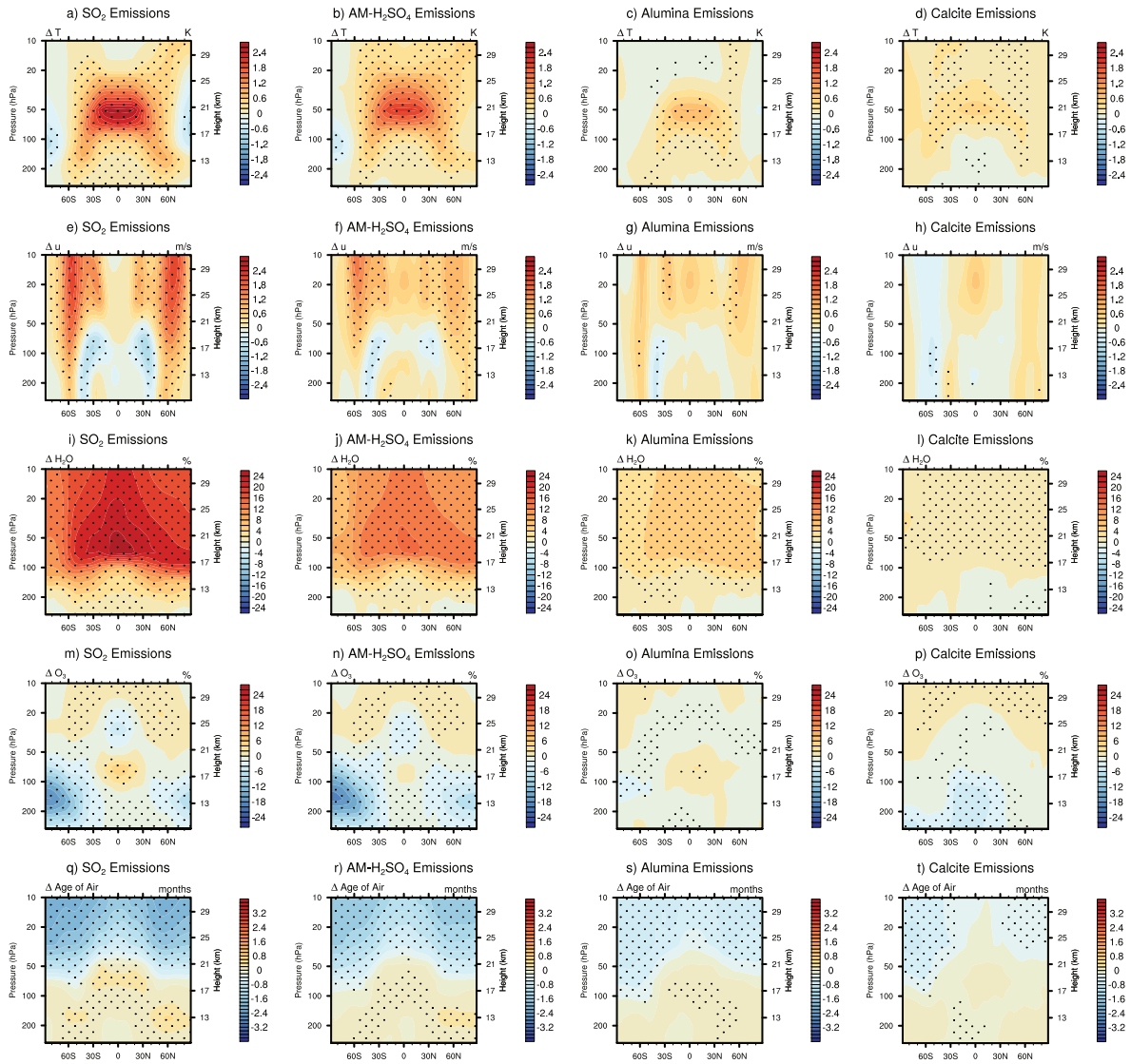


Figure 6.12: The uppermost row shows the zonally averaged temperature anomaly compared to the reference run for all scenarios for 2090 boundary conditions. The second row shows the corresponding anomaly of the zonal winds. The third row shows the corresponding anomaly of H<sub>2</sub>O. The fourth row shows the corresponding ozone anomaly and the last row shows the corresponding change in AoA. Dotted area indicates statistically significant changes at the 95% significance level (t-test).

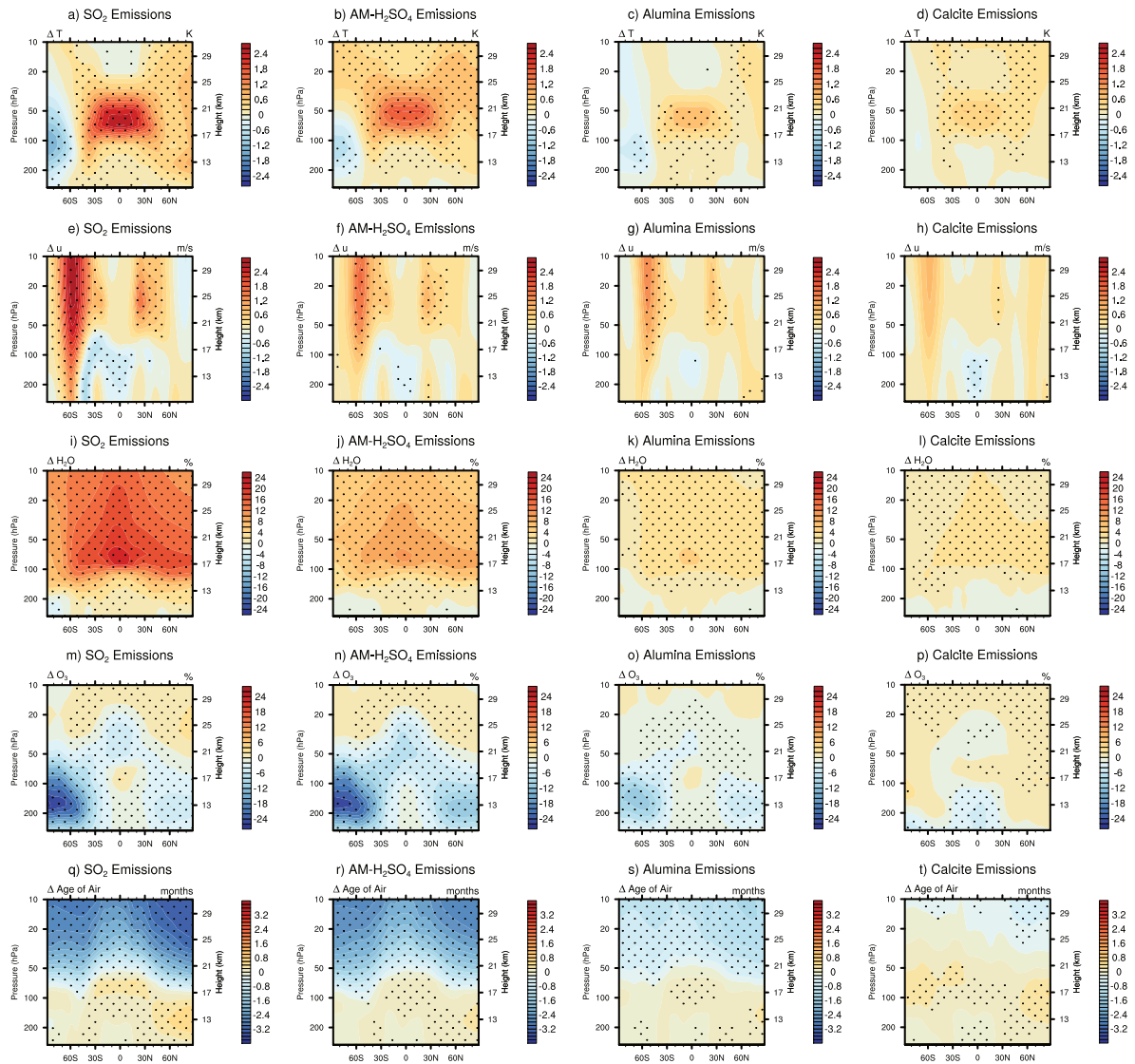


Figure 6.13: The uppermost row shows the zonally averaged temperature anomaly compared to the reference run for all scenarios for 2020 boundary conditions. The second row shows the corresponding anomaly of the zonal winds. The third row shows the corresponding anomaly of H<sub>2</sub>O. The fourth row shows the corresponding ozone anomaly and the last row shows the corresponding change in AoA. Dotted area indicates statistically significant data at the 95% significance level (t-test).



# Chapter 7

## Outlook

While this thesis presents first results from simulations of SAI of solid particles with SOCOL-AERv2, there are more studies underway, which did not make it into this thesis anymore due to time constraints. These follow up studies include the simulation of other particle injection types such as diamond particles, which were shown to have better optical properties than alumina and calcite particles (Dykema et al., 2016). Additionally, a detailed sensitivity analysis on the impact of SAI of calcite particles on stratospheric ozone is underway. Furthermore, the ESM SOCOLv4 was used to simulate G4 and G6 GeoMIP simulations with alumina, calcite and diamond injections to analyze the impacts of SAI of solid particles on tropospheric climate. The model presented in this work will also allow for sensitivity analysis of future laboratory experiments on heterogeneous chemistry or microphysics of various solid particle types.

The following subchapters provide some further research proposals, which aim at addressing the major uncertainties highlighted in this thesis. These uncertainties are sulfuric acid aerosol microphysics under SAI conditions (Section 7.1) and solid particle microphysics within temporal and spatial scales ranging from injections from an aircraft over plume dispersion to the ESM grid scale as well as the optical properties of resulting agglomerates (Section 7.2). The proposed research could further reduce the uncertainties on risks and benefits of SAI. These proposals were submitted to a call for proposals of the Simons foundation in collaboration with Daniele Visoni, Zamin Kanji, Gabriel Chiodo, Thomas Peter, Martin Gysel-Beer, Markus Ammann, Iris de Vries, Steven Hulshoff, Christof Vockenhuber, Arnold Müller, Heri Kuswanto, Roxann Stennett-Brown and R. Krishnan. With agreement from these collaborators parts of the submitted proposals are used verbatim in the two subchapters below. Further substantial uncertainty highlighted in this thesis concerns heterogeneous chemistry on solid particles. Additional research using HI-ERDA and AP-XPS with improved dosing schemes accounting for a wider range of stratospheric conditions (i.e., temperature and RH ranges, trace gases (e.g., also  $\text{H}_2\text{SO}_4$ ) and a variety of different particle materials could be beneficial to further reduce uncertainties. Furthermore, uncertainty on heterogeneous chemistry could be further reduced by performing flow tube experiments to measure reaction kinetics as well as by performing experiments on particle aging processes.

However, despite all research efforts via modelling and experimental work it will never be possible to have absolute certainty about risks and benefits of SAI applications in the real world. Every experimental setup in the laboratory as well as every model will always be only an idealisation of the real world. This idealisation might be subject to biases like it is also illustrated in this thesis. Therefore, to reduce uncertainties on the real risks and benefits of SAI it would be crucial to perform small scale field experiments such as proposed with SOPEX (Dykema et al., 2014). The experiment proposes to carry a payload including instruments such as a LIDAR to the stratosphere with a propeller controlled balloon to inject small amounts ( $< 10$  kg) of material, which would then allow to observe the formation and evolution of aerosol plumes. Such experiments would not only be beneficial for SAI, but also for research on stratospheric aerosols and chemistry in general.

Despite, every trans-ocean aircraft flight releasing more emission to the stratosphere than proposed in ScoPEX, the experiment is subject to intense ethical debates due to the large controversy of the matter. The big dilemma on SAI research remains that we will never be able to quantify the real effects of SAI with absolute certainty without implementation on a global scale due to the lack of observations. Therefore, future decisions about implementation of SAI will most likely not only be a result of scientific arguments, but more on ethical and political discourses on how the world should look like in which future generations will be living in. Research can only contribute to this discussion by providing scientific evidence. Since no one can predict the future, it is best to be prepared for a variety of potential scenarios, including SAI.

## 7.1 Aerosol Microphysics, Optics and Radiation Model Intercomparison Project (AMOR-MIP)

To date general climate models (GCMs) are the only tool to estimate the impacts of SAI. The geoengineering model intercomparison project (GeoMIP) has contributed substantially to highlight uncertainties on resulting stratospheric aerosol burden, surface area densities, radiative forcing patterns and their impact on stratospheric heating, ozone alteration and climate impacts on global and regional scale (Vioni et al., 2023). The project has revealed substantial uncertainty, for example, in the stratospheric aerosol burden required to achieve a global surface cooling of 1 K, which varies by a factor of up to 2 depending on the GCM used (Vioni et al., 2021; WMO, 2022). Other studies found differences of up to a factor of 3 for resulting stratospheric aerosol burden and top of the atmosphere radiative forcing, when simulating the same emission scenarios with different aerosol-GCMs (WMO, 2022; Weisenstein et al., 2022). Similar inter model differences were identified by the Volcano Model Intercomparison Project VolMIP and by the Interactive Sulphate Aerosol Model Intercomparison Project ISA-MIP (for Pinatubo and Tambora Marshall et al., 2018; Clyne et al., 2021; Quaglia et al., 2023). Most of these MIP studies are conducted with general circulation models of very different complexity (e.g., different parameterizations of processes, interactive aerosol microphysics and chemistry) and different spatial and temporal resolution, making it difficult to attribute the differences between models. Reducing model uncertainty is a critical step in evaluating the risks and benefits of SAI.

The formation and distribution of sulfuric acid aerosols from  $\text{SO}_2$  emissions and the intended surface cooling depend on the representation of (1) chemistry, e.g.  $\text{SO}_2$  oxidation by OH,  $\text{O}_3$  and  $\text{H}_2\text{O}$ , (2) aerosol microphysics, e.g. condensation, nucleation, coagulation and sedimentation, and (3) optical properties, i.e. scattering and absorption coefficients of aerosols (Vioni et al., 2021). The aerosol, in turn, depends on temperature, advection as well as temporal, spatial and spectral model resolution. Deficiencies and inconsistencies in (1)-(3) as well as in the representation of aerosols in size-resolved distributions (“sectional”) or in a much simpler modal representation can propagate, leading to errors in SAI sedimentation mass flux, cooling efficiency, and global and regional climate impacts. Dedicated comparisons of processes (1)-(3) are needed to determine the reasons for the documented model differences. Previous intercomparisons of aerosol modules (Weisenstein et al., 2007; Mann et al., 2012) and shortwave radiative forcing by sulfuric acid aerosols (Boucher et al., 1998) have been performed more than a decade ago, and since then the models were further developed and their complexity increased. Furthermore,

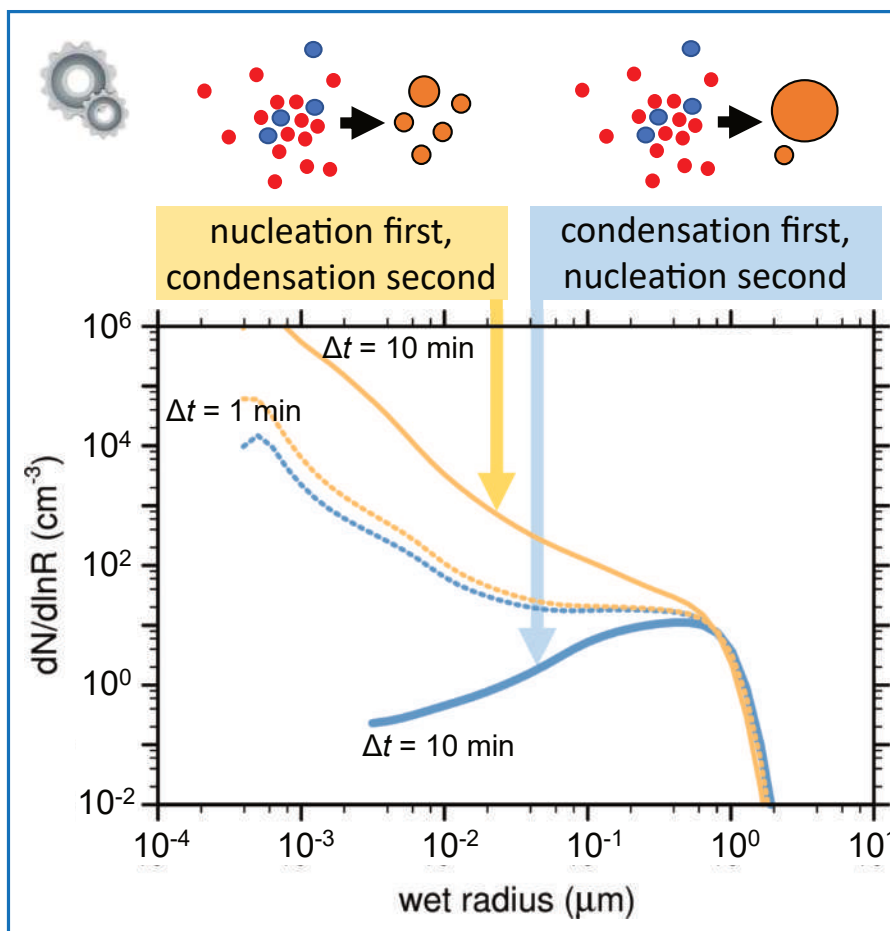


Figure 7.1: Resulting aerosol size distribution simulated by SOCOL averaged between 15°N and 15°S at 55 hPa resulting from emission of 5 Mt/yr in form of SO<sub>2</sub> when calling first nucleation or condensation. Results converge at small microphysical time steps.

those MIPs did not focus on SAI-conditions, but on tropospheric aerosols, volcanoes and chemistry (Forster et al., 2011). A detailed analysis of the aerosol microphysics module (AMM) AER incorporated in the ESM SOCOLv4 (Sukhodolov et al., 2021) has shown that it adequately represents aerosol burdens, distributions and surface area densities (SAD) under both volcanically quiescent and active conditions (e.g. Mt. Pinatubo), but that significant deficiencies exist under SAI conditions (see Chapter 2). Depending on the call sequence of nucleation and condensation within the AMM, differences of up to 25% were found in the resulting global stratospheric aerosol burden when emitting 5 Mt of Sulfur per year as SO<sub>2</sub>, with resulting globally averaged surface coolings of 0.6 K and 1.0 K, respectively. This is due in part to the choice of a microphysical time step that, while appropriate under background conditions, but way too large for the substantial H<sub>2</sub>SO<sub>4</sub> supersaturations under SAI conditions (see Figure 7.1). Given the H<sub>2</sub>SO<sub>4</sub> supersaturations involved in SAI studies, it is therefore critical to update the AMM with a SAI-specific focus to understand the adequacy of current aerosol microphysics approaches in the GCMs used for SAI assessments.

The overall goal is to assess the role of AMMs, as well as of aerosol optical properties and radiative transfer codes (RTC) used in various state-of-the-art aerosol-GCMs. This could be done by running these modules as zero-dimensional and one-dimensional process models (box and column models) under prescribed boundary conditions allowing us to

quantify and attribute model-differences under conditions ranging from background to SAI, including effects on microphysics and radiative forcing efficiencies.

### 7.1.1 Anticipated outcomes

AMOR-MIP will shed light on the key processes driving uncertainties associated with SAI in aerosol GCMs. This will inform future international assessments of SAI risks and benefits, such as IPCC or WMO reports. Furthermore, its results will provide a benchmark for future model development, especially when it comes to improving the assessment capabilities of GCMs for SAI. Given the relatively low computational cost of box-models, our results will be easily replicable and have the potential to be readily integrated with new information related to better measurements of physicochemical and optical properties of sulfuric acid aerosol.

## 7.2 Stratospheric Aerosol Injection across Scales (SAIaS): From near-field agglomerates and size distributions to global and regional impacts

To date, a major limitation of ESMs in simulating SAI is that particles are represented by a uniform distribution in each model grid box with horizontal resolution of  $\sim 200$  km. This neglects local variations in the sub-grid near-field turbulent plume directly behind the emitting aircraft affecting aerosol size distributions, particle shapes, compactness, and other particle properties. The global temperature response and many side effects of SAI depend crucially on the properties of the particle population, as it develops during the first moments after emission and then continues to evolve slowly, such as number densities of monomers, higher order agglomerates, particle morphology, sedimentation speed and optical properties (Dykema et al., 2016; Weisenstein et al., 2015; Arias et al., 2021, see Figure 7.2).

Furthermore, it is uncertain whether solid particle aerosol size distributions with the required properties for efficient global cooling can develop within the injection plume. Therefore, experimentally informed modeling of turbulence, mixing and microphysics in the injection plume at different temporal and spatial sub-ESM scales is key for estimating effects of SAI on a global scale, and providing the required information for regional impact assessment. Conditions governing the characteristics of aerosols of environmentally benign materials with the properties required for SAI should be investigated and compared to the characteristics of sulfuric acid aerosols.

### 7.2.1 Objectives and Research Questions

The goal of SAIaS is to investigate the influence of sub-ESM-grid processes on the evolution of aerosol size distribution and particle morphology, to provide aerosol characteristics for ESMs, which in turn quantify the radiative impact of SAI over their residence time from injection into the stratosphere to reentry into the troposphere (after many months) including their regional impacts. In particular the aim is to investigate microphysical processes on the clusters and aerosol particles in the turbulent near-field plume – e.g., bouncing, sticking, fragmentation – affect their size distributions, morphologies, sedimentation speeds and optical properties, especially backscatter efficiencies, for different solid



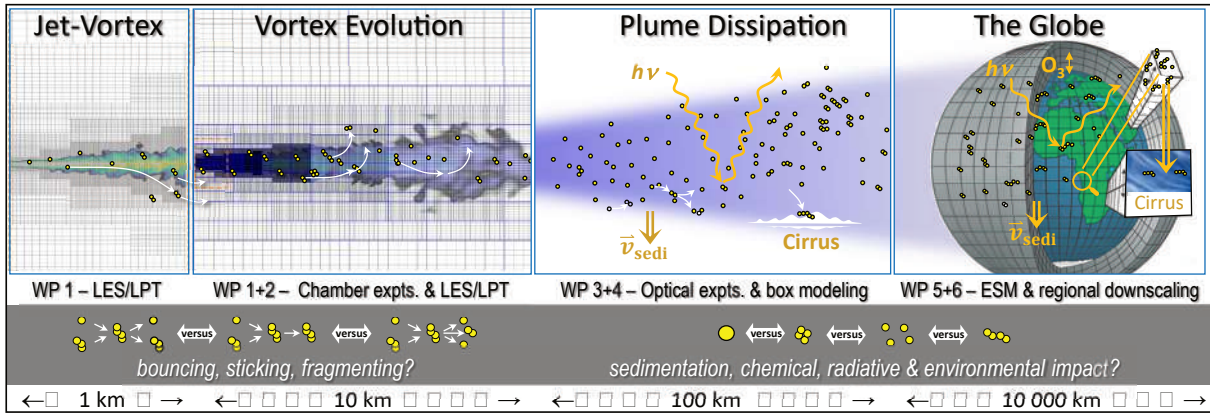


Figure 7.2: Dynamical regimes and the microphysical/radiative processes downstream of an aircraft, which injects particles or gas into the stratosphere. Gas can nucleate/condense into particles, and particles can stick, bounce, or fragment upon collision. This depends on properties such as particle number density, size, composition, porosity, coating, and on the turbulence-dependent relative velocity. These processes further determine the surface area density and chemical reactivity, sedimentation speed and backscatter fraction, they affect the ozone layer, cirrus cloudiness, as well as the regional and global climate. (LES = Large Eddy Simulation; LPT = Lagrangian Particle Tracking; ESM = Earth System Model;  $\bar{v}_{sedi}$  = particle sedimentation speed;  $h\nu$  = photon energy.)

particle candidate materials and how they compare to aerosol populations resulting from injection of gaseous  $H_2SO_4$ . Furthermore, research should be conducted on how near-field and mesoscale processes translate to scales relevant for input to global Earth System Models, and what the consequences are for the overall cooling efficiency, stratospheric chemistry, the ozone layer, cirrus cloudiness, atmospheric circulation and climate.

## 7.2.2 Proposed work in SAIaS

The turbulent wake directly behind the aerosol injecting aircraft determines the collision frequency of particles along their trajectories, which will intersect streamlines due to particle inertia. A detailed description of the velocity and temperature fields in the aircraft's wake could be produced with large-eddy simulations (LES Fathi et al., 2022) using aerodynamic, propulsion, and atmospheric parameters characteristic of aircraft operations in the stratosphere (Janssens et al., 2020). A composite wake description could be used for Lagrangian Particle Tracking (LPT) to determine the frequency of solid aerosol particle collisions and ultimately particle size distributions as a function of downstream position.

Furthermore, experimentally work could be conducted using aerosol suspension and coagulation chamber to measure the sticking probabilities ( $\#agglomerations/\#collisions$ ) and coagulation coefficients of  $H_2SO_4$ -coated and uncoated solid particles of different materials under turbulent conditions (Kanji et al., 2013). The chamber could be equipped with hotwire probes to measure the turbulent kinetic energy spectra at different locations in an aerosol-free tank to determine the range of turbulence that can be generated by the high-speed fan in the tank. By introducing sub- $\mu m$  solid particles into the chamber with known turbulence levels, the evolution of the aerosol size distribution, yielding aerosol number density, agglomerate size, and fractal dimension can be measured (Gao et al., 2022).

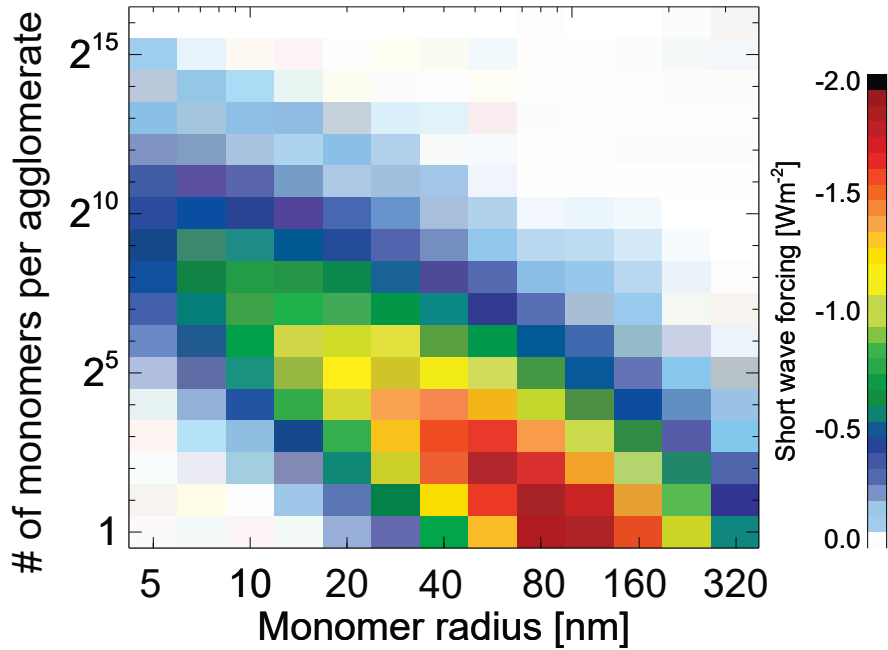


Figure 7.3: Short wave forcing of 5 Mt/yr injection of  $\text{Al}_2\text{O}_3$  particles as function of injected monomer size and number of monomers per agglomerate forming after monomer injection. In this model, adjacent agglomerate sizes result from monomer number doubling. The short wave forcing is a function of the scattering efficiency and gravitational removal of the agglomerates accounting for the full spectrum of incoming solar radiation. The change of burden due to different sedimentation speed is taken into account using the projected area of the agglomerates. The mass specific hemispheric backscatter cross section is estimated assuming uniform porous spheres with equal projection area.

Combining experiments and simulations of aerosol optics, the phase functions of light scattering by agglomerates with variable morphology and optical material properties could be determined using in-situ polar nephelometry (Moallemi et al., 2023) and photo-acoustic absorption spectroscopy. The experimental results can be compared with numerical predictions using multi-sphere T-matrix calculations (Romshoo et al., 2021) to develop an optimal forward kernel for calculating aerosol optical properties. Using experimentally determined aerosol size distribution and morphology parameters, the optical kernel will provide the extinction coefficient, single scattering albedo and asymmetry parameter. The mobility of aggregates as a function of their morphology, which directly affects particle sedimentation speeds and thus their stratospheric residence time. These parameters will feed into radiative transfer simulations and transport modules of the ESM to account for particle morphology effects, which has not been considered.

In the end, findings will be used as input into the ESM SOCOL (see Chapter 3, Sukhodolov et al., 2021) for an impact assessment for different SAI scenarios on the global and regional scale. The results will be compared to climate change scenarios without any intervention, to provide policy-relevant information on the risks of SRM versus the risks of climate change for societally important impacts on e.g., natural hazard probability (temperature and precipitation extremes) and agricultural productivity (Stennett-Brown et al., 2017; Kuswanto et al., 2022).

### 7.2.3 Relevance and impact of SAIs

This project aims to enable the comprehensive representation of the atmospheric processes relevant to SAI across scales, i.e., directly from particle injection all the way to re-entry into the troposphere. Through a combination of experimental and modeling work, we aim to fill the knowledge gap that exists for sub-ESM-grid processes in the turbulent near field. This includes experimentally constrained consideration of particle morphology effects on optical properties and lifetime. This sub-ESM-grid output will be fed into state-of-the-art sectional aerosol-ESMs allowing to determine, as a function of aerosol injection strategy, (1) radiative backscatter efficiency and cooling at the Earth surface, including potential feedbacks from changes in cirrus clouds, (2) changes in diffuse radiation at surface levels, (3) thermal, dynamical and chemical changes in the stratosphere including impact on the ozone layer, (4) changes in the troposphere, including drivers of extreme events, (5) identification of regions particularly vulnerable to SAI impacts, particularly in the Global South. This project will help improve representations of SAI scenarios featuring novel aerosol candidates and their physical properties, to ultimately improve assessments of their environmental impact and associated uncertainties and risks. This will allow comparison of different SAI scenarios, including the well-researched injection of  $\text{SO}_2$  and  $\text{H}_2\text{SO}_4$  relative to scenarios without SAI under conditions of continued greenhouse gas emissions.



# Addenda

## Bibliography

- Abalos, M., Orbe, C., Kinnison, D. E., Plummer, D., Oman, L. D., Jöckel, P., Morgenstern, O., Garcia, R. R., Zeng, G., Stone, K. A., and Dameris, M.: Future trends in stratosphere-to-troposphere transport in CCM1 models, *Atmospheric Chemistry and Physics*, 20, 6883–6901, <https://doi.org/10.5194/acp-20-6883-2020>, 2020.
- Aguzzi, A. and Rossi, M. J.: The kinetics of the uptake of  $\text{HNO}_3$  on ice, solid  $\text{H}_2\text{SO}_4\text{--H}_2\text{O}$  and solid ternary solutions of  $\text{H}_2\text{SO}_4\text{--HNO}_3\text{--H}_2\text{O}$  in the temperature range 180–211 K, *Phys. Chem. Chem. Phys.*, 3, 3707–3716, <https://doi.org/10.1039/B100546O>, 2001.
- Al-Hosney, H. A. and Grassian, V. H.: Water, sulfur dioxide and nitric acid adsorption on calcium carbonate: A transmission and ATR-FTIR study, *Physical Chemistry Chemical Physics*, 7, <https://doi.org/10.1039/b417872f>, 2005.
- Ammann, M., Cox, R. A., Crowley, J. N., Jenkin, M. E., Mellouki, A., Rossi, M. J., Troe, J., and Wallington, T. J.: Evaluated kinetic and photochemical data for atmospheric chemistry: Volume VI – heterogeneous reactions with liquid substrates, *Atmospheric Chemistry and Physics*, 13, 8045–8228, <https://doi.org/10.5194/acp-13-8045-2013>, 2013.
- Aquila, V., Garfinkel, C. I., Newman, P., Oman, L., and Waugh, D.: Modifications of the quasi-biennial oscillation by a geoengineering perturbation of the stratospheric aerosol layer, *Geophysical Research Letters*, 41, 1738–1744, <https://doi.org/10.1002/2013GL058818>, 2014.
- Arfeuille, F., Luo, B. P., Heckendorn, P., Weisenstein, D., Sheng, J. X., Rozanov, E., Schraner, M., Brönnimann, S., Thomason, L. W., and Peter, T.: Modeling the stratospheric warming following the Mt. Pinatubo eruption: uncertainties in aerosol extinctions, *Atmos. Chem. Phys.*, 13, 11 221–11 234, <https://doi.org/10.5194/acp-13-11221-2013>, 2013.
- Arias, P., Bellouin, N., Coppola, E., Jones, R., Krinner, G., Marotzke, J., Naik, V., Palmer, M., Plattner, G.-K., Rogelj, J., Rojas, M., Sillmann, J., Storelvmo, T., Thorne, P., Trewin, B., Achuta Rao, K., Adhikary, B., Allan, R., Armour, K., Bala, G., Barimalala, R., Berger, S., Canadell, J., Cassou, C., Cherchi, A., Collins, W., Collins, W., Connors, S., Corti, S., Cruz, F., Dentener, F., Dereczynski, C., Di Luca, A., Diongue Niang, A., Doblas-Reyes, F., Dosio, A., Douville, H., Engelbrecht, F., Eyring, V., Fischer, E., Forster, P., Fox-Kemper, B., Fuglestvedt, J., Fyfe, J., Gillett, N., Goldfarb, L., Gorodetskaya, I., Gutierrez, J., Hamdi, R., Hawkins, E., Hewitt, H., Hope, P., Islam, A., Jones, C., Kaufman, D., Kopp, R., Kosaka, Y., Kossin, J., Krakovska, S., Lee, J.-Y., Li, J., Mauritsen, T., Maycock, T., Meinshausen, M., Min, S.-K., Monteiro, P., Ngo-Duc, T., Otto, F., Pinto, I., Pirani, A., Raghavan, K., Ranasinghe, R., Ruane, A., Ruiz, L., Sallee, J.-B., Samset, B., Sathyendranath, S., Seneviratne, S., Sorensen, A., Szopa, S., Takayabu, I., Treguier, A.-M., van den Hurk, B., Vautard, R., von Schuckmann, K., Zaehle, S., Zhang, X., and Zickfeld, K.: *Climate Change 2021: The Physical Science Basis. Contribution of Working Group I to the Sixth Assessment Report of the Intergovernmental Panel on Climate Change, Technical Summary*, Cambridge University Press, pp. 33–144, <https://doi.org/10.1017/9781009157896.002>, 2021.

- Assmann, W., Huber, H., Steinhausen, C., Dobler, M., Glückler, H., and Weidinger, A.: Elastic recoil detection analysis with heavy ions, *Nuclear Instruments and Methods in Physics Research Section B: Beam Interactions with Materials and Atoms*, 89, 131–139, [https://doi.org/10.1016/0168-583X\(94\)95159-4](https://doi.org/10.1016/0168-583X(94)95159-4), 1994.
- Ayers, G., Gillett, R., and Gras, J.: On the vapor pressure of sulfuric acid, *Geophys. Res. Lett.*, 7, 433–436, <https://doi.org/10.1029/GL007i006p00433>, 1980.
- Bala, G., Duffy, P. B., and Taylor, K. E.: Impact of geoengineering schemes on the global hydrological cycle, *Proceedings of the National Academy of Sciences*, 105, 7664–7669, <https://doi.org/10.1073/pnas.0711648105>, 2008.
- Banerjee, A., Butler, A. H., Polvani, L. M., Robock, A., Simpson, I. R., and Sun, L.: Robust winter warming over Eurasia under stratospheric sulfate geoengineering – the role of stratospheric dynamics, *Atmospheric Chemistry and Physics*, 21, 6985–6997, <https://doi.org/10.5194/acp-21-6985-2021>, 2021.
- Baran, A. J. and Foot, J. S.: New application of the operational sounder HIRS in determining a climatology of sulphuric acid aerosol from the Pinatubo eruption, *J. Geophys. Res.*, 99, 25 673–25 679, <https://doi.org/10.1029/94JD02044>, 1994.
- Bednarz, E. M., Butler, A. H., Vioni, D., Zhang, Y., Kravitz, B., and MacMartin, D. G.: Injection strategy – a driver of atmospheric circulation and ozone response to stratospheric aerosol geoengineering, *Atmospheric Chemistry and Physics*, 23, 13 665–13 684, <https://doi.org/10.5194/acp-23-13665-2023>, 2023.
- Benduhn, F., Schallock, J., and Lawrence, M. G.: Early growth dynamical implications for the steerability of stratospheric solar radiation management via sulfur aerosol particles, *Geophysical Research Letters*, 43, 9956–9963, <https://doi.org/10.1002/2016GL070701>, 2016.
- Biermann, F., Oomen, J., Gupta, A., Ali, S. H., Conca, K., Hajer, M. A., Kashwan, P., Kotze, L. J., Leach, M., Messner, D., Okereke, C., Persson, A., Potocnik, J., Schloberg, D., Scobie, M., and VanDeveer, S. D.: Solar geoengineering: The case for an international non-use agreement, *WIREs Climate Change*, 13, e754, <https://doi.org/10.1002/wcc.754>, 2022.
- Biermann, U. M., Presper, T., Koop, T., Mößinger, J., Crutzen, P. J., and Peter, T.: The unsuitability of meteoritic and other nuclei for polar stratospheric cloud freezing, *Geophysical Research Letters*, 23, 1693–1696, <https://doi.org/10.1029/96GL01577>, 1996.
- Blackstock, J. J., Battisti, D. S., Caldeira, K., Eardley, D. M., Katz, J. I., Keith, D. W., Patrinos, A. A. N., Schrag, D. P., Socolow, R. H., and Koonin, S. E.: Climate Engineering Responses to Climate Emergencies, <https://doi.org/10.48550/arXiv.0907.5140>, 2009.
- Bluth, G., Doiron, S., Schnetzler, C., Krueger, A., and Walter, L.: Global tracking of the SO<sub>2</sub> clouds from the June, 1991 Mount Pinatubo eruptions, *Geophysical Research Letters*, 19, <https://doi.org/10.1029/91GL02792>, 1992.
- Bohren, C. F. and Huffman, D. R.: *Absorption and scattering of light by small particles*, John Wiley & Sons, 2008.

- Boucher, O., Schwartz, S. E., Ackerman, T. P., Anderson, T. L., Bergstrom, B., Bonnel, B., Chýlek, P., Dahlback, A., Fouquart, Y., Fu, Q., Halthore, R. N., Haywood, J. M., Iversen, T., Kato, S., Kinne, S., Kirkevåg, A., Knapp, K. R., Lacis, A., Laszlo, I., Mishchenko, M. I., Nemesure, S., Ramaswamy, V., Roberts, D. L., Russell, P., Schlesinger, M. E., Stephens, G. L., Wagener, R., Wang, M., Wong, J., and Yang, F.: Intercomparison of models representing direct shortwave radiative forcing by sulfate aerosols, *Journal of Geophysical Research: Atmospheres*, 103, 16 979–16 998, <https://doi.org/10.1029/98JD00997>, 1998.
- Brasseur, G. and Solomon, S.: *Aeronomy of the middle atmosphere: chemistry and physics of the stratosphere and mesosphere.*, Aeronomy of the middle atmosphere: chemistry and physics of the stratosphere and mesosphere., 1984.
- Brodowsky, C., Sukhodolov, T., Feinberg, A., Hoepfner, M., Peter, T., Stenke, A., and Rozanov, E.: Modeling the Sulfate Aerosol Evolution After Recent Moderate Volcanic Activity, 2008–2012, *Journal of Geophysical Research: Atmospheres*, 126, e2021JD035 472, <https://doi.org/10.1029/2021JD035472>, 2021.
- Brodowsky, C. et al.: SOCOL-AERv2 model code, Zenodo, <https://doi.org/10.5281/zenodo.5733121>, 2018.
- Brodowsky, C. V., Sukhodolov, T., Chiodo, G., Aquila, V., Bekki, S., Dhomse, S. S., Laakso, A., Mann, G. W., Niemeier, U., Quaglia, I., Rozanov, E., Schmidt, A., Sekiya, T., Tilmes, S., Timmreck, C., Vattioni, S., Visionsi, D., Yu, P., Zhu, Y., and Peter, T.: Analysis of the global atmospheric background sulfur budget in a multi-model framework, *EGUsphere*, 2023, 1–49, <https://doi.org/10.5194/egusphere-2023-1655>, 2023.
- Budyko, M.: *Climatic Changes*, American Geophysical Union, Washington, DC, <https://doi.org/10.1029/SP010>, 1977.
- Budyko, M. I.: *Climate and Life*, Academic Press, New York, USA, 1974.
- Burkholder, J., Sander, S., Abbatt, J., Barker, J., Cappa, C., Crouse, J., Dibble, T., Huie, R., Kolb, C., Kurylo, M., Orkin, V., Percival, C., Wilmouth, D., and PH, W.: Chemical kinetics and photochemical data for use in atmospheric studies; evaluation number 19, Tech. Rep. 19-5, Pasadena, CA: Jet Propulsion Laboratory, National Aeronautics and Space, URL <http://jpldataeval.jpl.nasa.gov>, 2020.
- Burns, W. C.: Climate geoengineering: solar radiation management and its implications for intergenerational equity, *Stanford Journal of Law, Science & Policy*, 4, 39–55, 2011.
- Carslaw, K. S. and Peter, T.: Uncertainties in reactive uptake coefficients for solid stratospheric particles-1. Surface chemistry, *Geophysical Research Letters*, 24, 1743–1746, <https://doi.org/10.1029/97GL01683>, 1997.
- Chemnick, J.: U.S. Blocks U.N. Resolution on Geoengineering., *Scientific American*, URL <https://www.scientificamerican.com/article/u-s-blocks-u-n-resolution-on-geoengineering/>, 2019.
- Cirisan, A., Spichtinger, P., Luo, B. P., Weisenstein, D. K., Wernli, H., Lohmann, U., and Peter, T.: Microphysical and radiative changes in cirrus clouds by geoengineering the stratosphere, *Journal of Geophysical Research: Atmospheres*, 118, 4533–4548, <https://doi.org/10.1002/jgrd.50388>, 2013.



- Clark, P., Shakun, J., Marcott, S., Mix, A., Eby, M., Kulp, S., Levermann, A., Milne, G., Pfister, P., Santer, B., Schrag, D., Solomon, S., Stocker, T., Strauss, B., Weaver, A., Winkelmann, R., Archer, D., Bard, E., Goldner, A., and Plattner, G.-K.: Consequences of Twenty-First-Century Policy for Multi-Millennial Climate and Sea-Level Change, *Nature Climate Change*, 6, <https://doi.org/10.1038/nclimate2923>, 2016.
- Clyne, M., Lamarque, J.-F., Mills, M. J., Khodri, M., Ball, W., Bekki, S., Dhomse, S. S., Lebas, N., Mann, G., Marshall, L., Niemeier, U., Poulain, V., Robock, A., Rozanov, E., Schmidt, A., Stenke, A., Sukhodolov, T., Timmreck, C., Toohey, M., Tummon, F., Zanchettin, D., Zhu, Y., and Toon, O. B.: Model physics and chemistry causing intermodel disagreement within the VolMIP-Tambora Interactive Stratospheric Aerosol ensemble, *Atmospheric Chemistry and Physics*, 21, 3317–3343, <https://doi.org/10.5194/acp-21-3317-2021>, 2021.
- Corti, T. and Krieger, U. K.: Improved inverted bubble method for measuring small contact angles at crystal-solution-vapor interfaces, *Applied optics*, 46, 5835–5839, <https://doi.org/10.1364/ao.46.005835>, 2007.
- Crowley, J. N., Ammann, M., Cox, R. A., Hynes, R. G., Jenkin, M. E., Mellouki, A., Rossi, M. J., Troe, J., and Wallington, T. J.: Evaluated kinetic and photochemical data for atmospheric chemistry: Volume v -heterogeneous reactions on solid substrates, *Atmospheric Chemistry and Physics*, 10, <https://doi.org/10.5194/acp-10-9059-2010>, 2010.
- Crutzen, P.: Albedo Enhancement by Stratospheric Sulfur Injections: A Contribution to Resolve a Policy Dilemma?, *Climatic Change*, 77, 211–220, <https://doi.org/10.1007/s10584-006-9101-y>, 2006.
- Cziczo, D. J., Wolf, M. J., Gasparini, B., Münch, S., and Lohmann, U.: Unanticipated side effects of stratospheric albedo modification proposals due to aerosol composition and phase, *Scientific Reports*, 9, 18 825, <https://doi.org/10.1038/s41598-019-53595-3>, 2019.
- Dagon, K. and Schrag, D. P.: Quantifying the effects of solar geoengineering on vegetation, *Climatic Change*, 153, 235–251, <https://doi.org/10.1007/s10584-019-02387-9>, 2019.
- Dai, Z., Weisenstein, D. K., Keutsch, F. N., and Keith, D. W.: Experimental reaction rates constrain estimates of ozone response to calcium carbonate geoengineering, *Communications Earth & Environment*, 1, 63, <https://doi.org/10.1038/s43247-020-00058-7>, 2020.
- Danabasoglu, G., Lamarque, J.-F., Bacmeister, J., Bailey, D. A., DuVivier, A. K., Edwards, J., Emmons, L. K., Fasullo, J., Garcia, R., Gettelman, A., Hannay, C., Holland, M. M., Large, W. G., Lauritzen, P. H., Lawrence, D. M., Lenaerts, J. T. M., Lindsay, K., Lipscomb, W. H., Mills, M. J., Neale, R., Oleson, K. W., Otto-Bliesner, B., Phillips, A. S., Sacks, W., Tilmes, S., van Kampenhout, L., Vertenstein, M., Bertini, A., Dennis, J., Deser, C., Fischer, C., Fox-Kemper, B., Kay, J. E., Kinnison, D., Kushner, P. J., Larson, V. E., Long, M. C., Mickelson, S., Moore, J. K., Nienhouse, E., Polvani, L., Rasch, P. J., and Strand, W. G.: The Community Earth System Model Version 2 (CESM2), *Journal of Advances in Modeling Earth Systems*, 12, e2019MS001916, <https://doi.org/10.1029/2019MS001916>, 2020.

- Danilin, M. Y., Shia, R.-L., Ko, M. K. W., Weisenstein, D. K., Sze, N. D., Lamb, J. J., Smith, T. W., Lohn, P. D., and Prather, M. J.: Global stratospheric effects of the alumina emissions by solid-fueled rocket motors, *Journal of Geophysical Research: Atmospheres*, 106, 12 727–12 738, <https://doi.org/10.1029/2001JD900022>, 2001.
- Deshler, T.: A review of global stratospheric aerosol: Measurements, importance, life cycle, and local stratospheric aerosol, *Atmos. Res.*, 90, 223–232, <https://doi.org/10.1016/j.atmosres.2008.03.016>, 2008.
- Deshler, T., Luo, B., Kovilakam, M., Peter, T., and Kalnajs, L. E.: Retrieval of Aerosol Size Distributions From In Situ Particle Counter Measurements: Instrument Counting Efficiency and Comparisons With Satellite Measurements, *Journal of Geophysical Research: Atmospheres*, 124, 5058–5087, <https://doi.org/10.1029/2018JD029558>, 2019.
- Dessler, A. E., Schoeberl, M. R., Wang, T., Davis, S. M., and Rosenlof, K. H.: Stratospheric water vapor feedback, *Proceedings of the National Academy of Sciences*, 110, 18 087–18 091, <https://doi.org/10.1073/pnas.1310344110>, 2013.
- Döbeli, M., Kottler, C., Glaus, F., and Suter, M.: ERDA at the low energy limit, *Nuclear Instruments and Methods in Physics Research Section B: Beam Interactions with Materials and Atoms*, 241, 428–435, <https://doi.org/10.1016/j.nimb.2005.07.090>, the *Application of Accelerators in Research and Industry*, 2005.
- Dykema, J. A., Keith, D. W., Anderson, J. G., and Weisenstein, D.: Stratospheric controlled perturbation experiment: a small-scale experiment to improve understanding of the risks of solar geoengineering, *Philosophical Transactions of the Royal Society A: Mathematical, Physical and Engineering Sciences*, 372, 20140 059, <https://doi.org/10.1098/rsta.2014.0059>, 2014.
- Dykema, J. A., Keith, D. W., and Keutsch, F. N.: Improved aerosol radiative properties as a foundation for solar geoengineering risk assessment, *Geophysical Research Letters*, 43, 7758–7766, <https://doi.org/10.1002/2016GL069258>, 2016.
- Egorova, T., Rozanov, E., Zubov, V., and Karol, I. L.: Model for Investigating Ozone Trends (MEZON), *Izvestiya, Atmos. Oceanic Phys.*, 39, 277–292, 2003.
- Eichinger, R., Dietmüller, S., Garny, H., Šácha, P., Birner, T., Bönisch, H., Pitari, G., Visioni, D., Stenke, A., Rozanov, E., Revell, L., Plummer, D. A., Jöckel, P., Oman, L., Deushi, M., Kinnison, D. E., Garcia, R., Morgenstern, O., Zeng, G., Stone, K. A., and Schofield, R.: The influence of mixing on the stratospheric age of air changes in the 21st century, *Atmospheric Chemistry and Physics*, 19, 921–940, <https://doi.org/10.5194/acp-19-921-2019>, 2019.
- Eirini Goudeli, A. J. G. and Pratsinis, S. E.: Sampling and dilution of nanoparticles at high temperature, *Aerosol Science and Technology*, 50, 591–604, <https://doi.org/10.1080/02786826.2016.1168922>, 2016.
- English, J. M., Toon, O. B., Mills, M. J., and Yu, F.: Microphysical simulations of new particle formation in the upper troposphere and lower stratosphere, *Atmos. Chem. Phys.*, 11, 9303–9322, <https://doi.org/10.5194/acp-11-9303-2011>, 2011.

- Fathi, M., Hickel, S., and Roekaerts, D.: Large eddy simulations of reacting and non-reacting transcritical fuel sprays using multiphase thermodynamics, *Physics of Fluids*, 34, 085 131, <https://doi.org/10.1063/5.0099154>, 2022.
- Feinberg, A., Sukhodolov, T., Luo, B.-P., Rozanov, E., Winkel, L. H. E., Peter, T., and Stenke, A.: Improved tropospheric and stratospheric sulfur cycle in the aerosol–chemistry–climate model SOCOL-AERv2, *Geosci. Model Dev.*, 12, 3863–3887, <https://doi.org/10.5194/gmd-12-3863-2019>, 2019.
- Fenter, F. F., Caloz, F., and Rossi, M. J.: Experimental evidence for the efficient “dry deposition” of nitric acid on calcite, *Atmospheric Environment*, 29, [https://doi.org/10.1016/1352-2310\(95\)00183-Y](https://doi.org/10.1016/1352-2310(95)00183-Y), 1995.
- Fernandez, M. A., Hynes, R. G., and Cox, R. A.: Kinetics of ClONO<sub>2</sub> Reactive Uptake on Ice Surfaces at Temperatures of the Upper Troposphere, *The Journal of Physical Chemistry A*, 109, 9986–9996, <https://doi.org/10.1021/jp053477b>, 2005.
- Ferraro, A. J., Highwood, E. J., and Charlton-Perez, A. J.: Stratospheric heating by potential geoengineering aerosols, *Geophysical Research Letters*, 38, <https://doi.org/10.1029/2011GL049761>, 2011.
- Ferraro, A. J., Charlton-Perez, A. J., and Highwood, E. J.: Stratospheric dynamics and midlatitude jets under geoengineering with space mirrors and sulfate and titania aerosols, *Journal of Geophysical Research: Atmospheres*, 120, 414–429, <https://doi.org/10.1002/2014JD022734>, 2015.
- Field, C., Cheung, W. W. L., Dilling, L., Frumhoff, P. C., Greely, H., Hordequin, M. E., Hurrell, J., Light, A., Lin, A., MacMartin, D., McHenry, R., Moreno-Cruz, J., Ricke, K., Russell, L., Sagar, A., and Wennberg, P.: Reflecting Sunlight: Recommendations for Solar Geoengineering Research and Research Governance, National Academies of Sciences, Engineering, and Medicine, Washington, DC, United States, <https://doi.org/10.2172/1781700>, 2021.
- Forster, P. M., Fomichev, V. I., Rozanov, E., Cagnazzo, C., Jonsson, A. I., Langematz, U., Fomin, B., Iacono, M. J., Mayer, B., Mlawer, E., Myhre, G., Portmann, R. W., Akiyoshi, H., Falaleeva, V., Gillett, N., Karpechko, A., Li, J., Lemennais, P., Morgenstern, O., Oberlaender, S., Sigmund, M., and Shibata, K.: Evaluation of radiation scheme performance within chemistry climate models, *Journal of Geophysical Research: Atmospheres*, 116, <https://doi.org/10.1029/2010JD015361>, 2011.
- Forster, P. M., Richardson, T., Maycock, A. C., Smith, C. J., Samset, B. H., Myhre, G., Andrews, T., Pincus, R., and Schulz, M.: Recommendations for diagnosing effective radiative forcing from climate models for CMIP6, *Journal of Geophysical Research: Atmospheres*, 121, 12,460–12,475, <https://doi.org/10.1002/2016JD025320>, 2016.
- Fouquart, Y. and Bonnel, B.: Computations of solar heating of the Earth’s atmosphere: A new parameterization, 1980.
- Frank Ogletree, D., Bluhm, H., Hebenstreit, E. D., and Salmeron, M.: Photoelectron spectroscopy under ambient pressure and temperature conditions, *Nuclear Instruments and Methods in Physics Research Section A: Accelerators, Spectrometers, Detectors*

- and Associated Equipment, 601, 151–160, <https://doi.org/10.1016/j.nima.2008.12.155>, special issue in honour of Prof. Kai Siegbahn, 2009.
- Friedel, M., Chiodo, G., Stenke, A., Domeisen, D. I. V., and Peter, T.: Effects of Arctic ozone on the stratospheric spring onset and its surface impact, *Atmospheric Chemistry and Physics*, 22, 13 997–14 017, <https://doi.org/10.5194/acp-22-13997-2022>, 2022.
- Fuchs, N.: *The Mechanics of Aerosols*, Pergamon Press, Oxford, 1964.
- Fujii, Y.: The role of atmospheric nuclear explosions on the stagnation of global warming in the mid 20th century, *Journal of Atmospheric and Solar-Terrestrial Physics*, 73, 643–652, <https://doi.org/10.1016/j.jastp.2011.01.005>, 2011.
- Gao, K., Friebel, F., Zhou, C.-W., and Kanji, Z. A.: Enhanced soot particle ice nucleation ability induced by aggregate compaction and densification, *Atmospheric Chemistry and Physics*, 22, 4985–5016, <https://doi.org/10.5194/acp-22-4985-2022>, 2022.
- Ghosh, G.: Dispersion-equation coefficients for the refractive index and birefringence of calcite and quartz crystals, *Optics Communications*, 163, 95–102, [https://doi.org/10.1016/S0030-4018\(99\)00091-7](https://doi.org/10.1016/S0030-4018(99)00091-7), 1999.
- Goering, L.: Proposal for U.N. to study climate-cooling technologies rejected., Reuters, URL <https://www.reuters.com/article/us-environment-climatechange-geoengineer-idUSKCN1QV2RL>, 2019.
- Golden, D. M., Spokes, G. N., and Benson, S. W.: Very Low-Pressure Pyrolysis (VLPP); A Versatile Kinetic Tool, *Angewandte Chemie International Edition in English*, 12, <https://doi.org/10.1002/anie.197305341>, 1973.
- Goodman, A. L.: A laboratory study of the heterogeneous reaction of nitric acid on calcium carbonate particles, *Journal of Geophysical Research Atmospheres*, 105, 29 053–29 064, <https://doi.org/10.1029/2000JD900396>, 2000.
- Goudeli, E., Eggersdorfer, M. L., and Pratsinis, S. E.: Coagulation–Agglomeration of Fractal-like Particles: Structure and Self-Preserving Size Distribution, *Langmuir*, 31, 1320–1327, <https://doi.org/10.1021/la504296z>, pMID: 25560979, 2015.
- Greczynski, G. and Hultman, L.: A step-by-step guide to perform x-ray photoelectron spectroscopy, *Journal of Applied Physics*, 132, <https://doi.org/10.1063/5.0086359>, 2022.
- Gržinić, G., Bartels-Rausch, T., Birrer, M., Tuerler, A., and Ammann, M.: Production and use of  $^{13}\text{N}$  labeled  $\text{N}_2\text{O}_5$  to determine gas–aerosol interaction kinetics, *Radiochimica Acta*, 102, 1025–1034, <https://doi.org/doi:10.1515/ract-2014-2244>, 2014.
- Gu, L., Baldocchi, D., Verma, S. B., Black, T. A., Vesala, T., Falge, E. M., and Dowty, P. R.: Advantages of diffuse radiation for terrestrial ecosystem productivity, *Journal of Geophysical Research: Atmospheres*, 107, ACL 2–1–ACL 2–23, <https://doi.org/10.1029/2001JD001242>, 2002.
- Hanisch, F. and Crowley, J. N.: Heterogeneous Reactivity of Gaseous Nitric Acid on  $\text{Al}_2\text{O}_3$ ,  $\text{CaCO}_3$ , and Atmospheric Dust Samples: A Knudsen Cell Study, *The Journal of Physical Chemistry A*, 105, 3096–3106, <https://doi.org/10.1021/jp001254+>, 2001.

- Heckendorn, P., Weisenstein, D., Fueglistaler, S., Luo, B. P., Rozanov, E., Schraner, M., Thomason, L. W., and Peter, T.: The impact of geoengineering aerosols on stratospheric temperature and ozone, *Environmental Research Letters*, 4, <https://doi.org/10.1088/1748-9326/4/4/045108>, 2009.
- Heitjans, P. and Kärger, J.: Diffusion in condensed matter: Methods, materials, models, <https://doi.org/10.1007/3-540-30970-5>, 2005.
- Hoffman, R. C., Kaleuati, M. A., and Finlayson-Pitts, B. J.: Knudsen cell studies of the reaction of gaseous  $\text{HNO}_3$  with NaCl using less than a single layer of particles at 298 K: A modified mechanism, *Journal of Physical Chemistry A*, 107, <https://doi.org/10.1021/jp030611o>, 2003.
- Honegger, M., Münch, S., Hirsch, A., Beuttler, C., Peter, T., Burns, W., Geden, O., Goeschl, T., Gregorowius, D., Keith, D., Lederer, M., Michaelowa, A., Pasztor, J., Schäfer, S., Seneviratne, S. I., Stenke, A., Patt, A., and Wallimann-Helmer, I.: Climate change, negative emissions and solar radiation management: It is time for an open societal conversation, <https://doi.org/10.5167/uzh-137059>, 2017.
- Huynh, H. N. and McNeill, V. F.: Heterogeneous Chemistry of  $\text{CaCO}_3$  Aerosols with  $\text{HNO}_3$  and HCl, *Journal of Physical Chemistry A*, 124, 3886–3895, <https://doi.org/10.1021/acs.jpca.9b11691>, 2020.
- Huynh, H. N. and McNeill, V. F.: Heterogeneous Reactivity of HCl on  $\text{CaCO}_3$  Aerosols at Stratospheric Temperature, *ACS Earth and Space Chemistry*, 5, 1896–1901, <https://doi.org/10.1021/acsearthspacechem.1c00151>, 2021.
- Hynes, R. G., Fernandez, M. A., and Cox, R. A.: Uptake of  $\text{HNO}_3$  on water-ice and coadsorption of  $\text{HNO}_3$  and HCl in the temperature range 210–235 K, *Journal of Geophysical Research: Atmospheres*, 107, AAC 19–1–AAC 19–11, <https://doi.org/10.1029/2001JD001557>, 2002.
- IPCC: Summary for Policymakers. In: *Climate Change 2023: Synthesis Report. Contribution of Working Groups I, II and III to the Sixth Assessment Report of the Intergovernmental Panel on Climate Change* [Core Writing Team, H. Lee and J. Romero (eds.)], IPCC, <https://doi.org/10.59327/IPCC/AR6-9789291691647.001>, 2023.
- Jablonski, A. and Powell, C.: NIST Electron Inelastic-Mean-Free-Path Database, National Institute of Standards and Technology, Gaithersburg, 2010.
- Jackman, C. H., Conside, D. B., and Fleming, E. L.: A global modeling study of solid rocket aluminum oxide emission effects on stratospheric ozone, *Geophysical Research Letters*, 25, 907–910, <https://doi.org/10.1029/98GL00403>, 1998.
- Jacob, D. J.: Chemistry of OH in remote clouds and its role in the production of formic acid and peroxymonosulfate, *J. Geophys. Res.*, 91, 9807–9826, <https://doi.org/10.1029/JD091iD09p09807>, 1986.
- Jacobson, M. Z. and Seinfeld, J. H.: Evolution of nanoparticle size and mixing state near the point of emission, *Atmos. Environ.*, 38, 1839–1850, <https://doi.org/10.1016/j.atmosenv.2004.01.014>, 2004.

- Janssens, M., de Vries, I. E., Hulshoff, S., and 16-02, D.: A specialised delivery system for stratospheric sulphate aerosols: design and operation, *Climatic Change*, 162, 67–85, <https://doi.org/10.1007/s10584-020-02740-3>, 2020.
- Johnson, E. R., Sciegienka, J., Carlos-Cuellar, S., and Grassian, V. H.: Heterogeneous uptake of gaseous nitric acid on dolomite ( $\text{CaMg}(\text{CO}_3)_2$ ) and calcite ( $\text{CaCO}_3$ ) particles: A Knudsen cell study using multiple, single, and fractional particle layers, *Journal of Physical Chemistry A*, 109, <https://doi.org/10.1021/jp0516285>, 2005.
- Jones, A., Haywood, J. M., Scaife, A. A., Boucher, O., Henry, M., Kravitz, B., Lurton, T., Nabat, P., Niemeier, U., Séférian, R., Tilmes, S., and Visionsi, D.: The impact of stratospheric aerosol intervention on the North Atlantic and Quasi-Biennial Oscillations in the Geoengineering Model Intercomparison Project (GeoMIP) G6sulfur experiment, *Atmospheric Chemistry and Physics*, 22, 2999–3016, <https://doi.org/10.5194/acp-22-2999-2022>, 2022.
- Jones, A. C., Haywood, J. M., and Jones, A.: Climatic impacts of stratospheric geoengineering with sulfate, black carbon and titania injection, *Atmospheric Chemistry and Physics*, 16, 2843–2862, <https://doi.org/10.5194/acp-16-2843-2016>, 2016.
- Jouzel, J.: A brief history of ice core science over the last 50 yr, *Climate of the Past*, 9, 2525–2547, <https://doi.org/10.5194/cp-9-2525-2013>, 2013.
- Jungclaus, J. H., Fischer, N., Haak, H., Lohmann, K., Marotzke, J., Matei, D., Mikolajewicz, U., Notz, D., and von Storch, J. S.: Characteristics of the ocean simulations in the Max Planck Institute Ocean Model (MPIOM) the ocean component of the MPI-Earth system model, *Journal of Advances in Modeling Earth Systems*, 5, 422–446, <https://doi.org/10.1002/jame.20023>, 2013.
- Kanji, Z. A., Welti, A., Chou, C., Stetzer, O., and Lohmann, U.: Laboratory studies of immersion and deposition mode ice nucleation of ozone aged mineral dust particles, *Atmospheric Chemistry and Physics*, 13, 9097–9118, <https://doi.org/10.5194/acp-13-9097-2013>, 2013.
- Kasten, F.: Falling speed of aerosol particles, *J. Appl. Meteorol.*, 7, 944–947, [https://doi.org/10.1175/1520-0450\(1968\)007<0944:FSOAP>2.0.CO;2](https://doi.org/10.1175/1520-0450(1968)007<0944:FSOAP>2.0.CO;2), 1968.
- Keith, D. W.: GEOENGINEERING THE CLIMATE: History and Prospect, *Annual Review of Energy and the Environment*, 25, 245–284, <https://doi.org/10.1146/annurev.energy.25.1.245>, 2000.
- Keith, D. W. and Dowlatabadi, H.: a serious look at geoengineering, *Eos, Transactions American Geophysical Union*, 73, 289–293, <https://doi.org/10.1029/91EO00231>, 1992.
- Keith, D. W. and MacMartin, D. G.: A temporary, moderate and responsive scenario for solar geoengineering, <https://doi.org/10.1038/nclimate2493>, 2015.
- Keith, D. W., Weisenstein, D. K., Dykema, J. A., and Keutsch, F. N.: Stratospheric solar geoengineering without ozone loss, *Proceedings of the National Academy of Sciences of the United States of America*, 113, 14910–14914, <https://doi.org/10.1073/pnas.1615572113>, 2016.

- Kelesidis, G. A. and Goudeli, E.: Self-preserving size distribution and collision frequency of flame-made nanoparticles in the transition regime, *Proceedings of the Combustion Institute*, 38, 1233–1240, <https://doi.org/10.1016/j.proci.2020.07.147>, 2021.
- Kelesidis, G. A. and Kholghy, M. R.: A Monodisperse Population Balance Model for Nanoparticle Agglomeration in the Transition Regime, *Materials*, 14, <https://doi.org/10.3390/ma14143882>, 2021.
- Kelesidis, G. A. and Pratsinis, S. E.: Soot light absorption and refractive index during agglomeration and surface growth, *Proceedings of the Combustion Institute*, 37, 1177–1184, <https://doi.org/10.1016/j.proci.2018.08.025>, 2019.
- Kelesidis, G. A., Goudeli, E., and Pratsinis, S. E.: Flame synthesis of functional nanostructured materials and devices: Surface growth and aggregation, *Proceedings of the Combustion Institute*, 36, 29–50, <https://doi.org/10.1016/j.proci.2016.08.078>, 2017a.
- Kelesidis, G. A., Goudeli, E., and Pratsinis, S. E.: Morphology and mobility diameter of carbonaceous aerosols during agglomeration and surface growth, *Carbon*, 121, 527–535, <https://doi.org/10.1016/j.carbon.2017.06.004>, 2017b.
- Kelesidis, G. A., Kholghy, M. R., Zuercher, J., Robertz, J., Allemann, M., Duric, A., and Pratsinis, S. E.: Light scattering from nanoparticle agglomerates, *Powder Technology*, 365, 52–59, <https://doi.org/10.1016/j.powtec.2019.02.003>, sI: In honor of LS Fan, 2020.
- Kelesidis, G. A., Neubauer, D., Fan, L.-S., Lohmann, U., and Pratsinis, S. E.: Enhanced Light Absorption and Radiative Forcing by Black Carbon Agglomerates, *Environmental Science & Technology*, 56, 8610–8618, <https://doi.org/10.1021/acs.est.2c00428>, pMID: 35652563, 2022.
- Kelesidis, G. A., Benz, S., and Pratsinis, S. E.: Process design for carbon black size and morphology, *Carbon*, 213, 118 255, <https://doi.org/10.1016/j.carbon.2023.118255>, 2023.
- Kennedy, J. J., Rayner, N. A., Atkinson, C. P., and Killick, R. E.: An Ensemble Data Set of Sea Surface Temperature Change From 1850: The Met Office Hadley Centre HadSST.4.0.0.0 Data Set, *Journal of Geophysical Research: Atmospheres*, 124, 7719–7763, <https://doi.org/10.1029/2018JD029867>, 2019.
- Kerkweg, A., Buchholz, J., Ganzeveld, L., Pozzer, A., Tost, H., and Jöckel, P.: Technical Note: An implementation of the dry removal processes DRY DEPosition and SEDImentation in the Modular Earth Submodel System (MESSy), *Atmos. Chem. Phys.*, 6, 4617–4632, <https://doi.org/10.5194/acp-6-4617-2006>, 2006.
- Kerkweg, A., Buchholz, J., Ganzeveld, L., Pozzer, A., Tost, H., and Jöckel, P.: Corrigendum to “Technical Note: An implementation of the dry removal processes DRY DEPosition and SEDImentation in the Modular Earth Submodel System (MESSy)” published in *Atmos. Chem. Phys.*, 6, 4617–4632, 2006, *Atmos. Chem. Phys.*, 9, 9569–9569, <https://doi.org/10.5194/acp-9-9569-2009>, 2009.
- Keyser, L. F., Moore, S. B., and Leu, M. T.: Surface reaction and pore diffusion in flow-tube reactors, *Journal of Physical Chemistry*, 95, <https://doi.org/10.1021/j100167a026>, 1991.

- Kleidon, A., Kravitz, B., and Renner, M.: The hydrological sensitivity to global warming and solar geoengineering derived from thermodynamic constraints, *Geophysical Research Letters*, 42, 138–144, <https://doi.org/10.1002/2014GL062589>, 2015.
- Kleinschmitt, C., Boucher, O., and Platt, U.: Sensitivity of the radiative forcing by stratospheric sulfur geoengineering to the amount and strategy of the SO<sub>2</sub> injection studied with the LMDZ-S3A model, *Atmospheric Chemistry and Physics*, 18, 2769–2786, <https://doi.org/10.5194/acp-18-2769-2018>, 2018.
- Kokkola, H., Hommel, R., Kazil, J., Niemeier, U., Partanen, A.-I., Feichter, J., and Timmreck, C.: Aerosol microphysics modules in the framework of the ECHAM5 climate model – intercomparison under stratospheric conditions, *Geosci. Model Dev.*, 2, 97–112, <https://doi.org/10.5194/gmd-2-97-2009>, 2009.
- Kong, X., Waldner, A., Orlando, F., Artiglia, L., Huthwelker, T., Ammann, M., and Bartels-Rausch, T.: Coexistence of Physisorbed and Solvated HCl at Warm Ice Surfaces, *The Journal of Physical Chemistry Letters*, 8, 4757–4762, <https://doi.org/10.1021/acs.jpcclett.7b01573>, 2017.
- Kottler, C., Doebeli, M., Glaus, F., and Suter, M.: A spectrometer for low energy heavy ion ERDA, *Nuclear Instruments & Methods in Physics Research Section B-beam Interactions With Materials and Atoms - NUCL INSTRUM METH PHYS RES B*, 248, 155–162, <https://doi.org/10.1016/j.nimb.2006.02.013>, 2006.
- Kovilakam, M., Thomason, L. W., Ernest, N., Rieger, L., Bourassa, A., and Millán, L.: The Global Space-based Stratospheric Aerosol Climatology (version 2.0): 1979–2018, *Earth. Syst. Sci. Data*, 12, 2607–2634, doi: 10.5194/essd-12-2607-2020, 2020.
- Kravitz, B., Robock, A., Boucher, O., Schmidt, H., Taylor, K. E., Stenchikov, G., and Schulz, M.: The Geoengineering Model Intercomparison Project (GeoMIP), *Atmospheric Science Letters*, 12, 162–167, <https://doi.org/10.1002/asl.316>, 2011.
- Kravitz, B., MacMartin, D. G., and Caldeira, K.: Geoengineering: Whiter skies?, *Geophysical Research Letters*, 39, <https://doi.org/10.1029/2012GL051652>, 2012a.
- Kravitz, B., Robock, A., Shindell, D. T., and Miller, M. A.: Sensitivity of stratospheric geoengineering with black carbon to aerosol size and altitude of injection, *Journal of Geophysical Research: Atmospheres*, 117, <https://doi.org/10.1029/2011JD017341>, 2012b.
- Kravitz, B., MacMartin, D. G., Tilmes, S., Richter, J. H., Mills, M. J., Cheng, W., Dagon, K., Glanville, A. S., Lamarque, J.-F., Simpson, I. R., Tribbia, J., and Vitt, F.: Comparing Surface and Stratospheric Impacts of Geoengineering With Different SO<sub>2</sub> Injection Strategies, *Journal of Geophysical Research: Atmospheres*, 124, 7900–7918, <https://doi.org/10.1029/2019JD030329>, 2019.
- Kremser, S., Thomason, L. W., von Hobe, M., Hermann, M., Deshler, T., Timmreck, C., Toohey, M., Stenke, A., Schwarz, J. P., Weigel, R., Fueglistaler, S., Prata, F. J., Vernier, J.-P., Schlager, H., Barnes, J. E., Antuña-Marrero, J.-C., Fairlie, D., Palm, M., Mahieu, E., Notholt, J., Rex, M., Bingen, C., Vanhellefont, F., Bourassa, A., Plane, J. M. C., Klocke, D., Carn, S. A., Clarisse, L., Trickl, T., Neely, R., James, A. D., Rieger, L.,



- Wilson, J. C., and Meland, B.: Stratospheric aerosol – Observations, processes, and impact on climate, *Rev. Geophys.*, 54, 278–335, <https://doi.org/10.1002/2015RG000511>, 2016.
- Kuebbeler, M., Lohmann, U., and Feichter, J.: Effects of stratospheric sulfate aerosol geo-engineering on cirrus clouds, *Geophysical Research Letters*, 39, <https://doi.org/10.1029/2012GL053797>, 2012.
- Kulmala, M. and Laaksonen, A.: Binary nucleation of water–sulfuric acid system: Comparison of classical theories with different  $\text{H}_2\text{SO}_4$  saturation vapor pressures, *J. Chem. Phys.*, 93, 696–701, <https://doi.org/10.1063/1.459519>, 1990.
- Kuswanto, H., Kravitz, B., Miftahurrohman, B., Fauzi, F., Sopahaluwaken, A., and Moore, J.: Impact of solar geoengineering on temperatures over the Indonesian Maritime Continent, *International Journal of Climatology*, 42, 2795–2814, <https://doi.org/10.1002/joc.7391>, 2022.
- Laakso, A., Niemeier, U., Vioni, D., Tilmes, S., and Kokkola, H.: Dependency of the impacts of geoengineering on the stratospheric sulfur injection strategy – Part 1: Inter-comparison of modal and sectional aerosol modules, *Atmos. Chem. Phys.*, 22, 93–118, <https://doi.org/10.5194/acp-22-93-2022>, 2022.
- Lacis, A.: Volcanic aerosol radiative properties, *Past Global Changes Magazine*, 23, 50–51, <https://doi.org/10.22498/pages.23.2.50>, 2015.
- Laurent, B., Marticorena, B., Bergametti, G., Léon, J. F., and Mahowald, N. M.: Modeling mineral dust emissions from the Sahara desert using new surface properties and soil database, *Journal of Geophysical Research: Atmospheres*, 113, <https://doi.org/10.1029/2007JD009484>, 2008.
- Lesins, G., Chylek, P., and Lohmann, U.: A study of internal and external mixing scenarios and its effect on aerosol optical properties and direct radiative forcing, *Journal of Geophysical Research: Atmospheres*, 107, AAC 5–1–AAC 5–12, <https://doi.org/10.1029/2001JD000973>, 2002.
- Liu, Y. J., Zhu, T., Zhao, D. F., and Zhang, Z. F.: Investigation of the hygroscopic properties of  $\text{Ca}(\text{NO}_3)_2$  and internally mixed  $\text{Ca}(\text{NO}_3)_2/\text{CaCO}_3$  particles by micro-Raman spectrometry, *Atmospheric Chemistry and Physics*, 8, <https://doi.org/10.5194/acp-8-7205-2008>, 2008.
- Long, L., Querry, M., Bell, R., and Alexander, R.: Optical properties of calcite and gypsum in crystalline and powdered form in the infrared and far-infrared, *Infrared Physics*, 34, 191–201, [https://doi.org/10.1016/0020-0891\(93\)90008-U](https://doi.org/10.1016/0020-0891(93)90008-U), 1993.
- L’Ecuyer, J., Brassard, C., Cardinal, C., Chabbal, J., Deschênes, L., Labrie, J. P., Terreault, B., Martel, J. G., and St.-Jacques, R.: An accurate and sensitive method for the determination of the depth distribution of light elements in heavy materials, *Journal of Applied Physics*, 47, 381–382, <https://doi.org/10.1063/1.322288>, 1976.
- MacMartin, D. G., Caldeira, K., and Keith, D. W.: Solar geoengineering to limit the rate of temperature change, *Philosophical Transactions of the Royal Society A: Mathematical, Physical and Engineering Sciences*, 372, 20140134, <https://doi.org/10.1098/rsta.2014.0134>, 2014.

- MacMartin, D. G., Kravitz, B., Tilmes, S., Richter, J. H., Mills, M. J., Lamarque, J.-F., Tribbia, J. J., and Vitt, F.: The Climate Response to Stratospheric Aerosol Geoengineering Can Be Tailored Using Multiple Injection Locations, *Journal of Geophysical Research: Atmospheres*, 122, 512–574, <https://doi.org/10.1002/2017JD026868>, 2017.
- MacMartin, D. G., Ricke, K. L., and Keith, D. W.: Solar geoengineering as part of an overall strategy for meeting the 1.5°C Paris target, *Philosophical Transactions of the Royal Society A: Mathematical, Physical and Engineering Sciences*, 376, 20160454, <https://doi.org/10.1098/rsta.2016.0454>, 2018.
- MacMartin, D. G., Vioni, D., Kravitz, B., Richter, J., Felgenhauer, T., Lee, W. R., Morrow, D. R., Parson, E. A., and Sugiyama, M.: Scenarios for modeling solar radiation modification, *Proceedings of the National Academy of Sciences*, 119, e2202230119, <https://doi.org/10.1073/pnas.2202230119>, 2022.
- Maloney, C., Portmann, R., Rosenlof, K. H., and Bardeen, C.: Stratospheric loading and radiative impacts from increased Al<sub>2</sub>O<sub>3</sub> emission caused by an anticipated increase in satellite re-entry frequency, <https://doi.org/10.2514/6.2024-2169>.
- Mann, G. W., Carslaw, K. S., Ridley, D. A., Spracklen, D. V., Pringle, K. J., Merikanto, J., Korhonen, H., Schwarz, J. P., Lee, L. A., Manktelow, P. T., Woodhouse, M. T., Schmidt, A., Breider, T. J., Emmerson, K. M., Reddington, C. L., Chipperfield, M. P., and Pickering, S. J.: Intercomparison of modal and sectional aerosol microphysics representations within the same 3-D global chemical transport model, *Atmospheric Chemistry and Physics*, 12, 4449–4476, <https://doi.org/10.5194/acp-12-4449-2012>, 2012.
- Marshall, L., Schmidt, A., Toohey, M., Carslaw, K. S., Mann, G. W., Sigl, M., Khodri, M., Timmreck, C., Zanchettin, D., Ball, W. T., Bekki, S., Brooke, J. S. A., Dhomse, S., Johnson, C., Lamarque, J.-F., LeGrande, A. N., Mills, M. J., Niemeier, U., Pope, J. O., Poulain, V., Robock, A., Rozanov, E., Stenke, A., Sukhodolov, T., Tilmes, S., Tsigaridis, K., and Tummon, F.: Multi-model comparison of the volcanic sulfate deposition from the 1815 eruption of Mt. Tambora, *Atmospheric Chemistry and Physics*, 18, 2307–2328, <https://doi.org/10.5194/acp-18-2307-2018>, 2018.
- Matthew, J.: Surface analysis by Auger and x-ray photoelectron spectroscopy. D. Briggs and J. T. Grant (eds). IMPublications, Chichester, UK and SurfaceSpectra, Manchester, UK, 2003. 900 pp., ISBN 1-901019-04-7, 900 pp, *Surface and Interface Analysis*, 36, 1647–1647, <https://doi.org/10.1002/sia.2005>, 2004.
- Mätzler, C.: MATLAB functions for Mie scattering and absorption, version 2, URL <https://boris.unibe.ch/146550/1/199.pdf>, 2002.
- Mauritsen, T., Bader, J., Becker, T., Behrens, J., Bittner, M., Brokopf, R., Brovkin, V., Claussen, M., Crueger, T., Esch, M., Fast, I., Fiedler, S., Flaeschner, D., Gayler, V., Giorgetta, M., Goll, D. S., Haak, H., Hagemann, S., Hedemann, C., Hohenegger, C., Ilyina, T., Jahns, T., Jimenéz-de-la Cuesta, D., Jungclaus, J., Kleinen, T., Kloster, S., Kracher, D., Kinne, S., Kleberg, D., Lasslop, G., Kornblueh, L., Marotzke, J., Matei, D., Meraner, K., Mikolajewicz, U., Modali, K., Moebis, B., Mueller, W. A., Nabel, J. E. M. S., Nam, C. C. W., Notz, D., Nyawira, S.-S., Paulsen, H., Peters, K., Pincus, R., Pohlmann, H., Pongratz, J., Popp, M., Raddatz, T. J., Rast, S., Redler, R., Reick,

- C. H., Rohrschneider, T., Schemann, V., Schmidt, H., Schnur, R., Schulzweida, U., Six, K. D., Stein, L., Stemmler, I., Stevens, B., von Storch, J.-S., Tian, F., Voigt, A., Vrese, P., Wieners, K.-H., Wilkenskjeld, S., Winkler, A., and Roeckner, E.: Developments in the MPI-M Earth System Model version 1.2 (MPI-ESM1.2) and Its Response to Increasing CO<sub>2</sub>, *Journal of Advances in Modeling Earth Systems*, 11, 998–1038, <https://doi.org/10.1029/2018MS001400>, 2019.
- McLachlan Jr, D. and Cox, H. M.: Apparatus for measuring the contact angles at crystal-solution- vapor interfaces, *Review of Scientific Instruments*, 46, 80–83, <https://doi.org/10.1063/1.1134019>, 1975.
- Meehl, G. A., Washington, W. M., Arblaster, J. M., Hu, A., Teng, H., Kay, J. E., Gettelman, A., Lawrence, D. M., Sanderson, B. M., and Strand, W. G.: Climate change projections in CESM1(CAM5) compared to CCSM4, *J. Climate*, 26, 6287–6308, <https://doi.org/10.1175/JCLI-D-12-00572.1>, 2013.
- Mills, M. J., Schmidt, A., Easter, R., Solomon, S., Kinnison, D. E., Ghan, S. J., Neely III, R. R., Marsh, D. R., Conley, A., Bardeen, C. G., and Gettelman, A.: Global volcanic aerosol properties derived from emissions, 1990–2014, using CESM1(WACCM), *Journal of Geophysical Research: Atmospheres*, 121, 2332–2348, <https://doi.org/10.1002/2015JD024290>, 2016.
- Mlawer, E. J., Taubman, S. J., Brown, P. D., Iacono, M. J., and Clough, S. A.: Radiative transfer for inhomogeneous atmospheres: RRTM, a validated correlated-k model for the longwave, *J. Geophys. Res.*, 102, 6,663–16,682, <https://doi.org/10.1029/97JD00237>, 1997.
- Moallemi, A., Modini, R. L., Brem, B. T., Bertozzi, B., Giaccari, P., and Gysel-Beer, M.: Concept, absolute calibration, and validation of a new benchtop laser imaging polar nephelometer, *Atmospheric Measurement Techniques*, 16, 3653–3678, <https://doi.org/10.5194/amt-16-3653-2023>, 2023.
- Molina, M. J., Molina, L. T., Zhang, R., Meads, R. F., and Spencer, D. D.: The reaction of ClONO<sub>2</sub> with HCl on aluminum oxide, *Geophysical Research Letters*, 24, 1619–1622, <https://doi.org/10.1029/97GL01560>, 1997.
- Moon, D. R., Taverna, G. S., Anduix-Canto, C., Ingham, T., Chipperfield, M. P., Seakins, P. W., Baeza-Romero, M.-T., and Heard, D. E.: Heterogeneous reaction of HO<sub>2</sub> with airborne TiO<sub>2</sub> particles and its implication for climate change mitigation strategies, *Atmospheric Chemistry and Physics*, 18, 327–338, <https://doi.org/10.5194/acp-18-327-2018>, 2018.
- Ni, M. and Ratner, B. D.: Differentiating calcium carbonate polymorphs by surface analysis techniques—an XPS and TOF-SIMS study, *Surface and Interface Analysis*, 40, 1356–1361, <https://doi.org/10.1002/sia.2904>, 2008.
- Niemeier, U. and Timmreck, C.: What is the limit of climate engineering by stratospheric injection of SO<sub>2</sub>?, *Atmos. Chem. Phys.*, 15, 9129–9141, <https://doi.org/10.5194/acp-15-9129-2015>, 2015.

- Niemeier, U., Schmidt, H., and Timmreck, C.: The dependency of geoengineered sulfate aerosol on the emission strategy, *Atmospheric Science Letters*, 12, 189–194, <https://doi.org/10.1002/asl.304>, 2011.
- Niemeier, U., Schmidt, H., Alterskjær, K., and Kristjánsson, J. E.: Solar irradiance reduction via climate engineering: Impact of different techniques on the energy balance and the hydrological cycle, *Journal of Geophysical Research Atmospheres*, 118, 905–11, <https://doi.org/10.1002/2013JD020445>, 2013.
- NRC: National Research Council, *Climate Intervention: Reflecting Sunlight to Cool Earth*, The National Academies Press, Washington, DC, <https://doi.org/10.17226/18988>, 2015.
- Orlando, F., Waldner, A., Bartels-Rausch, T., Birrer, M., Kato, S., Lee, M.-T., Proff, C., Huthwelker, T., Kleibert, A., Van Bokhoven, J., et al.: The environmental photochemistry of oxide surfaces and the nature of frozen salt solutions: a new in situ XPS approach, *Topics in Catalysis*, 59, 591–604, <https://doi.org/10.1007/s11244-015-0515-5>, 2016.
- Orlando, F., Artiglia, L., Yang, H., Kong, X., Roy, K., Waldner, A., Chen, S., Bartels-Rausch, T., and Ammann, M.: Disordered Adsorbed Water Layers on TiO<sub>2</sub> Nanoparticles under Subsaturated Humidity Conditions at 235 K, *The Journal of Physical Chemistry Letters*, 10, 7433–7438, <https://doi.org/10.1021/acs.jpcllett.9b02779>, 2019.
- Ozolin, I. E.: Modeling diurnal variations of trace gases in the atmosphere and the procedure of diurnal averaging in photochemical models, *Akademiia Nauk SSSR Fizika Atmosfery i Okeana*, 28, 135–143, 1992.
- O’Neill, B., Kriegler, E., Ebi, K., Kemp-Benedict, E., Riahi, K., Rothman, D., van Ruijven, B., Vuuren, D., Birkmann, J., Kok, K., Levy, M., and Solecki, W.: The roads ahead: Narratives for shared socioeconomic pathways describing world futures in the 21st century, *Global Environmental Change*, 42, <https://doi.org/10.1016/j.gloenvcha.2015.01.004>, 2015.
- Pasztor, J.: The Need for Governance of Climate Geoengineering, *Ethics & International Affairs*, 31, 419–430, <https://doi.org/10.1017/S0892679417000405>, 2017.
- Pierce, J. R., Weisenstein, D. K., Heckendorn, P., Peter, T., and Keith, D. W.: Efficient formation of stratospheric aerosol for climate engineering by emission of condensable vapor from aircraft, *Geophys. Res. Lett.*, 37, <https://doi.org/10.1029/2010GL043975>, 2010.
- Pitari, G., Aquila, V., Kravitz, B., Robock, A., Watanabe, S., Cionni, I., Luca, N. D., Genova, G. D., Mancini, E., and Tilmes, S.: Stratospheric ozone response to sulfate geoengineering: Results from the Geoengineering Model Intercomparison Project (GeoMIP), *Journal of Geophysical Research: Atmospheres*, 119, 2629–2653, <https://doi.org/10.1002/2013JD020566>, 2014.
- Polyanin, A. D. and Manzhirov, A. V.: *Handbook of mathematics for engineers and scientists*, CRC Press, 2006.

- Pope, F. D., Braesicke, P., Grainger, R. G., Kalberer, M., Watson, I. M., Davidson, P. J., and Cox, R. A.: Stratospheric aerosol particles and solar-radiation management, <https://doi.org/10.1038/nclimate1528>, 2012.
- Potter, A. E.: Environmental effects of the Space Shuttle, *Journal of Environmental Sciences*, 21, 1978.
- Preston, C. J.: Ethics and geoengineering: reviewing the moral issues raised by solar radiation management and carbon dioxide removal, in: *The Ethics of Nanotechnology, Geoengineering, and Clean Energy*, pp. 269–283, Routledge, <https://doi.org/10.1002/wcc.198>, 2020.
- Prince, A. P., Kleiber, P., Grassian, V. H., and Young, M. A.: Heterogeneous interactions of calcite aerosol with sulfur dioxide and sulfur dioxide-nitric acid mixtures, *Physical Chemistry Chemical Physics*, 9, <https://doi.org/10.1039/b703296j>, 2007.
- Quaglia, I., Timmreck, C., Niemeier, U., Visionsi, D., Pitari, G., Brodowsky, C., Brühl, C., Dhomse, S. S., Franke, H., Laakso, A., Mann, G. W., Rozanov, E., and Sukhodolov, T.: Interactive stratospheric aerosol models' response to different amounts and altitudes of SO<sub>2</sub> injection during the 1991 Pinatubo eruption, *Atmospheric Chemistry and Physics*, 23, 921–948, <https://doi.org/10.5194/acp-23-921-2023>, 2023.
- Raabe, J., Tzvetkov, G., Flechsig, U., Böge, M., Jaggi, A., Sarafimov, B., Vernooij, M., Huthwelker, T., Ade, H., Kilcoyne, D., et al.: PolLux: A new facility for soft x-ray spectromicroscopy at the Swiss Light Source, *Review of scientific instruments*, 79, <https://doi.org/10.1063/1.3021472>, 2008.
- Rabitz, F.: Going rogue? Scenarios for unilateral geoengineering, *Futures*, 84, 98–107, <https://doi.org/10.1016/j.futures.2016.11.001>, 2016.
- Rahman, A. A., Artaxo, P., Asrat, A., and Parker, A.: Developing countries must lead on solar geoengineering research, *Nature*, 556, 22–24, <https://doi.org/10.1038/d41586-018-03917-8>, 2018.
- Rannou, P., McKay, C., Botet, R., and Cabane, M.: Semi-empirical model of absorption and scattering by isotropic fractal aggregates of spheres, *Planetary and Space Science*, 47, 385–396, [https://doi.org/10.1016/S0032-0633\(99\)00007-0](https://doi.org/10.1016/S0032-0633(99)00007-0), 1999.
- Revell, L. E., Stenke, A., Tummon, F., Feinberg, A., Rozanov, E., Peter, T., Abraham, N. L., Akiyoshi, H., Archibald, A. T., Butchart, N., Deushi, M., Jöckel, P., Kinnison, D., Michou, M., Morgenstern, O., O'Connor, F. M., Oman, L. D., Pitari, G., Plummer, D. A., Schofield, R., Stone, K., Tilmes, S., Visionsi, D., Yamashita, Y., and Zeng, G.: Tropospheric ozone in CCM1 models and Gaussian process emulation to understand biases in the SOCOLv3 chemistry–climate model, *Atmos. Chem. Phys.*, 18, 16155–16172, <https://doi.org/10.5194/acp-18-16155-2018>, 2018.
- Revell, L. E., Kuma, P., Le Ru, E. C., Somerville, W. R., and Gaw, S.: Direct radiative effects of airborne microplastics, *Nature*, 598, 462–467, 2021.
- Richter, J. H., Tilmes, S., Mills, M. J., Tribbia, J. J., Kravitz, B., Macmartin, D. G., Vitt, F., and Lamarque, J. F.: Stratospheric dynamical response and ozone feedbacks in the presence of SO<sub>2</sub> injections, *Journal of Geophysical Research: Atmospheres*, 122, 557–12, <https://doi.org/10.1002/2017JD026912>, 2017.

- Robock, A.: Volcanic eruptions and climate, *Reviews of Geophysics*, 38, 191–219, <https://doi.org/10.1029/1998RG000054>, 2000.
- Robock, A.: 20 Reasons Why Geoengineering May Be a Bad Idea, *Bulletin of The Atomic Scientists - BULL ATOM SCI*, 64, 14–18, <https://doi.org/10.2968/064002006>, 2008.
- Robock, A.: Stratospheric aerosol geoengineering, in: *AIP Conference Proceedings*, vol. 1652, pp. 183–197, American Institute of Physics Inc., <https://doi.org/10.1063/1.4916181>, 2015.
- Robock, A., Marquardt, A., Kravitz, B., and Stenchikov, G.: The Practicality Of Geoengineering, *Geophysical Research Letters*, 2009.
- Roeckner, E., Bäuml, G., Bonaventura, L., Brokopf, R., Esch, M., Giorgetta, M., Hagemann, S., Kirchner, I., Kornblueh, L., Manzini, E., Rhodin, A., Schlese, U., Schulzweida, U., and Tompkins, A.: The atmospheric general circulation model ECHAM 5. PART I: Model description, MPI-Report No. 349, Max-Planck-Institut für Meteorologie, Hamburg, URL [www.mpimet.mpg.de/fileadmin/publikationen/Reports/max\\_scirep\\_349.pdf](http://www.mpimet.mpg.de/fileadmin/publikationen/Reports/max_scirep_349.pdf), 2003.
- Roeckner, E., Brokopf, R., Esch, M., Giorgetta, M., Hagemann, S., Kornblueh, L., Manzini, E., Schlese, U., and Schulzweida, U.: Sensitivity of simulated climate to horizontal and vertical resolution in the ECHAM5 atmosphere model, *J. Climate*, 19, 3771–3791, <https://doi.org/10.1175/JCLI3824.1>, 2006.
- Rogak, S. N., Flagan, R. C., and Nguyen, H. V.: The Mobility and Structure of Aerosol Agglomerates, *Aerosol Science and Technology*, 18, 25–47, <https://doi.org/10.1080/02786829308959582>, 1993.
- Rogelj, J., Den Elzen, M., Höhne, N., Fransen, T., Fekete, H., Winkler, H., Schaeffer, R., Sha, F., Riahi, K., and Meinshausen, M.: Paris Agreement climate proposals need a boost to keep warming well below 2 C, *Nature*, 534, 631–639, <https://doi.org/10.1038/nature18307>, 2016.
- Romshoo, B., Müller, T., Pfeifer, S., Saturno, J., Nowak, A., Ciupek, K., Quincey, P., and Wiedensohler, A.: Optical properties of coated black carbon aggregates: numerical simulations, radiative forcing estimates, and size-resolved parameterization scheme, *Atmospheric Chemistry and Physics*, 21, 12989–13010, <https://doi.org/10.5194/acp-21-12989-2021>, 2021.
- Ross, M. N. and Sheaffer, P. M.: Radiative forcing caused by rocket engine emissions, *Earth’s Future*, 2, 177–196, <https://doi.org/10.1002/2013EF000160>, 2014.
- Rozanov, E. V., Zubov, V. A., Schlesinger, M. E., Yang, F., and Andronova, N. G.: The UIUC three-dimensional stratospheric chemical transport model: Description and evaluation of the simulated source gases and ozone, *J. Geophys. Res.*, 104, 11 755–11 781, <https://doi.org/10.1029/1999JD900138>, 1999.
- Rozanov, E. V., Schlesinger, M. E., and Zubov, V. A.: The University of Illinois, Urbana-Champaign three-dimensional stratosphere-troposphere general circulation model with interactive ozone photochemistry: Fifteen-year control run climatology,

- Journal of Geophysical Research: Atmospheres, 106, 27 233–27 254, <https://doi.org/10.1029/2000JD000058>, 2001.
- Santschi, C. and Rossi, M. J.: Uptake of CO<sub>2</sub>, SO<sub>2</sub>, HNO<sub>3</sub> and HCl on calcite (CaCO<sub>3</sub>) at 300 K: Mechanism and the role of adsorbed water, *Journal of Physical Chemistry A*, 110, <https://doi.org/10.1021/jp056312b>, 2006.
- Schäfer, S., Lawrence, M., Stelzer, H., Born, W., Low, S., Aaheim, A., Adriázola, P., Betz, G., Boucher, O., Carius, A., et al.: The European transdisciplinary assessment of climate engineering (EuTRACE): Removing greenhouse gases from the atmosphere and reflecting sunlight away from Earth, 2015.
- Seinfeld, J. H. and Pandis, S. N.: *Atmospheric Chemistry and Physics: From Air Pollution to Climate Change*, John Wiley & Sons Inc., 1997.
- Sheng, J., Weisenstein, D. K., Luo, B., Rozanov, E., Stenke, A., Anet, J., Bingemer, H., and Peter, T.: Global atmospheric sulfur budget under volcanically quiescent conditions: Aerosol-chemistry-climate model predictions and validation, *J. Geophys. Res.-Atmos.*, 120, 256–276, <https://doi.org/10.1002/2014JD021985>, 2015.
- Shepherd, J.: *Geoengineering the climate: science, governance and uncertainty*, Project report, URL <https://eprints.soton.ac.uk/156647/>, 2009.
- Shepherd, J. G.: *Geoengineering the climate: an overview and update*, *Philosophical Transactions of the Royal Society A: Mathematical, Physical and Engineering Sciences*, 370, 4166–4175, 2012.
- Shiraiwa, M., Pfrang, C., Koop, T., and Pöschl, U.: Kinetic multi-layer model of gas-particle interactions in aerosols and clouds (KM-GAP): linking condensation, evaporation and chemical reactions of organics, oxidants and water, *Atmospheric Chemistry and Physics*, 12, 2777–2794, <https://doi.org/10.5194/acp-12-2777-2012>, 2012.
- Simpson, I. R., Tilmes, S., Richter, J. H., Kravitz, B., MacMartin, D. G., Mills, M. J., Fasullo, J. T., and Pendergrass, A. G.: The Regional Hydroclimate Response to Stratospheric Sulfate Geoengineering and the Role of Stratospheric Heating, *Journal of Geophysical Research: Atmospheres*, 124, 12 587–12 616, <https://doi.org/10.1029/2019JD031093>, 2019.
- Smith, J. P., Dykema, J. A., and Keith, D. W.: Production of Sulfates Onboard an Aircraft: Implications for the Cost and Feasibility of Stratospheric Solar Geoengineering, *Earth and Space Science*, 5, 150–162, <https://doi.org/10.1002/2018EA000370>, 2018.
- Smith, W.: The cost of stratospheric aerosol injection through 2100, *Environmental Research Letters*, 15, 114 004, <https://doi.org/10.1088/1748-9326/aba7e7>, 2020.
- Solomon, S.: Stratospheric ozone depletion: A review of concepts and history, *Rev. Geophys.*, 37, 275–316, <https://doi.org/10.1029/1999RG900008>, 1999.
- Solomon, S., Stone, K., Yu, P., Murphy, D., Kinnison, D., Ravishankara, A., and Wang, P.: Chlorine activation and enhanced ozone depletion induced by wildfire aerosol, *Nature*, 615, 259–264, <https://doi.org/10.1038/s41586-022-05683-0>, 2023.

- Spyrogianni, A., Karadima, K. S., Goudeli, E., Mavrantzas, V. G., and Pratsinis, S. E.: Mobility and settling rate of agglomerates of polydisperse nanoparticles, *The Journal of chemical physics*, 148, <https://doi.org/10.1063/1.5012037>, 2018.
- Stahlbuhk, A.: Calcium chloride - Saltwiki, URL [https://saltwiki.net/index.php/Calcium\\_chloride](https://saltwiki.net/index.php/Calcium_chloride), accessed: 22.03.2022, 2016.
- Steiger, M., Charola, A. E., and Sterflinger, K.: *Weathering and Deterioration*, pp. 276–282, Springer Berlin Heidelberg, Berlin, Heidelberg, [https://doi.org/10.1007/978-3-642-14475-2\\_4](https://doi.org/10.1007/978-3-642-14475-2_4), 2011.
- Stenke, A., Schraner, M., Rozanov, E., Egorova, T., Luo, B., and Peter, T.: The SOCOL version 3.0 chemistry–climate model: description, evaluation, and implications from an advanced transport algorithm, *Geosci. Model Dev.*, 6, 1407–1427, <https://doi.org/10.5194/gmd-6-1407-2013>, 2013.
- Stenke, A., Vattioni, S., Chiodo, G., Luo, B., Sukhodolov, T., and Peter, T.: Simulation data for testing the aerosol microphysical scheme of SOCOL-AERv2, ETH Zurich, <https://doi.org/10.3929/ethz-b-000610854>, 2023.
- Stennett-Brown, R. K., Jones, J. J. P., Stephenson, T. S., and Taylor, M. A.: Future Caribbean temperature and rainfall extremes from statistical downscaling, *International Journal of Climatology*, 37, 4828–4845, <https://doi.org/10.1002/joc.5126>, 2017.
- Stephens, J. C. and Surprise, K.: The hidden injustices of advancing solar geoengineering research, *Global Sustainability*, 3, e2, <https://doi.org/10.1017/sus.2019.28>, 2020.
- Stevens, B., Giorgetta, M., Esch, M., Mauritsen, T., Crueger, T., Rast, S., Salzmann, M., Schmidt, H., Bader, J., Block, K., Brokopf, R., Fast, I., Kinne, S., Kornbluh, L., Lohmann, U., Pincus, R., Reichler, T., and Roeckner, E.: Atmospheric component of the MPI-M Earth System Model: ECHAM6, *Journal of Advances in Modeling Earth Systems*, 5, 146–172, <https://doi.org/10.1002/jame.20015>, 2013.
- Stier, P., Feichter, J., Kinne, S., Kloster, S., Vignati, E., Wilson, J., Ganzeveld, L., Tegen, I., Werner, M., Balkanski, Y., Schulz, M., Boucher, O., Minikin, A., and Petzold, A.: The aerosol-climate model ECHAM5-HAM, *Atmos. Chem. Phys.*, 5, 1125–1156, <https://doi.org/10.5194/acp-5-1125-2005>, 2005.
- Stipp, S. L. and Hochella, M. F.: Structure and bonding environments at the calcite surface as observed with X-ray photoelectron spectroscopy (XPS) and low energy electron diffraction (LEED), *Geochimica et Cosmochimica Acta*, 55, [https://doi.org/10.1016/0016-7037\(91\)90142-R](https://doi.org/10.1016/0016-7037(91)90142-R), 1991.
- Stott, P. A. and Harwood, R. S.: An implicit time-stepping scheme for chemical species in a global atmospheric circulation model, *Ann. Geophys.*, 11, 377–388, 1993.
- Sukhodolov, T., Sheng, J.-X., Feinberg, A., Luo, B.-P., Peter, T., Revell, L., Stenke, A., Weisenstein, D. K., and Rozanov, E.: Stratospheric aerosol evolution after Pinatubo simulated with a coupled size-resolved aerosol–chemistry–climate model, SOCOL-AERv1.0, *Geosci. Model Dev.*, 11, 2633–2647, <https://doi.org/10.5194/gmd-11-2633-2018>, 2018.



- Sukhodolov, T., Egorova, T., Stenke, A., Ball, W. T., Brodowsky, C., Chiodo, G., Feinberg, A., Friedel, M., Karagodin-Doyennel, A., Peter, T., Sedlacek, J., Vattioni, S., and Rozanov, E.: Atmosphere–ocean–aerosol–chemistry–climate model SOCOLv4.0: description and evaluation, *Geosci. Model Dev.*, 14, 5525–5560, <https://doi.org/10.5194/gmd-14-5525-2021>, 2021.
- Sullivan, R. C., Moore, M. J., Petters, M. D., Kreidenweis, S. M., Roberts, G. C., and Prather, K. A.: Timescale for hygroscopic conversion of calcite mineral particles through heterogeneous reaction with nitric acid, *Physical Chemistry Chemical Physics*, 11, <https://doi.org/10.1039/b904217b>, 2009.
- Sun, H., Eastham, S., and Keith, D.: Developing a Plume-in-Grid Model for Plume Evolution in the Stratosphere, *J. Adv. Model. Earth Syst.*, 14, e2021MS002816, <https://doi.org/10.1029/2021MS002816>, 2022.
- Sun, Z., Luo, S., Qi, P., and Fan, L. S.: Ionic diffusion through Calcite ( $\text{CaCO}_3$ ) layer during the reaction of CaO and  $\text{CO}_2$ , *Chemical Engineering Science*, 81, <https://doi.org/10.1016/j.ces.2012.05.042>, 2012.
- Szerszynski, B., Kearnes, M., Macnaghten, P., Owen, R., and Stilgoe, J.: Why Solar Radiation Management Geoengineering and Democracy Won't Mix, *Environment and Planning A: Economy and Space*, 45, 2809–2816, <https://doi.org/10.1068/a45649>, 2013.
- Tabazadeh, A. and Turco, R. P.: A model for heterogeneous chemical processes on the surfaces of ice and nitric acid trihydrate particles, *Journal of Geophysical Research: Atmospheres*, 98, 12 727–12 740, <https://doi.org/10.1029/93JD00947>, 1993.
- Tabazadeh, A., Toon, O. B., Clegg, S. L., and Hamill, P.: A new parameterization of  $\text{H}_2\text{SO}_4/\text{H}_2\text{O}$  aerosol composition: Atmospheric implications, *Geophys. Res. Lett.*, 24, 1931–1934, <https://doi.org/10.1029/97GL01879>, 1997.
- Tang, M., Keeble, J., Telford, P. J., Pope, F. D., Braesicke, P., Griffiths, P. T., Abraham, N. L., McGregor, J., Watson, I. M., Cox, R. A., Pyle, J. A., and Kalberer, M.: Heterogeneous reaction of  $\text{ClONO}_2$  with  $\text{TiO}_2$  and  $\text{SiO}_2$  aerosol particles: implications for stratospheric particle injection for climate engineering, *Atmospheric Chemistry and Physics*, 16, 15 397–15 412, <https://doi.org/10.5194/acp-16-15397-2016>, 2016.
- Tang, M. J., Telford, P. J., Pope, F. D., Rkiouak, L., Abraham, N. L., Archibald, A. T., Braesicke, P., Pyle, J. A., McGregor, J., Watson, I. M., Cox, R. A., and Kalberer, M.: Heterogeneous reaction of  $\text{N}_2\text{O}_5$  with airborne  $\text{TiO}_2$  particles and its implication for stratospheric particle injection, *Atmospheric Chemistry and Physics*, 14, 6035–6048, <https://doi.org/10.5194/acp-14-6035-2014>, 2014.
- Taylor, K. E., Williamson, D., and Zwiers, F.: The sea surface temperature and sea ice concentration boundary conditions for AMIP II simulations, Program for Climate Model Diagnosis and Intercomparison, PCMDI report 60, Lawrence Livermore National Laboratory, URL <https://pcmdi.llnl.gov/report/pdf/60.pdf?id=32>, (last access: 3 January 2023), 2000.
- Teller, E., Wood, L., and Hyde, R.: Global warming and ice ages: I. Prospects for physics-based modulation of global change, Tech. rep., Lawrence Livermore National Lab., 1996.

- Thomason, L. and Peter, T.: SPARC Assessment of Stratospheric Aerosol Properties (ASAP), SPARC Report No. 4, WCRP-124,WMO/TD-No. 1295, Stratospheric Processes And their Role in Climate (SPARC), URL <http://www.sparc-climate.org/publications/sparc-reports/>, (last access: 18 January 2023), 2006.
- Thomason, L. W., Ernest, N., Millán, L., Rieger, L., Bourassa, A., Vernier, J.-P., Manney, G., Luo, B., Arfeuille, F., and Peter, T.: A global space-based stratospheric aerosol climatology: 1979–2016, *Earth Syst. Sci. Data*, 10, 469–492, <https://doi.org/10.5194/essd-10-469-2018>, 2018.
- Tilmes, S., Müller, R., and Salawitch, R.: The Sensitivity of Polar Ozone Depletion to Proposed Geoengineering Schemes, *Science*, 349, 1201–1204, <https://doi.org/10.1126/science.1153966>, 2008.
- Tilmes, S., Fasullo, J., Lamarque, J.-F., Marsh, D. R., Mills, M., Alterskjær, K., Muri, H., Kristjánsson, J. E., Boucher, O., Schulz, M., Cole, J. N. S., Curry, C. L., Jones, A., Haywood, J., Irvine, P. J., Ji, D., Moore, J. C., Karam, D. B., Kravitz, B., Rasch, P. J., Singh, B., Yoon, J.-H., Niemeier, U., Schmidt, H., Robock, A., Yang, S., and Watanabe, S.: The hydrological impact of geoengineering in the Geoengineering Model Intercomparison Project (GeoMIP), *Journal of Geophysical Research: Atmospheres*, 118, 11,036–11,058, <https://doi.org/10.1002/jgrd.50868>, 2013.
- Tilmes, S., Richter, J. H., Mills, M. J., Kravitz, B., MacMartin, D. G., Vitt, F., Tribbia, J. J., and Lamarque, J.-F.: Sensitivity of Aerosol Distribution and Climate Response to Stratospheric SO<sub>2</sub> Injection Locations, *Journal of Geophysical Research: Atmospheres*, 122, 512–591, <https://doi.org/doi:10.1002/2017JD026888>, 2017.
- Tilmes, S., Richter, J. H., Kravitz, B., Macmartin, D. G., Mills, M. J., Simpson, I. R., Glanville, A. S., Fasullo, J. T., Phillips, A. S., Lamarque, J. F., Tribbia, J., Edwards, J., Mickelson, S., and Ghosh, S.: CESM1(WACCM) stratospheric aerosol geoengineering large ensemble project, *Bulletin of the American Meteorological Society*, 99, 2361–2371, <https://doi.org/10.1175/BAMS-D-17-0267.1>, 2018.
- Tilmes, S., Visioni, D., Jones, A., Haywood, J., Séférian, R., Nabat, P., Boucher, O., Bednarz, E. M., and Niemeier, U.: Stratospheric ozone response to sulfate aerosol and solar dimming climate interventions based on the G6 Geoengineering Model Intercomparison Project (GeoMIP) simulations, *Atmospheric Chemistry and Physics*, 22, 4557–4579, <https://doi.org/10.5194/acp-22-4557-2022>, 2022.
- Timmreck, C., Mann, G. W., Aquila, V., Hommel, R., Lee, L. A., Schmidt, A., Brühl, C., Carn, S., Chin, M., Dhomse, S. S., Diehl, T., English, J. M., Mills, M. J., Neely, R., Sheng, J., Toohey, M., and Weisenstein, D.: The Interactive Stratospheric Aerosol Model Intercomparison Project (ISA-MIP): motivation and experimental design, *Geosci. Model Dev.*, 11, 2581–2608, <https://doi.org/10.5194/gmd-11-2581-2018>, 2018.
- Tollefson, J.: Geoengineering debate shifts to UN environment assembly, *Nature*, 567, 156–157, <https://doi.org/10.1038/d41586-019-00717-6>, 2019.

- Tost, H., Jöckel, P., Kerkweg, A., Sander, R., and Lelieveld, J.: Technical note: A new comprehensive SCAVenging submodel for global atmospheric chemistry modelling, *Atmos. Chem. Phys.*, 6, 565–574, <https://doi.org/10.5194/acp-6-565-2006>, 2006.
- Tost, H., Jöckel, P., Kerkweg, A., Pozzer, A., Sander, R., and Lelieveld, J.: Global cloud and precipitation chemistry and wet deposition: tropospheric model simulations with ECHAM5/MESSy1, *Atmos. Chem. Phys.*, 7, 2733–2757, <https://doi.org/10.5194/acp-7-2733-2007>, 2007.
- Tropf, W. J. and Thomas, M. E.: - Aluminum Oxide ( $\text{Al}_2\text{O}_3$ ) Revisited, in: *Handbook of Optical Constants of Solids*, edited by Palik, E. D., pp. 653–682, Academic Press, Burlington, <https://doi.org/10.1016/B978-012544415-6.50124-2>, 1997.
- Tsipiras, K. and Grant, W. J.: What do we mean when we talk about the moral hazard of geoengineering?, *Environmental Law Review*, 24, 27–44, <https://doi.org/10.1177/14614529211069839>, 2022.
- Underwood, G. M., Li, P., Usher, C. R., and Grassian, V. H.: Determining Accurate Kinetic Parameters of Potentially Important Heterogeneous Atmospheric Reactions on Solid Particle Surfaces with a Knudsen Cell Reactor, *Journal of Physical Chemistry A*, 104, <https://doi.org/10.1021/jp9930292>, 2000.
- Vattioni, S.: Data for: "Chemical impact of stratospheric alumina particle injection for solar radiation modification and related uncertainties" [Dataset], ETH Zurich, URL [10.3929/ethz-b-000626837](https://doi.org/10.3929/ethz-b-000626837), 2023a.
- Vattioni, S.: SOCOL-AER\_solid\_particles [Software], <https://doi.org/10.5281/zenodo.8398627>, 2023b.
- Vattioni, S.: Simulation data for "A fully coupled solid particle microphysics scheme for stratospheric aerosol injections within the aerosol-chemistry-climate-model SOCOL-AERv2", ETH Zurich, <https://doi.org/10.3929/ethz-b-000659234>, 2024a.
- Vattioni, S.: Simulation data for: Risks and benefits of stratospheric solar climate intervention via solid particle injections, ETH Zurich, <https://doi.org/10.3929/ethz-b-000670453>, 2024b.
- Vattioni, S., Weisenstein, D., Keith, D., Feinberg, A., Peter, T., and Stenke, A.: Exploring accumulation-mode  $\text{H}_2\text{SO}_4$  versus  $\text{SO}_2$  stratospheric sulfate geoengineering in a sectional aerosol-chemistry-climate model, *Atmos. Chem. Phys.*, 19, 4877–4897, <https://doi.org/10.5194/acp-19-4877-2019>, 2019.
- Vattioni, S., Luo, Beiping, F. A., Andrea, S., Vockenhuber, C., Weber, R., Dykema, J. A., Krieger, U., Ammann, M., Keutsch, F., and Peter, T.: Chemical impact of stratospheric alumina particle injection for solar radiation modification and related uncertainties, *Geophysical Research Letters*, <https://doi.org/10.1029/2023GL105889>, 2023a.
- Vattioni, S., Stenke, A., Chiodo, G., Luo, B., Sukhodolov, T., and Peter, T.: Simulation data for testing the aerosol microphysical scheme of SOCOL-AERv2, ETH Zurich, <https://doi.org/10.3929/ethz-b-000622193>, 2023b.

- Vehkamäki, H., Kulmala, M., Napari, I., Lehtinen, K. E. J., Timmreck, C., Noppel, M., and Laaksonen, A.: An improved parameterization for sulfuric acid–water nucleation rates for tropospheric and stratospheric conditions, *J. Geophys. Res.*, 107, AAC 3–1–AAC 3–10, <https://doi.org/10.1029/2002JD002184>, 2002.
- Visioni, D., Pitari, G., Aquila, V., Tilmes, S., Cionni, I., Di Genova, G., and Mancini, E.: Sulfate geoengineering impact on methane transport and lifetime: Results from the geoengineering model intercomparison project (GeoMIP), *Atmospheric Chemistry and Physics*, 17, 11 209–11 226, <https://doi.org/10.5194/acp-17-11209-2017>, 2017.
- Visioni, D., Pitari, G., di Genova, G., Tilmes, S., and Cionni, I.: Upper tropospheric ice sensitivity to sulfate geoengineering, *Atmospheric Chemistry and Physics*, 18, 14 867–14 887, <https://doi.org/10.5194/acp-18-14867-2018>, 2018.
- Visioni, D., Slessarev, E., Macmartin, D. G., Mahowald, N. M., Goodale, C. L., and Xia, L.: What goes up must come down: Impacts of deposition in a sulfate geoengineering scenario, *Environmental Research Letters*, 15, <https://doi.org/10.1088/1748-9326/ab94eb>, 2020.
- Visioni, D., MacMartin, D. G., Kravitz, B., Boucher, O., Jones, A., Lurton, T., Martine, M., Mills, M. J., Nabat, P., Niemeier, U., Séférian, R., and Tilmes, S.: Identifying the sources of uncertainty in climate model simulations of solar radiation modification with the G6sulfur and G6solar Geoengineering Model Intercomparison Project (GeoMIP) simulations, *Atmospheric Chemistry and Physics*, 21, 10 039–10 063, <https://doi.org/10.5194/acp-21-10039-2021>, 2021.
- Visioni, D., Kravitz, B., Robock, A., Tilmes, S., Haywood, J., Boucher, O., Lawrence, M., Irvine, P., Niemeier, U., Xia, L., Chiodo, G., Lennard, C., Watanabe, S., Moore, J. C., and Muri, H.: Opinion: The scientific and community-building roles of the Geoengineering Model Intercomparison Project (GeoMIP) – past, present, and future, *Atmospheric Chemistry and Physics*, 23, 5149–5176, <https://doi.org/10.5194/acp-23-5149-2023>, 2023.
- Vlasenko, A., Sjogren, S., Weingartner, E., Stemmler, K., Gäggeler, H. W., and Ammann, M.: Effect of humidity on nitric acid uptake to mineral dust aerosol particles, *Atmospheric Chemistry and Physics*, 6, <https://doi.org/10.5194/acp-6-2147-2006>, 2006.
- Vlasenko, A., Huthwelker, T., Gäggeler, H. W., and Ammann, M.: Kinetics of the heterogeneous reaction of nitric acid with mineral dust particles: an aerosol flowtube study, *Phys. Chem. Chem. Phys.*, 11, 7921–7930, <https://doi.org/10.1039/B904290N>, 2009.
- Walcek, C. J.: Minor flux adjustment near mixing ratio extremes for simplified yet highly accurate monotonic calculation of tracer advection, *J. Geophys. Res.*, 105, 9335–9348, <https://doi.org/10.1029/1999JD901142>, 2000.
- Wan, H., Rasch, P. J., Zhang, K., Kazil, J., and Leung, L. R.: Numerical issues associated with compensating and competing processes in climate models: an example from ECHAM-HAM, *Geosci. Model Dev.*, 6, 861–874, <https://doi.org/10.5194/gmd-6-861-2013>, 2013.

- Wang, Y., Su, H., Jiang, J. H., Livesey, N. J., Santee, M. L., Froidevaux, L., Read, W. G., and Anderson, J.: The linkage between stratospheric water vapor and surface temperature in an observation-constrained coupled general circulation model, *Climate dynamics*, 48, 2671–2683, <https://doi.org/10.1007/s00382-016-3231-3>, 2017.
- Weisenstein, D. K., Yue, G. K., Ko, M. K., Sze, N., Rodriguez, J. M., and Scott, C. J.: A two-dimensional model of sulfur species and aerosols, *J. Geophys. Res.*, 102, 13 019–13 035, <https://doi.org/10.1029/97JD00901>, 1997.
- Weisenstein, D. K., Penner, J. E., Herzog, M., and Liu, X.: Global 2-d intercomparison of sectional and modal aerosol modules, *Atmos. Chem. Phys.*, 7, 2339–2355, <https://doi.org/10.5194/acp-7-2339-2007>, 2007.
- Weisenstein, D. K., Keith, D. W., and Dykema, J. A.: Solar geoengineering using solid aerosol in the stratosphere, *Atmospheric Chemistry and Physics*, 15, 11 835–11 859, <https://doi.org/10.5194/acp-15-11835-2015>, 2015.
- Weisenstein, D. K., Vioni, D., Franke, H., Niemeier, U., Vattioni, S., Chiodo, G., Peter, T., and Keith, D. W.: An interactive stratospheric aerosol model intercomparison of solar geoengineering by stratospheric injection of SO<sub>2</sub> or accumulation-mode sulfuric acid aerosols, *Atmos. Chem. Phys.*, 22, 2955–2973, <https://doi.org/10.5194/acp-22-2955-2022>, 2022.
- Wesely, M.: Parameterization of surface resistances to gaseous dry deposition in regional-scale numerical models, *Atmospheric Environment*, 41, 52–63, <https://doi.org/10.1016/j.atmosenv.2007.10.058>, 1989.
- Wieners, C. E., Hofbauer, B. P., de Vries, I. E., Honegger, M., Vioni, D., Russchenberg, H. W. J., and Felgenhauer, T.: Solar radiation modification is risky, but so is rejecting it: a call for balanced research, *Oxford Open Climate Change*, 3, kgad002, <https://doi.org/10.1093/oxfclm/kgad002>, 2023.
- Wilson, J. C., Jonsson, H. H., Brock, C. A., Toohey, D. W., Avallone, L. M., Baumgardner, D., Dye, J. E., Poole, L. R., Woods, D. C., DeCoursey, R. J., Osborn, M., Pitts, M. C., Kelly, K. K., Chan, K. R., Ferry, G. V., Loewenstein, M., Podolske, J. R., and Weaver, A.: In Situ Observations of Aerosol and Chlorine Monoxide After the 1991 Eruption of Mount Pinatubo: Effect of Reactions on Sulfate Aerosol, *Science*, 261, 1140–1143, <https://doi.org/10.1126/science.261.5125.1140>, 1993.
- Winickoff, D. E., Flegal, J. A., and Asrat, A.: Engaging the Global South on climate engineering research, *Nature Climate Change*, 5, 627–634, <https://doi.org/10.1038/nclimate2632>, 2015.
- WMO: Scientific Assessment of Ozone Depletion: 2018, Global Ozone Research and Monitoring Project, World Meteorological Organization, Report No. 278, 509, 2018.
- WMO: Scientific Assessment of Ozone Depletion: 2022, Global Ozone Research and Monitoring Project, World Meteorological Organization, Report No. 278, 509, 2022.
- Xia, L., Robock, A., Tilmes, S., and Neely, R. R.: Stratospheric sulfate geoengineering could enhance the terrestrial photosynthesis rate, *Atmospheric Chemistry and Physics*, 16, 1479–1489, <https://doi.org/10.5194/acp-16-1479-2016>, 2016.

- Xiao, C., Shi, P., Yan, W., Chen, L., Qian, L., and Kim, S. H.: Thickness and structure of adsorbed water layer and effects on adhesion and friction at nanoasperity contact, <https://doi.org/10.3390/colloids3030055>, 2019.
- Xiaoyu, T., Zhenshan, L., Fan, F., Ningsheng, C., and Haitao, Y.: AFM investigation of the morphology of CaSO<sub>4</sub> product layer formed during direct sulfation on polished single-crystal CaCO<sub>3</sub> surfaces at high CO<sub>2</sub> concentrations, *Proceedings of the Combustion Institute*, 33, <https://doi.org/10.1016/j.proci.2010.07.075>, 2011.
- Yang, H., Boucly, A., Gabathuler, J. P., Bartels-Rausch, T., Artiglia, L., and Ammann, M.: Ordered Hydrogen Bonding Structure of Water Molecules Adsorbed on Silver Iodide Particles under Subsaturated Conditions, *The Journal of Physical Chemistry C*, 125, 11 628–11 635, <https://doi.org/10.1021/acs.jpcc.1c01767>, 2021.
- Yeh, J.: Atomic Calculation of Photoionization Cross-Section and Asymmetry Parameters Gordon and Breach Science Publishers, Gordon and Breach Science Publishers, Langhorne, PE (USA), <https://doi.org/10.1002/rcm.1290080716>, 1993.
- Yeh, J. and Lindau, I.: Atomic subshell photoionization cross sections and asymmetry parameters:  $1 \leq Z \leq 103$ , *Atomic Data and Nuclear Data Tables*, 32, 1–155, [https://doi.org/10.1016/0092-640X\(85\)90016-6](https://doi.org/10.1016/0092-640X(85)90016-6), 1985.
- Yu, F., Nadykto, A. B., Luo, G., and Herb, J.: H<sub>2</sub>SO<sub>4</sub>–H<sub>2</sub>O binary and H<sub>2</sub>SO<sub>4</sub>–H<sub>2</sub>O–NH<sub>3</sub> ternary homogeneous and ion-mediated nucleation: lookup tables version 1.0 for 3-D modeling application, *Geosci. Model Dev.*, 13, 2663–2670, <https://doi.org/10.5194/gmd-13-2663-2020>, 2020.
- Yu, F., Luo, G., Nair, A. A., Eastham, S., Williamson, C. J., Kupc, A., and Brock, C. A.: Particle number concentrations and size distributions in the stratosphere: implications of nucleation mechanisms and particle microphysics, *Atmos. Chem. Phys.*, 23, 1863–1877, <https://doi.org/10.5194/acp-23-1863-2023>, 2023.
- Yue, G., Poole, L., Wang, P.-H., and Chiou, E.: Stratospheric aerosol acidity, density, and refractive index deduced from SAGE II and NMC temperature data, *Journal of Geophysical Research: Atmospheres*, 99, 3727–3738, <https://doi.org/10.1029/93JD02989>, 1994.
- Zarnetske, P. L., Gurevitch, J., Franklin, J., Groffman, P. M., Harrison, C. S., Hellmann, J. J., Hoffman, F. M., Kothari, S., Robock, A., Tilmes, S., Vioni, D., Wu, J., Xia, L., and Yang, C.-E.: Potential ecological impacts of climate intervention by reflecting sunlight to cool Earth, *Proceedings of the National Academy of Sciences*, 118, e1921854 118, <https://doi.org/10.1073/pnas.1921854118>, 2021.
- Zhu, F., Zhou, H., Wang, X., Zhou, Y., Liu, H., Fang, C., and Fang, Y.: Raman spectroscopy and ab initio quantum chemical calculations of ion association behavior in calcium nitrate solution, *Journal of Raman Spectroscopy*, 49, 852–861, <https://doi.org/10.1002/jrs.5349>, 2018.
- Zimmermann, S., Kippenberger, M., Schuster, G., and Crowley, J. N.: Adsorption isotherms for hydrogen chloride (HCl) on ice surfaces between 190 and 220 K, *Phys. Chem. Chem. Phys.*, 18, 13 799–13 810, <https://doi.org/10.1039/C6CP01962E>, 2016.

## Thanks and acknowledgements

The project presented could only be realized with significant contributions and support from countless colleagues and collaborators across various institutions. I am very thankful for having received the opportunity to carry out such an interdisciplinary and multifaceted PhD project with so many motivated and passionate fellow researchers.

My most enormous thanks and sincere appreciation go to my supervisors, Tom Peter and Gabriel Chiodo. I could not be more thankful for the chance to be actively engaged in writing and shaping the proposal for this PhD project and enjoying a high degree of freedom in what I wanted to focus on while constantly being supported in everything I was doing. This is not a given, especially since the project was not primarily related to Gabriel's original research focus. Nevertheless, both of you invariably provided the support I needed: helping with problems, discussing results, hiring people with the required expertise, hiring students working on the project, or figuring out administrative solutions for all the crazy ideas I was trying to push through.

I also want to highlight the substantial contributions to this project's success from Beiping Luo and Andrea Stenke. Beiping's inputs influenced the correct representation of sulfuric acid aerosol microphysics in SOCOL, the implementation of the representation of sulfuric acid coating on alumina particles, and the representation of heterogeneous reactions in SOCOL. With his persistence and conscientious way of working, he significantly contributed to the improvement and further development of the model. Working with you was a great pleasure, and I appreciate your support. The same goes for Andrea, with her vast expertise on SOCOL-AERv2: She always devised a solution to SOCOL problems. I am also indebted to Andrea for writing up the draft for the paper on the sulfuric acid aerosol microphysics under conditions of stratospheric climate intervention and for thoroughly sanity-checking the implementation of the solid particle microphysics scheme in SOCOL-AER. Likewise, I want to thank Ari Feinberg for his valuable support in implementing the solid particle microphysics scheme into SOCOL-AER during the project's initial phase. I enjoyed the many online meetings and discussions with Ari via Zoom during the Covid lockdown; they were very instructive. I was also grateful for the many bugs Andrea and Ari discovered in the code.

I further want to express my heartfelt thanks to Max Döbeli and Christof Vockenhuber from the Ion Beam Laboratory at ETHZ for performing the ERDA measurements and a detailed analysis of the measurements. Your help and the many hours invested in analyzing and interpreting the data significantly contributed to this thesis.

I am very appreciative of the collaboration and excellent support from Markus Ammann and his research group at the Paul Scherrer Institute (PSI), including Luca Longetti, Thorsten Bartels-Rausch, Yanisha Manoharan, Jérôme Gabathuler, Huanyu Yang and Lazo Andrés, during the AP-XPS beamtimes at Swiss Light Source (SLS), which also included many night shifts at the beamline. Thank you very much for having me as a guest scientist in your group and carefully supervising the XPS measurements. I also gratefully acknowledge SLS at PSI, who granted three beam times to this project using the AP-XPS beamline. In this respect, my special thanks are mainly directed towards Luca Artillia, beamline scientist at the in-situ AP-XPS beamline, who provided excellent assistance and support during the beam times by setting the boundary conditions for reliable measurements without technical problems.

Regarding the experimental work with XPS, I especially want to thank Pantanassa Telliou for her fantastic work during her internship in our group. Her support during beam

times and her careful data analysis were essential to this thesis' experimental chapter on calcite particles. Likewise, Oliver Klaus contributed with a detailed literature review on experimental work on the uptake of HCl and HNO<sub>3</sub> on calcite surfaces. In his semester project he proposed the representation of uptake coefficients as a function of exposure, which resulted in a central figure of this thesis.

I am very grateful to Frank Keutsch and his research group at Harvard University for having me for six months and funding this project via a fellowship from the Harvard Solar Geoengineering Research Program (SGRP). I appreciated the enriching discussions in the many meetings with Frank and the entire group. I enjoyed collaborating with David Verbart, Corey Petersen, and Yaowei Li and teaching them how to use SOCOL. I want to thank John Dykema, senior scientist in the Keutsch Group, for providing the optical properties of the different solid particles, which were subsequently fed into SOCOL. This represented a pivotal contribution to the project. Huge thanks also go to Rahel Weber, who joined the Keutsch Group with me to write her master thesis. With her work, Rahel substantially contributed to developing some of the central plots of this thesis, sanity-checking the final version of the solid particle scheme of SOCOL-AERv2 and analyzing these results. In the context of her master thesis, she measured the contact angle of H<sub>2</sub>SO<sub>4</sub> on alumina surfaces, which is an essential part of this project. Overall, I want to thank the whole Keutsch group. Visiting you was a great experience, and the positive group atmosphere will always leave a good memory.

I must also thank David Keith and Debra Weisenstein, with whom I wrote my master thesis at Harvard University in 2017, which was the start of my research career in SAI. I am grateful for the valuable exchanges we had during that project. Receiving the original 2D-AER code used in previous studies, which served as a basis for implementing the solid particles in SOCOL-AERv2, was very helpful. As the former head of the Harvard SGRP David Keith also needs to be acknowledged for granting me the SGRP fellowship. I cannot thank you enough for everything. A special thanks goes to Timofei Sukhodolov from Physical Meteorological Observatory Davos/World Radiation Center (PMOD/WCR), the new principal investigator of the SOCOL model family. Together with Timofei and Gabriel, we supervised semester projects and bachelor and master theses of several talented students. I thank the students, Gabriel and Timofei for the interesting and inspiring discussions during our weekly meetings.

I am very grateful for the students I supervised and co-supervised. Fabrice Stefanetti and Iris Schuring significantly contributed to successfully implementing the solid particle microphysics scheme into SOCOLv4 by carefully analyzing and proof-checking the model output. A fully coupled microphysics scheme implemented in SOCOLv4 would not have been possible without you.

An exceptional thanks goes to Sina Käslin, who wrote her bachelor thesis on the analysis of the injection of particles other than calcite and alumina with SOCOL-AERv2. She significantly helped develop illustrative figures. Furthermore, I want to thank Elia Wunderlin and Andrin Jörimann for their hard work on their master theses on GeoMIP simulations and geoengineering CCMi activities using SOCOLv4, respectively. Likewise, Christina Brodovsky and Jingyou Wang performed excellent master theses on the background stratospheric sulfur cycle and on evaluating the climate sensitivity of SOCOLv4, respectively. Despite my limited involvement in these projects, I immensely enjoyed discussing them.

I very much appreciated the help I received from Georgios Kelesidis and his student Alexander Bruun, who performed the discrete element model simulations to retrieve the



mobility radius of calcite and alumina agglomerates resulting from coagulation at different particle sizes and initial concentrations. Their work was crucial for the agglomerate representation in the model. I further want to express my gratitude to Martin Gysel-Beer from PSI, Zamin Kanji, Iris de Vries, and Arnold Müller from ETHZ Zurich, as well as Steven Hulshoff from TU Delft for their efforts and the lively discussions during meetings while writing up letters of interests and proposals to the Simon's Foundation to receive follow-up funding for this project. Regardless of the outcome of the applications, I will never forget our exciting collaboration.

I am immensely grateful to Gabriel, Tom, and Markus for allowing me to assist them with teaching the stratospheric chemistry master and atmospheric chemistry bachelor lectures. I also want to thank Urs Brändle for the excellent organization of the bachelor seminar "Environmental Systems" in which I coached and supervised a group of students during one semester. Teaching exercise classes was a valuable experience, and I will treasure the memory of the many positive encounters with students.

A special thanks also goes to the entire Atmospheric Chemistry Group, including Ulrich Krieger, for his support with the experimental part of the project, Liviana Klein for carrying out contact angle measurements, and Uwe Weers for helping with the ERDA measurements. Furthermore, Claudia Marcolli's comment on the contact angle of sulfuric acid on alumina during my second PhD interview was of great help. It led to the contact angle measurements and their implementation into the model. I also want to thank Marcel Müller for letting me use the overleaf template of his PhD thesis, which saved me many hours of work. Generally and most importantly, I want to thank the whole Atmospheric Chemistry Group for the fantastic time we shared during the almost four years of my PhD, be it during heated discussions in group meetings, great group retreats, or social activities.

I am happy that Jim Haywood from the University of Exeter accepted to serve as the external referee of my thesis. I am grateful for the valuable feedback he provided and the discussions we had on this work. In the same way, I want to thank Heini Wernli for spontaneously jumping in as a co-examiner, even though my thesis content is not his core topic of expertise. Additionally, I want to thank Ulrike Lohmann for valuable feedback during the PhD interviews as well as Daniela Domeisen and her group for formally accepting me into her group after Tom's retirement and for the welcoming group atmosphere. I also want to thank Petra Forney, Kate Stevens, and Arianne Maniglia, the present and former administrative assistants of the Atmospheric Chemistry Group, for their excellent support. I know that many issues related to this project required finding complicated solutions and making extra efforts. This was not easy, yet you invariably managed to find a solution for everything. Thank you very much for this. Also, I want to thank Urs Beyerle, Mathias Hauser, Hans-Heini Vogel, and Peter Isler for their excellent IT support. You always quickly found a solution to every problem.

Funding for this thesis was granted mainly by the ETH Research Grant no. ETH-1719-2. Further financial support was pledged by the Harvard SGRP fellowship, the Swiss Science Foundation (grant no. PZ00P2\180043), and group budget of Tom Peters Group at ETH as well as Frank Keutsch's Group at Harvard University. I want to thank Vanessa Schenker and Kevin Kilchhofer, my flatmates during the first Covid lockdown, for the lovely time, for putting up with the ups and downs I went through because of my PhD, for the uncountable heated Catan sessions (as well as for still talking to me after those), and for the productive and constructive home-office work atmosphere. This all made the whole pandemic much more than just bearable.

I sincerely want to thank my parents, Johanna and Bruno, and my sister, Jana, for providing me with many opportunities, believing in me, and supporting me in everything I do. Big thanks also go to my former teachers, who taught me everything that ultimately guided me towards writing this thesis. Furthermore, I want to thank all my friends, especially Jan and Sam, for their support, especially during the difficult times of the PhD.

Finally, I want to thank the most important person in my life, my partner, Camilla. We first met on August 3<sup>rd</sup>, 2019, two days before Tom, Gabriel and I had our first meeting to discuss the outline of the proposal for this project. During all that time, you have been my biggest supporter, especially when I was facing challenges with my PhD project. I know that this was not always easy for us, but I could not be more thankful for having you in my life.

**A big thank you to everyone!**

## CV Sandro Vattioni

Date of birth: December 21, 1991  
 Nationality: Swiss  
 Place of origin: Schwellbrunn, AR

### Education

---

03/2020 - 01/2024 **Doctorate at the Institute for Atmospheric and Climate Science, ETH Zurich, Switzerland**  
 PhD Thesis: 'Chemical and Climatic Impacts of Stratospheric Solar Climate Intervention', in collaboration with Paul Scherrer Institute, Harvard University and the Physical Meteorological Observatory Davos

09/2015 - 01/2024 **Teaching Diploma in Geography for Swiss Gymnasial Matura Schools, ETH Zurich, Switzerland**

01/2021 - 06/2021 **Research stays at Harvard University, Cambridge, USA**  
 09/2017 - 05/2018 Collaborating with the research groups of Prof. David Keith and Prof. Frank Keutsch on a SGRP fellowship

01/2017 - 06/2017 **Exchange Semester at the Hong Kong University of Science and Technology, Hong Kong**

09/2015 - 07/2018 **MSc in Atmospheric and Climate Sciences, ETH Zurich, Switzerland**  
 Master Thesis: 'Exploring accumulation-mode H<sub>2</sub>SO<sub>4</sub> versus SO<sub>2</sub> stratospheric sulfate geoengineering with SOCOL-AERv1'

09/2012 - 09/2015 **BSc in Earth Sciences, ETH Zurich, Switzerland**  
 Bachelor Thesis: 'Lake level reconstructions of Lake Sils in the Engadine valey using dendrochronology and C-14 dating'

06/2011 - 09/2018 **Swiss Army Weather Officer, Bière, Switzerland**  
 Swiss Army Officers School & Leadership Course 1

08/2007 - 06/2011 **Gymnasium, Kantonsschule Trogen, Switzerland**  
 Matura Thesis: 'The impact of volcanos on human society'

### Supervised Students, Teaching Experience and Funding Acquisition

---

#### Master Theses:

Rahel Weber, Elia Wunderlin,  
 Andrin Jörimann, Iris Schuring

#### Supervised Internship:

Pantanassa Telliou

#### Bachelor Thesis:

Sina Käslin

#### Semester Projects:

Oliver Klaus, Fabrice Stefanetti

#### Teaching Experience:

Teacher for Geography at the Gymnasim Liestal (FS2019)  
 Dynamische Erde, ETH (SS2016) Seminar Umweltsysteme, ETH (SS2020)  
 Atmosphärenchemie, ETH (FS2021&22) Stratospheric Chemsitry, ETH (FS21&22)

#### Involvement in Funding Acquisition:

ETH Research Grant (500k \$) Harvard SGRP Fellowship (20k \$)

---

**Scientific publications**

---

Vattioni, S., Luo, Beiping, F. A., Andrea, S., Vockenhuber, C., Weber, R., Dykema, J. A., Krieger, U., Ammann, M., Keutsch, F., Peter, T. and Chiodo, G.: Chemical impact of stratospheric alumina particle injection for solar radiation modification and related uncertainties, *Geophysical Research Letters*, <https://doi.org/10.1029/2023GL105889>, 2023

Vattioni, S., Stenke, A., Luo, B., Chiodo, G., Sukhodolov, T., Wunderlin, E., and Peter, T.: Importance of microphysical settings for climate forcing by stratospheric SO<sub>2</sub> injections as modelled by SOCOL-AERv2, *EGUsphere*, 2023, 1–25, <https://doi.org/10.5194/egusphere-2023-1726>, 2023

Li, Y., Pedersen, C., Dykema, J., Vernier, J.-P., Vattioni, S., Pandit, A. K., Stenke, A., Asher, E., Thornberry, T., Todt, M. A., Bui, T. P., Dean-Day, J., and Keutsch, F. N.: In situ measurements of perturbations to stratospheric aerosol and modeled ozone and radiative impacts following the 2021 La Soufrière eruption, *EGUsphere*, 2023, 1–22, <https://doi.org/10.5194/egusphere-2023-1891>, 2023.

Brodowsky, C. V., Sukhodolov, T., Chiodo, G., Aquila, V., Bekki, S., Dhomse, S. S., Laakso, A., Mann, G. W., Niemeier, U., Quaglia, I., Rozanov, E., Schmidt, A., Sekiya, T., Tilmes, S., Timmreck, C., Vattioni, S., Visionsi, D., Yu, P., Zhu, Y., and Peter, T.: Analysis of the 755 global atmospheric background sulfur budget in a multi-model framework, *EGUsphere*, 2023, 1–49, <https://doi.org/10.5194/egusphere-2023-1655>, 2023

Weisenstein, D. K., Visionsi, D., Franke, H., Niemeier, U., Vattioni, S., Chiodo, G., Peter, T., and Keith, D. W.: An interactive stratospheric aerosol model intercomparison of solar geoengineering by stratospheric injection of SO<sub>2</sub> or accumulation-mode sulfuric acid aerosols, *Atmos. Chem. Phys.*, 22, 2955–2973, <https://doi.org/10.5194/acp-22-2955-2022>, 2022.

Sukhodolov, T., Egorova, T., Stenke, A., Ball, W. T., Brodowsky, C., Chiodo, G., Feinberg, A., Friedel, M., Karagodin-Doyennel, A., Peter, T., Sedlacek, J., Vattioni, S., and Rozanov, E.: Atmosphere–ocean–aerosol–chemistry–climate model SOCOLv4.0: description and evaluation, *Geosci. Model Dev.*, 14, 5525–5560, <https://doi.org/10.5194/gmd-14-5525-2021>, 2021.

Vattioni, S., Weisenstein, D., Keith, D., Feinberg, A., Peter, T., and Stenke, A.: Exploring accumulation-mode H<sub>2</sub>SO<sub>4</sub> versus SO<sub>2</sub> stratospheric sulfate geoengineering in a sectional aerosol–chemistry–climate model, *Atmos. Chem. Phys.*, 19, 4877–4897, <https://doi.org/10.5194/acp-19-4877-2019>, 2019.

Schlüchter, C., Bonani, G., Donau, F., Grischott, R., Nicolussi, K., Pfenninger, A., Schlüchter, B., Seifert, M., Vattioni, S., and Hajdas, I.: Rätselhafte Unterwasserbäume in den Oberengadiner Seen, *Jahresbericht der Naturforschenden Gesellschaft Graubünden*, 120, 41–49, <https://boris.unibe.ch/id/eprint/120037>, 2018.